



Repeatability of Self-Healing in ECC with Various Mineral Admixtures

A Thesis submitted in fulfilment of requirements for the award of Doctor of
Philosophy in Architecture

By

Guangwei CHEN

School of Architecture and Built Environment
The University of Newcastle

April 2021

Statement of Originality

I hereby certify that the work embodied in this thesis is my own work, conducted under normal supervision. This thesis contains no material which has been accepted or is being examined for the award of another degree or diploma in any university or other tertiary institution and to the best of my knowledge and belief, contains no material previously published or written by another person, except where due reference has been made in the text. I give consent to the final version of my thesis being made available worldwide when deposited in the University's Digital Repository, subject to the provisions of Copyright Act 1968 and any approved embargo.

Your signature

.....

Guangwei CHEN

Acknowledgements

The research work studied in this thesis was sponsored by the Chinese Scholarship Council (CSC) and University of Newcastle, Australia. I would like to express my appreciation to these institutions.

Many people have supported me in this research, and they are recognized here. I would like to express my sincere gratitude to my supervisor, Prof. Patrick Tang, for his continuous support of my PhD study, and for his patience, motivation, and immense knowledge. His guidance helped me throughout the research and writing of this thesis.

I am thankful that my friendships with him and his family has made my life abroad more colourful and warm. I am especially thankful for the care and help his family gave us after the birth of our newborns, which made me feel extremely inspired during the most difficult phase of my study abroad. I could not have imagined having a better supervisor for my PhD study.

My greatest appreciation goes to my co-supervisor, Prof. Shanyong Wang, for his guidance, support, and encouragement throughout the whole course of my research.

I would like to express my gratitude to Ian Jeans, Dr Shaun Manning, Dr Yun Lin, Goran Simundic, Ross Gibson for their assistance in the experimental testing. I am very thankful to Maria Roberts, who has help me with the English writing of this thesis.

Appreciations also go to Dr Florencia Theograsia, Dr Juan Pablo Quijano Baron, Ms Lilly Großstück, Dr Andrei Pomana, Mr Michael Shen, Ms Lucy Guzmán, Mr Andrew McRae, Dr Nguyen Khanh Hung, Dr Quang Anh Tran, Mr Tommy Lin, Ms Iris Wu, Mr Chris Priestley, and Mrs

Halina Priestley for their supports and helps in my daily life during these years in Newcastle.

Last but not least, I would like to express my deepest gratitude to my wife, Sylvia Chen, for her unconditional love, support and endless encouragements. My twin daughters, Selene and Sally, have brought me extensive happiness and made my life beautiful. Their lovely smiles and love is my best gift.

Publications

Publications

- Tang, Waiching, Guangwei Chen, and Shanyong Wang. Self-Healing Capability of ECC Incorporating with Different Mineral Additives - a Review. 3rd International RILEM Conference on Microstructure Related Durability of Cementitious Composites, RILEM Publications, 2016.
- Prediction of self-healing in ECC - Machine learning comparative analysis, Journal of Building Engineering, 2021. (Under review)

Abstract

Concrete structures are susceptible to cracking that is primarily responsible for the reduction of the strength and stiffness of the concrete structure. This has substantial negative influences on the durability and sustainability of concrete, as well as significantly reducing the service life of the whole concrete infrastructure. For prolonging the service life of concrete infrastructure affected by cracks, self-healing of cementitious materials has attracted more and more attention. Engineered Cementitious Composite (ECC) has an intrinsic ability to control the width of cracks and to promote self-healing, which makes ECC the most promising self-healing material for improving the durability and serviceability of concrete structures.

The aim of this research is to evaluate the self-healing behaviour of ECC when incorporated with different minerals, focusing on self-healing capability, repeatability and modelling prediction. In addition, it is expensive and time-consuming to quantify self-healing capability by conducting experiments, and difficult to mathematically predict self-healing based on available data. Therefore, an accurate and reliable self-healing prediction model will be designed to reduce time and costs for enhancing the durability design of ECC.

For this purpose, ECC mixtures were created in which Fly Ash (FA) was partially replaced by 5%, 10% and 15% of Hydrated Lime Powder (LP) or Silica Fume (SF), and an ECC mixture without LP or SF was used as a control. The samples were precracked using a newly developed splitting tensile test apparatus at the age of 28 days. After that, the specimens were exposed to curing conditions with 10 Wet-Dry (W/D) cycles for self-healing of cracks. To study the self-healing capability and repeatability,

the load was re-applied to the specimens after each 10 W/D cycles. A Rapid Chloride Permeability Test (RCPT) and splitting tensile test were utilized to assess the self-healing repeatability of ECC in terms of chloride ion permeability and mechanical properties, respectively. The recovery rate of crack width associated with different mixtures was supported and analysed by digital microscope observations. The precipitations formed at the surface of cracks were detected by Scanning Electron Microscope (SEM) equipped with an Energy Dispersive Spectroscopy (EDS), and then further examined by X-ray Diffraction Analysis (XRD).

Experimental results show that all mixtures exhibited self-healing with slight differences. The microstructure was also assessed using SEM–EDS and XRD analysis. The microstructural analysis of healed cracks in LP-incorporated ECC mixtures showed the presence of calcite, portlandite and Calcium Silicate Hydrates (C-S-H) gels as well as monocarboaluminate, which confirmed a possible reaction between FA and LP.

Digital microscope analysis of crack width recovery showed that the addition of 5% SF is only beneficial for improving the recovery of crack width that is around $20\text{ }\mu\text{m}$. The addition of 15% LP significantly improves the crack width recovery ability and repeatability compared to the reference sample. When SF and LP are added at the same time, the synergistic effect of 5% SF and 10% LP shows the best crack width recovery results.

RCPT results show that all mixtures exhibited repeated self-healing with slight differences. The addition of 10% SF shows two times significant self-healing ability under three times repetitive loading; however, 15% SF is not conducive to repeated self-healing under multiple loading. The addition of 10% LP shows the best recovery rate. When SF and LP were simultaneously added to ECC mixtures, the RCPT results of FA55-SF10-LP5 and FA55-SF5-LP10 are all below the low level before and after three times of preloading and self-healing, in accordance with ASTM C1202.

For the case where the load is applied only once, the exposure time of the W/D environment affects the self-healing capability of splitting tensile strength. The addition of 5% or 10% of SF to FA70 can increase the splitting tensile strength recovery rate of ECC samples within 30 W/D cycles. The addition of 15% SF to FA70 is beneficial for short term mechanical recovery but is not conducive to the recovery of mechanical properties in the long term. The addition of 10% LP is most conducive to improvement in the recovery of mechanical properties, especially for samples undergoing 60 W/D cycles. When SF and LP were simultaneously added to ECC mixtures, the addition of SF and LP at the same time shows a better recovery effect than adding only one mineral alone. FA55-SF5-LP10 shows the best recovery rate after 60 W/D cycles. In the case of repeated load application, FA55-SF15 shows the highest healing efficiency in the first round of self-healing, FA60-LP10 shows the highest splitting tensile strength recovery rate after three loads, and the recovery rate can still reach 66.43%. When SF and LP are simultaneously added, after three rounds of self-healing the splitting strength recovery rate of FA55-SF5-LP10 is significantly higher than other mixes, reaching 81.56%.

The SEM and XRD analysis of healed cracks in different mineral-incorporated ECC mixtures showed that a mixture of CaCO_3 and C-S-H are found as main self-healing products, however, the dominant healing product depends on the type and the proportion of minerals in ECC.

The recovery in the mechanical and durability performance of the mixtures due to self-healing proposed in this research is anticipated to positively affect life cycle costs and lead to increased civil infrastructure sustainability.

In order to develop a robust prediction tool for modelling the self-healing capability of ECC, a comparative study was conducted to evaluate the efficacy of machine learning models in predicting the self-healing ability of ECC using empirical data from the experimental study. In this study,

four individual models, including Linear Regression (LR), Support Vector Regression (SVR), Back-propagation Neural Network (BPNN), and Classification and Regression Tree (CRAT), and three ensemble models namely bagging, AdaBoost and stacking, are adopted to develop 13 prediction models in total.

The comparative analysis showed all 13 models came with expected accuracy and predictability. The BPNN model was prominent in the individual models in terms of forecast error, Root Mean Square Error (RMSE) and accuracy, R^2 . Stacking model was superior to all other individual or ensemble models on the basis of all three performance measures.

The efficiency analysis of different machine learning methods for self-healing prediction in the comparative study provides a reference for choosing machine learning methods to predict the repeatability of crack self-healing in ECC. Therefore, the BPNN model is further optimized by the Evolutionary Algorithm (EA) in structured tree and list to construct two predictive tools to model the self-healing repeatability of ECC for improving the prediction performance. The proposed EA-based BPNN models overcame the drawback of BPNN with slow convergence and getting trapped in local minima. Especially, the EA-based BPNN in structured tree model ensures genetic diversity and keep fit solutions guaranteeing quality children of following generations, and is more space efficient leading to quick searching and convergence. Computational results reveal that the EA-based BPNN in structured tree model is superior to EA-based BPNN in structured list model which improves the performance of BPNN on all three statistical measurements on all three datasets including training, validation and testing.

Glossary

CW_l The crack width after loading.

CW_s The crack width after self-healing cycle.

P Maximum applied load indicated by the testing machine, N .

R Correlation coefficient.

R^2 Coefficient of determination.

R^n n -dimensional space.

R_{cw} Recovery rate of crack width.

R_s Recovery of splitting tensile strength.

S Splitting tensile strength, MPa.

$S_{preload}$ Splitting tensile strength of specimen during preloading.

S_{reload} Splitting tensile strength of specimen during reloading.

δ Standard Deviation.

μ Mean.

\bar{y} Mean of the target or observed output.

ξ, ξ_i^* Slack variables.

a_i The constant regression coefficients.

b An error term.

f Linear or nonlinear function.

f_x Properties of concrete.

l, d lenght and diameter, mm .

n The number of samples.

w Regression coefficient.

x The structured influencing attribute, input varaiable.

x' The scaled value of the varaiable x .

x_i The i th structured influencing attributes.

x_{max} The maximum value of the varaiable x .

x_{min} The minmum value of the varaiable x .

y_i The target or observed output.

y'_i The predicted output.

Acronyms

AAE Average Absolute Deviation.

AI Artificial Intelligence.

ANN Artificial Neural Network.

BAS Beetle Antennae Search.

BFS Blast Furnace Slag.

BPNN Back-propagation Neural Network.

BSE Back Scattered Electron.

C-S-H Calcium Silicate Hydrates.

CA Coarse Aggregates.

COV Coefficient of Variation.

CRAT Classification and Regression Tree.

CT-scanning X-ray Computed Tomography.

DT Decision Tree.

EA Evolutionary Algorithm.

ECC Engineered Cementitious Composite.

EDS Energy Dispersive Spectroscopy.

EM Ensemble Methods.

ESEM Environmental Scanning Electron Microscopy.

FA Fly Ash.

FHW First Healed Crack Width.

GA Genetic Algorithm.

GBRT Gradient Boosted Regression Tree.

GPC General Purpose Cement.

GPR Gaussian Process Regression.

HPC High Performance Concrete.

HPFRCC High Performance Fibre Reinforced Cementitious Composite.

HRWR High Range Water Reducer.

LP Hydrated Lime Powder.

LR Linear Regression.

LSP Limestone Powder.

LSSVR Least Squares Support Vector Regression.

MAE Mean Absolute Error.

MAPE Mean Absolute Percentage Error.

MART Multiple Additive Regression Tree.

ML Machine Learning.

MSE Mean Square Error.

MTS Material Testing Systems.

POFA Palm Oil Fuel Ash.

PSO Particle Swarm Optimization.

PSS-ECC Passive Smart Self-Healing Engineered Cementitious Composite.

PVA Polyvinyl Alcohol.

RCPT Rapid Chloride Permeability Test.

RF Random Forest.

RH Relative Humidity.

RMSE Root Mean Square Error.

RWS Roulette Wheel Selection.

S Fine Aggregates.

SAC fiber Sealing Agent Carrying fibre.

SAP Super Absorbent Polymer.

SCMs Supplementary Cementitious Materials.

SE Secondary Electron.

SEM Scanning Electron Microscope.

SF Silica Fume.

SFW Second Final Crack Width.

SHCC Strain-Hardening Cement Composite.

SIW Second Initial Crack Width.

SP Superplasticizer.

SSE Sum of the Squares Error.

SVC Support Vector Classification.

SVM Support Vector Machine.

SVR Support Vector Regression.

UHP-SHCC Ultra-High Performance Strain-Hardening Cement Composite.

VP Variable Pressure.

W/CM Water to Cementitious Materials Ratio.

W/D Wet-Dry.

XRD X-ray Diffraction Analysis.

Contents

Glossary	10
Acronyms	12
1 Introduction	1
1.1 Research background	1
1.2 Aim and objectives of this research	3
1.3 Outline of this thesis	5
2 Literature Review	7
2.1 Introduction	7
2.2 Self-healing concept and mechanisms	8
2.3 Self-healing approaches	8
2.3.1 Adhesive agents	8
2.3.2 Bacteria	9
2.3.3 Mineral admixtures	10
2.3.4 Autogenous self-healing	10
2.4 Engineered cementitious composites	12
2.5 Methods to produce ECC with self-healing property	12
2.5.1 Superabsorbent polymer (SAP) particles	13
2.5.2 Hollow glass fibres	14
2.5.3 Mineral admixtures	15
2.6 Self-healing of ECC with mineral admixtures	17
2.6.1 Expansive additive	18
2.6.2 Crystalline additive	19
2.6.3 Silica-based pozzolans	20

2.6.4	Combination of minerals	21
2.7	Test method for self-healing of ECC with mineral admixtures	22
2.7.1	Method of producing cracks	22
2.7.2	Evaluation method of ECC self-healing	23
2.8	Machine learning in prediction of properties of concrete	24
2.8.1	Evaluation of machine learning models	26
2.8.2	Prediction of mechanical properties of concrete	29
2.8.2.1	Artificial neural network	31
2.8.2.2	Support vector regression	34
2.8.2.3	Decision tree	38
2.8.2.4	Ensemble methods	39
2.8.3	Prediction of self-healing capacity of concrete	41
2.9	Summary	41
3	Experimental Study	44
3.1	Introduction	44
3.2	Materials and samples preparation	45
3.2.1	Materials	45
3.2.2	Mix proportions and samples preparation	46
3.2.3	Mixing and casting procedures	46
3.3	Pre-cracking and self-healing evaluation methods	48
3.3.1	Producing controlled cracks	48
3.3.2	Multiple loading and healing process	50
3.3.3	Digital microscope study	51
3.3.4	Rapid chloride permeability test	54
3.3.5	Splitting tensile test	54
3.3.6	SEM/EDS	57
3.3.7	XRD	60
3.4	Results and discussion	60
3.4.1	Digital microscope study with the crack width recovery	60
3.4.1.1	Visual closure of the cracks and the appearance of the healing products	60

3.4.1.2	The effect of adding SF on crack width recovery	68
3.4.1.3	The effect of adding LP on crack width recovery	69
3.4.1.4	The effect of adding two minerals on crack width recovery	71
3.4.1.5	The influence of content change between LP and SF on crack width recovery	76
3.4.2	RCPT test and repeated self-healing behaviour	78
3.4.2.1	Changes in chloride ion permeability after repeated preload	78
3.4.2.2	Percent variations in chloride ion permeability	84
3.4.3	Splitting tensile strength recovery	88
3.4.3.1	Effect of W/D environment exposure time on recovery of splitting tensile strength	89
3.4.3.2	Repeatability of splitting tensile strength recovery after multiple loading cycles	93
3.4.4	Self-healing product analysis(SEM/EDS/XRD)	95
3.4.4.1	SEM Morphological analysis	96
3.4.4.2	Chemical elements	101
3.4.4.3	XRD material identification	104
3.5	Summary	105
3.5.1	Crack width recovery	106
3.5.2	Recovery of chloride ion permeability	107
3.5.3	Mechanical recovery	108
3.5.4	Self-healing products	109
4	Machine Learning Comparative Analysis of Self-Healing Abilities of ECC	111
4.1	Introduction	111
4.2	State-of-the-art prediction of the self-healing ability of ECC	112
4.3	Data description and preparation	113
4.3.1	Data collection	113
4.3.2	Preprocessing of data	114

4.4	Methodology	114
4.4.1	Linear regression	115
4.4.2	Support vector regression	115
4.4.3	Artificial neural network	117
4.4.4	Classification and regression tree	119
4.4.5	Ensemble methods	120
4.4.5.1	Bagging	121
4.4.5.2	AdaBoost	121
4.4.5.3	Stacking	121
4.4.6	Model construction	122
4.5	Validation and evaluation	123
4.5.1	Cross-validation method	123
4.5.2	Performance evaluation	123
4.6	Results and discussion	125
4.7	Summary	137
5	Modeling Self-healing Repeatability of ECC With Evolutionary Algorithm Based Artificial Neural Network	139
5.1	Introduction	139
5.2	Data collection and preprocessing	140
5.3	Modelling self-healing repeatability of ECC	141
5.3.1	BPNN architecture	141
5.3.2	Principle of EA-based BPNN	144
5.3.3	Structured evolutionary algorithm	147
5.3.3.1	Individuals, population and initialization	147
5.3.3.2	Fitness function	149
5.3.3.3	Selection criterion	150
5.3.3.4	Crossover and mutation	150
5.4	Computational results and discussion	152
5.5	Summary	163

6 Conclusions and Prospects	165
6.1 Conclusions	165
6.1.1 Self-healing capability and repeatability of ECC	165
6.1.1.1 The effect of crack size on repeated self-healing	165
6.1.1.2 Crack width recovery	165
6.1.1.3 Chloride ion permeability recovery	166
6.1.1.4 Splitting tensile strength recovery	167
6.1.2 Self-healing products after re-healing	168
6.1.3 Prediction of the self-healing capability of ECC	169
6.1.4 Predict the repeatability of self-healing	170
6.2 Prospects	170
Appendices	172
A Programming of comparative analysis	172
B Programming of BPNN optimized with EA in structured tree and list	175
C Summary of machine learning application	184
References	191

List of Figures

1.1	Outline of this thesis	6
2.1	Visualization of crack-sealing with hardened adhesive agents by means of X-ray Computed Tomography	9
2.2	Simplified representation of carbonate precipitation induced by the hydrolysis of urea with the help of bacteria	10
2.3	Main mechanisms of autogenous healing (a) formation of calcium carbonate from calcium hydroxide; (b) settlement of the debris and loose cement particles in presence of water; (c) hydration of unhydrated cementitious particles; (d) further swelling of the hydrated cementitious matrix	11
2.4	Manufacture of the capsules	13
2.5	Formation of through crack in Environmental Scanning Electron Microscopy (ESEM) specimens	15
2.6	Commonly used machine learning types and algorithms	26
2.7	Structure of an ANN model with m input variables and n hidden layers.	32
2.8	Hyperplane classification	35
2.9	Nonlinear mapping in Support Vector Machine (SVM)	36
3.1	Concrete cylinders were cut using a diamond blade saw to obtain 50 mm-thick discs: (a) standard plastic molds for casting cylinder specimens; (b) se-moulded cylinder specimens; (c) concrete cutting; (d) samples after cutting	47
3.2	The apparatus used to produce cracks	49
3.3	Wet-Dry (W/D) cycling environment: (a) wet cycles; (b) dry cycles .	51
3.4	Preloading and reloading schedule of self-healing repeatability study .	51

3.5	Crack marking and measurement: (a) producing cracks; (b) observation area; (c) divide the observation interval; (d) AmScope Optical microscope observation	52
3.6	Schematic diagram of measuring observation areas on the surface of ECC mixture specimen	53
3.7	Rapid chloride permeability test setup. (a) Vacuum saturated machine; (b) Specimen setup; (c) RCPT equipment	55
3.8	Preloading and reloading schedule of splitting tensile strength study .	55
3.9	Splitting tensile strength test	56
3.10	Sample preparation	59
3.11	Cressington 208C High Vacuum Turbo Carbon Coater (a), and Scanning electron microscope (b)	59
3.12	Typical crack surface appearance during W/D process, 20 μm	63
3.13	Typical crack surface appearance during wetting-drying process, 50 μm	64
3.14	Typical crack surface appearance during wetting-drying process, 100 μm	65
3.15	Appearance of self-healing substances under digital microscope	67
3.16	Effect of two minerals on crack width recovery, FA and SF	69
3.17	Effect of two minerals on crack width recovery, FA and LP	70
3.18	When the content of SF is constant, replace FA with LP, SF content is 5%	73
3.19	When the content of SF is constant, replace FA with LP, SF content is 10%	74
3.20	When the content of LP is constant, replace FA with SF, LP content is 5%	75
3.21	When the content of LP is constant, replace FA with SF,LP content is 10%	76
3.22	Effect of two minerals on crack width recovery, the LP in FA55-LP15 is gradually replaced by SF	77
3.23	RCPT results of different cycles (comparison of the influence of SF content)	79

3.24 RCPT results of different cycles (comparison of the influence of LP content)	80
3.25 RCPT results of different cycles (Replace 10% FA in FA65-SF5 with LP)	81
3.26 RCPT results of different cycles (Replace 5% FA in FA60-SF10 with LP)	82
3.27 RCPT results of different cycles (Replace 5% FA in FA60-LP10 with SF)	82
3.28 RCPT results of different cycles (Replace 10% FA in FA65-LP5 with SF)	83
3.29 RCPT results of different W/D cycles (the process of SF being gradually replaced by LP in FA55-SF15; 1). FA55-SF15, relative to FA70, replace 15% FA with SF; 2)FA55-SF10-LP5, relative to FA55-SF15, replace 5% SF with LP; 3)FA55-SF5-LP10, relative to FA55-SF10-LP5, replace 5% SF with LP; 4)FA55-LP15, relative to FA55-SF5-LP10, replace 5% SF with LP;5	83
3.30 Percent variations in chloride ion permeability values of ECC mixtures containing different proportions of SF	85
3.31 Percent variations in chloride ion permeability values of ECC mixtures containing different proportions of LP	87
3.32 Percent variations in chloride ion permeability values of ECC mixtures due to repetitive preloading (SF and LP are included)	88
3.33 Effect of W/D environment exposure time on splitting tensile strength recovery of samples ECC incorporating SF	89
3.34 Effect of W/D environment exposure time on splitting tensile strength recovery of samples ECC incorporating LP	90
3.35 Effect of W/D environment exposure time on splitting tensile strength recovery of samples ECC incorporating multiple minerals (SF in FA65-SF15 is gradually replaced by LP)	92
3.36 The effect of SF on splitting tensile strength recovery in the process of multiple loading	93

3.37 The effect of LP on splitting tensile strength recovery in the process of multiple loading	94
3.38 The effect of samples incorporated multiple minerals on recovery during multiple loadings. (The SF in FA65-SF15 is gradually replaced by LP)	95
3.39 SEM micrograph with EDS pattern of products in self-healed cracks, FA70	96
3.40 SEM micrograph with EDS pattern of products in self-healed cracks, FA55-SF15	97
3.41 SEM micrograph with EDS pattern of products in self-healed cracks,FA55-LP15	99
3.42 SEM micrograph with EDS pattern of products in self-healed cracks, FA55-SF10-LP5	100
3.43 SEM micrograph with EDS pattern of products in self-healed cracks, FA55-SF5-LP10	101
3.44 Chemical analysis of healing products by EDS	103
3.45 XRD patterns of self-healing products in ECC mixtures, after first self-healing	104
4.1 Flow chart for implementing prediction machine learning models for self-healing capability of ECC	113
4.2 Schematic diagram of BPNN model for predicting self-healing capability of ECC	118
4.3 Structure of a classification and regression tree	119
4.4 Schematic diagram of Stacking model	122
4.5 Ten-fold cross-validation approach	124
4.6 Average MAE for performance of self-healing of ECC on all machine learning models	126
4.7 Average RMSE for performance of self-healing of ECC on all machine learning models	127
4.8 Average R^2 for performance of self-healing of ECC on all machine learning models	127

4.9	Comparison of observed and predict crack width after self-healing process of ECC by LR	130
4.10	Comparison of observed and predict crack width after self-healing process of ECC by BPNN	131
4.11	Comparison of observed and predict crack width after self-healing process of ECC by SVR	131
4.12	Comparison of observed and predict crack width after self-healing process of ECC by CRAT	132
4.13	Comparison of observed and predict crack width after self-healing process of ECC by Ada_LR	132
4.14	Comparison of observed and predict crack width after self-healing process of ECC by Ada_BPNN	133
4.15	Comparison of observed and predict crack width after self-healing process of ECC by Ada_SVR	133
4.16	Comparison of observed and predict crack width after self-healing process of ECC by Ada_CRAT	134
4.17	Comparison of observed and predict crack width after self-healing process of ECC by Bag_LR	134
4.18	Comparison of observed and predict crack width after self-healing process of ECC by Bag_BPNN	135
4.19	Comparison of observed and predict crack width after self-healing process of ECC by Bag_SVR	135
4.20	Comparison of observed and predict crack width after self-healing process of ECC by Bag_CRAT	136
4.21	Comparison of observed and predict crack width after self-healing process of ECC by Stack_LR	136
5.1	The architecture of the BPNN model for predicting self-healing repeatability of ECC	142
5.2	Schematic diagram of BPNN model for predicting self-healing repeatability of ECC	145

5.3	Demonstration of encoding the weights and biases of BPNN in chromosomes of EA	147
5.4	Individuals hierarchically structured in a four level ternary tree with 13 clusters in EA	149
5.5	Operators of single-point crossover and mutation	151
5.6	Comparison of target and predicted SFW of ECC on training dataset by BPNN	154
5.7	Comparison of target and predicted SFW of ECC on training dataset by EA-based BPNN in structured list	154
5.8	Comparison of target and predicted SFW of ECC on training dataset by EA-based BPNN in structured tree	155
5.9	Comparison of target and predicted SFW of ECC on validation dataset by BPNN	155
5.10	Comparison of target and predicted SFW of ECC on validation dataset by EA-based BPNN in structured list	156
5.11	Comparison of target and predicted SFW of ECC on validation dataset by EA-based BPNN in structured tree	156
5.12	Comparison of target and predicted SFW of ECC on testing dataset by BPNN	157
5.13	Comparison of target and predicted SFW of ECC on testing dataset by EA-based BPNN in structured list	157
5.14	Comparison of target and predicted SFW of ECC on testing dataset by EA-based BPNN in structured tree	158
5.15	Target and predicted SFW of ECC on training dataset by BPNN . .	158
5.16	Target and predicted SFW of ECC on training dataset by EA-based BPNN in structured list	159
5.17	Target and predicted SFW of ECC on training dataset by EA-based BPNN in structured tree	159
5.18	Target and predicted SFW of ECC on validation dataset by BPNN . .	160
5.19	Target and predicted SFW of ECC on validation dataset by EA-based BPNN in structure list	160

5.20 Target and predicted SFW of ECC on validation dataset by EA-based BPNN in structure tree	161
5.21 Target and predicted SFW of ECC on testing dataset by BPNN	161
5.22 Target and predicted SFW of ECC on testing dataset by EA-based BPNN in structured list	162
5.23 Target and predicted SFW of ECC on testing dataset by EA-based BPNN in structured tree	162

List of Tables

1.1	Detailed structure of research objectives, strategies and results	4
2.1	Mineral admixtures for self-healing of ECC and other matrixes reported in literature	17
2.2	Test methods used to assess the self-healing of ECC with mineral admixtures	23
3.1	Physical properties and chemical composition of different minerals . .	45
3.2	Properties of PVA fibres	45
3.3	Mix proportions of ECC.	46
3.4	Crack pattern of ECC mixtures.	61
3.5	Chemical compositions of healing materials	102
4.1	Number of instances and range of input and output features collected from nine ECC mixes	114
4.2	Prediction model parameter settings	123
4.3	Ten-fold cross-validation results of machine learning models on self-healing prediction for ECC	125
4.4	Performance deviation of ensemble models from benchmark models on self-healing of ECC	129
5.1	Statistical parameters of training, validation, and test datasets	141
5.2	Statistical performance of proposed BPNN and EA-based BPNN models on training, validation and testing datasets	152
C.1	Summary of the application of ML models in the prediction of the mechanical properties of concrete.	185

Chapter 1

Introduction

1.1 Research background

Concrete is a fundamental construction material amounting to 12 billion metric tons annual consumption throughout the world [1]. However, concrete structures are susceptible to cracking that is primarily responsible for the reduction of the strength and stiffness of the concrete structure. This has substantial negative influences on the durability and sustainability of concrete as well as significantly reducing the service life of the whole concrete infrastructure [2]. A market research project was commissioned by Materials for Life (M4L), which shows cracking damage in concrete was experienced more than any other problems [3].

For prolonging the service life of concrete infrastructure affected by cracks, man-made maintenance and repair is a common solution [4] leading to a high financial burden on societies [5]. Annual costs spent on inspection, monitoring, maintenance, refurbishment and repair of such concrete structures is estimated at around one third of the annual construction budget in the Netherlands [5] while in Europe, the number goes to almost 50% [6]. In the U.S., the cost of the maintenance and repairs of civil infrastructure is estimated to be 3.6 trillion dollars from 2016 to 2020 [7]. Some structures, such as bridges and tunnels, have to be taken out of service to be repaired. As a result of traffic jams and loss of productivity caused by infrastructure that is out of service, the indirect costs are typically 10 times higher than the direct cost of repairing those structures [8]. Apart from the financial aspects, it is difficult to obtain durable repairs and repeated maintenance is required [9]. Most of these man-made repairs are often short-lived, only lasting for ten to fifteen years even though the quality of reconstruction has substantially increased in recent years [4].

Moreover, it is even impossible to execute crack repair in some cases that are not accessible, such as cracks in underground concrete facilities [10].

Based on such circumstances, self-healing of cementitious materials is highly desirable in terms of their ability to heal themselves and regain the loss of performance without any external intervention [11]. As one of the major mechanisms of self-healing in cementitious materials, autogenous self-healing of cracks in concrete has been noticed in water-retaining structures, such as culverts and sandstone, by Hyde [12] as early as the end of the nineteenth century [13]. Autogenous self-healing indicates that self-healing ability results from the physical and/or chemical composition of the cementitious matrix [2]. The reaction process of autogenous self-healing is attributed to the combined effects of multiple mechanisms which include calcium hydroxide carbonation and further hydration of cement particles and/or swelling of calcium silicate hydrate [14]. However, it has an essential requirement, which is the presence of water capable of further reaction for effective self-healing of cracks [15].

Although concrete has shown self-healing ability, it is rarely observed in concrete structures. Because the crack width as a critical factor is required to be below 200 μm , preferably less than 50 μm for promoting self-healing behaviour in concrete [16], it is therefore necessary to restrict crack width to ensure robust self-healing ability in concrete.

Engineered Cementitious Composite (ECC) is a High Performance Fibre Reinforced Cementitious Composite (HPFRCC) designed with micro-mechanical principles [17]. It features high tensile strain of 3–5% with a moderate fibre-volume fraction [16, 18], typically 2% by volume, while maintaining very tight crack width. The width of cracks in ECC is typically below 100 μm even when strained to several percent [19]. This intrinsic ability of ECC to control crack width naturally promotes its self-healing capability, which makes ECC the most promising self-healing material for improving the durability and serviceability of concrete structures [20].

Over the lifetime of a piece of infrastructure, cracks are likely to occur more than once, even in cases where cracks reoccur in the same location after self-healing. A concern has arisen about the repeatability of self-healing related to the robustness of the self-healing mechanism. Sahmaran [9] has observed that the self-healing mechanism of ECC is widely dispersive under six repetitive loading conditions, and

suggested more detailed studies are needed on the related topic. Moreover, self-healing repeatability of ECC is strongly influenced by the composition of the matrix associated with the mechanisms of self-healing in concrete. Although studies have reported the influence of different mineral admixtures, such as Limestone Powder (LSP) [21, 22], Fly Ash (FA) [20, 23], Hydrated Lime Powder (LP) [24], and Blast Furnace Slag (BFS) [9, 25–27] on self-healing behaviour, research on the self-healing repeatability of ECC with different mineral admixtures is relatively rare, and with a combination of multiple mineral admixtures is even rarer.

Moreover, there is a lack of quantitative information about the relationship between the potential for self-healing of ECC and the amount of mineral admixtures. The potential for self-healing of ECC is complex and non-linear due to its material nature, interactivity between different components, such as the volume of mineral admixtures, in the cementitious matrix [28] and unpredictable crack location, orientation and width [29]. It is expensive and time-consuming to quantify self-healing capability by conducting experiments and difficult to predict self-healing mathematically based on available data. Therefore, an accurate and reliable self-healing prediction model would be very helpful and would reduce the time and costs needed for enhancing the durability design of ECC.

1.2 Aim and objectives of this research

The aim of this research is to investigate the effects of minerals on the self-healing properties of ECC and to predict the potential self-healing capability of ECC. In order to achieve this aim, the principal objectives have been identified and are outlined in the following paragraphs. A detailed research objective, research strategies and results are shown in Table 1.1.

- There has been little research on the self-healing property of ECC using expansive minerals and indeed the research on ECC with a combination of various minerals is extremely limited. The first objective of this research is to investigate the potential of self-healing capability of ECC incorporating different minerals.

Table 1.1: Detailed structure of research objectives, strategies and results

Objective	Research content	Strategy	Result
Self-healing capability and repeatability of ECC	Crack width recovery Permeability recovery Mechanical recovery	Digital microscope study Rapid chloride permeability test (RCPT) Splitting tensile test	Section 3.4.1 Section 3.4.2 Section 3.4.3
Self-healing products after rehealing	Morphology and chemical composition Determine dominant healing products	Scanning electron microscope (SEM) Energy dispersive spectroscopy (EDS) X-ray diffraction analysis (XRD)	Section 3.4.4.1 Section 3.4.4.2 Section 3.4.4.3
Predict of the self-healing capability of ECC	Comparison of prediction results of different models	Linear Regression (LR), Back-propagation Neural Network (BPNN), Support Vector Regression (SVR), Classification and Regression Tree (CRAT), Bagging, AdaBoost and stacking	Section 4.6
Predict of the repeatability of self-healing	Develop an prediction model of repeatability of self-healing	Evolutionary algorithm based BPNN	Section 5.4

- The repeatability of the self-healing of a crack under repeated loads is still uncertain, and the recovery of mechanical properties and permeability after repeated cracking is not clear. The second objective, therefore, is to analyse the repeatability of self-healing on crack width and the recovery of mechanical properties and permeability under repeated tensile splitting tests.
- There has been very few investigations carried out to study the morphological characteristics and chemical composition of self-healing products, and the self-healing properties of ECC with a combination of various minerals are still unclear. The third research objective is to study the self-healing products of ECC with a combination of various minerals after repeated loads.
- To date, no model has been developed to predict self-healing capability of ECC based on mineral admixtures. The fourth objective of this research is to provide a comprehensive study using advanced machine learning techniques to predict self-healing of ECC influenced by several factors, such as different

mineral admixtures and the crack width.

- No model has been studied to predict the repeatability of self-healing of ECC. The fifth objective of this research is to develop an accurate and reliable prediction model of repeatability of self-healing capability in ECC with multiple factors.

1.3 Outline of this thesis

As shown in Figure 1.1, this dissertation includes six chapters. Chapter 2 presents a comprehensive literature survey on methods used to improve the efficiency of the self-healing capability of ECC and machine learning models used to predict the mechanical properties and self-healing capability of concrete. The knowledge gaps that have to be bridged by this research are specified.

In Chapter 3, the repeatability of self-healing is verified through experiments. ECC incorporating various minerals are cracked using a newly developed apparatus, and the recovery rate of crack width and chloride ions permeability are observed by digital microscope and Rapid Chloride Permeability Test (RCPT), respectively. The splitting test is also used to measure the mechanical performance recovery. Moreover, the precipitations formed at the surface of cracks due to self-healing are characterized through Scanning Electron Microscope (SEM) equipped with an Energy Dispersive Spectroscopy (EDS), and then further examined using X-ray Diffraction Analysis (XRD).

Chapter 4 focuses on the modelling of the self-healing capability of ECC. In order to do this, four individual models, including LR, SVR, BPNN and CRAT, are developed to predict the recovery rate of crack width as self-healing ability of ECC. Those four individual models are used as base learners in three Ensemble Methods (EM), including bagging, AdaBoost, and stacking, to construct nine EM models for the prediction of self-healing of ECC.

In Chapter 5, the model that has the best prediction performance with highest accuracy among all individual models in Chapter 4, is selected to model the self-healing repeatability of ECC. The proposed model is further optimized by Evolutionary Algorithm (EA) to develop a robust computational tool for modelling

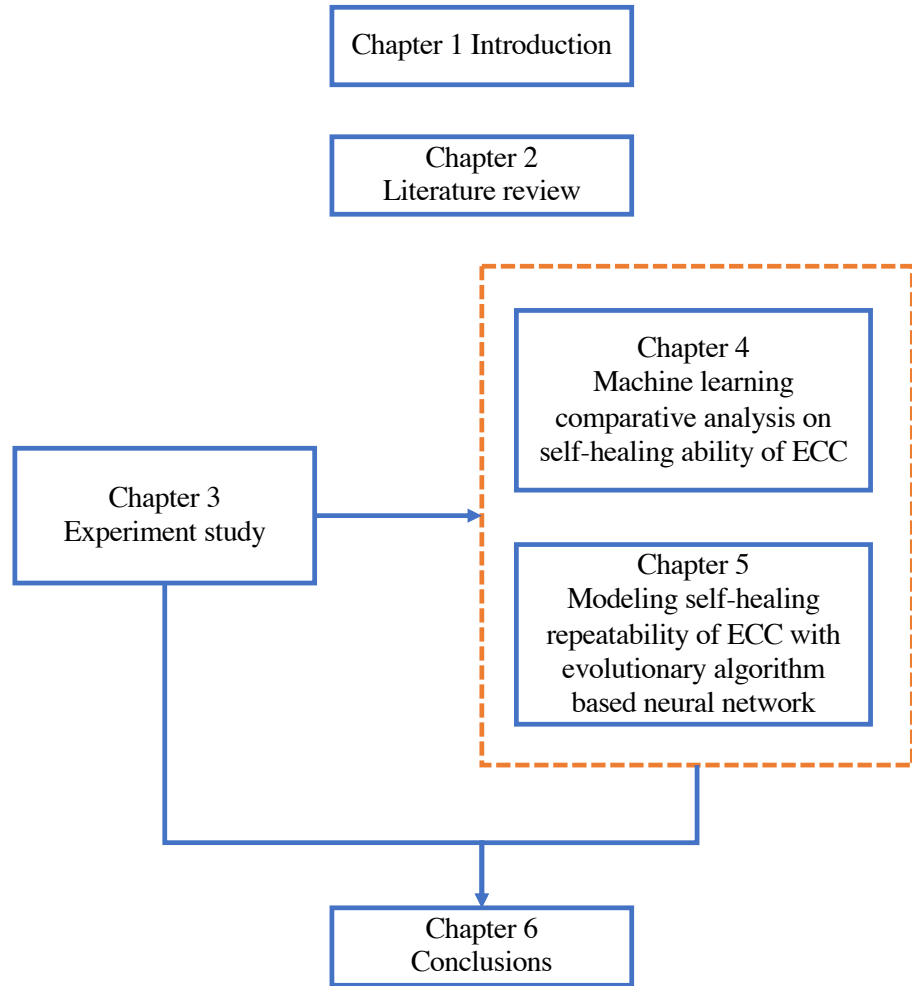


Figure 1.1: Outline of this thesis

the self-healing repeatability of ECC by improving the prediction performance with lower error values and higher accuracy.

Chapter 6, summarizes the results of this research and presents the conclusions. More factors that may affect the self-healing ability of ECC incorporating various minerals are proposed, and factors that affect ECC engineering practices are also given.

Chapter 2

Literature Review

2.1 Introduction

Concrete is a fundamental construction material amounting to 12 billion metric tons annual consumption throughout the world [1]. However, concrete structures are susceptible to cracking which has substantial negative effects on the durability and sustainability of concrete infrastructure [2]. Cracking associated problems increase the maintenance, repair and replacement costs of concrete structures, which is around 35 to 45% of the infrastructure budget in the UK, and 50% in the EU [3]. Because of this, concrete materials that self heal without external human interference are highly desirable in terms of their ability to heal themselves and regain the loss of performance.

Over the last decade, the self-healing capability of Engineered Cementitious Composite (ECC) has been the concern of many researchers. Extensive studies indicate that ECC has the potential to achieve effective self-healing of cracks [30], and many interesting outcomes and test techniques have been presented.

This chapter gives an overview of ECC in Section 2.4, various methods utilized to improve the efficiency of the self-healing ability of ECC mixtures in Section 2.5, followed by recent work on applying different mineral admixtures, such as silica-based (pozzolans), crystalline, and expansive agents, to ECC for enhancing self-healing ability in Section 2.6. After that, the application of machine learning techniques to predict the properties of concrete materials and self-healing are reviewed. By doing this, the knowledge gap that has to be bridged in this research is specified.

2.2 Self-healing concept and mechanisms

Self-healing can be defined as the ability of a material to heal (recover/repair) damage automatically and autonomously, that is, without any external intervention [11]. According to Hearn [31], the phenomena of autogenous self-healing had already been noticed in water-retaining structures, culverts and pipes by Hyde [12, 30] by the end of the nineteenth century. In the 1920s, a more systematical analysis of autogenous self-healing was reported by Glanville [32]. After that, autogenous self-healing of cracks in concrete bridges was also investigated [33, 34]. Over the last two decades, the concept of self-healing ability of concrete structures has been studied intensively and a number of reviews have become available on various self-healing approaches in concrete [2, 35].

The main causes of self-healing has been attributed to two mechanisms, self-tightening and self-healing. For self-tightening, the crack is blocked by small particles from the crack faces or small parts present in fluids that flow through the crack; for self-healing, a chemical reaction takes place connecting the two cracked surfaces. The reaction can be continuing hydration of the cement or a chemical reaction that occurs after hydration (like the formation of calcium carbonate) [36]. In this report, both mechanisms were called “self-healing”. More analysis of autogenous self-healing mechanisms is in section 2.3.4.

2.3 Self-healing approaches

Based on the literature survey, the self-healing of cracks in cementitious materials can be grouped into four categories: self-healing based on adhesive agents, self-healing based on bacteria, self-healing based on mineral admixture, and autogenous self-healing.

2.3.1 Adhesive agents

The idea of using adhesive agents is to seal the cracks and connect the cracked surfaces with one-component or two-component adhesive agents or a multi-component agent. The healing effect depends on the hardening process which is affected by the

properties of the agents. The adhesive agents often used for self-healing include two-component epoxy [37–39], one-component epoxy [40], Methylmethacrylate (MMA) [10, 41, 42], Cyanoacrylate [10, 43–46], silicon and tung oil [5]. In order to supply adhesive agents, microcapsules [41], sealed glass tubes [40] or a multi-channel vascular system need to be built inside concrete [42]. Visualization of crack-sealing with hardened adhesive agents by means of X-ray Computed Tomography (CT-scanning) is seen in Figure 2.1.

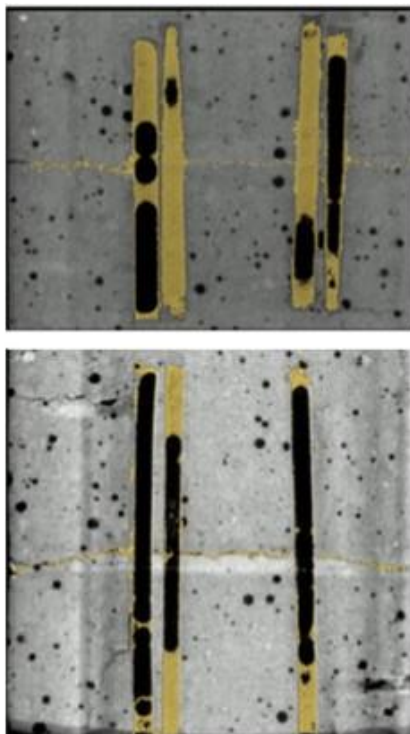


Figure 2.1: Visualization of crack-sealing with hardened adhesive agents by means of X-ray Computed Tomography [47]

2.3.2 Bacteria

The idea of bacteria-based self-healing is to utilize bacteria to promote precipitation of calcium carbonate in cracks. This approach dates back to the mid-1990s in the research by Gollapudi et al. [48], who suggested a method for repairing cracks using environmentally friendly processes. The idea is to incorporate ureolytic bacteria, which aids in the precipitation of calcium carbonate (CaCO_3) in the micro-crack region. The microbial precipitation of calcium carbonate (CaCO_3) is determined by a number of factors, which include the concentration of dissolved inorganic carbon,

the pH, the concentration of calcium ions, and the presence of nucleation sites (areas of extremely localized budding or reaction). However, in order to use bacteria to heal cracks in concrete, some technical problems have to be solved. The bacteria should be protected not only against the alkaline environment in concrete, but also against the decreasing space in the matrix when hydration of cement proceeds [49, 50]. Figure 2.2 is a simplified representation of carbonate precipitation induced by the hydrolysis of urea with the help of bacteria.

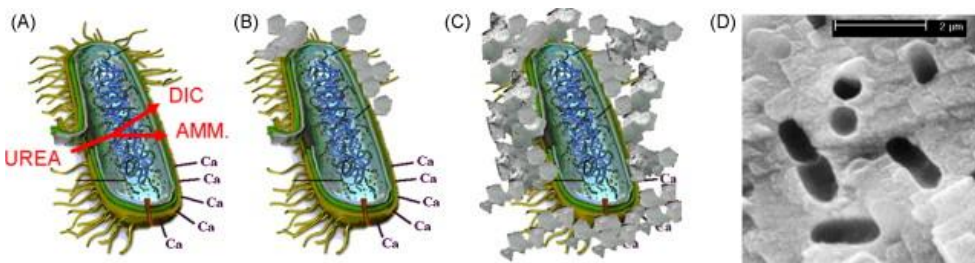


Figure 2.2: Simplified representation of carbonate precipitation induced by the hydrolysis of urea with the help of bacteria [51]

2.3.3 Mineral admixtures

The idea of mineral admixtures-based self-healing is to utilize a mineral reaction to produce healing products to seal the cracks. Minerals can be added in concrete mixture directly during mixing. After the concrete cracks, some unreacted mineral admixtures are present at crack surfaces. When water penetrates into the cracks, these mineral admixtures start to react with water in the cracks. The cracks are then expected to be filled with reaction products. There is a further discussion of the self-healing of ECC incorporating various minerals in Section 2.6.

2.3.4 Autogenous self-healing

Autogenous self-healing in concrete is associated with the physico-chemical process in the cementitious matrix. This process mainly relies on one or more of the following four mechanisms [2]: (1) formation of calcium carbonate from calcium hydroxide; (2) settlement of the debris and loose cement particles in the presence of water; (3) hydration of unhydrated cementitious particles; (4) further swelling of the hydrated cementitious matrix (Figure 2.3). While the hydration of unreacted particles has

been shown to be the main crack healing mechanism for young concrete [52], at later ages, formation of calcium carbonate becomes more prominent [53, 54]. However, all of the mechanisms mentioned require the presence of water in order to be effective in crack healing.

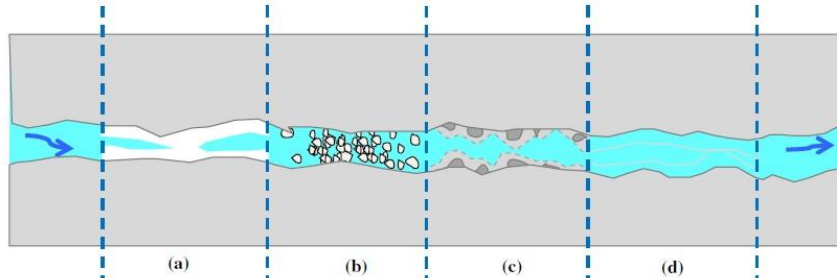


Figure 2.3: Main mechanisms of autogenous healing (a) formation of calcium carbonate from calcium hydroxide; (b) settlement of the debris and loose cement particles in presence of water; (c) hydration of unhydrated cementitious particles; (d) further swelling of the hydrated cementitious matrix [2]

It is believed that self-healing of cracks in cementitious materials is a combination of complicated chemical and physical processes and mechanical interactions [28, 53, 55]. As revealed in most of the literature studied, two main mechanisms are considered predominant in this self-healing: when water and dissolved CO₂ gain access into cracks, further hydration of unhydrated cementitious materials is triggered by water and calcite or portlandite precipitate at the crack surface [29, 31]. These two mechanisms can occur together at the same time, but their extent likely depends on the age and composition of concrete (amount of anhydrous clinker) [53, 56].

From a practical implementation viewpoint, autogenous self-healing is the most attractive [23]. In most concrete, and particularly in those with a low water/cement ratio, the amount of unhydrated cement is expected to be as much as 25% or higher. These unhydrated cement particles are known to be long lasting in time. Autogenous self-healing is also economical, when compared with chemical encapsulation or other approaches [23].

Perhaps the most serious challenge to autogenous healing is its known dependence on tight crack width, which is very difficult to achieve in a consistent manner for concrete in the field [23]. In previous studies [14, 57–60], the crack width of

concrete material was found to be critical for self-healing to take place. The maximum sealable crack width is $53\text{ }\mu\text{m}$ [60]. The requirement of crack width to promote autogenous healing falls roughly below $100\mu\text{m}$ [14, 61], and preferably lower than $50\text{ }\mu\text{m}$ [23]. So a material with excellent crack width control capacity is highly desirable so as to promote the self-healing behaviour of concrete.

2.4 Engineered cementitious composites

Two decades ago, a group of novel construction materials possessing remarkable mechanical properties including excellent healing ability was designed based on micro-mechanical concepts; these materials were called ECC [62–73]. ECC is a new class of High Performance Fibre Reinforced Cementitious Composite (HPFRCC) micro-mechanically designed to achieve high damage tolerance under severe loading and high durability under normal service conditions [62, 64, 74]. Unlike ordinary concrete materials, ECC has a typical moderate tensile strength of 4–6 MPa and a high ductility of more than 3%, which is hundreds times that of normal concrete [75]. Small crack width in ECC specimens before rupture can promote self-healing behaviour and further improve durability of the structure [76].

Over the last decade, the self-healing of ECC has been concerned by many researchers, extensive studies have shown that ECC has the potential to achieve effective self-healing [30], and a lot of interesting outcomes and test techniques have been presented.

2.5 Methods to produce ECC with self-healing property

For the self-healing ability of ECC, the essence is to provide the necessary products which can then fill in the cracks when damage happens. In regard to how to endow ECC with self-healing properties and improve self-healing efficiency, many experimental investigations have been conducted and have generated many innovative approaches during the past few decades. Some of those works are summarized as below.

2.5.1 Superabsorbent polymer (SAP) particles

Hua [77] investigated the self-healing potential of ECC with Super Absorbent Polymer (SAP) capsules. SAP was used as the water reservoir enclosed in the capsules, which could provide available water for the self-healing process when the capsules were ruptured by cracking. Paraffin wax and epoxy-cement material was chosen to be the sealing materials, as shown in Figure 2.4. The results showed that, when the capsule is opened, the moisture is firstly desorbed from the SAP particles and moves to the crack surface. Moisture transportation happened in more than half of the capsules, which means that the low efficiency of self-healing of the ECC may be attributed to the insufficient water supply. In this research no apparent healed crack was observed and the mechanical properties were not significant.



Figure 2.4: Manufacture of the capsules [77]

Deng et al. [78] investigated the self-healing behaviour of ECC mixing SAPs. ECC specimens at the age of 7 and 28 days were preloaded by four points bending tests and then subject to different curing methods: 95% Relative Humidity (RH)/room air cycle curing (CR1), 95% RH curing (CR2) and room air curing (CR3). Environmental Scanning Electron Microscopy (ESEM) observation showed that cracks can be fully healed when crack width is $15 \mu\text{m}$ and $25 \mu\text{m}$, while they only partially healed when crack width is $60 \mu\text{m}$, which demonstrates the feasibility of mixing SAPs to enhance the capacity of self-healing. In addition, flexural

test results showed that specimens cured in CR1 and CR2 recover their mechanical properties to a certain extent.

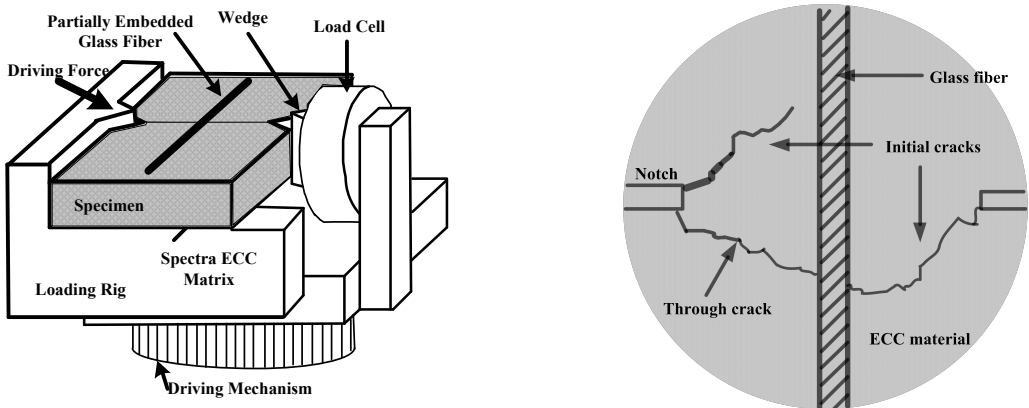
Both Hua [77] and Deng et al. [78] have improved the self-healing ability of ECC to a certain extent, but they also face problems, such as low water supply leading to low self-healing rate[77], uncertainty in healing efficiency of larger cracks, and repeatability[77, 78].

2.5.2 Hollow glass fibres

Dry [79] combined fibres and sealants together for the internal release of chemicals from hollow fibres. This research was focused on the self-healing of cracks by the internal release of self-healing chemicals from inside fibres into the hardened matrix. The hollow fibers are used to store healing agents within the hollow fibres, hollow pipettes or tubes, which will be embedded into a composite matrix. When cracking happens, the healing agents in the hollow glass will flow out and start the healing process. Li et al. [46] argued that the self-healing mechanism described by Dry [79] could not work in normal concrete, cement or even fibre-reinforced concrete, because the width of the tensile cracks in such materials could not be easily tuned. The storage capability for functional agents of hollow glass fibres in a hardened matrix is limited. If cracking occurs within the same area several times, the functional agents will be consumed quickly, which will affect the subsequent repair process. A large hollow glass tube needs to be designed to solve the capacity issue of the lack of self-healing agents.

Li et al. [46] investigated the feasibility of a Passive Smart Self-Healing Engineered Cementitious Composite (PSS-ECC) by conducting two different levels of experiments under standard Material Testing Systems (MTS) load frames. The first-level experiments are designed to confirm the sensing and actuation mechanisms of the PSS-ECC in very small specimens (custom-made hollow glass fibres 500 μm in diameter and 60 μm in wall thickness are used), through direct observation under the ESEM. The second-level tests involve flexural specimens of PSS-ECC systems (micropipettes for blood sampling were adopted) which contain glass fibres filled with sealing agent, named Sealing Agent Carrying fibre (SAC fiber). Superglue with fast air curing capability and low viscosity is selected as the sealing agent. Wedges

are driven into the notches, forcing them to open in a controlled manner. Cracks are initiated from the tips of the notches and propagated toward the glass fibre, as shown in Figure 2.5 (a), the matrix crack bridged by the glass fibre can induce local debonding along the interface between the glass fibre and matrix, as shown in 2.5 (a). Once the glass fibres break, the chemical is released into the cracks of the cementitious matrix so that the cracks can be sealed and the composite re-healed. Hence, the cementitious matrix serves as the ubiquitous sensor, and the hollow glass fibres serve as the ubiquitous actuators. In their experimental study, the authors intended to establish the re-healing effectiveness of the sealing agent after the material suffered crack damage in load cycles. Their experiments showed that the elastic modulus regained its original value in a repeat loading subsequent to damage in the first load cycle and supported the concept and viability of the self-healing passive solutions in the PSS-ECC. Meanwhile, there were many remaining issues the needed to be further studied and addressed before its use in practical applications, e.g. the method for filling and placing of the hollow glass fibers in large-scale applications, the economic analysis for practical applications, and the self-healing effectiveness and repeatability.



(a) ESEM specimen, loading stage and configuration (b) Formation of through crack in ESEM specimens

Figure 2.5: Formation of through crack in ESEM specimens [46]

2.5.3 Mineral admixtures

Like the healing behaviour of all types of concrete, the extent of self-healing in ECC is determined by the matrix [16, 27]. Some scholars have studied the effects of

mineral admixtures on the self-healing behaviour of different matrix materials, i.e. concrete, mortars, ECC, cement pastes, and Strain-Hardening Cement Composite (SHCC). Table 2.1 summarizes the latest self-healing research work on ECC and other matrixes with the use of mineral admixtures reported in the literature. The most commonly used mineral admixtures can be classified into three different groups, namely, expansive, crystalline, and silica-based pozzolans. It can be seen from Table 2.1 that the research works on silica-based pozzolans in ECC, especially Fly Ash (FA) [16, 20, 24, 30, 80], and slag [9, 25–27], have been extensive; however, there is little research on the self-healing property of ECC using expansive or crystalline minerals, and indeed the research on ECC with a combination of various minerals is extremely limited.

Table 2.1: Mineral admixtures for self-healing of ECC and other matrixes reported in literature

Categorization	Materials	Specimens			
		Concrete	Mortars	ECC	Others
Expansive	Calcium sul-faoaluminate (4CaO·3Al ₂ O ₃ ·SO ₃)	[81]		[82–84]	
	Free lime	[81]		[84]	
	Limestone Powder (LSP)	[85]			[70, 71, 86–89]
	Hydrated lime				[24]
	Anhydrite(CaSO ₄)	[81]		[84]	
	UEA			[90]	
	Bentonite			[90, 91]	
Crystalline	Geo-material	[81, 92]			
	Types of carbon-ates	[81, 93]		[90]	
	Talcum powder			[90]	
Silica-based (pozzolans)	Sodium silicate	[94, 95]	[96]		[97]
	Blast Furnace Slag (BFS)	[98]		[9, 25, 26, 99]	SHCC [88] Cement paste [100]
	FA	[98, 99]	[73, 90, 101, 102]	[7, 9, 20, 24–27, 69, 71, 73, 76, 89, 103–105]	SHCC [88] Cement paste [106]
	Silica Fume (SF)	[107]	[90, 101, 108]	[7]	SHCC [109]
	Palm oil fuel ash (POFA)	[110]		[102]	[111]

2.6 Self-healing of ECC with mineral admixtures

As mentioned before, the mineral admixtures for self-healing of ECC can be categorized into three groups: expansive additive and crystalline additive and silica-based pozzolans. The detailed research and corresponding experimental methods are summarized in this section.

2.6.1 Expansive additive

In the case of an expansive additive, some research studies used cements containing LSP as an ingredient of ECC, which gave good self-healing capability. Qian et al. [88] investigated strain hardening cementitious composites with local waste materials (BFS and LSP), where four-point bending tests were used to pre-load the SHCC beam specimens with a deflection up to 2.4 mm and followed by standard curing in water and air for 28 days. The observations under ESEM and Energy Dispersive Spectroscopy (EDS) confirmed that the microcracks in the specimens submerged in water were healed with a significant amount of calcium carbonate, and the reason is very likely due to the continuous hydration of cementitious materials. The results indicated that the deflection capacity of water-cured specimens after self-healing can recover by about 65–105% compared with those virgin specimens, while this ratio is about 40–60% for air cured specimens. In another study, Qian et al. [87] investigated the self-healing behaviour of ECC with a focus on the influence of curing condition and precracking time. Portland cement (CEM I 42.5 N type) was used in the mixture along with BFS and LSP. Nanoclay was also used to enhance the self-healing behaviour of ECC. The results showed that the flexural stiffness was retained significantly compared with that from virgin samples, even though the level of retaining decreases with the increase of precracking time. The samples under air curing, CO₂ curing, cyclic Wet-Dry (W/D) curing and water curing can reach about 80–120%, 85–200%, 60–150% and 115–160% of the deflection capacity of the reference samples. This recovery level is very significant considering these samples have been pre-cracked to 1.5 mm deflection. Furthermore, it is effective to utilize nanoclay as distributed internal water reservoirs to promote self-healing behaviour within ECC without relying on external water supply. Turk et al. [86] produced ECC specimens which were partially replaced by four levels of replacements (25%, 50%, 75%, and 100% by weight of total silica sand) of LSP. They found that the mechanical properties of the ECC mixtures with LSP were in general higher than the reference mixture with only silica sand for all curing ages. Increase in the LSP content had a positive effect on the performance of the compressive strength, fracture toughness, and flexural strength at the ages of 3 and 28 days, while this was not valid at the age of 90 days when compared to the reference mixture. Also, the ductility of

the ECC beams was strongly dependent on the LSP content and specimen age. Siad et al. [89] studied the effect of LSP on ECC. ECC mixtures were created in which the FA was partially replaced by 5%, 10% and 20% of LSP and an ECC mixture without LSP was used as a control. The samples were precracked at the age of 28 days and left under continuous water curing for recovery of their properties. They found that all mixtures exhibited self-healing with slight differences. At later ages, ECC mixtures with a 5% level of replacement showed better compressive strength and MOR results than the other mixtures. The flexural deflection results were more pronounced in ECC mixtures with a 20% level of replacement, recovery of up to 27% was observed between 28 + 0 and 28 + 90 day ages. The microstructural analysis of healed cracks in LSP incorporated ECC mixtures showed the presence of calcite, portlandite and Calcium Silicate Hydrates (C-S-H) gels as well as monocarboaluminate, which confirmed a possible reaction between FA and LSP. Generally, in the case of an expansive additive, the volume of the reaction products is larger than that of the admixture itself and the ratio of expansion depends on the composition of the admixtures [112].

2.6.2 Crystalline additive

Regarding the crystalline additive, its components can react with $\text{Ca}(\text{OH})_2$ to form crystalline products [84]. The literature has very limited information about the use of crystalline additives in ECC. Huang et al. [97] investigated the application of sodium silicate solution as self-healing agent in ECC. The sodium silicate solution was stored in capsules that were embedded in the ECC. Three-point bending tests were carried out to pre-crack the ECC specimens at the age of 14 days. The healing agent was released into the cracks to promote self-healing. The self-healing phenomenon was observed by ESEM and EDS. From the EDS results, the healing products formed in the cracks are the composites of C-S-H and sodium silicate. Thus, the main mechanism of self-healing by sodium silicate solution is the reaction of calcium cations with the dissolved sodium silicate and the crystallization of the sodium silicate. The pre-cracked specimens after self-healing were bent again to evaluate the strength recovery efficiency. Their results demonstrated that the concentration

of the sodium silicate solution is the main influencing factor which determines the self-healing efficiency.

2.6.3 Silica-based pozzolans

Silica-based pozzolans are the most commonly used mineral admixtures in ECC. ECC has been successfully developed with different silica-based pozzolans, such as BFS [9, 25, 26, 99], FA [9, 20, 24–27, 76, 89, 103, 104], SF [109], and Palm Oil Fuel Ash (POFA) [111].

FA has become an important component of ECC [19, 113, 114]. It is reported that the incorporation of high volumes of FA inside ECC systems leads to crack widths that are reduced up to $10 \mu\text{m}$ [19, 113, 114]. Utilization of high volumes of FA also creates a possibility for greater self-healing, since most FA particles remain unhydrated inside the cementitious matrix for longer periods. Some researchers have studied the self-healing of ECC with high volume FA [16, 24, 80], different volumes of FA [20, 103], or different kinds of FA admixtures [25, 26]. Others have investigated the self-healing of ECC with FA combined with different Supplementary Cementitious Materials (SCMs) [24, 89]. Evident self-healing products were also observed in ECC mixtures incorporating slag [27], Alyousif [25] found that ECC specimens with slag were influential in lowering sorptivity results through self-healing, even more than FA bearing ECCs in some cases. In addition, it was observed that the slag particles exhibited a high contribution to achieving strain hardening behaviour [115]. Sahmaran et al. [27] found that ECC incorporated Class-F FA could heal cracks with a width of $30 \mu\text{m}$. This value was around $50 \mu\text{m}$ for ECC with Class-C FA and slightly above $100 \mu\text{m}$ for ECC specimens with slag. Apart from using FA and slag, Kunieda et al. [109] investigated the self-healing behaviour of Ultra-High Performance Strain-Hardening Cement Composite (UHP-SHCC) with SF, where 15% of the cement was replaced by SF. Loading tests were carried out twice, and load was provided up to the strain of 0.1% or 0.2%. After each loading, air permeability tests and water permeability tests were performed. After each loading test and measurement of air and water permeability, water curing was conducted. The results showed that UHP-SHCC has potentially autogenous self-healing properties, and the recovery is better when re-curing in water. Recovery of the transport

property, which was represented by reduction of air and water permeability, was observed twice. Altwair et al. [111] investigated the compressive properties of ECC with POFA with direct tensile test and matrix fracture test. The results show that at 28 and 90 days, increasing the POFA/cement ratio up to 0.2 led to an increase in the compressive strength of the ECC. In addition, the test results show that mechanically pre-loaded POFA–ECC specimens exposed to chloride solution remain durable. The results also indicated strong evidence of self-healing of micro-crack POFA-ECC specimens, which can still carry a considerable flexural load.

2.6.4 Combination of minerals

The mineral type greatly affects the self-healing capability of cementitious composites [11]. The self-healing behaviour of ECC incorporating different mineral admixtures has been investigated during recent years.

Siad et al. [89] found that the ECC mixtures with FA and LSP showed better compressive strength results at the age of 7 days, and the flexural deflection recovery was up to 27%, whereas 17% was recorded for ECC mixtures without LSP. The analysis of the self-healing products confirmed a possible reaction between FA and LSP. The research into the self-healing of ECC with slag also studied the combination of LSP [10, 42]. Qian et al. [88] found that the recovery of deflection capacity was about 65-105% for ECC specimens with BFS and LSP. Then they precracked ECC beams at different ages, followed by different curing conditions, the results showed that for all curing conditions in their experiments, deflection capacity after self-healing can recover or even exceed that from virgin samples with almost all pre-cracking ages, and after self-healing, flexural stiffness was also retained significantly compared with that from virgin samples [87].

Self-healing of ECC with a combination of silica-based pozzolans and expansive agents, under some particular conditions, is significantly effective [87–89]. However, there has little been researched in this area. In addition, there is little research on the self-healing property of ECC using expansive or crystalline minerals and indeed the research on ECC with a combination of various minerals is extremely limited. It is desirable to design a more suitable mix using various proportions of mineral admixtures in ECC so as to enhance its self-healing efficacy.

2.7 Test method for self-healing of ECC with mineral admixtures

2.7.1 Method of producing cracks

It has been reported that crack width control is critical to the generation and accumulation of self-healing substances [14, 57, 116–118]. Relatively finer cracks can maintain an alkaline environment, which is more conducive to the precipitation of self-healing substances [14]. Unfortunately, such tight cracks are often difficult to achieve in normal concrete structures [116].

To generate cracks, a splitting tensile test was commonly used. Sisomphon et al.[84] used a splitting tensile test to introduce a surface crack width of about 100–400 μm . Yang et al. [76] and Qiu et al.[119] utilized a uniaxial tension test to produce crack widths in the range of 0–300 μm . The width of the cracks produced by the above methods varies relatively largely, and the distribution direction of the cracks is also inconsistent, which increases the difficulty of observation and measurement. In order to facilitate the study of the changes in the width of the cracks, some scholars have tried to control the direction of the crack extension and to limit the width of the cracks to within a certain range, thereby forming a crack that is easy to observe. Luo et al.[120] produce cracks on prismatic and cylindrical specimens using an embedded method. Compressive loading was applied to the specimens until visible micro cracks appeared. Then two different diameter nails were embedded in microcracks at both ends to form different width cracks in the range of 0.1–1 mm. However, due to the large coverage of crack width, it is difficult to use the embedded method to produce small cracks, such as 50 μm . Furthermore, when fibres are mixed in, it is not possible to create one single crack, as multiple cracks will appear upon loading [121].

Some scholars believe that cracks can geometrically determine the degree of their crack healing [122]. Therefore, it is very important to control the cracks to within a certain width to ensure that the repeatability of self-healing can be studied without premature cracking. To control crack width (essential), length and depth, and cracking pattern (branched crack and accumulated crack), and to reduce the influence due to crack differences, a newly developed splitting tensile test apparatus

Table 2.2: Test methods used to assess the self-healing of ECC with mineral admixtures

Assessment category	Test method	References
Mechanical	Tensile test	[7, 16, 24, 27, 69, 73, 76, 103]
	Bending test	[20, 69, 80, 86–89, 105, 111]
	Compression test	[67, 69, 86, 89, 111]
Non-mechanical	Resonant frequency measurements	[9, 24, 76, 103]
	Rapid Chloride Permeability Test (RCPT)	[9, 16, 24, 27, 111]
Transport properties	Water permeability	[25, 73, 76, 109]
	Air permeability	[109]
	Sorptivity	[20]
Resistivity	Ultrasonic pulse velocity measurements	[26]
	Concrete resistivity meter	[89]
Microscopy	ESEM	[7, 20, 88]
	Scanning Electron Microscope (SEM)	[16, 27, 67, 89, 103]
Spectroscopy	EDS	[76, 88, 89, 103]
	X-ray Diffraction Analysis (XRD)	[24, 89, 111]

was used to produce cracks in this study. For a detailed description of this crack making device, please see Section 3.3.1.

2.7.2 Evaluation method of ECC self-healing

The self-healing performance of ECC has been assessed in different ways by various researchers. Different test methods were used to assess the self-healing efficiency of ECC with mineral admixtures. Tang et al. [2] gave a general classification of assessment methods for self-healing of cementitious materials. Following their classification, six groups of assessment techniques for the self-healing efficiency of ECC with mineral admixtures, including the detailed test methods and relevant literature, are summarized in Table 2.2.

The self-healing of mechanical properties was observed using tensile tests [16, 24, 27, 76, 103], bending tests [20, 69, 80, 86–89, 105, 111], compression tests [86, 89, 111], and resonant frequency measurements [9, 24, 76, 103]. For transport properties, RCPT [9, 16, 24, 27, 111], water permeability [25, 76, 109], air permeability [109] and soptivity were used [20]. In addition, the self-healing of ECC with minerals was also evaluated through the recovery of resistivity, such as ultrasonic pulse

velocity measurements [26] and concrete resistivity meter [89]. The above summary indicates that splitting tensile test and RCPT are the two most common experimental methods used to evaluate the mechanical properties and penetration performance of ECC. Previous studies using the splitting tensile test [16, 24, 27, 76, 103] and RCPT [9, 16, 24, 27, 111] have focused on one-time self-healing of ECC; however, as described in Chapter 1, cracks tend to recur in engineering practice, so it is also necessary to investigate the repeatability of ECC using these commonly adopted methods.

To observe the micro-texture and structure of specimen before and after the healing, microscopic methods are one of the most widely used evaluation techniques for cementitious materials [2]. For ECC with minerals, researchers also utilized microscopic methods such as ESEM [20, 88] and SEM [16, 27, 89, 103]. The chemical composition and precipitated products in a healed specimen were determined using spectroscopic examinations such as EDS [76, 88, 89, 103] and XRD [24, 89, 111]. The above studies on self-healing substances also focus on one-time self-healing of ECC, and there is a lack of studies on the composition and morphological characteristics of the healing substances after repeated self-healing.

As indicated above, the phenomenon of self-healing of ECC with minerals admixtures has been demonstrated to be effective in the recovery of transport [16, 20, 24–27, 76, 80, 111] and mechanical [16, 20, 26, 76, 80, 89, 111] properties. Unfortunately, the repeatability of self-healing of ECC with the combination of different minerals is unknown.

2.8 Machine learning in prediction of properties of concrete

The rapid development of novel concrete types has driven further research to develop robust models that can estimate the properties of concrete accurately, helping to satisfy the requirements of various design codes and standards for the construction industry [123]. Conventional approaches used for predicting properties of concrete based on empirical data collected from experiments are the linear or nonlinear regression models, which determine the coefficients as the relationship between various

properties of concrete and their influence factors and can be expressed in a general form as follows [124]:

$$f_x = f(a_i \times x_i) \quad (2.1)$$

where f_x indicates properties of concrete, f expresses linear or nonlinear function, a_i represents the constant regression coefficients, and x_i indicates structured influencing attributes.

Even though these regression models have proven effective in some cases, their development comes with multiple drawbacks. Multiple expensive and time-consuming trials are required to construct conventional regression models, which generally fail to acquire expected accuracy prediction results with complex and unstructured problems. Chou et al. [125] stated that regression models are unsuitable for modelling some properties of High Performance Concrete (HPC) due to the intricate interaction between compressive strength and influence factors.

In order to compensate the drawbacks of traditional linear or nonlinear regression models based on empirical data, machine learning algorithms have been applied to develop accurate and effective models for predicting properties of concrete.

Within a subfield in Artificial Intelligence (AI), Machine Learning (ML) deals with the study of computer algorithms to identify complex patterns automatically through experience by showing a set of empirical data in a desired input-output pair. The ML algorithms can be viewed as a searching process through a large space of candidate programs to obtain a program that optimizes the performance guided by training instances [126].

A learning problem can be defined as the problem of improving some measures of performance when executing a task, through some type of training experience. Depending on the training data types, machine learning is generally categorized as supervised, unsupervised, semi-supervised and reinforcement learning [127, 128]. Among these four categories, supervised and unsupervised learning are the most widely adopted in the fields of engineering application [129]. Some of the most influential algorithms that have been widely used in supervised and unsupervised learning types are illustrated in Figure 2.6.

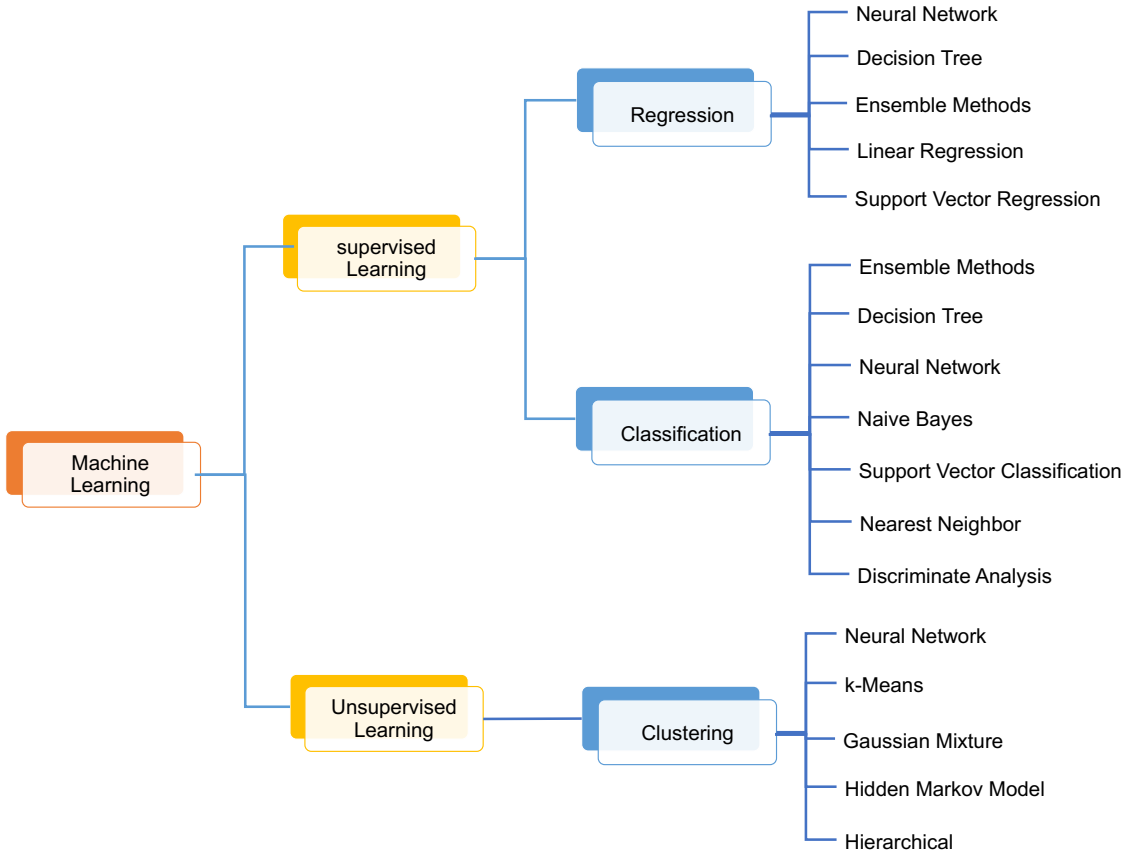


Figure 2.6: Commonly used machine learning types and algorithms [129]

Supervised learning methods illustrate the function approximate problem where a training database consists of a set of input-output (x, y) pairs and the task is to build a mapping function $f(x)$ which performs a prediction output y' in response to input x' . The task of prediction can be either with continuous target variables as regression or with discrete target variables as classification [128]. A diversity of ML architectures and algorithms has been developed, which reflects applications in various problems by capturing different kinds of mathematical structures.

2.8.1 Evaluation of machine learning models

Performance assessment of ML algorithms has been measured by using several statistical methods that describe the errors between predicted values and target or observed values. These methods are also used as a reference for comparison of performance of different algorithms. The mathematical expressions of potential statistical methods used for evaluating ML algorithms are listed in the following

equations.

- Mean Absolute Error (MAE). This is a measure of errors between the predicted values and the target or observed values, which is an arithmetic average of the absolute errors that is non-negative. MAE uses the same scale as the data being measured. A lower value of MAE indicates a better prediction performance of one algorithm.

$$MAE = \frac{1}{n} \sum_{i=1}^n |y_i - y'_i| \quad (2.2)$$

- Mean Square Error (MSE). This measures the average of the squares of errors, which is the difference between the predicted values and the target or observed value. MSE incorporates both the variance (dispersion of one data sample to another) and the bias (distance between the predicted values and the target or observed value), which is non-negative, and values closer to zero are better.

$$MSE = \frac{1}{n} \sum_{i=1}^n (y_i - y'_i)^2 \quad (2.3)$$

- Root Mean Square Error (RMSE). This is the square root of the MSE, which is the standard deviation of the residuals (errors between the predicted values and the target or observed values). Residuals are a measure of the distance from data points to the regression line, and RMSE measures the distribution of residuals. Therefore, RMSE is a measure of accuracy that compares the prediction errors of different algorithms for a particular dataset. However, comparisons across multiple datasets would be invalid due to scale-dependent measurement on the dataset. RMSE is always non-negative, and a lower value is better than a higher one. A value of 0 would indicate a perfect fit to the data.

$$RMSE = \sqrt{\frac{1}{n} \sum_{i=1}^n (y_i - y'_i)^2} \quad (2.4)$$

- Mean Absolute Percentage Error (MAPE). This is also known as mean absolute percentage deviation, and commonly used as a loss function in regression problems and model evaluation. MAPE is a measure of prediction accuracy

in percentage terms, which calculates the average absolute error between the predicted value and the target or observed value divided by the target or observed value for each time. It is commonly used in quantitative prediction models

$$MAPE(\%) = \frac{1}{n} \sum_{i=1}^n \left| \frac{y_i - y'_i}{y_i} \right| \times 100 \quad (2.5)$$

- Correlation coefficient R . This is a numerical measure of correlation as a statistical relationship between the predicted value and the target or observed value, which shows the strength and direction of the linear relationship. R is defined as the covariance of predicted value and the target or observed value divided by the product of their standard deviations.

$$R = \frac{n \sum_{i=1}^n (y_i \cdot y'_i) - (\sum_{i=1}^n y_i)(\sum_{i=1}^n y'_i)}{\sqrt{n(\sum_{i=1}^n y_i^2) - (\sum_{i=1}^n y_i)^2} \sqrt{n(\sum_{i=1}^n y'^2) - (\sum_{i=1}^n y'_i)^2}} \quad (2.6)$$

- Coefficient of determination (R^2). This is the square of the R , which is the proportion of variance in the dependent variable explained by the independent variables. It means R^2 provides an indication of goodness of fit, of how well non-training datasets are likely to be predicted by the model through the proportion of variance. The range of R^2 is 0 to 1, and a greater value close to 1 represents a better prediction performance that commendably replicates the target or observed values.

$$R^2 = 1 - \frac{\sum_{i=1}^n (y_i - y'_i)^2}{\sum_{i=1}^n (y_i - \bar{y})^2} \quad (2.7)$$

- Mean (μ). This is the average of the target or observed value divided by the predicted value.

$$\mu = \frac{1}{n} \sum_{i=1}^n \frac{y_i}{y'_i} \quad (2.8)$$

- Standard deviation (δ). This is a statistic that measures the dispersion of the ratio of target or observed value to predicted value to its mean, which is calculated through the square root of the variance. If the measure values are far from the mean, there is a high deviation. Therefore, the more spread out the data, the higher the standard deviation.

$$\delta = \sqrt{\frac{1}{n} \sum_{i=1}^n \left(\frac{y_i}{y'_i} - \mu \right)^2} \quad (2.9)$$

- Coefficient of Variation (COV). This is a statistical measurement of the dispersion of data around the mean, which is the ratio of the standard deviation to the mean.

$$COV(\%) = \frac{\delta}{\mu} \times 100 \quad (2.10)$$

- Average Absolute Deviation (AAE). This is the average of the absolute deviations from a central point, which is a summary statistic of statistical dispersion or variability.

$$AAE = \frac{1}{n} \sum_{i=1}^n \frac{|y_i - y'_i|}{y_i} \quad (2.11)$$

- Sum of the Squares Error (SSE). This is the sum of the square error.

$$SSE = \sum_{i=1}^n (y_i - y'_i)^2 \quad (2.12)$$

Where y_i is the target or observed output, y'_i is the predicted output, n is the number of samples, $\bar{y} = \frac{1}{n} \sum_{i=1}^n y_i$ is the mean of the target or observed output.

2.8.2 Prediction of mechanical properties of concrete

ML algorithms including regression and classification models have been extensively used as an effective tool for predicting properties of concrete. However, their implementation in the self-healing capability of concrete is yet limited. To the best of our knowledge, there are only two publications (see Section 2.8.3) which have applied ML regression models to the prediction of the self-healing ability of concrete. Therefore, to enhance the understanding of the application of ML algorithms to prediction of the self-healing ability of concrete, we define the scope of ML algorithms under the categorization of regression models in terms of continuous target variables, typically Artificial Neural Network (ANN), Support Vector Regression (SVR), Decision Tree (DT), and Ensemble Methods (EM) in this work.

Regression models are attractive categories for prediction because of their robustness and efficacy in dealing with inadequate information, uncertainty, and noise [129]. Regression models are generally built on an extensive dataset which is usually divided into three subsets; training (TR), validation (V) and testing (TS) datasets.

The training dataset is employed to train the model to obtain a mapping program. Then the validation dataset provides unbiased evaluation of the model fit on training data and prevents model overfitting by stopping the training process when error increases. Finally, the testing dataset is used to assess the predictive performance of the trained model through the evaluation methods discussed in Section 2.8.1. The performance comparisons of all studies reveal that machine learning based models demonstrate satisfactory accuracy of prediction and outperform conventional approaches.

Due to the lack of references for the prediction of self-healing ability of concrete, we extend the review of prediction of self-healing ability of concrete to the prediction of mechanical properties of concrete (continuous target variables) which is often observed in modelling with ML regression algorithms rather than classification algorithms (often used for modelling concrete properties with discrete target variables such as crack and noncrack classification on the concrete surface [130]). Therefore, the application of four types of ML regression models (ANN, SVR, DT, and EM), and hybrid methods based on these four regression models for predicting mechanical properties and self-healing ability of concrete, are reviewed and classified into four categories in the following subsections, which then contributes to a comprehensive review of the application of regression models for prediction in this chapter.

Moreover, the implementation of ML regression models for prediction consists of several essential characteristics involving the dataset size with training, validation and testing subsets, together with the input, output variables and concrete type, and the evaluation methods of prediction performance. In Table C.1, we have summarized and listed those essential characteristics appearing in the literature, which shows *RMSE*, *MAE* and *R*² statistical methods have been widely used for prediction performance evaluation, and ten-fold cross validation is commonly employed for modelling validation. For ease of presentation, we use a number of abbreviations in this table. In the first row, ‘Size’ represents the dataset size used in the model, and ‘TR’, ‘V’ and ’TS’ indicate the size of the training, validation and testing dataset as subsets of the whole dataset size, respectively, ‘Output’ shows the target output variable, and ‘Ref’ indicates the reviewed paper. A ‘NA’ in the table indicates that the characteristic shown in that column is not considered in the paper mentioned.

Note that, although Table C.1 may not include all the available relevant literature, our intention was to include the major and most recent relevant studies therein.

2.8.2.1 Artificial neural network

ANN is a nonlinear model inspired by the biological neural networks of animal brains [131], which is generally composed of neurons connected by directed links [132]. A general structure schema of ANN is shown in Figure 2.7. Neurons are arranged in an input layer, one or more hidden layers and one output layer [133]. In ANN, information propagation is transferred from input neurons to output neurons through links between the neurons affected by a weight in order to reflect the significance of input variables to output variables [129]. The input layer conveys input parameters for training and testing a model. The hidden layers are linked with the input layer. Neurons in hidden layers receive information from the input layer which is computed through a weighted sum and then applied as an activation function to form a mathematical combination result. The combination information is then transported to the following neurons in the output layer that deliver the prediction results of model [134]. Furthermore, ANN train the prediction model through learning algorithms, which enable the model to understand the concept of the problem based on the input-output data pairs rather than a specific mathematical equation form. Therefore, ANN is adopted as an efficient computational analysis technique to model the mechanical properties of concrete.

Nehdi, et al. [135] used an ANN model to predict the performance of cellular concrete mixtures including production yield, foamed density, unfoamed density, and compressive strength. They showed the prediction results were much more accurate than those predicted by existing parametric methods.

Öztaş, Ahmet, et al. [136] implemented a Back-propagation Neural Network (BPNN) model for prediction of the compressive strength and slump of high strength concrete. The statistical values indicated the proposed BPNN model was impressive, with R^2 over 99%.

Sobhani et al. [137] proposed a BPNN model and a proposed fuzzy inference system for predicting compressive strength of no-slump concrete with satisfactory

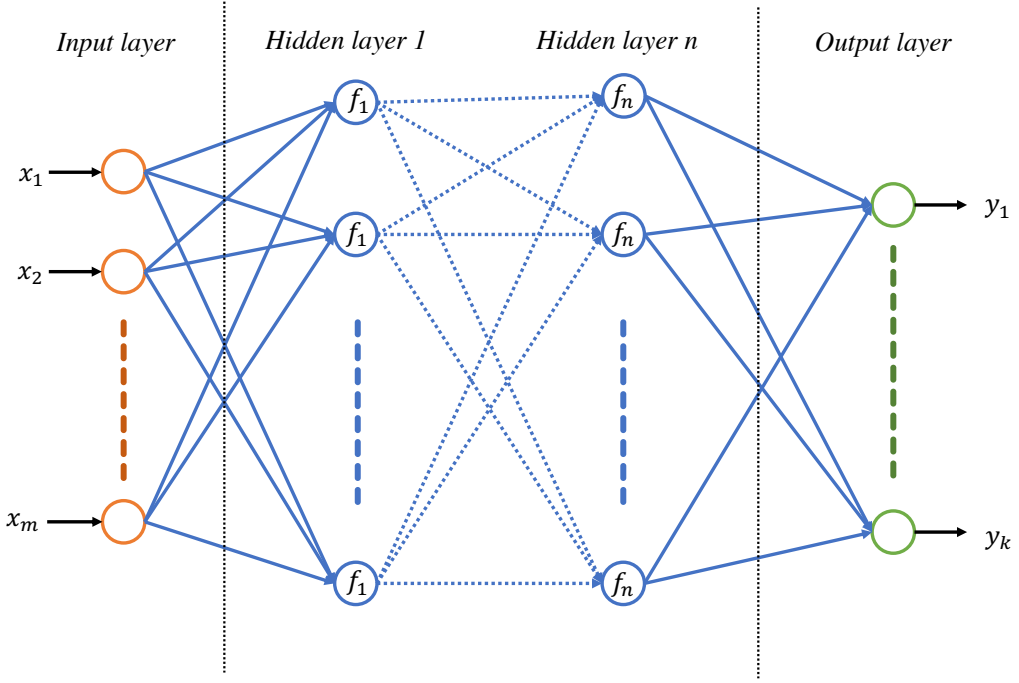


Figure 2.7: Structure of an ANN model with m input variables and n hidden layers.

performance, and indicated the proposed models were more feasible than traditional regression models.

Cheng, et al. [138] constructed a hybrid system using fuzzy logic, weighted Support Vector Machine (SVM) and fast messy genetic algorithm for predicting HPC compressive strength with time series data. The proposed models demonstrated the superior ability of prediction with time series data than SVM and BPNN.

Boğa, et al. [139] applied ANN with four layers and adaptive neuro-fuzzy inference system to predict compressive strength, splitting tensile strength, and chloride ion permeability of concrete. The results showed experimental data were estimated to a notably close extent via both models.

Duan, et al. [140] predicted the compressive strength of recycled aggregate concrete using a BPNN model consisting of 14 neurons in the input layer, 16 neurons in the hidden layer and one output in the output layer. They later extended their work to explore the applicability of BPNN model to the prediction of elastic modulus of recycled aggregate concrete [141].

Chou and Pham [142] investigated the efficacy of individual methods and ensemble methods for predicting HPC compressive strength using IBM SPSS MODELER. This work was then extended by Chou, et al. [125] to compare performance of individual and ensemble methods for predicting the mechanical properties of high performance concrete.

Yuan, et al. [124] developed two models, BPNN and an adaptive network-based fuzzy inference system optimized by genetic algorithm, respectively, to predict concrete compressive strength. Chandwani, et al. [143] built a genetic algorithm based BPNN model to model the slump of ready mix concrete.

Bui, et al. [144] developed an expert system in which an ANN model is constructed to predict the compressive and tensile strength of HPC optimized by a modified firefly algorithm with the initial weights and biases of ANN. The results confirmed that the proposed model provided an adequate prediction of the compressive and tensile strength of HPC, and can be used as an efficient tool for providing speedy and truthful forecasting.

Yaseen, et al. [145] developed an ANN-based model that used a continuous probability distribution function in the feed-forward ANN model. They compared the performance of an extreme learning machine for predicting compressive strength of lightweight foamed concrete with multivariate adaptive regression spline, M5 Tree models and SVR. The results indicated the proposed extreme learning machine model obtained a satisfactory accuracy of prediction and improved the performance of multivariate adaptive regression spline, M5 Tree models and SVR.

Hammoudi, Abdelkader, et al. [146] compared the response surface methodology and the ANN approach on prediction of the 7, 28 and 56 days compressive strength of recycled concrete aggregates. The results indicated both models were a powerful tool for prediction, but ANN is more accurate than the response surface methodology.

Amlashi, et al. [147] applied three models, including BPNN, multivariate adaptive regression splines, and M5 model tree, to predict the slump, compressive strength, and elastic modulus of bentonite plastic concrete. The results showed that the performance difference of BPNN between training and testing datasets was less than other models.

Gupta, Trilok, et al. [148] developed an ANN model for predicting the mechanical properties, including compressive strength, static modulus of elasticity, dynamic modulus of elasticity and mass loss of rubberised concrete subjected to elevated temperature. The sensitivity analysis of input parameters indicated the elevated temperature had the highest impact on all output parameters.

Golafshani, et al. [149] developed ANN and Adaptive Neuro-Fuzzy Inference System (ANFIS) models that were hybridized with Grey Wolf Optimizer for predicting compressive strength of concrete. The results indicated that the hybridization of models improved the performance of both ANN and ANFIS models in terms of the training and generalization capability.

Dao, et al. [150] implemented Gaussian Process Regression (GPR) with five kernels and an ANN to predict the compressive strength of HPC. The results demonstrated that all models performed well and the GPR using Matern 3/2 was the most efficient one among all models.

Shahmansouri, Amir Ali, et al. [151] used a BPNN model to predict the compressive strength of pozzolanic geopolymers concrete based on ground granulated blast-furnace slag at different ages of 7, 28 and 90 days. The prediction results showed accuracy and high performance of the proposed model, which revealed the effect of sodium hydroxide (NaOH) solution concentration on the compressive strength.

2.8.2.2 Support vector regression

SVM is a supervised machine learning method and was first introduced by Vapnik [152, 153] based on statistical learning theory [154]. Since then, it has gained popularity due to attractive features and promising empirical performance. SVM includes two main categories: Support Vector Classification (SVC) and SVR.

For classification problem, SVM aims to find an optimal separating hyperplane to assign data into two different categories [155] to minimize the generalization error and thereby maximize the margin. The SVC algorithm maps training data to points in space in order to maximize the margin, shown as the width of the hyperplane and the closest point of each category in Figure 2.8, so that SVC obtains a quality classification performance on test data [133]. As shown in Figure 2.8, H_1 does not separate the two categories, and H_2 separates the two categories with a small margin.

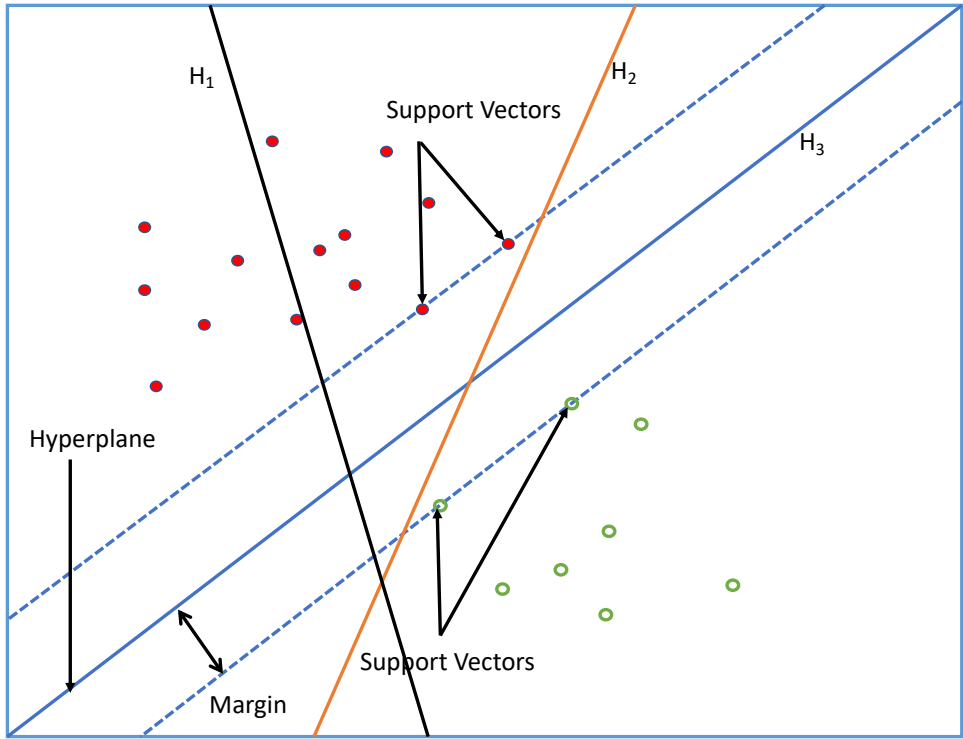


Figure 2.8: Hyperplane classification

Only H_3 separate two categories with the maximal margin, which is selected as the optimal hyperplane. When the optimal separating hyperplane is determined, the input training data located at the margin of the decision boundary are called support vectors which then specify the decision function for the classification solution. Instead of minimizing a global error in a gradient descent process, which suffers from being trapped in local minima solutions, the parameters of an optimal separating hyperplane can be obtained by solving a convex optimization problem.

However, there are some categories that cannot be separated by a linear hyperplane. In these cases, the idea is to map the nonlinear separated input training data into a higher dimensional space to find a hyperplane that can make the liner separation of possible categories [132] shown in Figure 2.9. A mapping function is used to map the training data into a higher dimensional space, then, the maximization and decision rule will depend on the dot products of the mapping function. Defining a kernel function, which is the inner-product in the transformed space, helps to determine a nonlinear decision boundary, which is linear in the higher-dimensional

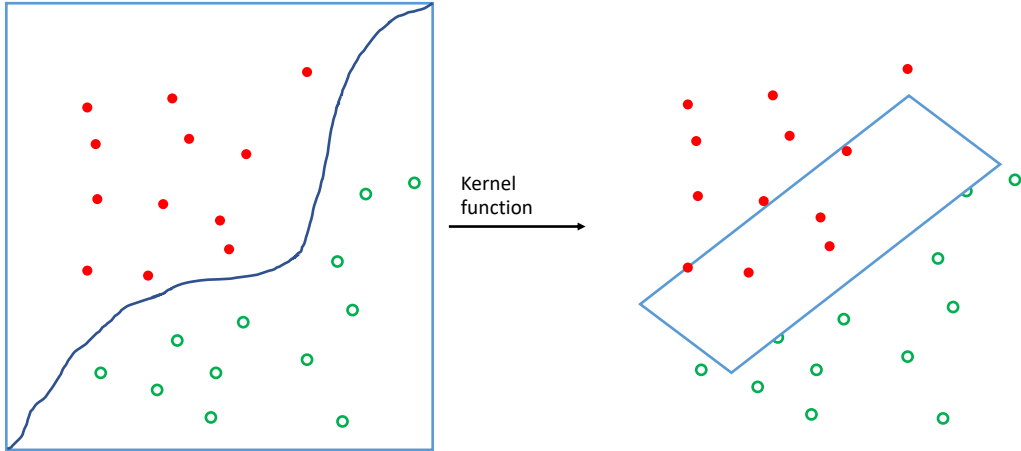


Figure 2.9: Nonlinear mapping in SVM

feature space, without computing the parameters of an optimal hyperplane in a feature space of possibly high dimensionality [156]. This reduces the complexity of finding the mapping function. The most-used kernel functions include the polynomial kernel, sigmoid kernel, Gaussian radial basis function kernel, and linear kernel [157]. The hyperplanes in the higher dimensional space are defined as a set of points whose dot product with the vector is constant in the space. Thus, the solution can be expressed as a combination of the weighted values of kernel functions at support vectors.

Regression analysis uses the same principles as SVC, with only a few minor differences. The margin of tolerance ϵ (the distance between hyperplane and boundary line) is set in approximation due to output in SVC are real number that has infinite possibilities [158]. Several studies have investigated the ability of SVR on predicting properties of concrete, where SVR algorithms are applied as standalone models and/or as base models optimized with metaheuristic algorithms.

Adewumi, et al. [159] developed SVR models to predict the compressive strength and tensile strength of permeable concrete. The results demonstrated SVR was a useful tool to model properties of permeable concrete with limited data, due to its sound mathematical foundation and non-convergence to local minimal.

Ahmad, et al. [160] developed an SVR model to predict the splice strength of reinforced concrete with a wide range of significant parameters. The statistical analysis concluded that SVR was an efficient tool to predict splice strength with a high accuracy in comparison to BPNN and nonlinear multi-regression models.

Yaseen, et al. [161] constructed a hybrid model, an SVR model coupled with Particle Swarm Optimization (PSO) (SVR-PSO), for predicting the shear strength of a fibre-reinforced concrete beam. The proposed SVR-PSO model is validated against with an ANN, and a PSO optimized ANN model (ANN-PSO). The SVR-PSO model demonstrated an effective prospective with an acceptable prediction accuracy compared with ANN and ANN-PSO.

Keshtegar, et al. [162] promoted a hybrid response surface method based SVR model (RSM-SVR) to predict the sheer strength of a steel fibre-reinforced concrete beam. They compared the capacity of RSM-SVR with several benchmark models, including ANN, SVR and response surface method. The achieved results indicated the RSM-SVR model achieved superior results over the comparable models.

Pham, et al. [163] employed the firefly algorithm to optimize the Least Squares Support Vector Regression (LSSVR) model for predicting the compressive strength of HPC. The computational results indicated the proposed LSSVR model achieved the most promising performance with low prediction error compared with benchmark methods, ANN and SVR. Later, Gholampour, et al. [164] investigated compressive strength, elastic modulus, flexural strength and splitting tensile strength of recycled aggregate concrete with no pozzolanic admixtures through multivariate adaptive regression splines, M5 model tree, and LSSVR models. The results indicated the LSSVR model provided the highest accuracy among all models.

Hoang, et al. [165] constructed a hybrid model of LSSVR and differential flower pollination to model the ultimate bond strength of corroded steel reinforcement and surrounding concrete, where differential flower pollination is used to optimize the performance of the LSSVR prediction model. To verify the performance of the proposed hybrid model, the ANN, the multivariate adaptive regression splines, and DT are used as benchmark methods. The results demonstrated the proposed hybrid model is superior to all of these benchmark models.

Sun, Junbo, et al. [166] developed a evolved support vector regression model tuned by Beetle Antennae Search (BAS) to predict the permeability coefficient and 28-day unconfined compressive strength of pervious concrete. The proposed evolved support vector regression model presented a relatively high predictive capability on prediction. Sensitivity analysis indicated the aggregate-to-cement ratio and aggregate size were the most sensitive variables for permeability coefficient and 28-day unconfined compressive strength, respectively.

Zhang, et al. [167] constructed a hybrid model, multi-output least squares support vector regression, to predict two parameters, permeability coefficient and uniaxial compressive strength of pervious concrete, in which the hyperparameters of multi-output least squares support vector regression are tuned by a BAS algorithm incorporating self-adaptive inertia weight and Levy flight. They indicated the searching efficiency was significantly improved by BAS, and the proposed hybrid model achieved the most desirable performance compared with SVR, ANN, and Linear Regression (LR) models in the literature.

2.8.2.3 Decision tree

DT algorithms are developed by splitting a dataset into branch-like segments, in which formal rules are acquired from patterns in the data [168] to predict the properties of a problem. For continuous datasets, the algorithm is called a regression tree, and it conducts a series of tests on the dataset in order to repeatedly partition it based on the relationships between the input variables and the output variables. The partition that minimizes the squared sum of the deviations from the mean in the two partitions is selected to continue partitioning until reaching the stopping rules, that a branch should not be split further but rather become a terminal node. This terminal node contains the predicted values of the output variable [133]. The most frequently used regression tree models include M5P tree, Multiple Additive Regression Tree (MART), and Classification and Regression Tree (CRAT).

Deepa, et al. [169] used Multilayer Perceptron, M5P Tree models and LR to predict compressive strength of HPC. The results indicated that the DT model, the M5P tree model, was the most efficient tool among the three models to predict the compressive strength of HPC.

Omran, et al. [170] investigated and compared the performance of predicting compressive strength of environmentally friendly concrete containing three alternative materials, FA, Haydite lightweight aggregate, and portland limestone, for nine models. These included three advanced predictive models (multilayer perceptron, SVR, and Gaussian processes regression), four DT models (M5P tree, REPTree, M5-Rules, and decision stump), and two ensemble methods (additive regression and bagging), with each of the seven individual models used as base learners. The comparison results suggested the Gaussian processes regression model and its related ensemble models outperformed other models with the highest accuracy.

Behnoood, et al. [171] employed the M5P tree model to predict the compressive strength of normal concrete and HPC. The results demonstrated the M5P tree algorithm had achieved quality prediction results for the compressive strength of normal concrete and HPC based on the values of mixture proportions and age of testing.

Chopra, Palika, et al. [172] investigated the compressive strength of concrete at the ages of 28, 56, and 91 days with a comparative analysis. Three models, DT, Random Forest (RF) and ANN, were used for prediction. The comparison results inferred that ANN was the best feasible prediction tool for predicting the compressive strength of concrete.

2.8.2.4 Ensemble methods

ML algorithms train multiple models, called weak learners or base learners, to solve the same problem and combine replicated independent results to form a better result [125, 142]. Instead of searching for the best hypothesis for explaining data, EM construct a set of hypotheses and then correctly combine them to obtain more accurate or robust models. Therefore, EM usually display more accuracy than single algorithms but require higher computation. Fast algorithms, such as decision trees, are often employed to build EM models. The widely used decision tree based EM algorithms are bagging and boosting. In bagging, multiple base learners are trained independently in parallel and then averaged for a regression result [173]. In boosting, base learners are trained sequentially, and each of them is trying to correct its predecessor [174]. The representative algorithms using tree-based bagging and boosting are RF and Gradient Boosted Regression Tree (GBRT), respectively.

Erdal [175] predicted the compressive strength of HPC with eleven models, including DT and three ensemble approaches: (1) three single ensemble methods, random sub-spaces (RS), bagging (Bag), and stochastic gradient boosting (GB), used DT as a base learner, constructing three models, RS-DT, Bag-DT, and GB-DT; (2) a two-level ensemble approach applied the ensemble learning methods twice, developing three models, RS-RS-DT, Bag-Bag-DT, and GB-GB-DT; (3) hybrid ensemble methods which integrate attribute-base ensemble (RS) with instance-base ensemble methods (Bag and GB) to develop four hybrid models, RS-GB DT, GB-RS DT, RS-Bag DT, Bag-RS DT. The prediction result of DT was used as a benchmark to compare the performance of the proposed ten ensemble models. The results indicated that the proposed ensemble models noticeably improve the accuracy of single ensemble methods, and GB-RS DT, RS-GB DT and GB-GB DT outperformed other models.

Han, et al. [176] constructed an RF model based on CRAT and bagging method to predict the compressive strength of HPC. They implemented the prediction in two steps which first measured variable importance using RF and then optimized the input variables to predict compressive strength in the second step. They suggested that overabundant variables resulted in poor accuracy of the prediction result because of lacking of key variables. The prediction results demonstrated that the RF model was able to accurately predict the compressive strength of HPC.

Zhang, Ma, et al. [177] used an RF model optimized by a BAS algorithm (BAS-RF) to predict the uniaxial compressive strength of lightweight self-compacting concrete. By tuning the hyper-parameters of the RF model, they built an effective model to accurately predict uniaxial compressive strength with a high R of 0.97. They also suggested temperature was the most sensitive variable to the development of uniaxial compressive strength, which is followed by scoria content and water-to-binder ratio through measurement of input variable importance.

Zhang, et al. [178] developed three tree-based models: single regression tree, GBRT and RF, to predict the mechanical properties, splitting tensile strength and uniaxial compressive strength of manufactured-sand concrete. A firefly algorithm was applied to tune the hyperparameters of three proposed algorithms. The results

indicated all tree-based models achieved high accuracy of prediction and the GBRT model preformed better than single regression tree and RF.

Nguyen, Hoang, et al. [179] employed four ML algorithms including two tree-based ensemble models, gradient boosting regressor, and extreme gradient boosting, as well as SVR and multilayer perceptron, to predict the compressive and tensile strengths of HPC. The comparative results revealed the proposed ensemble models performed better than SVR and multilayer perceptron.

Farooq, et al. [180] provided a comprehensive study on predicting compressive strength of HPC prepared with waste materials. Four individual algorithms, ANN, DT, multiple linear regressions and SVR, are employed and then applied as base learners in bagging and boosting (adaboost and xgboost) ensemble methods. They compared network-based (ANN, multiple linear regressions, and SVR) and tree-based (DT) bagging and boosting ensemble models and RF on prediction performance.

2.8.3 Prediction of self-healing capacity of concrete

Although researchers have utilized different ML models to anticipate and evaluate various mechanical properties of concrete, the application of ML focusing on self-healing is considerably rare. Suleiman and Nehdi [181] applied a GA-ANN model to predict the self-healing ability of cement-based materials, and stated that the proposed GA-ANN model was capable of capturing the complex effects of various self-healing agents (e.g., biochemical material, silica-based additive, expansive and crystalline components) on the self-healing performance in cement-based materials. A comparative study was conducted by [182] to predict the self-healing capability of bacteria-based concrete. To the best of our knowledge, no studies have applied a ML model to predict the self-healing of ECC, let alone presenting a comparative analysis by comparing prediction performance of different ML algorithms.

2.9 Summary

A general literature survey has been presented in this chapter. Methods to produce ECC with self-healing and ML algorithms for predicting mechanical properties of concrete have been discussed.

From the comparisons of the methods of self-healing, it was found that more scholars chose to use different minerals to improve the self-healing ability of ECC, because this design is relatively low-cost and more environment friendly than other mechanisms of self-healing as no “strange” additives are needed. Remaining scientific challenges concerning the self-healing with minerals are the following:

1. There is little research on the self-healing property of ECC using expansive or crystalline minerals and indeed the research on ECC with a combination of various minerals is extremely limited.
2. The repeatability of self-healing of a crack under repeated loads is still uncertain, and the recovery of mechanical properties and permeability after repeated cracking is not clear.
3. There has been very few investigations carried out to determine the amount of reaction products formed in ECC cracks, and the self-healing products of ECC with a combination of various minerals are still unclear.
4. The application of machine learning to self-healing of concrete is considerably rare, and no studies have compared different machine learning algorithms for predicting self-healing of ECC.

From the list of studies in Table C.1, it has been demonstrated that ML models are powerful tools for predicting the mechanical properties of various concretes, and the applicability of ML algorithms for prediction of self-healing capability of cement-based materials and bacteria-based concrete has also been demonstrated. Remaining scientific challenges concerning the prediction of self-healing capability of ECC are the following:

1. The application of ML models for predicting self-healing capability and repeatability of ECC has not been studied yet.
2. An accurate and reliable model that can mitigate the problem of convergence to local optima for prediction of self-healing repeatability of ECC has not been developed yet.

The challenges defined in this chapter will be dealt with in the following chapters. By focusing on these challenges, the self-healing ability and efficiency of ECC with a combination of various minerals will be evaluated, and better insight is gained into the changes in mechanical properties and permeability of ECC during repeated self-healing process. The potential of self-healing in ECC with a combination of various minerals is determined and recommendations for enhancing the capacity of self-healing are given. A comparative analysis of multiple ML models will be studied to predict the self-healing ability of ECC, and further contribute to the development of an accurate prediction model for self-healing repeatability of ECC.

Chapter 3

Experimental Study

3.1 Introduction

In this chapter, experiments will be conducted to compare the effects of multiple minerals in different proportions on the efficiency of Engineered Cementitious Composite (ECC) self-healing, and to verify whether ECC samples still have the ability to heal after being subjected to multiple loads. Materials and samples preparation are introduced in Section 3.2. To study the self-healing capability of ECC incorporating different minerals, a four-part investigation is outlined below.

The first part is focused on a study of the crack width recovery of ECC that incorporates multiple minerals in different proportions after three cycles of repeated loading. See Section 3.3.3 for specific experimental methods, and Section 3.4.1 for results.

The second part is focused on the effect of different mineral ratios on the recovery of chloride ion permeability of ECC samples, and the effect of repeated self-healing capabilities. See Section 3.3.4 for specific experimental methods, and Section 3.4.2 for results.

The third part is focused on the recovery of the mechanical properties of the ECC samples, specifically the effect of self-healing time on the self-healing ability, and the recovery of mechanical properties after three rounds of repeated loads. See Section 3.3.5 for specific experimental methods, and Section 3.4.3 for results.

The main focus of the fourth part is to report the morphologies of self-healing location we observe in a Scanning Electron Microscope (SEM). See Section 3.3.6 for specific experimental methods. Some description and speculation regarding the formation of these morphologies is provided in Section 3.4.4.1, and semi-quantitative

analysis of self-healing products is conducted by using Bruker Energy Dispersive Spectroscopy (EDS) system, and the results are reported in Section 3.4.4.2. X-ray Diffraction Analysis (XRD) is also used to re-identify and verify self-healing products (see Section 3.3.7), and the results are reported in Section 3.4.4.3

3.2 Materials and samples preparation

3.2.1 Materials

The binder content for the ECC mixes examined herein consisted of General Purpose Cement (GPC), Fly Ash (FA), Silica Fume (SF) and Hydrated Lime Powder (LP) as shown in Table 3.1.

Table 3.1: Physical properties and chemical composition of different minerals

Chemical composition (%)	GPC	FA	LP	SF
SiO ₂	19.8	65.9	1.8	95.1
Al ₂ O ₃	5.3	24	0.5	0.21
Fe ₂ O ₃	3	2.87	0.6	0.29
CaO	64.2	1.59	72	/
MgO	1.3	0.42	1	/
R ₂ O	0.6	1.93	/	/
SO ₃	2.7	/	/	/
TiO ₂	0.28	0.91	/	/
Mn ₂ O ₃	0.22			
ZrO ₂ +HfO ₂	/	/	/	3.46
Loss on ignition (%)	2.8	1.53	24	1.4
Density (g/cm ³)	3.08	2.43	2.25	2.26
Specific surface area (m ² /kg)	/	655	460	1.5 × 10 ⁴

Table 3.2: Properties of PVA fibres

Length (mm)	Length/diameter ratio	Young's modulus (MPa)	Elongation (%)	Tensile strength (MPa)	Density (g/cm ³)
8	200	42000	7	1600	1.3

The GPC and FA were supplied by Boral in accordance with Australian Standard AS 3972-2010 [183]. The LP used was the Adelaide Brighton Hydrated Lime with a specific gravity of 2.2-2.3, and a typical fineness of 0.1% retained on a 75-micron sieve and less than 0.05% on a 250-micron sieve. Fine sand with an average grain size of 150 µm and fineness modulus of 2.01 was employed. Polyvinyl Alcohol (PVA)

fibres supplied from Domocrete were utilised and their mechanical and geometrical properties are described in Table 3.2

3.2.2 Mix proportions and samples preparation

Nine ECC mixtures with different minerals were prepared and the mix proportion details are indicated in Table 3.3. The abbreviations for labelling specimens were adopted in such a way that the letters FA, SF and LP stand for ECC samples incorporating FA, SF and LP, respectively. The cementitious materials included in Water to Cementitious Materials Ratio (W/CM) are GPC + FA + LP+SF. In this experimental study, FA70 is the reference mixture. It can be seen from Table 3.3 that other mixtures use different ratios of SF or LP to replace FA in FA70. When a description of the addition of a certain proportion of minerals (such as 10% SF) to FA70 appears in the text, it specifically refers to replacing the FA in FA70 with this mineral. The number after the letters shows the replacement percentage of FA with the materials in the mixture. For instance, the SF15 mixture is related to a sample with 15% replacement of FA with SF, accordingly.

Table 3.3: Mix proportions of ECC.

Mix	W/CM	Sand	Water	Fibre (V)	GPC	FA	SF	LP	HRWR
FA70	0.29	419.67	338.07	26	349.73	816.03	0	-	5.13
FA65-SF5	0.29	419.67	338.07	26	349.73	757.74	58.29	-	5.13
FA60-SF10	0.29	419.67	338.07	26	349.73	699.45	116.58	-	5.13
FA55-SF15	0.29	419.67	338.07	26	349.73	641.16	174.86	-	5.13
FA65-LP5	0.29	419.67	338.07	26	349.73	757.74	-	58.29	5.13
FA60-LP10	0.29	419.67	338.07	26	349.73	699.45	-	116.58	5.13
FA55-LP15	0.29	419.67	338.07	26	349.73	641.16	-	174.86	5.13
FA55-SF5-LP10	0.29	419.67	338.07	26	349.73	641.16	58.29	116.58	5.13
FA55-SF10-LP5	0.29	419.67	338.07	26	349.73	641.16	116.58	58.29	5.13

3.2.3 Mixing and casting procedures

The W/CM was kept constant as 0.29. GPC and sand to cementitious materials (PC + FA + LP+SF) ratios were 0.3 and 0.36, respectively. A planetary-type mixer with a 50 L capacity was used for the production of ECC mixtures. All the fine aggregates were in saturated surface dried condition prior to concrete mixing.

The mixing process is described as follows. Solid ingredients including cement, mineral admixtures and sand were first mixed for 30 seconds. Water pre-mixed

with High Range Water Reducer (HRWR) was then added into the dry mixtures and mixed for 2 minutes. Then PVA fibres were slowly added into the matrix and the mixtures were blended continually until the fibres were evenly distributed. The mixtures were then cast into standard moulds. The moulds were cast on a vibrating table. The standard cylinder molds were filled in two equal lifts. A vibration time of 0–10 s was used after each lift to release entrapped air. After 24 hours, the samples were de-moulded.

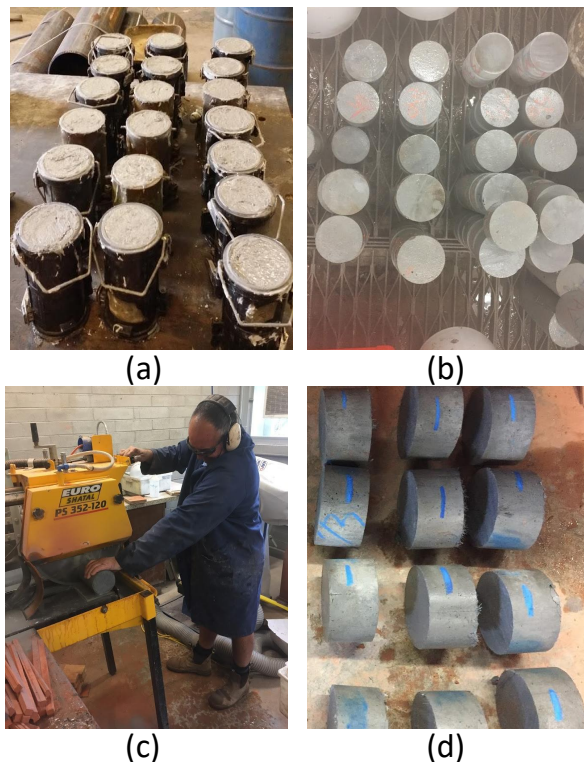


Figure 3.1: Concrete cylinders were cut using a diamond blade saw to obtain 50 mm-thick discs: (a) standard plastic molds for casting cylinder specimens; (b) demoulded cylinder specimens; (c) concrete cutting; (d) samples after cutting

After being demoulded, the ECC specimens were cured in a curing room for 28 days, where the temperature was $23 \pm 2^\circ\text{C}$ and the Relative Humidity (RH) was $90 \pm 5\%$. To study the self-healing behaviour, samples with dimension of 50mm \times \varnothing 100mm were employed and they were cut from standard 200mm \times \varnothing 100mm cylindrical specimens (see Figure 3.1). Two discs were extracted from each central portion of the cylinder in order to avoid any end effect.

3.3 Pre-cracking and self-healing evaluation methods

To investigate the self-healing capacity of ECC incorporating different minerals, and the feasibility of self-healing after repeated loading, a newly designed apparatus will be used to create consistent cracks (see Section 3.3.1), and then the samples will undergo Wet-Dry (W/D) cycles (see Section 3.3.2). The autogenous healing effectiveness and the feasibility of repeated self-healing were verified and evaluated by crack area reduction as measured using digital microscope (see Section 3.3.3), by chloride ion permeability recovery (see Section 3.3.4), and by tensile strength recovery (see Section 3.3.5) after healing. Furthermore, a series of techniques comprising SEM and EDS was utilized to identify the healing morphology and to characterize the distribution of healing elements (see Section 3.3.6), and XRD analysis was also used to re-identify and verify self-healing products (see Section 3.3.7).

3.3.1 Producing controlled cracks

It has been reported that crack width control is critical to the generation and accumulation of self-healing substances [14, 57, 116–118]. Relatively finer cracks can maintain an alkaline environment, which is more conducive to the precipitation of self-healing substances [14]. Unfortunately, such tight cracks are often difficult to achieve in normal concrete structures [116].

To generate cracks, a splitting tensile test was commonly used. Sisomphon et al.[84] used a splitting tensile test to introduce a surface crack width of about 100–400 μm . Yang et al. [76] and Qiu et al.[119] utilized a uniaxial tension test to produce crack widths in the range of 0–300 μm . The width of the cracks produced by the above methods varies by a relatively large amount, and the distribution direction of the cracks is also inconsistent, which increases the difficulty of observation and measurement.

In order to facilitate the study of the changes in the width of the cracks, some scholars have tried to control the direction of the crack extension to limit crack width to a certain range, thereby forming a crack that is easy to observe. Luo et al.[120] produced cracks on prismatic and cylindrical specimens using an embedded

method. Compressive loading was applied to the specimens until visible micro cracks appeared. Then two different diameter nails were embedded in microcracks at both ends to form different width cracks in the range of 0.1-1 mm. However, due to the large coverage of crack width, it is difficult to use the embedded method to produce small cracks, such as 50 μm . Furthermore, when fibres are mixed in, it is not possible to create one single crack as multiple cracks will appear upon loading [121].

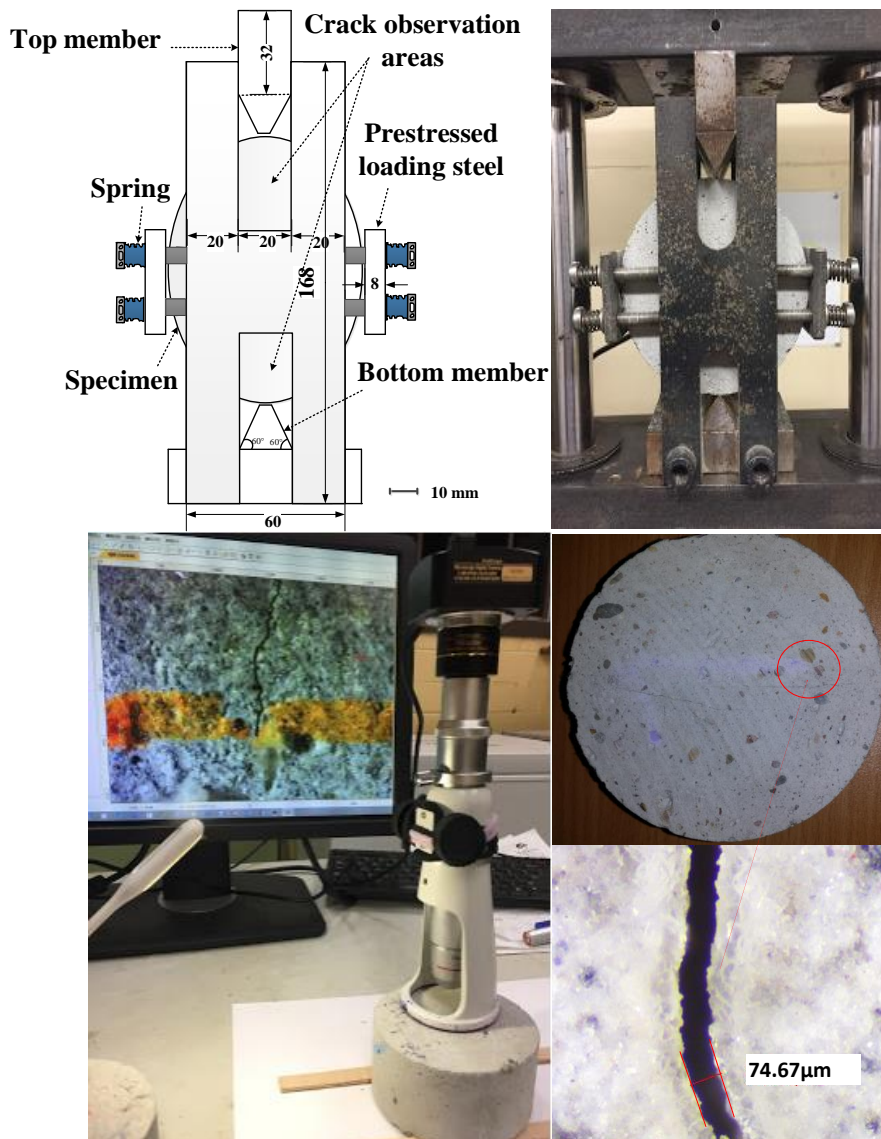


Figure 3.2: The apparatus used to produce cracks

Some scholars believe that cracks can geometrically determine the degree of their crack healing [122]. Therefore, it is very important to control the cracks to within a certain width to ensure that the repeatability of self-healing can be studied without

premature cracking.

To control crack width (essential), length and depth, and cracking pattern (branched crack and accumulated crack), and reduce the influence due to crack differences, micro-cracks were produced using a newly developed splitting tensile test apparatus as shown in Figure 3.2. The newly developed splitting tensile test apparatus consisted of a steel frame, top member, bottom member, prestressed loading steel plates (5 mm thick) on both sides with loading nuts and wire springs. Both steel plates were connected to the steel frame by nuts and wire springs, as shown in Figure 3.2. When a specimen was placed inside the steel frame, the specimen was pre-stressed by the steel plates from both sides to limit crack propagation and crack size, as well as to prevent the crack from growing too fast. Based on this design, constraining localized brittle fractures and guaranteeing more uniform distribution of micro-cracks can be achieved. As Section 2.7.1 has analysed, the size of the crack has a significant effect on self-healing capacity, and in order to reduce this effect, the size of the crack is required to be compared within a certain range. This new method will be used in this study to produce cracks, and after applying the first round of load, most of the cracks are less than 100 μm , as shown in Section 3.4.1.

3.3.2 Multiple loading and healing process

After the 28 days curing period, the specimens were first pre-loaded up to 70% of their maximum splitting strength using the newly designed apparatus, followed by the Rapid Chloride Permeability Test (RCPT) test, before self-healing took place. The self-healing process consisted of 10 W/D cycles. Each W/D cycle consisted of submersion in water at $23 \pm 2^\circ\text{C}$ for 24 hours and drying in laboratory conditions at $50 \pm 5\%$ RH and $23 \pm 2^\circ\text{C}$ for 24 hours, as shown in Figure 3.3.

As shown in Figure 3.4, after 10 W/D cycles, the self-healed specimen was evaluated by the RCPT test again before the second preloading and healing cycle. Identical samples (which underwent the same preloading and healing process) were prepared to obtain the corresponding maximum/resulting tensile strengths at the end of each healing cycle, so a pre-loading stress of up to 70% of the corresponding maximum splitting strength was always applied. As a result, the crack widths less than 100 mm were controlled and the risk of premature breakage of the specimen

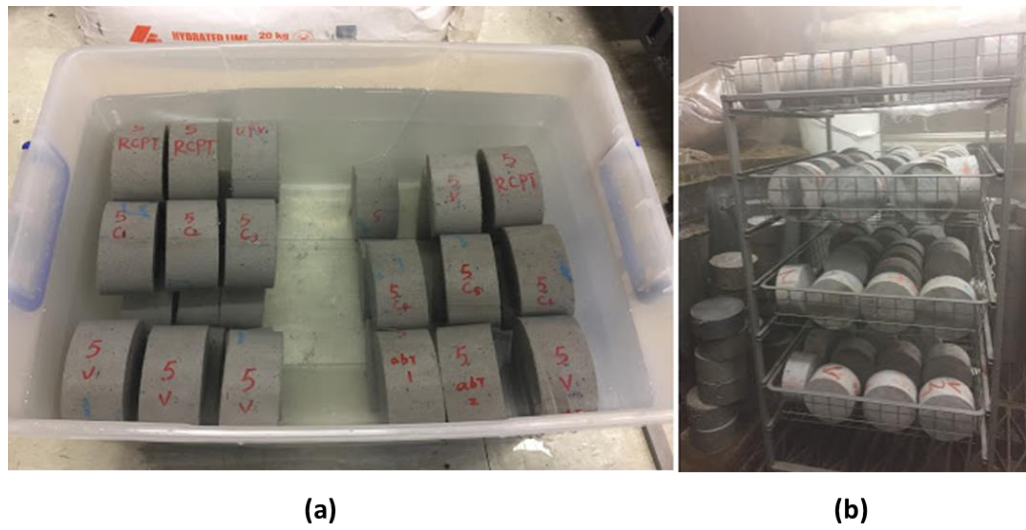


Figure 3.3: Wet-Dry (W/D) cycling environment: (a) wet cycles; (b) dry cycles

was prevented. A total of three preloading and healing cycles were studied. A digital microscope was used to observe the change in the width of the crack surface, as shown in Figure 3.2. After the multiple preloading and healing cycles described above, the extents of repeated self-healing were evaluated and compared.

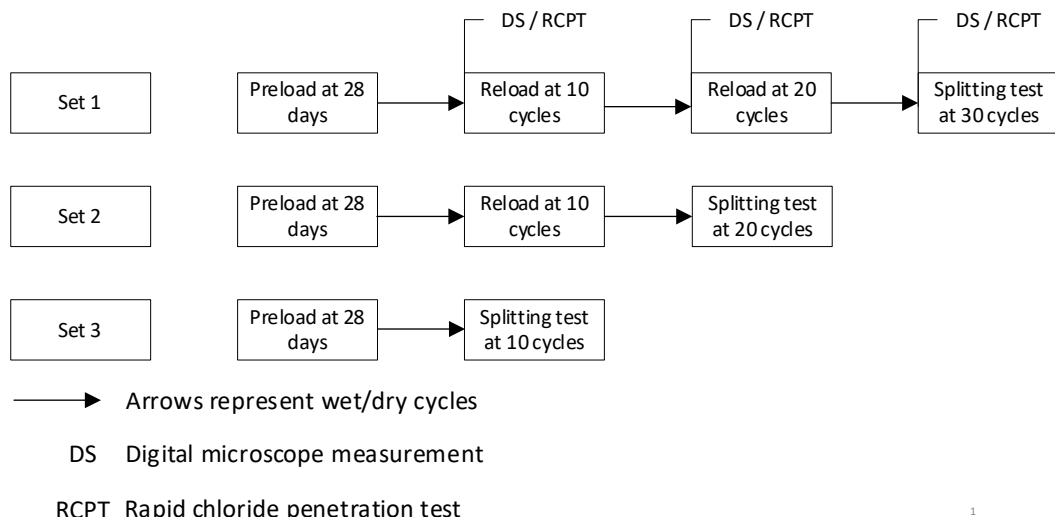


Figure 3.4: Preloading and reloading schedule of self-healing repeatability study

3.3.3 Digital microscope study

Observation of crack width reduction is a preliminary method to assess healing efficiency on the surface of a material [84, 184]. In this study, Optical microscopy observation was conducted using an AmScope Optical Microscope (consisting of a

40X crack width magnifier and a AmScope 5MP box camera) to capture the crack width after 10 W/D cycle, see Figure 3.5.

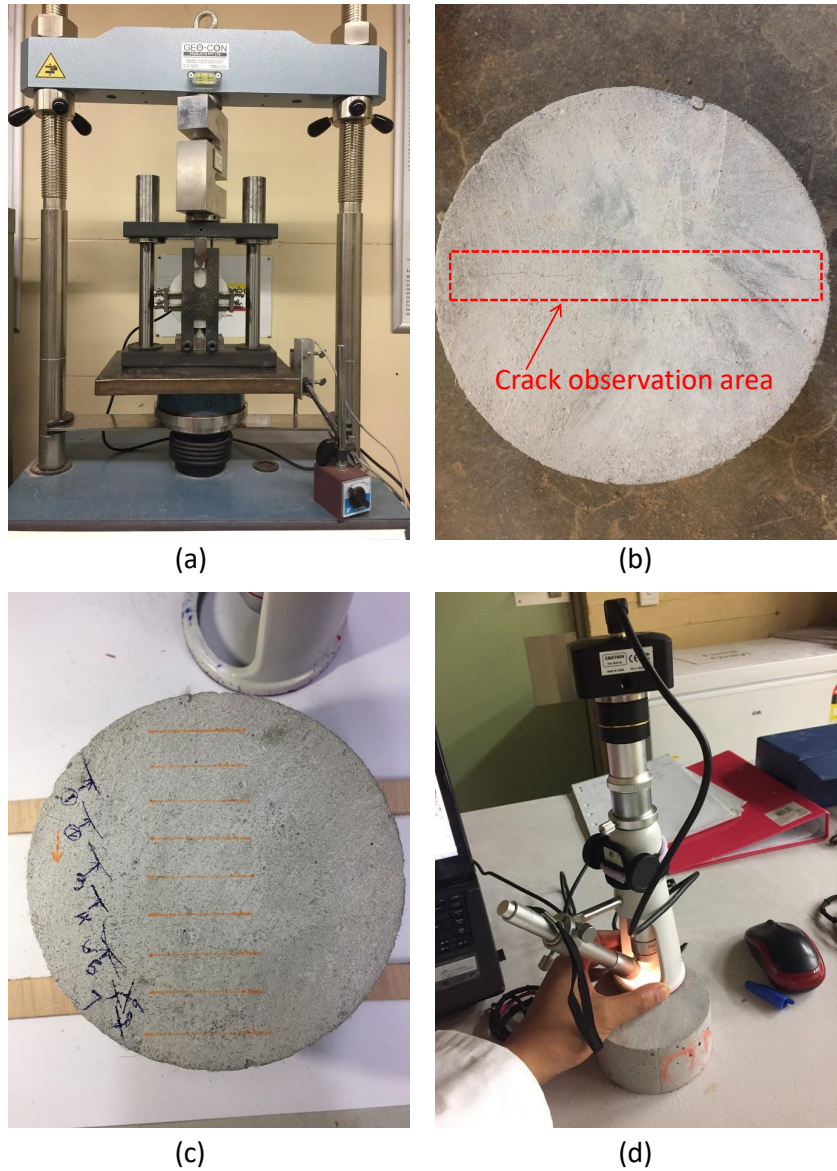


Figure 3.5: Crack marking and measurement: (a) producing cracks; (b) observation area; (c) divide the observation interval; (d) AmScope Optical microscope observation

There are six specimens with dimension of $\text{Ø}50\text{mm} \times 100\text{mm}$ for each of nine mixtures, which were observed using digital microscope to collect crack width samples before self-healing and after self-healing.

Four horizontal lines were drawn on the surface of each specimen along the direction of vertical force, which divided the specimen into five observation areas. The schematic diagram of observation measurement is shown in Figure 3.6. In

each observation area, one crack data will be recorded if the crack width showed little change along the vertical force direction. Otherwise, we recorded multiple data samples with different crack widths separately before and after self-healing, for which the crack width is inconsistent along the vertical force. For example, the front end of the crack is wide, and the rear part is narrow.

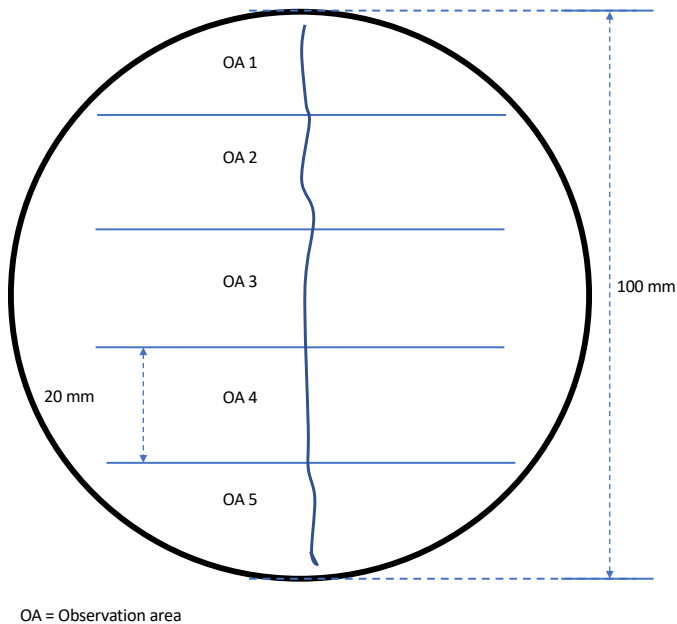


Figure 3.6: Schematic diagram of measuring observation areas on the surface of ECC mixture specimen

After preloading, the cracks that needed to be observed and tracked were identified. Applying the second and third rounds of loads according to the method introduced in Section 3.3.1 can largely avoid the spread of cracks and generation of new cracks.

Repeated measurements can be performed at the same spot and recorded on the crack record sheet to monitor changes over time. In order to avoid reading errors caused by different people during the measuring process, all of the reading work was completed by one person. Due to the different sizes of cracks on different samples, it is not accurate to directly compare the closure width of the two samples. In this study, the crack width recovery rate was used to describe the surface crack healing efficiency of different mixtures.

The recovery rate of crack width (R_{cw}) was calculated using

$$R_{cw} = \frac{CW_l - CW_s}{CW_l} \quad (3.1)$$

Where CW_l and CW_s indicate the crack width after loading and the crack width after self-healing cycle, respectively. During the preliminary test, it was found that the crack width recovery rate of different sizes of cracks is quite different. During the analysis, the crack sizes were divided into four size groups for discussion: less than 20 μm , 20 to 50 μm , 50 to 100 μm , and more than 100 μm , see Section 3.4.1. It should be noted that, as described in Section 3.3.1, a novel method was used to create cracks in this study, and most of the cracks produced in the first round were smaller than 100 μm in size, as shown in Section 3.4.1.

3.3.4 Rapid chloride permeability test

As noted previously, RCPT test was applied before and after each loading to evaluate the degree of damage and self-healing ability of ECC. Previous studies have shown that the chloride ion penetrability measurement (RCPT) based on ASTM C1202 [185] appears to be particularly promising for evaluating the extent and rate of autogenous healing [20, 25, 27, 76, 89, 186, 187]. For this reason, RCPT was used to observe self-healing capacity and repeatability results.

In RCPT test, water saturated samples ($\varnothing 100 * 50$ mm) were subjected to a 60 V applied DC voltage for 6 h, as shown in Figure 3.7. The specimens were placed between the cathode and anode cells with one end of the specimen in contact with a 0.3M NaOH solution, whereas the other end was in contact with a 3.0% NaCl solution. The total charge that passed in 6 h was obtained as an indicator to evaluate the permeability of chloride ions in ECC specimens. As more chloride ions migrate into the specimens, more current can pass through, and the total charge passed increases. Three samples were tested for each case and the average was presented.

3.3.5 Splitting tensile test

Splitting tensile strength was assessed to understand the effect of self-healing on ECC mechanical performance. This test followed the same protocol as the pre-loading process described above (see Figure 3.4). However, in order to study the

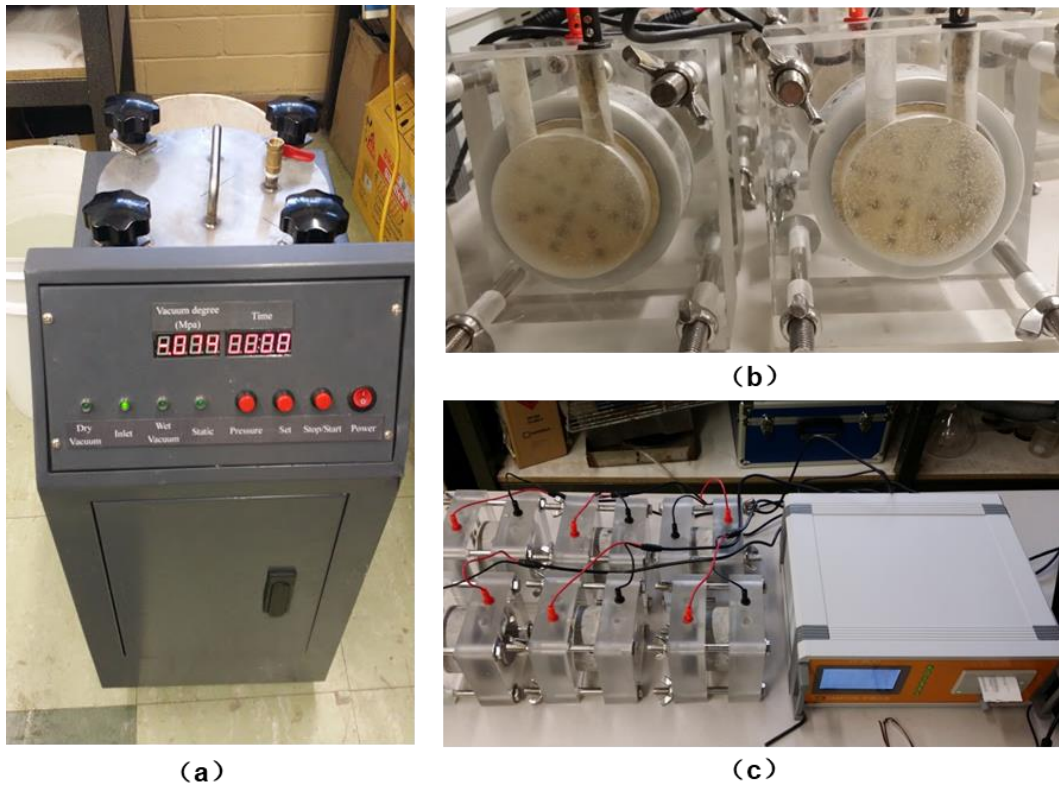


Figure 3.7: Rapid chloride permeability test setup. (a) Vacuum saturated machine; (b) Specimen setup; (c) RCPT equipment

effect of self-healing time on mechanical performance recovery, Set 4 and Set 5 were newly added to compare with Set 3 in Figure 3.4. The preloading and reloading schedule of this new comparison group is shown in Figure 3.8.

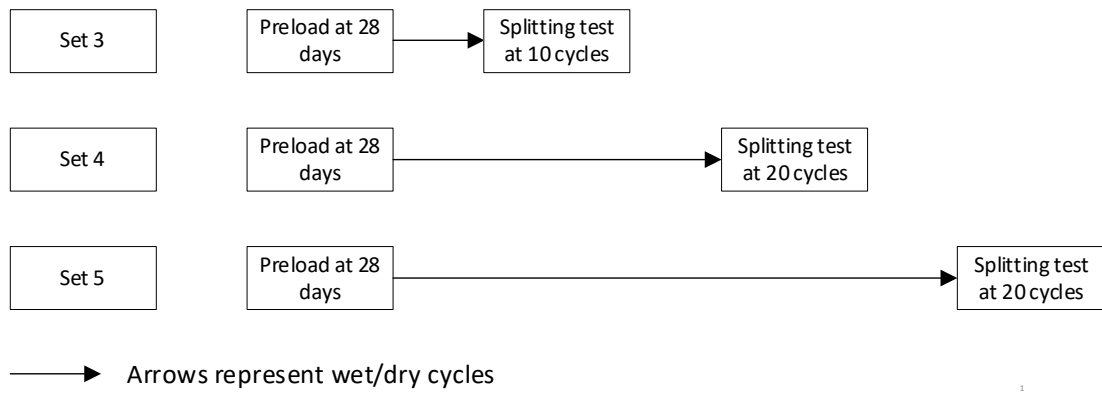


Figure 3.8: Preloading and reloading schedule of splitting tensile strength study

For splitting tensile strength measurement, a cylindrical sample (100 mm diameter and 50 mm height, see Figure 3.9) was conducted, according to ASTM: C 496 [188]. Two bearing strips of nominal 3.0 mm thick plywood, free of imperfections,

approximately 25 mm wide, and of a length equal to the specimen were provided for each specimen. The bearing strips were placed between the specimen and both the upper and lower bearing blocks of the testing machine. In order to ensure the accuracy of test data, bearing strips have not been reused. The load was applied continuously and without shock, at a constant rate of 1.2 MPa/min splitting tensile stress until failure of the specimen. Three samples were tested for each case and the average was presented. The splitting tensile test is calculated by the following equation [188]:

$$S = 2P/\pi ld \quad (3.2)$$

where S is the splitting tensile strength, MPa; P is the maximum applied load indicated by the testing machine, N; l, d are length and diameter, mm, respectively.



Figure 3.9: Splitting tensile strength test

To study the self-healing ability of ECC samples with different mineral ratios, and repeatability of self-healing after multiple loads, the splitting tensile strength recovery rates of ECC with different minerals were compared. The recovery of

splitting tensile strength was determined by comparing the value measured during reloading with the value measured during preloading.

The recovery of splitting tensile strength (R_s) was then calculated using

$$R_s = \frac{S_{reload}}{S_{preload}} \quad (3.3)$$

where S indicates the splitting tensile strength, then S_{reload} and $S_{preload}$ demonstrate the splitting tensile strength of the specimen during reloading and preloading, respectively. The recovery of splitting tensile strength after three rounds of self-healing is analysed in Section 3.4.3.

3.3.6 SEM/EDS

The Scanning Electron Microscope (SEM) is an important research and production tool extensively used in many phases of industry throughout the world [189]. It provides higher resolution analysis and inspection than that afforded by current techniques using the optical microscope. SEM uses a focused beam of high-energy electrons to generate a variety of signals at the surface of solid specimens. The SEM used in this study is Zeiss Sigma VP High resolution, rated up to 1,300,000 x magnification, with multiple detectors – Variable Pressure (VP), Back Scattered Electron (BSE), Secondary Electron (SE), as shown in Figure 3.11 (b). It is capable of performing analyses of selected points or an area on the sample. This approach is especially useful for qualitatively or semi-quantitatively determining chemical compositions, crystalline structure and crystal orientations.

In addition, EDS equipped together with SEM enables chemical element analyses of the samples. The Bruker EDS system was used in this study. Its characterization ability is based on the fundamental principle that each element with a unique atomic structure has a unique set of peaks on its X-ray spectrum [190]. Therefore, the mineralogy of the reaction products can be observed by using SEM, while their chemical elements can be analysed with EDS.

Sample restrictions Samples must be dry, as water will accelerate the volatilization of the cathode material of the electron gun, thereby greatly reducing the life of

the filament, and water will scatter the electron beam and increase the energy dispersion of the electron beam, thereby increasing the colour difference and reducing the resolution. Maximum sample size: up to 15mm height.

Sample cutting The samples were selected from the samples that had completed the splitting tensile test. They were cut to a required size with a diamond saw, as shown in Figure 3.10 (a) and (b). After cutting, the cracks on the top of the sample block and the internal cracks of the original ECC test block can be observed.

Coating for Examination For those systems that require a high vacuum, a thin coating of carbon serves to dissipate excess charge from the specimen while exhibiting little effect on image contrast and little interference with elements of interest. The samples were coated with Cressington 208C High Vacuum Turbo Carbon Coater, see Figure 3.10 (c) and Figure 3.11 (a).

Before the sample is put into the scanning electron microscope, samples were purged with a larger airflow to blow off the unadhered sample particles, as shown in Figure 3.10 (d).

To do morphological analysis, images were taken by a BSE detector with water vapour mode. In order to acquire high contrast images, refer to previous related research[190–193]. An acceleration voltage of 20 kV was used.

To analyse chemical elements of the reaction products, random points on the surfaces of the reaction products were tested with EDS. In order to choose a more representative observation point, it is necessary to select some long cracks and analyse the self-healing conditions of different positions on those cracks. First, 500X or lower magnification was used to find suitable cracks, and then 2000X high magnification was used to observe the morphology and growth trend of the self-healing products. The ratios of the main chemical elements, i.e. Ca/Si and Al/Si, in the self-healing products formed on crack surfaces were calculated [29, 118, 194]. Using the proportional relationship of the elements, combined with the morphological structure of the self-healing material at the crack, the composition of the healing products was analysed.

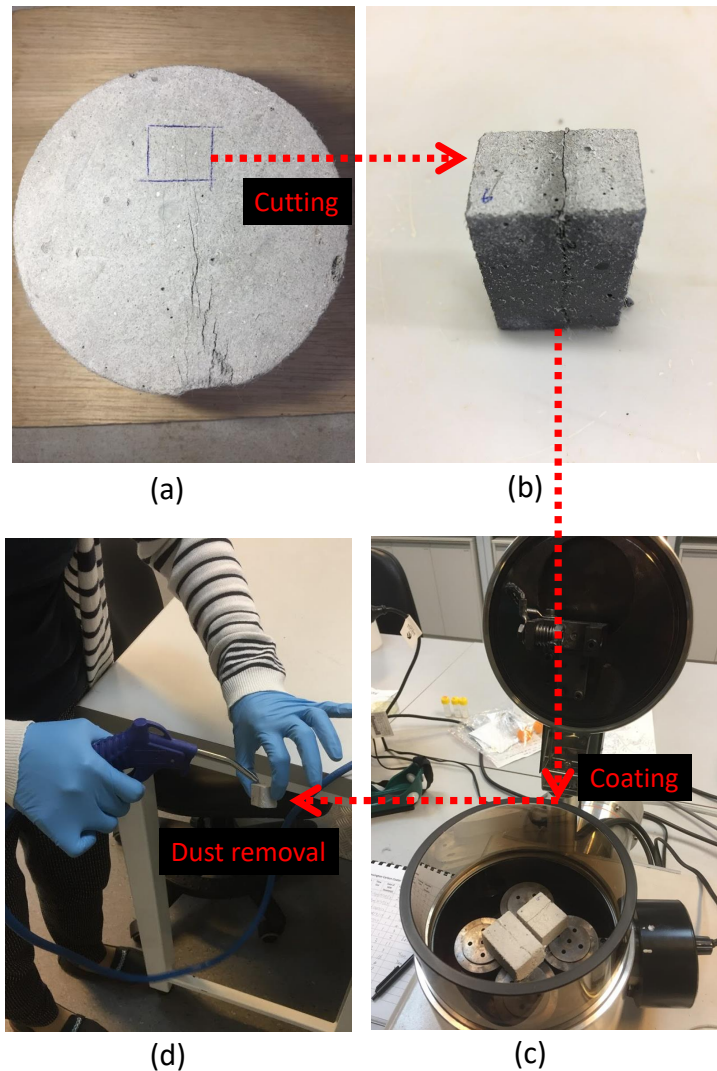


Figure 3.10: Sample preparation



Figure 3.11: Cressington 208C High Vacuum Turbo Carbon Coater (a), and Scanning electron microscope (b)

The main focus of this test is to report the morphologies of self-healing locations we observe in an SEM. Some description and speculation regarding the formation of these morphologies is provided in Section 3.4.4.1. Semi-quantitative analysis of self-healing products was analysed by using the Bruker EDS system, and the results are reported in Section 3.4.4.2.

3.3.7 XRD

XRD analysis was also used to re-identify and verify self-healing products. The same samples were used for XRD analysis to verify EDS analysis results. XRD is a powerful tool for monitoring changes in lattice parameters [195], which has been extensively used to identify the crystalline phases present in the concrete [196]. Self-healing products obtained from the crack were studied using XRD, the XPert Highscore software program suite was used to analyse the results, and the results are reported in Section 3.4.4.3.

3.4 Results and discussion

3.4.1 Digital microscope study with the crack width recovery

There are six specimens with dimension of $\text{Ø}50\text{mm} \times 100\text{mm}$ for each of nine mixtures which were observed using digital microscope to collect crack width samples before self-healing and after self-healing. The specific measurement time is shown in Figure 3.4, and the measurement method is shown in Figure 3.5. In total, 617 cracks were collected, and the crack pattern of nine ECC mixtures is shown in Table 3.4. Abbreviations are used in the Table, the average crack width (labelled as “MEAN”) of cracks (labelled as “number”) that were generated in the first loading (labelled as “1st”), second loading (labelled as “2nd”), and third loading (labelled as “3rd”) in accordance with distribution (labeled as “crack width”).

3.4.1.1 Visual closure of the cracks and the appearance of the healing products

The crack width measures the amount of closure that was carried out according to the method introduced in Figure 3.5. The crack width reduction is quantitatively

Table 3.4: Crack pattern of ECC mixtures.

Mixture	crack width	number	1st	2nd	3rd
			MEAN	MEAN	MEAN
FA55LP15	< 20	15	14.15	13.99	13.63
	20 - 50	24	32.24	37.40	34.18
	50 - 100	21	64.93	72.31	68.83
	> 100	5	132.65	122.30	125.85
FA55SF10LP5	< 20	10	11.16	9.59	12.55
	20 - 50	15	35.25	37.69	35.59
	50 - 100	7	60.52	76.56	79.13
	> 100	2	131.57	115.26	138.57
FA55SF15	< 20	45	11.59	11.46	12.64
	20 - 50	35	32.18	32.18	33.66
	50 - 100	7	53.22	70.38	75.02
	> 100	2	115.80	134.27	123.30
FA55SF5LP10	< 20	18	12.89	12.22	11.65
	20 - 50	7	27.31	33.08	35.72
	50 - 100	8	65.80	71.64	58.79
	> 100	3	123.09	117.84	126.79
FA60LP10	< 20	16	14.18	14.92	12.24
	20 - 50	9	31.12	35.48	49.87
	50 - 100	11	65.28	68.63	86.49
	> 100	3	126.82	112.80	114.91
FA60SF10	< 20	42	13.78	11.18	10.11
	20 - 50	35	27.76	37.60	33.23
	50 - 100	10	63.21	70.84	72.76
	> 100	4	121.78	157.19	119.24
FA65LP5	< 20	47	15.46	11.68	12.04
	20 - 50	56	29.65	29.25	37.25
	50 - 100	8	53.95	55.41	67.35
	> 100	3	119.45	132.55	116.25
FA65SF5	< 20	11	11.12	12.18	13.70
	20 - 50	36	32.97	35.72	28.57
	50 - 100	29	62.22	71.62	72.84
	> 100	2	135.47	126.76	127.41
FA70	< 20	35	11.93	8.32	11.02
	20 - 50	31	33.05	33.28	35.25
	50 - 100	20	63.74	64.21	70.76
	> 100	2	134.69	177.08	184.67
Total		634			

analysed. In previous related studies, many scholars mentioned that the healing effect of cracks is related to the size of the cracks. Therefore, randomly comparing the self-healing width of different cracks on the same sample does not reflect the actual recovery ability of the sample. Therefore, in this study, the size of the cracks under study was divided into four groups: less than $20\ \mu\text{m}$, 20 to $50\ \mu\text{m}$, $50\ \mu\text{m}$ to $100\ \mu\text{m}$, greater than $100\ \mu\text{m}$. Cracks on ECC samples incorporating different minerals were compared according to this grouping. During the crack width closure data collection process, the shape, colour, and growth trend of the healing material was observed.

Please note that the healing rate mentioned in this chapter specifically refers to the crack width recovery rate, see Section 3.3.3 for the calculation method. The completely healed mentioned in this section also only involves the crack width recovery. The efficiency of permeability and mechanical recovery are discussed in Section 3.4.2 and Section 3.4.3.

Typical healing process for $20\ \mu\text{m}$ cracks Figure 3.12 shows a typical healing process for $20\ \mu\text{m}$ cracks after three rounds of loading. For the crack in Figure 3.12, it completely healed after the first self-healing cycle due to the relatively small crack width, which is consistent with other studies [122, 197]. Some studies have found that small cracks repair faster after a single load is applied[197, 198], however, this does not indicate that all small cracks can always be fully healed after multiple rounds of loading. Although most cracks smaller than $20\ \mu\text{m}$ were found to be fully repaired in the first two cycles during the crack observations, this does not indicate that small cracks are fully repaired after every applied load. The actual healing effect is also related to the type of minerals contained in the sample [27], and the proportion [19, 199]. For analysis of various mineral combinations and different mineral proportions on repeatability of crack width self-healing, please refer to Section 3.4.1.2 to 3.4.1.5.

It is worth noting that many cracks smaller than $20\ \mu\text{m}$ have not changed significantly in the width of the cracks after multiple cycles of loading. For example, the crack in Figure 3.12 has a crack width of $21.85\ \mu\text{m}$ after the first applied load and a crack width of $16.38\ \mu\text{m}$ after the second applied load, which is very close in size.

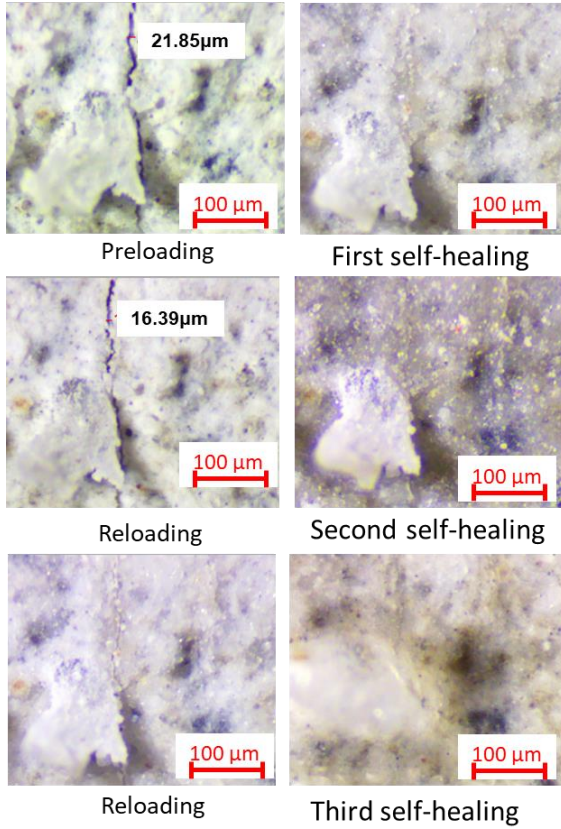


Figure 3.12: Typical crack surface appearance during W/D process, 20 μm

This phenomenon shows that the self-healing of cracks smaller than 20 μm is not only a caulking healing of the surface, but may also be accompanied by the recovery of mechanical properties. In previous studies of self-healing, some scholars have also found that after the first self-healing of small cracks, they may heal completely and may potentially increase the mechanical properties [14, 57]. In contrast to other studies of self-healing with only one load application, the observations in this experiment revealed that cracks smaller than 20 μm are likely to remain accompanied by mechanical property heal after repeated load application. It is possible that this is due to the fact that fine cracks only require less consumption of the surrounding minerals to seal. The composition of these healing products will be discussed in Section 3.4.4.

Typical healing process for 50 μm cracks Figure 3.13 shows a typical healing process for 50 μm cracks after three rounds of loading. After the first load was applied, the crack was completely healed, which is similar to the results of previous studies that used minerals to improve the self-healing ability [200]. After the second

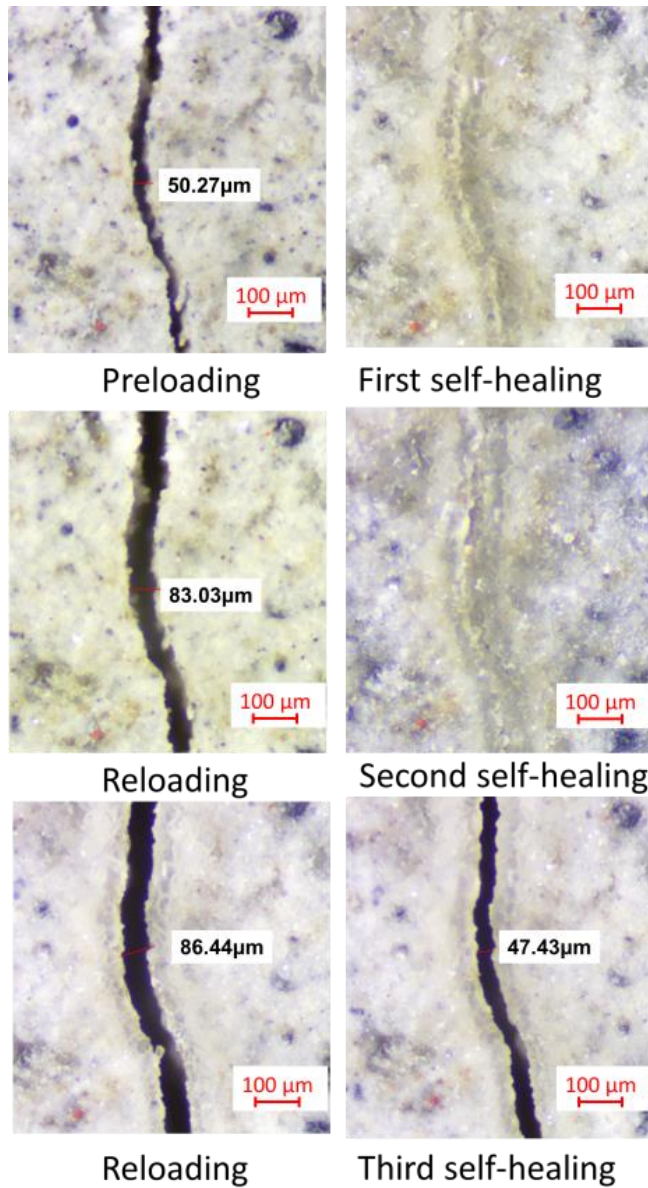


Figure 3.13: Typical crack surface appearance during wetting-drying process, 50 μm

round of load application, the newly formed cracks are larger than the initial cracks formed by the first round of load application. This may be due to the fact that the cracks with an initial size of about 50 μm have poorer mechanical properties than the representative cracks with a size of about 20 μm in the previous analysis. This is also in line with the previous view that for small cracks it is easier to achieve mechanical performance recovery [14, 57]. Although the width of the crack was completely healed in the second round of self-healing, after the third load was applied, the crack was once again larger than the previous width. This shows that the effect of the second self-healing may only be that the produced repair material fills the

cracks, and does not achieve a significant recovery of mechanical properties. Previous research also found that the self-healing substance will almost completely bridge cracks around $50 \mu\text{m}$ wide [201], but this bridging effect is not always accompanied by the recovery of mechanical properties. After the third round of self-healing, the recovery rate of this crack width reached 46.4%. This indicates that this crack of about $50 \mu\text{m}$ has the ability to repeat self-healing. Therefore, it can be considered that this crack can be completely healed twice under repeated loads and partially healed the third time. The third failure to completely heal may be due to the depletion of minerals around the cracks, or that the surrounding mineral content is reduced, and longer healing time is required to complete a full healing. Unlike the cracks around $20 \mu\text{m}$, after multiple cycles of loading, most of the cracks around $50 \mu\text{m}$ will continue to increase. Although part of the crack was completely healed twice on the surface, the cracks continued to expand after the load was applied again, indicating that the mechanical properties were not completely restored.

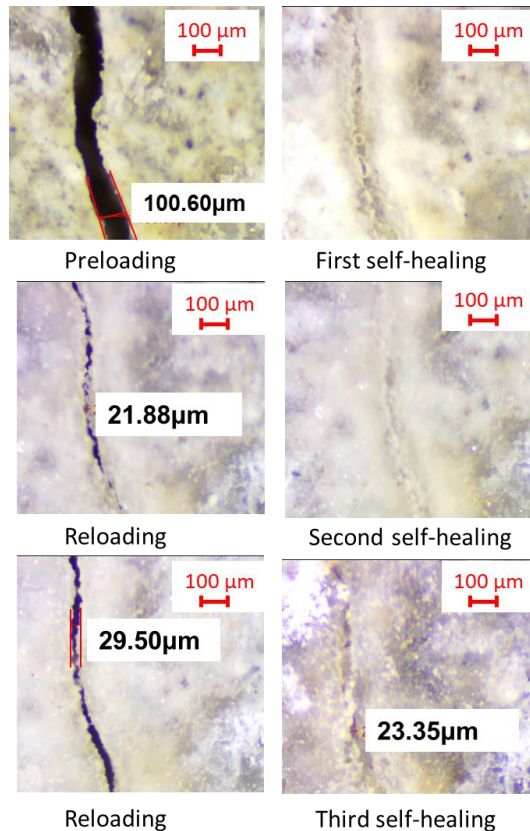


Figure 3.14: Typical crack surface appearance during wetting-drying process, $100 \mu\text{m}$

Typical healing process for 100 μm cracks Figure 3.14 shows a typical healing process for 100 μm cracks after three rounds of loading. The cracks of about 100 μm shown in Figure 3.14 undergo two rounds of complete self-healing, and the healing rate for the third time is 20.8%. The healing rate of this third round is lower than the healing rate of the 50 μm cracks selected earlier, which is 46.4%. Nevertheless, after three rounds of self-healing, the initial crack width of about 100 μm can still be kept below 30 μm . This shows that the cracks of about 100 μm can still show the ability of repeated self-healing after repeated loading. It is possible that mechanical performance has been improved after the first round of self-healing. In some studies on the design of ECC, the researchers found that 50- μm cracks caused mechanical properties to improve after self-healing [202, 203]. However, the focus of these studies is on the design of ECC with repeated self-healing capabilities, but there are few studies that discuss closure of crack width and the recovery of mechanical properties after repeated loads.

Appearance of self-healing substance under digital microscope A large crack was specially made and placed in the same self-healing environment. After 30 W/D cycles, the morphology of the healing material was observed with a microscope. The morphology of healing material under the microscope is shown in Figure 3.15.

A white crystal was formed on both sides of the crack opening, roughly reaching 130 μm , as shown in Figure 3.15 (b). This white substance is generated along the edge of the crack, one end is attached to the crack opening, and the other end points to the other end of the opening like an arrow, as shown in Figure 3.15 (c). This substance is also attached to the PVA fibre under the crack, as shown in Figure 3.15 (d). It is preliminarily inferred that this white substance is the self-healing product of ECC samples. In Section 3.4.4, SEM, EDS and XRD techniques are specifically used to analyse these substances.

Summary For the selected typical cracks around 20 μm , 50 μm and 100 μm , the development of a crack closing process was found, however, with different rates.

Cracks around 20 μm and 50 μm are completely healed after the first load is applied. This is consistent with Li[75], Yang [202] and Snoeck's research results[203],

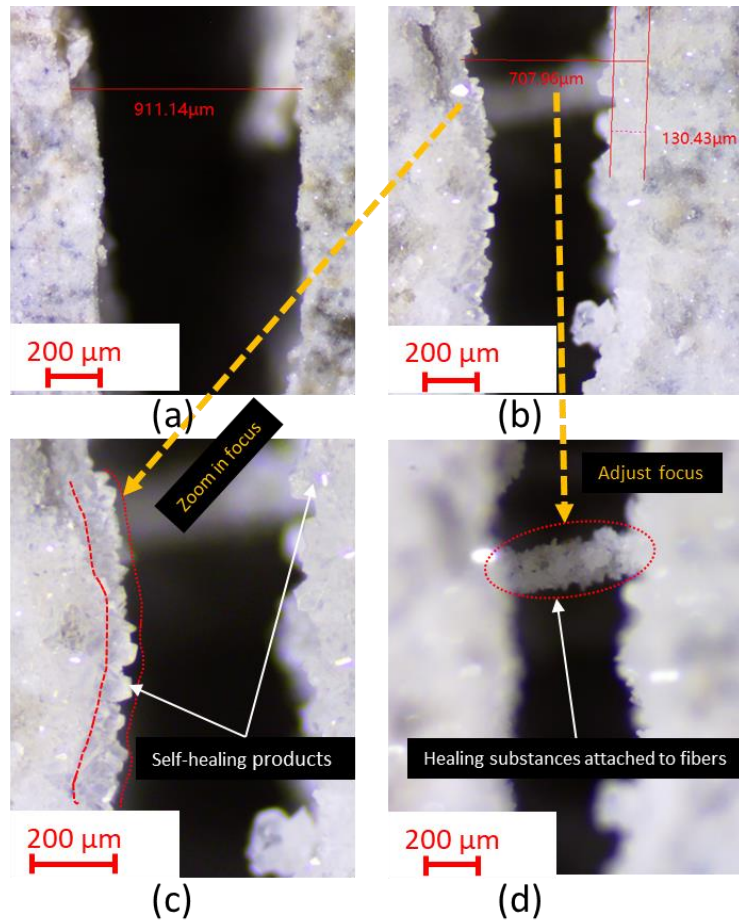


Figure 3.15: Appearance of self-healing substances under digital microscope

which found that cracks narrower than 30 to 50 μm closed completely. However, Snoeck pointed out that cracks with widths between 50 μm and 100 μm closed only partially [203]. In this study, some cracks around 100 μm were completely healed. This may be related to different aggregate ratios and environmental factors in which the samples are located.

Under the premise of certain aggregate and mixing ratio, some scholars believe that the healing ability is completely determined by the initial crack width [122, 203]. The control of the crack width is the key to analysing the self-healing ability of the cracks on the surface. Because this study involves repeated load application, it is difficult to control the fluctuation of the crack size of the same mixture within a small range (20 μm). Therefore, in Section 3.4.1.2, Section 3.4.1.4, and Section 3.4.1.5, the cracks were grouped by size, as shown in Table 3.4. The crack healing effect of different mixtures were analysed directly through the average crack recovery rate.

3.4.1.2 The effect of adding SF on crack width recovery

In this study, a total of nine mixes were designed. As previously analysed, it is difficult to evaluate the self-healing efficiency of a certain mixture based on the healing of a single or a few cracks. Selecting more cracks from a single mixture sample for measurement, and taking the average value to calculate the crack width recovery rate, can better reflect the healing ability of a certain mixture.

When replacing FA in FA70 with different proportions of SF, the healing efficiency of four groups is shown in Figure 3.16. The experiment involved three repeated application of loads and three times of self-healing. After each round of load application, the cracks in FA70, FA65-SF5, FA60-SF10, and FA55-SF15 exhibit different degrees of recovery. In any healing cycle, as the initial width of the crack increases, the healing rate gradually decreases.

Among these four mixtures, FA65-SF5 and FA70 have the best healing rates for cracks smaller than $20\ \mu\text{m}$, reaching 87% and 86%, respectively. FA55-SF15 has the lowest healing rate. For cracks larger than $100\ \mu\text{m}$, the healing rate is only 3%.

When analysing the healing of cracks smaller than $20\ \mu\text{m}$, it was found that the healing rates of FA70, FA65-SF5, FA60-SF10 and FA55-SF15 in the first healing cycle were all above 80%, and when 5% of SF was added they showed the best healing effect. This shows that adding 5% SF improved the crack healing rate in the first healing cycle. In the second and third healing cycles, as the SF content gradually increased, the healing rate decreased.

From the above analysis, it can be seen that for cracks smaller than $20\ \mu\text{m}$, adding 5% of SF can improve the crack healing rate in the first round. For cracks above $20\ \mu\text{m}$, as the content of SF increases, the crack width healing rate decreases. This may be due to the larger surface area of SF particles, which is more prone to chemical reaction. SF consumes the calcium hydroxide in the concrete and forms more calcium silicate hydrates [204]. Due to the larger surface area of SF particles, calcium hydroxide is rapidly reacted [204, 205], and the concentration of calcium ions around the cracks will decrease. Previous studies have shown that calcium ions play a very critical role in the healing process of the crack [28]. The addition of 15% of SF will cause the calcium ions around the cracks to be consumed faster, and therefore it is more unfavourable for crack width recovery.

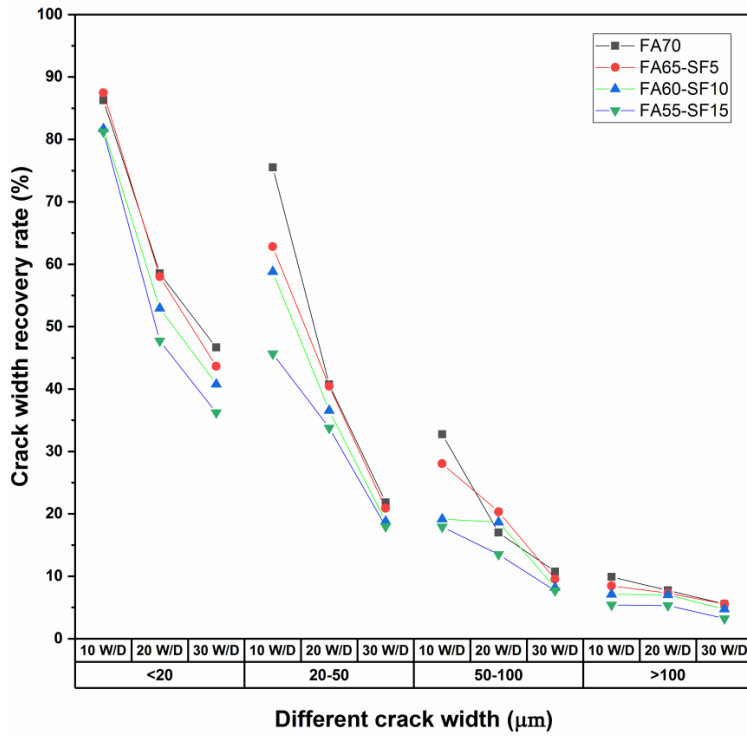


Figure 3.16: Effect of two minerals on crack width recovery, FA and SF

3.4.1.3 The effect of adding LP on crack width recovery

When replacing FA in FA70 with different proportions of LP, the healing efficiency of four groups of different sizes of cracks is shown in Figure 3.17. After each round of load application, the cracks of FA70, FA65-LP5, FA60-LP10, FA55-LP15 have different degrees of recovery. In any healing cycle, as the initial width of the crack increases, the healing rate gradually decreases.

For cracks smaller than $20 \mu\text{m}$, it was found that the healing rates of FA70, FA65-LP5, FA60-LP10 and FA55-LP15 in the first healing cycle were all above 90%, and this is due to tighter cracks that tend to heal faster and more completely [197, 198]. Among these four mixtures, FA55-LP15, and FA60-LP10 have the best healing rates in the first self-healing round for cracks smaller than $20 \mu\text{m}$, reaching 95.74% and 94.71%, respectively. This indicates that the addition of LP has significantly improved the crack width recovery of the first round. This may be due to the fact that the calcium content in FA55-LP15 and FA60-LP10 is higher than FA (the control). The contribution of calcium ions from FA would be negligible due to the low CaO content in the low-calcium FA (Table 3.1). Therefore, in terms of reaction

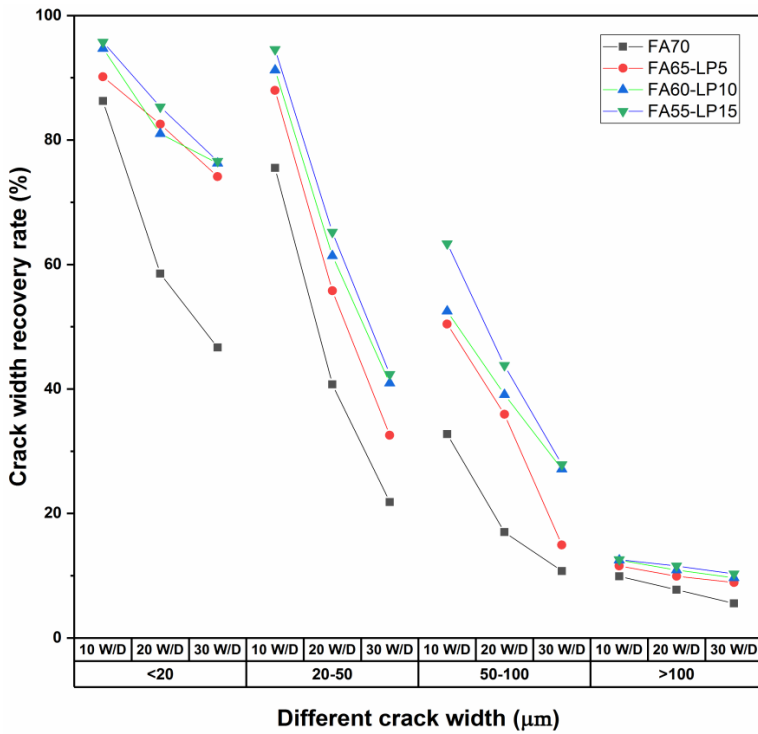


Figure 3.17: Effect of two minerals on crack width recovery, FA and LP

mechanism, the main effect of LP addition is to elevate the concentration of calcium ions [206]. When 15% of LP was added, the content of calcium ions is relatively higher, and it also exhibits the highest recovery rate.

After the second round of load, the healing rate of cracks smaller than 20 μm for samples containing LP is still higher than 80%. The healing rate of FA70 for cracks smaller than 20 μm in the second cycle is only 59%, which means that adding LP can significantly improve the repeated self-healing efficiency of crack width. For cracks smaller than 20 μm , the specimens adding 15% LP exhibit best repeated self-healing effect. This may be due to the fact that small cracks consume less repair products [122], so there is a relative surplus of mineral elements around the cracks that can be used for the next round of self-healing.

For cracks between 20 and 50 μm , FA60-LP10 and FA55-LP15 achieved 91% and 95% healing rates in the first round of self-healing. In the second round of healing, 61% and 65% of healing rates were still maintained, while the healing rate of FA70 in the same period dropped to only 41%. For cracks of 50 to 100 μm , FA60-LP10 and FA55-LP15 can reach 52% and 63% in the first self-healing cycle. For cracks larger than 100 μm , the healing efficiency of FA60-LP10 and FA55-LP15 is 12% and

13% in the first round of healing, which is not very different from the 10% healing rate of FA.

After the third load is applied, the healing rate of FA60-LP10 and FA55-LP15 for cracks less than 20 μm can reach more than 76%; for cracks of about 20-50 μm , the healing rate can reach more than 40%. The healing rate of cracks of about 50-100 μm can reach more than 27%. Most self-healing studies have concluded that self-healing rate is much more pronounced in early-age specimens [122, 207]. However, compared with FA70, FA65-LP5, and FA60-LP10, the specimens adding 15% LP still exhibit better self-healing effect, in all three healing rounds (10 W/D cycles, 20 W/D cycles and 30 W/D cycles). This shows that increasing the content of LP can improve the repeat self-healing ability in terms of crack width recovery.

For cracks larger than 100 μm , the healing rate is below 10%. The addition of 15% of LP is not enough to seal cracks larger than 100 μm within 10 W/D cycles. The wider the crack, the more time it takes to repair. Previous research also showed that the narrower the cracks, the more efficient the self-healing [122]. Taking 10 W/D cycles as a self-healing round, the addition of 15% LP is more pronounced for the self-healing capacity of cracks below 100 microns.

The above analysis indicated that the addition of LP in FA70 can significantly improve the the repeatability of self-healing of crack width. For cracks less than 100 μm , adding 10% and 15% LP can significantly improve the crack healing rate in three self-healing, and adding 5% of LP will improve the self-healing ability of the first two rounds. The self-healing improvement is not significant for cracks greater than 100 μm .

3.4.1.4 The effect of adding two minerals on crack width recovery

When the content of SF is constant, replace FA with LP. In this study, the process of adding two other minerals to FA70 was achieved by replacing FA with new minerals. For example, FA55-SF5-LP is equivalent to adding 5% of SF to FA70, and then adding 10 % of LP.

As analysed in the previous section, compared to FA70, FA65-SF5 can improve the healing efficiency of cracks below 20 μm in the first cycle, and this may be due to the SF being a very reactive pozzolanic material, with more than 95% of the particles

being less than $1 \mu\text{m}$ [208, 209]. The small amount of SF may react quickly with calcium hydroxide (CH) and form the strength contributing substance of C-S-H gel [210]. C-S-H bridges between crack lips [211]. Previous related research results also show that C-S-H is one of the common self-healing products[20, 211]. However, this improvement is limited to the first round of self-healing of the samples, as shown in Figure 3.18. This is consistent with previous studies on young specimens that show that they heal faster [122, 207, 212], and then as time progresses, the mineral content of the specimen is further reduced, which affects the second self-healing.

There is no obvious improvement for cracks larger than $20 \mu\text{m}$. However, as shown in Figure 3.18 comparing FA65-SF5 and FA55-SF5-LP10, after further increasing the LP by 10%, the efficiency of self-healing cracks has been significantly improved. For less than $20 \mu\text{m}$ cracks, the first round of healing rate increased from 87.48% to 92.52%, and the second round of healing rate increased from 58.1% to 63.48. For $20\text{-}50 \mu\text{m}$ cracks, the first and second rounds of healing also increased from the original 62.38%, 40.47 increased to 89.77% and 50.12%. For cracks between $50\text{-}100 \mu\text{m}$, the healing rate in the first round increased from 28% to 36.14%, and in the second round from 20.35% to 30.83%.

This multi-mineral synergy may be one of the reasons for improving the self-healing efficiency of FA55-SF5-LP10, which resulted in the addition of two minerals to FA70 and has a higher healing efficiency than adding SF only. SF is a very reactive pozzolanic material [208, 209], and when SF and LP are added at the same time, SF particles will react with calcium ions brought in by LP to form C-S-H [210, 211], which may serve as the self-healing substance for the first round of self-healing.

It is worth noting that the SF content in FA55-SF5-LP10 is only 5%, which is likely to play a role in the first round of self-healing, and the excess LP will play a major role during subsequent self-healing processes. The morphological analysis of FA55-SF5-LP10 after repeated self-healing also showed obvious calcium carbonate crystals (see Section 3.4.4.1). This was also verified by analyzing the repeated self-healing products, as described in Section 3.4.4.2. The addition of 10% LP will increase the content of calcium ions in the sample, which is more conducive to the production of more self-healing products [206]. As a non-reactive material LP will continue to form calcium carbonate precipitates to seal cracks when moisture and

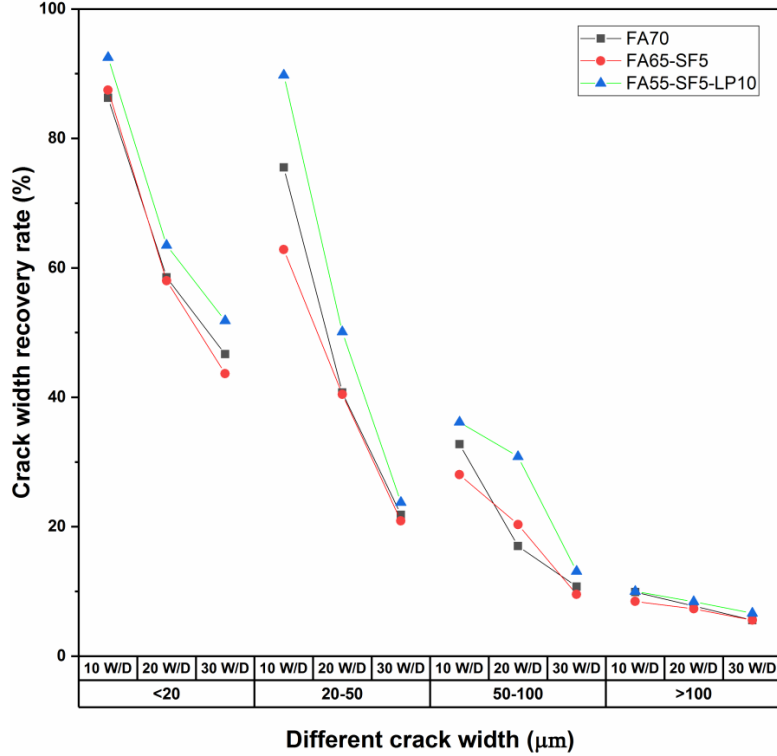


Figure 3.18: When the content of SF is constant, replace FA with LP, SF content is 5%

carbon dioxide are sufficient in the later stage [28, 212]. The self-healing products under the synergistic effect of multiple minerals will be studied in Section 3.4.4. It is worth noting that excess non-reactive LP may increase porosity, thus causing reduction in strength[213]. Under the synergistic effect of various minerals, the influence of mechanical performance recovery will be specifically studied in Section 3.4.3.

For cracks larger than 100 μm , the healing rate has been around 10% in three rounds of repeated self-healing, and the healing rates of FA70, FA65-SF5, and FA55-SF5-LP10 did not change significantly during the three healing cycles. Large cracks require more healing products and longer healing time. The repeated healing ability of cracks greater than 100 μm cannot be observed in 10 W/D cycles (20 days, one round of self-healing).

As shown in Figure 3.19, comparing FA60-SF10 with FA55-SF10-LP5, while keeping the SF content at 10%, adding 5% LP to FA60-SF10 will promote crack-healing rate. For example, for cracks smaller than 20 μm , the crack healing rate of FA60-SF10 and FA55-SF10-LP5 decreased from the original 81.96% and 87.65%

in the first healing round to 40.78% and 46.86% of the third healing round. For cracks of 20-50 μm in the first healing cycle, the crack healing rate has improved to a certain extent, from the original 58.8% (FA60-SF10) to 65.1% (FA55-SF10-LP5). It is worth noting that for 20-100 μm cracks, although the healing efficiency of FA55-SF10-LP5 is better than FA60-SF10, the healing rate is still lower than FA70, which may be due to the way SF consumes calcium hydroxide, and reduces the self-healing potential compare with FA70 [59]. This also explains why the crack recovery rate of cracks larger than 50 microns in Figure 3.19 is less than 15%.

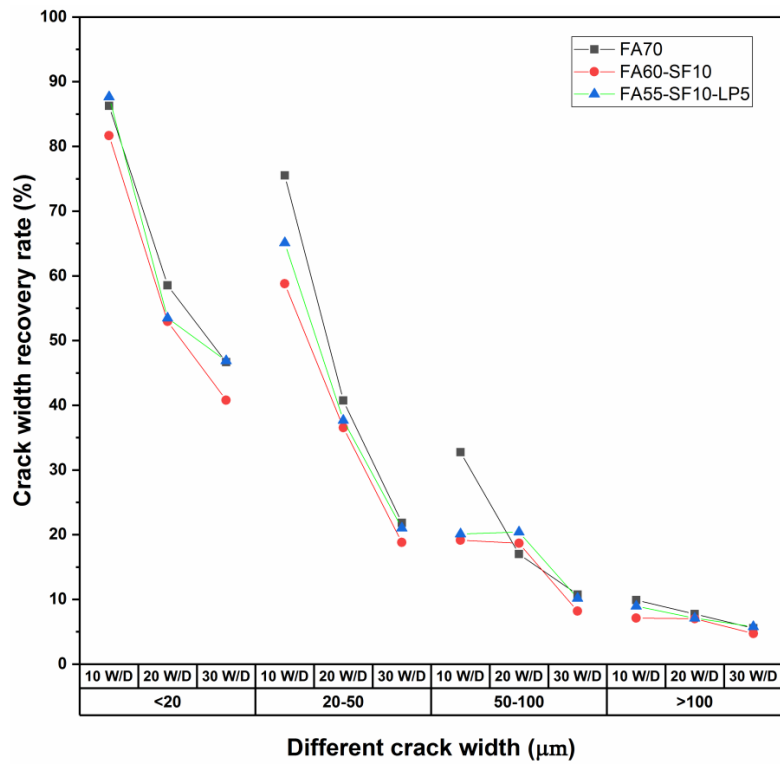


Figure 3.19: When the content of SF is constant, replace FA with LP, SF content is 10%

The above analysis has indicated that the addition of 10% SF decreases the self-healing ability, and the addition of 5% LP to FA60-SF5 is only conducive to the self-healing of cracks below 20 μm .

When the content of LP is constant, replace FA with SF As shown in Figure 3.20, comparing FA60-LP5 with FA55-SF10-LP5, while keeping the SF content at 5%, adding 10% LP to FA60-SF10, the healing rate of cracks becomes lower, generally even lower than the original FA70 healing rate (for cracks of all sizes).

This may be mainly due to the fact that many calcium ions provided by 5% LP participate in the hydration reaction [206]. Especially in the presence of 10% SF, due to the small characteristics of silicon ions, it is easier to be contacted [204], and more LP will be consumed. Previous related studies have shown that the healing efficiency of the crack surface is related to the calcium ion concentration at the crack opening [27, 28, 190], and the decrease of the calcium ion concentration around the crack will inevitably affect the healing of the crack width.

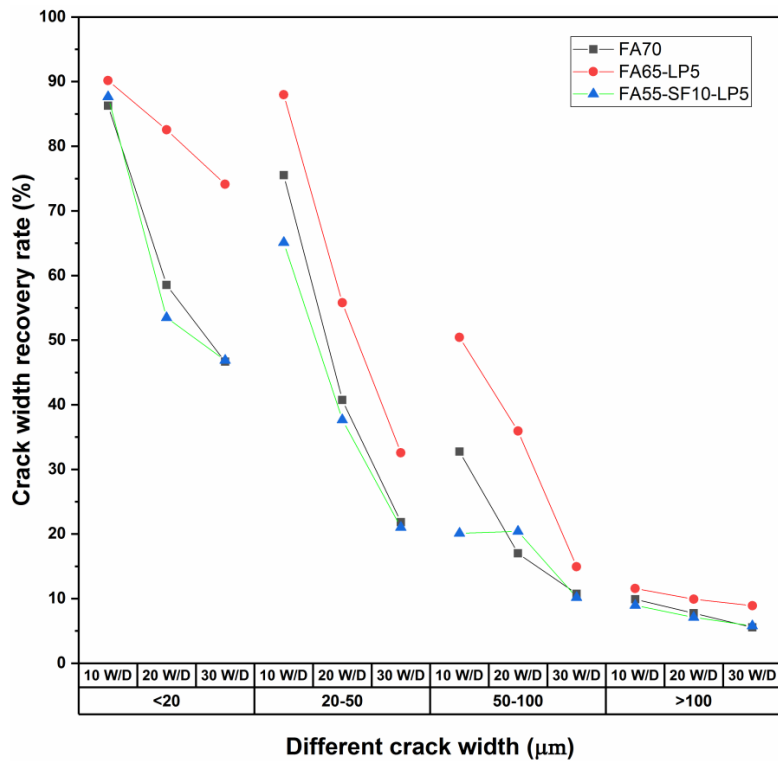


Figure 3.20: When the content of LP is constant, replace FA with SF, LP content is 5%

Figure 3.21 compares the crack width healing rate of FA60-LP10 and FA55-SF5-LP10. After adding 5% SF to FA60-LP10, the crack width healing rate decreases, and this trend exists in cracks of all sizes. The added SF will consume the calcium hydroxide in FA60-LP10 [59], thereby reducing the calcium ion concentration around the cracks. The healing of the crack surface is related to the calcium ion concentration at the crack opening [27, 28, 190], and the decrease of the calcium ion concentration around the crack will inevitably affect the healing of the crack width. Nevertheless, the healing rate of FA55-SF5-LP10 in each healing cycle is still higher than that of FA70, which shows that adding two minerals (SF and LP) in an

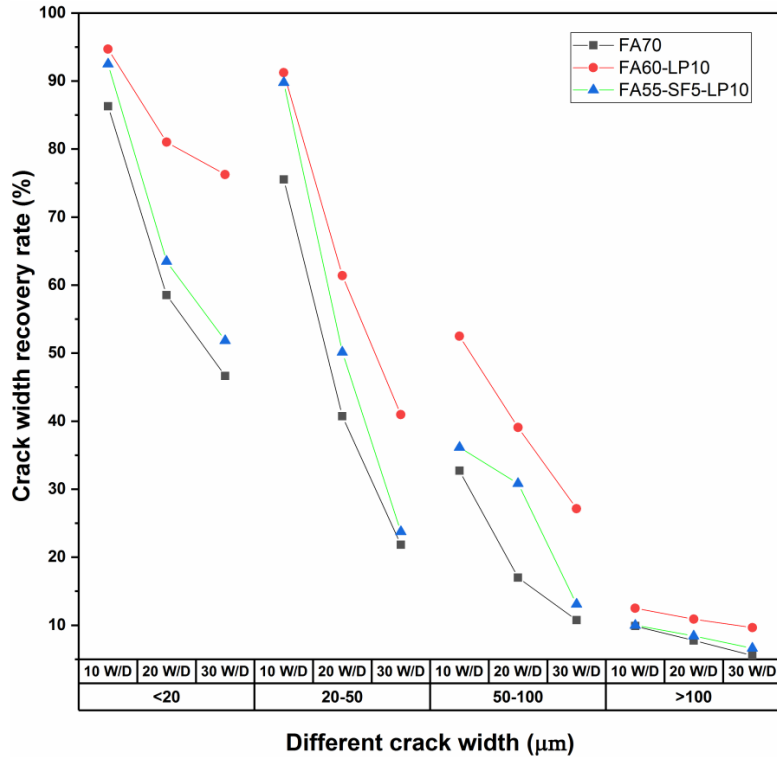


Figure 3.21: When the content of LP is constant, replace FA with SF,LP content is 10%

appropriate proportion to FA70 can also increase the crack healing rate to a certain extent.

3.4.1.5 The influence of content change between LP and SF on crack width recovery

Figure 3.22 shows the changes in the crack healing rate during the gradual replacement of LP in FA55-LP15 by SF. The self-healing rate of the crack width decreased significantly for all cracks of different sizes after multiple cycles of loading. Among them, FA55-LP15 showed the highest crack healing efficiency, followed by FA55-SF5-LP10.

After three rounds of loading, the healing rate of FA55-LP15 can still reach 76.7% for cracks below 20 μm , and the healing rate can still reach 42.35% for cracks about 20-50 μm . For cracks about 50-100 μm , the crack healing rate was 27.87%. From the perspective of the self-healing mechanism, 15% of LP provides calcium ions for ECC samples [206]. When cracks recur and water and carbon dioxide are sufficient, calcite forms by combining with leached-away calcium ions from C-S-H gels and LP [24, 28]. On the other hand, the high content of LP will provide more

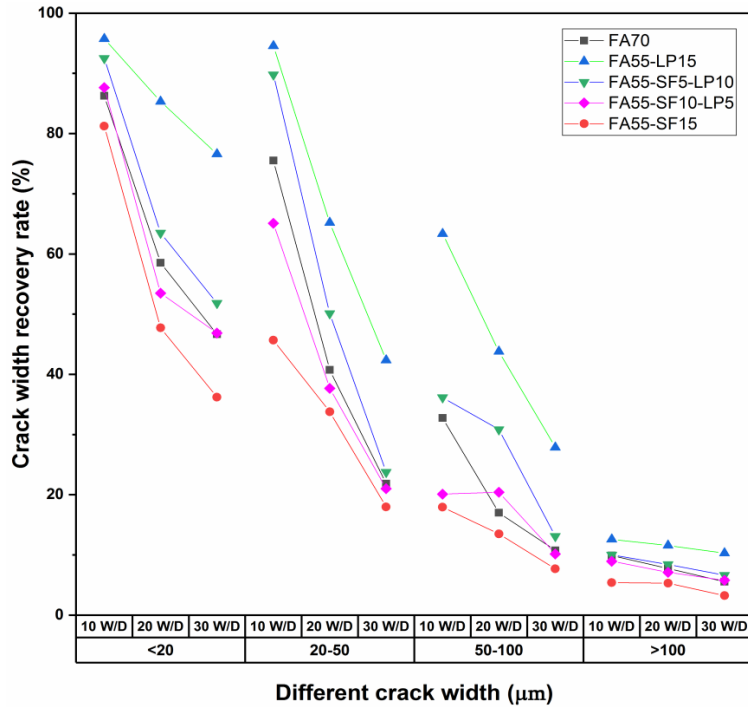


Figure 3.22: Effect of two minerals on crack width recovery, the LP in FA55-LP15 is gradually replaced by SF

calcium hydroxide in the cementitious systems, which may significantly contribute to higher pH levels, causing faster disassociation of carbonic acids into bicarbonate and carbonate ions [14], and further promoting calcite formation [14, 28]. After three cycles of loading, FA55-SF5-LP10 also achieved 76.26% and 42.35% healing rates for cracks below 20 μm and about 20-50 μm . The crack recovery rate of FA55-SF5-LP10 is lower than FA55-LP15 after multiple rounds of loading which may be attributed to the chemical characteristics of SF. SF is an extremely small reactive pozzolanic material that can consume more calcium ions [208, 209]. SF reacts quickly with calcium hydroxide (CH) and forms C-S-H gel [210]. The content of calcium ions is reduced, potentially reducing the repeated self-healing ability. For cracks larger than 100 μm , the healing rate after three rounds of self-healing is less than 20%. This is because healing large cracks requires more repair healing materials and time. For details about the healing characteristics of cracks around 100 μm , please refer to Section 3.4.1.1.

For cracks of all sizes, FA55-SF15 has the lowest crack healing rate. Combining the analysis of the relationship between the amount of SF added and the crack width

recovery rate in Section 3.4.1.2, it can be concluded that adding more than 10% SF to FA70 is not conducive to the healing of cracks.

The above analysis shows that FA55-LP15 and FA55-SF5-LP10 exhibit a relatively high crack width recovery rate after three rounds of loading. FA55-LP15 and FA55-SF5-LP10 have a healing rate of more than 76% for cracks below 20 μm , and the healing rate of cracks about 50-100 μm can reach 42.35% and 27.87%, respectively. For cracks larger than 100 μm , the crack healing rate of all mixes is less than 11%. This may be due to the fact that large cracks require more healing products [122], but the mineral content used to healing the cracks at the crack openings is gradually decreasing [28], which also makes large cracks more difficult to healing.

3.4.2 RCPT test and repeated self-healing behaviour

3.4.2.1 Changes in chloride ion permeability after repeated preload

By comparing the changes in permeability of specimens after several preloading and healing conditions, the influence of different minerals combinations on self-healing performances can be revealed. Nine different mixtures were divided into seven groups to analyse the effects of silica fume, hydrated lime powder and the combination of these two minerals on the chloride ion permeability of ECC samples.

Figures 3.23 to 3.29 represent the average charges passed through the pre-cracked ECC specimen before and after preloading. Every ten W/D cycles (20 days) is one observation cycle. It can be seen from Figure 3.23 to 3.29 that the permeability of all ECC specimens increased significantly after the first preloading was applied, and then the permeability decreased after they underwent 10 W/D cycles. The charges passed through pre-cracked ECC specimens are likely to increase as cracks offer an extra preferable path allowing charges to pass besides the matrix [214]. After the wet-dry cycles in each observation period, the permeability of ECC samples decreased in varying degrees.

As shown in Figure 3.23, the charges passed through sound FA70 ECC specimens was 3237 C which can be classified as the moderate level for the chloride ion penetrability in accordance with ASTM C1202. With 5% silica fume, the permeability of SF5 dropped to 1186 C, at the level of low, which is consistent with the finding that a small amount of silica fume can also significantly reduce the permeability of

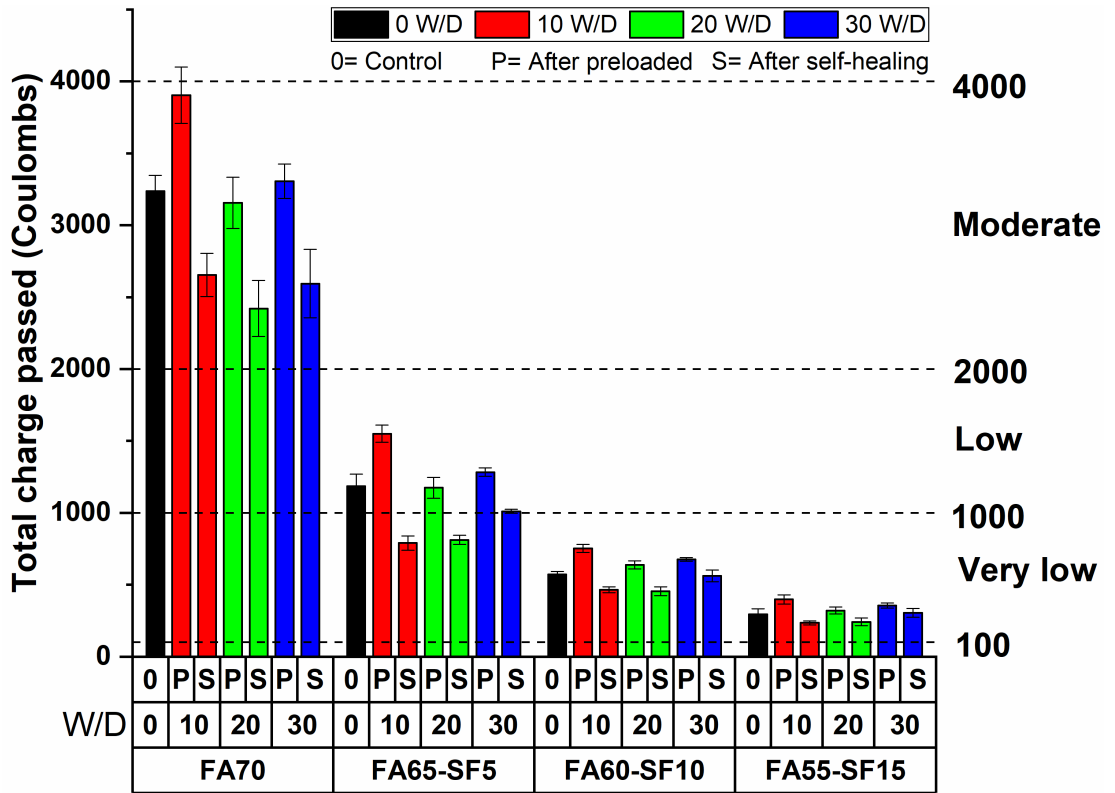


Figure 3.23: RCPT results of different cycles (comparison of the influence of SF content)

concrete [214]. The replacement of fly ash with 10% and 15% silica fume caused the charges passed through sound specimens to decrease to 573 C and 294 C, which is classified as very low level for a chloride ion penetrability. This result shows that increasing the silica content has the effect of reducing the permeability. Silica fume is a very reactive pozzolan, and most of the pore refinement effect was caused by the pozzolanic activity of the silica [215]. The refinement function of silica (i.e. less of the pore space consisted of capillary pores) leads to reduced permeability [214]. As shown in Figure 3.23, after three rounds of repeated application of loads and self-healing process, the total charge passed through was at a very low level. This reduction could be primarily attributed to the increased density of the matrix in the presence of silica fume. The addition of silica fume reduces the pores in the paste, and the permeability at the interface between cement paste and aggregate [?]. In addition, previous related studies have also shown that as the relative content of FA increases, the charge passed increases [20]. Considering that different mineral ratios have a significant effect on the total chage passed (e.g., the content of SF), the initial charge passed value before the application of load on the 28th day will be

chosen as the reference value for the subsequent analysis of permeability repetitive self-healing ability. The amount of total charge passed was converted into a rate of change based on this reference value, and the percent variations will be used to analyze permeability repetitive self-healing capacity, see section 3.4.2.2 for details.

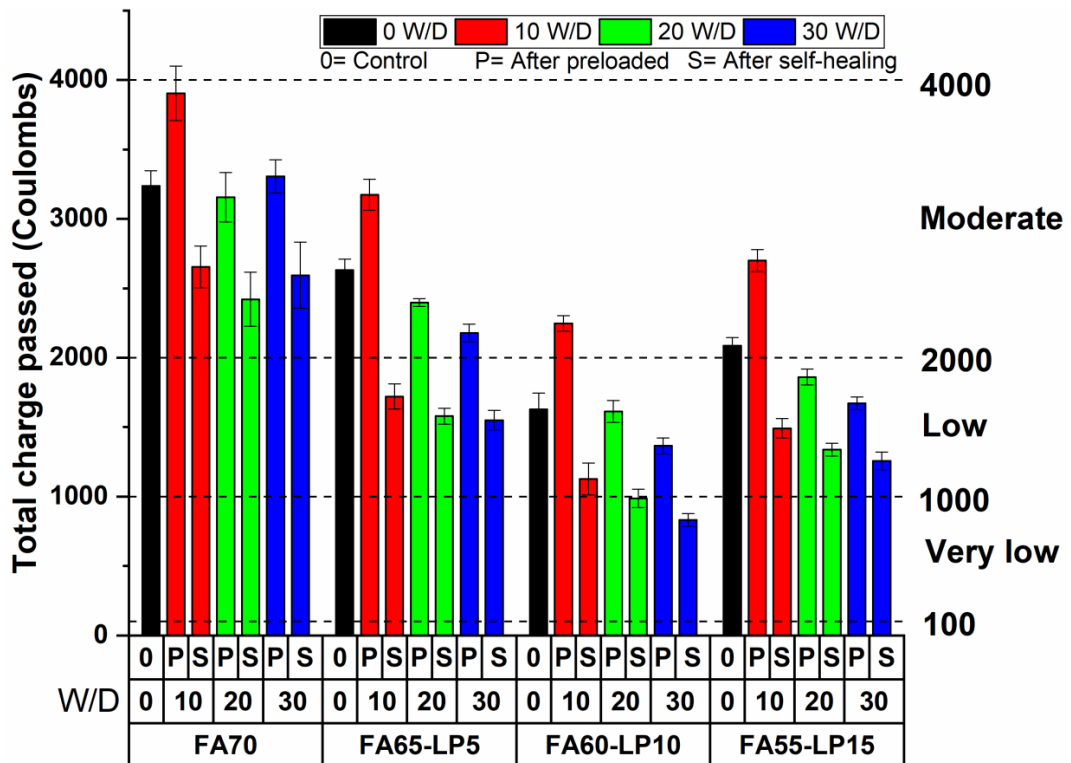


Figure 3.24: RCPT results of different cycles (comparison of the influence of LP content)

When fly ash was replaced with various contents of LP, the total charges passed observed for FA65-LP5 and FA60-LP10 and FA55-LP15 decreased to 2595 C, 1747 C, 2104C at 0 cycle, respectively, compared with FA which was 3368 C as shown in Figure 3.24. The probable reason for the higher charges passed through FA55-LP15 at 0 W/D cycle is that the higher dosage of LP may result in the presence of non-reactive hydrated lime in the binder paste matrix, which would increase its porosity, thus causing an increase in the RCPT value at 0 W/D cycle [213].

After the first round of loading, the total charges passed observed for FA65-LP5, FA60-LP10 and FA55-LP15 were 3173 C, 2247 C, and 2700 C, respectively, and were all at a moderate level. After 10 W/D cycles of self-healing, the total charges passed and observed in those three mixtures dropped to the low level. The charges observed

in FA65-LP5 rose to moderate level after the second round of preloading, however, FA60-LP10 and FA55-LP15 were still at a lower level. This indicated that the ECC specimens incorporated with 10% and 15% LP seemed to have a more significant healing effect and the reason is probably due to the fact that a high dosage of LP in specimens may release calcium ions, which can react with carbonate ions in water or carbon dioxide in air to form calcium carbonate precipitates, and thus contributing to closure of the cracks [184]. This is consistent with the results of the crack width recovery rate of FA60-LP10 and FA55-LP15 in Section 3.4.1.3.

After 30 W/D cycles, the total charges passed through FA60-LP10 were still kept at a very low level. This showed that replacing fly ash with 10% LP is beneficial for improving the repeated self-healing ability of ECC.

When FA in FA70 is partially replaced by SF or LP, it was found that different mineral combinations and ratios influence the self-healing of ECC specimens.

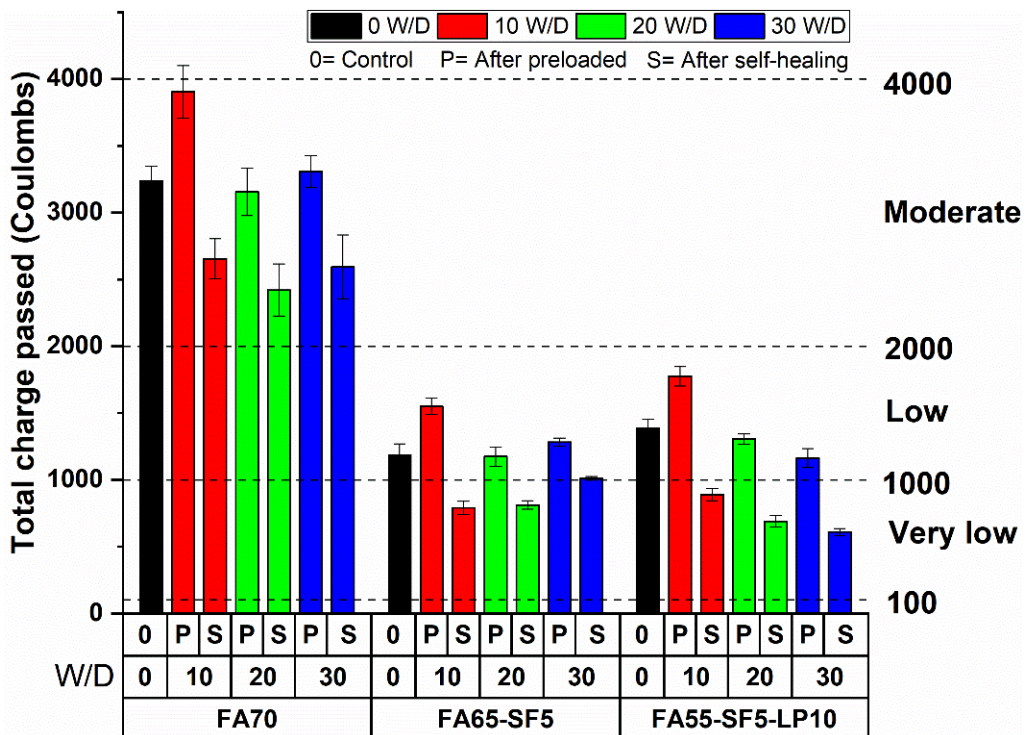


Figure 3.25: RCPT results of different cycles (Replace 10% FA in FA65-SF5 with LP)

For the case where the SF content is constant, and in comparison with FA65-SF5, replacing fly ash with 10% LP enhanced the second and third time self-healing capabilities of ECC, and maintained the total charge passed at a relatively low level,

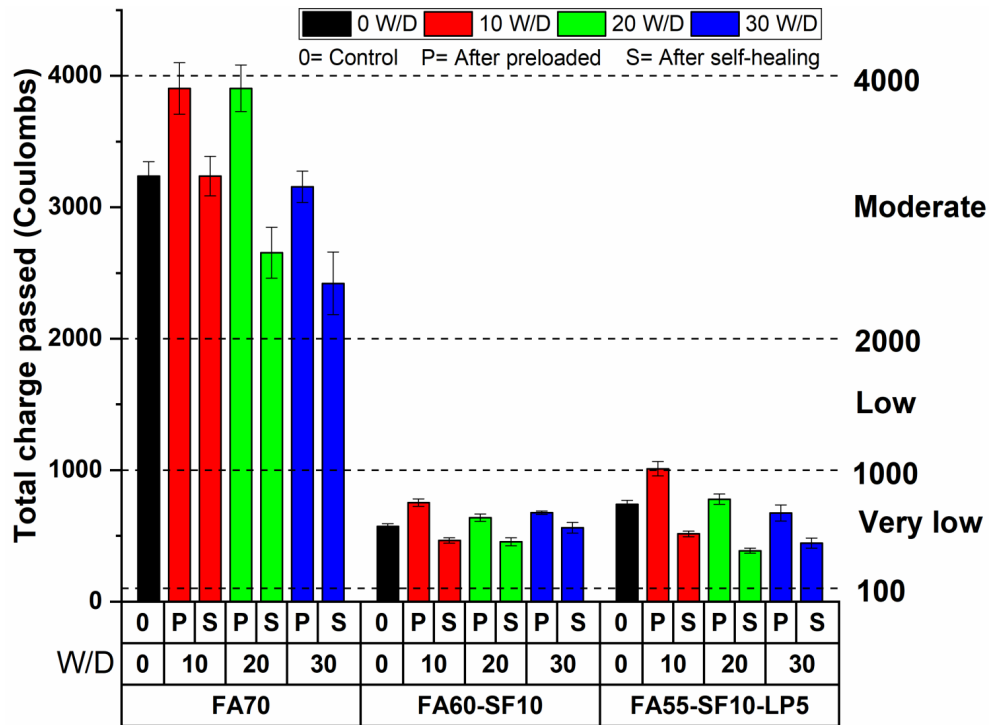


Figure 3.26: RCPT results of different cycles (Replace 5% FA in FA60-SF10 with LP)

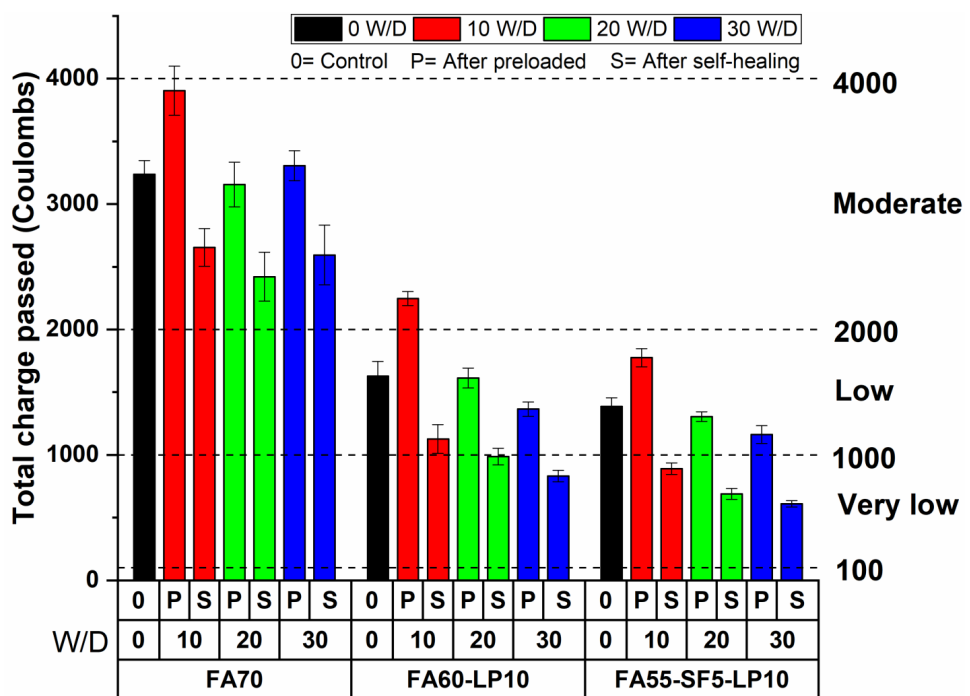


Figure 3.27: RCPT results of different cycles (Replace 5% FA in FA60-LP10 with SF)

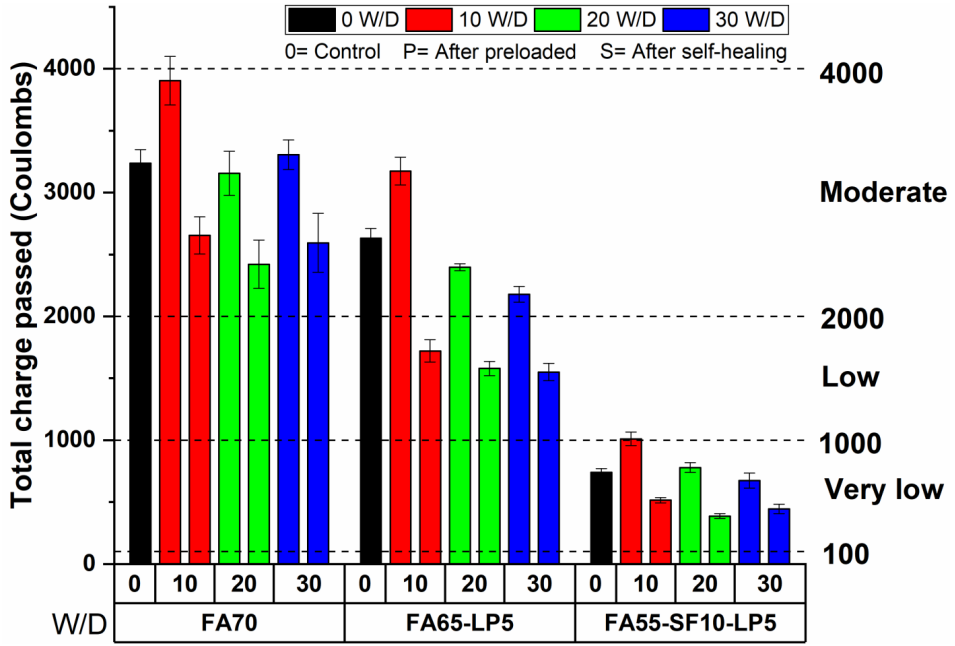


Figure 3.28: RCPT results of different cycles (Replace 10% FA in FA65-LP5 with SF)

as shown in Figure 3.25. The addition of 5% LP to FA60-SF10 caused a decrease in permeability after the second and third rounds, which suggested that the repeated self-healing ability can be enhanced by adding 5% LP to FA60-SF10, as shown in

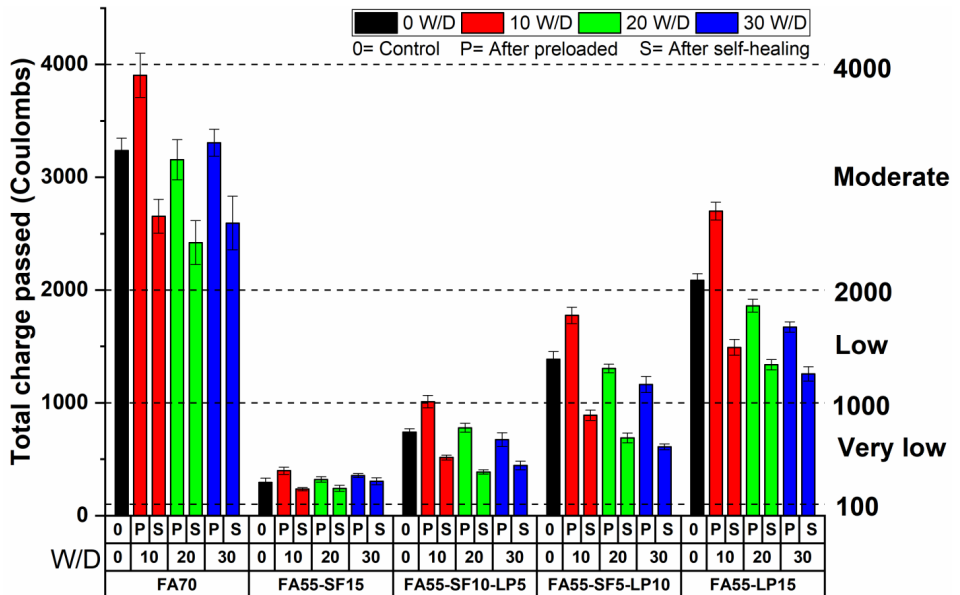


Figure 3.29: RCPT results of different W/D cycles (the process of SF being gradually replaced by LP in FA55-SF15; 1). FA55-SF15, relative to FA70, replace 15% FA with SF; 2)FA55-SF10-LP5, relative to FA55-SF15, replace 5% SF with LP; 3)FA55-SF5-LP10, relative to FA55-SF10-LP5, replace 5% SF with LP; 4)FA55-LP15, relative to FA55-SF5-LP10, replace 5% SF with LP;5

Figure 3.26.

For the case where the LP content is constant, replacing FA with 5% SF in FA65-LP5 (as shown in Figure 3.27) and 10% SF in FA60-LP10 (as shown in Figure 3.28) also significantly reduced the total charge passed value. This may also be due to the refinement effect of silica fume [215].

In the third discussion case, keeping the content of FA unchanged, 15% of SF is gradually replaced by LP. As shown in Figure 3.29, as the content of LP increased, the total charge passed before and after self-healing is on the rise in each observation round. However, after three rounds of self-healing, the total charge passed values of FA55-SF10-LP5 and FA55-SF5-LP10 were still at a very low level. It seems that when FA content is constant, higher silica fume is effective in keeping the chloride ion permeability at a relatively low level after repeated loading. Figure 3.29 shows the permeability level of different mixtures with SF or LP added after multiple loads. See Section 3.4.2.2 for the analysis of repeatability of self-healing in term of chloride ion permeability.

3.4.2.2 Percent variations in chloride ion permeability

As seen in Figure 3.30, Figure 3.31 and Figure 3.32 both ECC mixtures showed repeated self-healing ability, with decreasing chloride ion penetrability results after each W/D cycle. The rate of change in ion permeability discussed below is relative to the initial values before the application of load at 28 days of each, so the rate of change is equal to the RCPT value for each cycle minus the initial RCPT value before the applied load is applied, and then divided by the initial value. This section evaluates the self-healing capacity of each round after applying the load by comparing the rate of change in chloride permeability of the cracked and sound samples.

At the end of the 10th W/D cycle, the chloride ion permeability of the specimens with 5%, 10% and 15% silica fume were able to reduce 33.4%, 18.8% and 20.1% with respect to the first results taken at the end of 28 days, whereas the corresponding sound specimens dropped 40.9%, 15.7%, and 23.8%, as shown in Figure 3.30. The values of FA60-SF10 and FA55-SF15 after self-healing were closer to the sound values

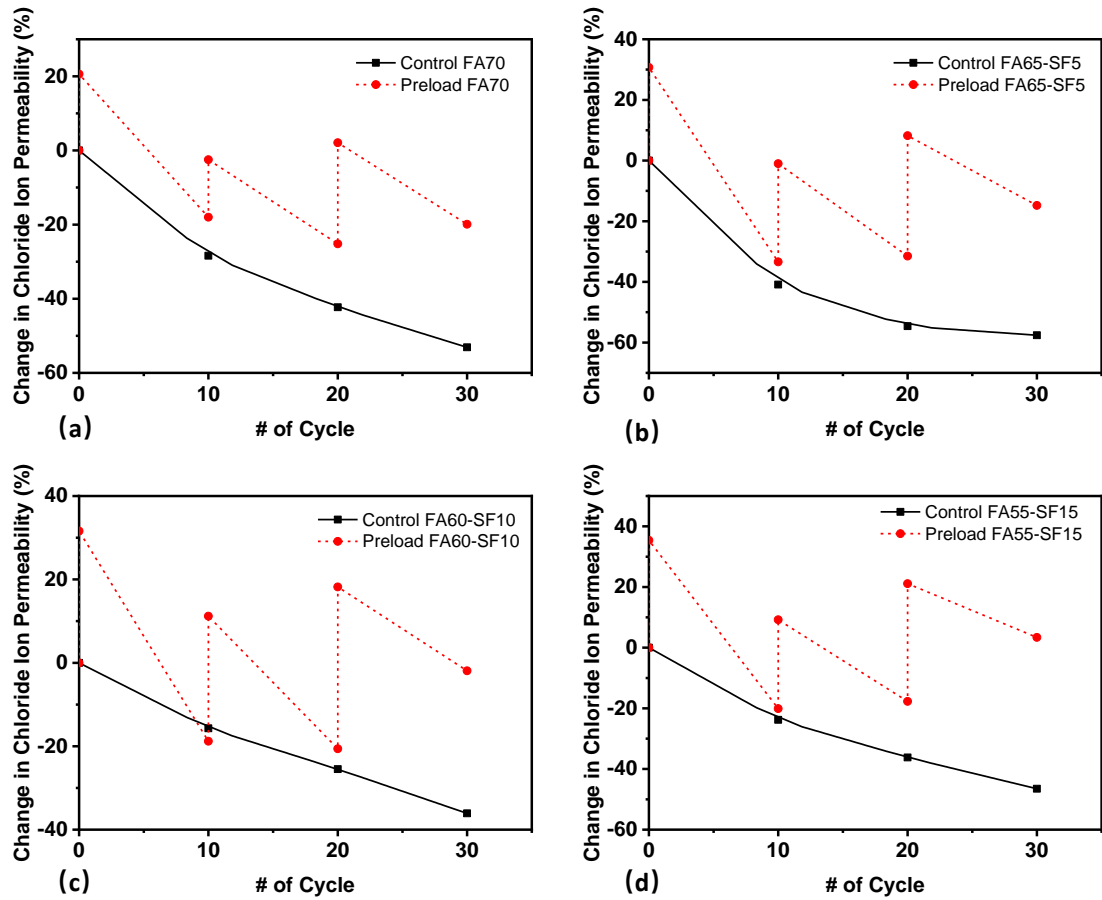


Figure 3.30: Percent variations in chloride ion permeability values of ECC mixtures containing different proportions of SF

in the same period than FA65-SF5, which indicated that 10% silica fume is more beneficial for improving the self-healing ability in the first 10 W/D cycles.

At the end of the 20th W/D cycle, the degree of decrease in RCPT values of sound specimens and cracked specimens was 42.3% and 25.2% (FA70), 54.6% and 31.5% (FA65-SF5), 25.5% and 20.6% (FA60-SF10), and 36.2% and 17.7% (FA55-SF15) as shown in Figure 3.30 (a-d). The difference for the four sets was 17.1%, 24.9%, 4.9%, and 18.5%, which showed that the RCPT result of cracked FA60-SF10 was closer to the sound at the end of 20th W/D cycles. This indicated that FA60-SF10, compared with FA70, FA65-SF5, and FA55-SF15 has a greater effect during the second self-healing process.

At the end of three repetitive preloading applications and 30 subsequent W/D cycles, RCPT results for FA 70, FA65-SF5 and FA60-SF10 decreased to 19.9%, 14.8%

and 1.9% compared to their initial values, however the RCPT results of FA55-SF15 increased to 3.4%. It seemed that the recover ability of all four mixtures significantly reduced, and a high dose of silica fume is not conducive to the recovery of RCPT values under repeated application of loading.

Therefore, it can be concluded that SF in the ECC mixtures can improve the self-healing of permeability to a certain extent after the first loading is applied, and the 10% replacement shows two times significant self-healing ability under three times repetitive loading. For specimens with 10% SF addition, after the first round of self-healing is completed, there may still be excess SF for continuous hydration, thereby achieving the second reduction in permeability. It is worth noting that the crack width recovery rate of the specimens with 10% SF addition is lower than the FA70, as shown in Section 3.4.1.2. However, the recovery of permeability is better than the FA70 (see Figure 3.30), which may be due to that SF consumes the calcium hydroxide in the concrete and forms more calcium silicate hydrates [204]. For cracked specimen, continuous hydration is equally important to crack surface self-healing [20]. Previous studies have also shown that tight crack width shows no impact on the charge passed [20, 27], the charge passed is mainly attributed to the overly porous matrix rather than micro-cracks [20]. The addition of 15% silica is not conducive to repeated self-healing under multiple loading. The probable reason is that silica fume is a highly reactive pozzolanic material and reacts more quickly than ordinary pozzolans [216–218]. A large amount of silicon from SF may preliminarily consumes calcium ions in the ECC matrix during the early stage of the hydration process. The self-healing effect is weakened due to the lack of calcium ions in the later stage.

For samples with LP, contrary to silica fume, at the end of every 10 W/D cycles, the RCPT change rate of the sample containing LP showed a downward trend with multiple applied loads, as shown in Figure 3.31. FA65-LP5, FA60-LP10 and FA55-LP15 all showed notable self-healing capacity at the end of the 10th W/D cycle.

At the end of the 20th and 30th W/D cycles, the RCPT values of the three samples containing LP decreased to varying degrees, however, FA60-LP10 decreased more significantly (closer to sound specimens) in the last two W/D cycles.

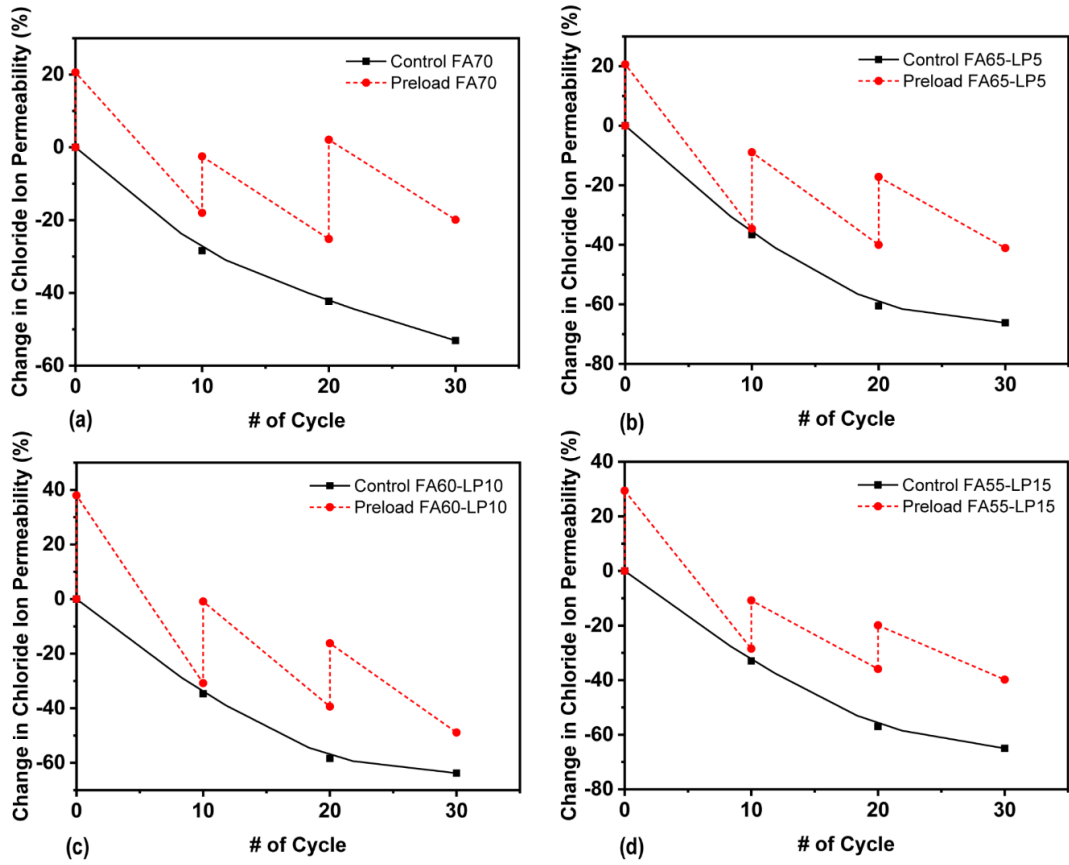


Figure 3.31: Percent variations in chloride ion permeability values of ECC mixtures containing different proportions of LP

At the end of three repetitive preloading applications and 30 subsequent W/D cycles, RCPT results for FA 70, FA65-LP5, FA60-LP10, and FA55-LP15 decreased to 19.9%, 41.1 %, 48.9% and 39.8% compared to the initial values, indicating that replacing FA with 10% LP has a better RCPT self-healing effect when repetitive load was applied.

When the sample contains both SF and LP, the RCPT value of FA55-SF5-LP10 can almost reduce to sound level at the end of all three W/D cycles, as shown in Figure 3.32 (d). Compared to FA60-SF10 as shown in Figure 3.32 (a), the RCPT of cracked FA55-SF10-LP5 dropped closer to the sound sample at the end of the 30th W/D cycle, as shown in Figure 3.32 (a) and (b). This shows that the presence of 5% LP is beneficial to improve the self-healing effect of the third round. Compared to FA60-LP10, the presence of 5% SF improved the self-healing ability in the 20th and 30th W/D cycles, as shown in Figure 3.32 (c) and (d). From the

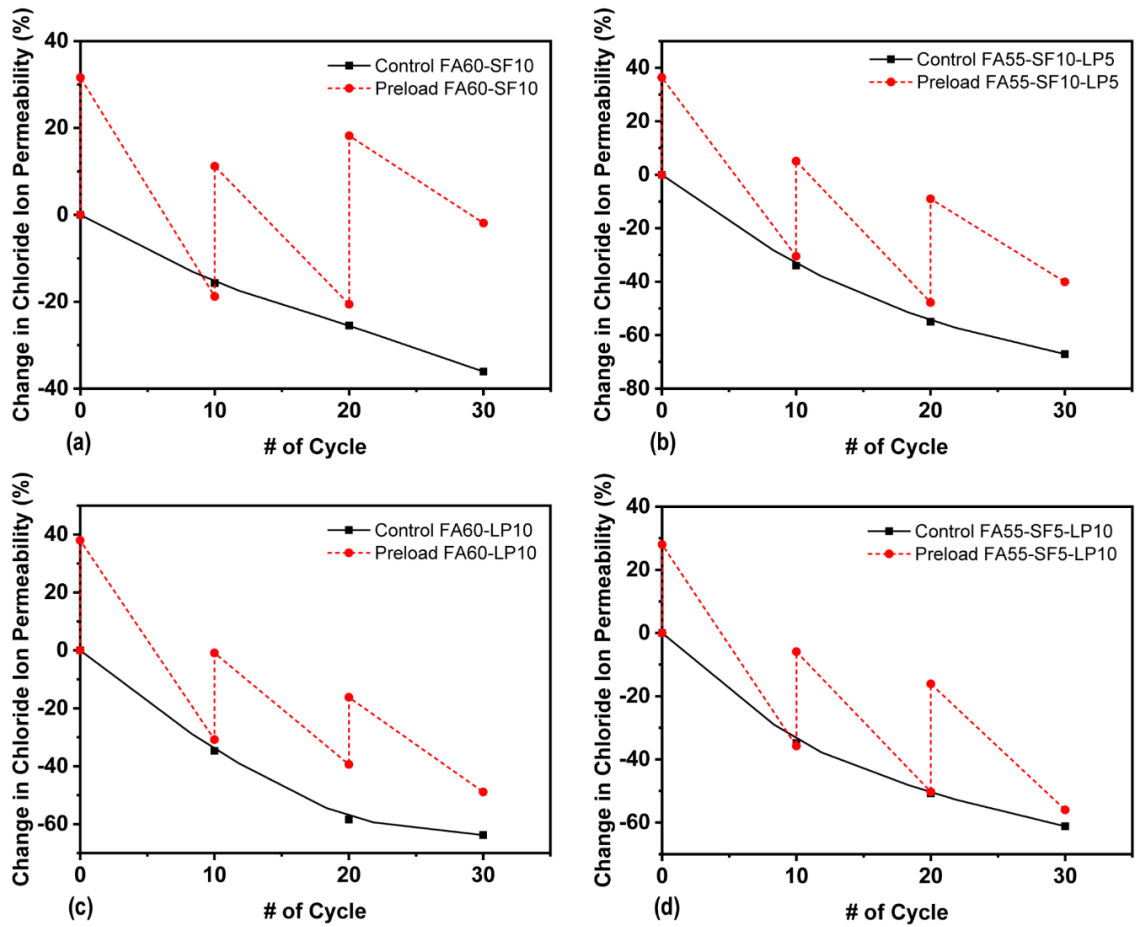


Figure 3.32: Percent variations in chloride ion permeability values of ECC mixtures due to repetitive preloading (SF and LP are included)

above analysis, it seems that the simultaneous addition of SF and LP (according to a certain proportion) to ECC can improve the repeated self-healing ability.

3.4.3 Splitting tensile strength recovery

The focus of this research is to study the self-healing ability of ECC containing different minerals and the possibility of repeated self-healing. To explore the recovery ability of mechanical properties of ECC incorporating different minerals, the recovery ability of splitting tensile strength was compared from two perspectives: 1) the effect of self-healing time on the recovery of mechanical properties (see section 3.4.3.1), and 2) repeated self-healing ability under multiple loads (see section 3.4.3.2).

3.4.3.1 Effect of W/D environment exposure time on recovery of splitting tensile strength

As shown in Figure 3.33, the tensile strength of FA70 can return to 73.6% of the original value after 10 W/D cycles. As the healing time increases, the recovery rate of tensile strength continues to rise, reaching 81.35% after 30 W/D cycles. It can be inferred from this that FA is a beneficial ingredient for long-term strength development in ECC due to its pozzolanic properties, and this is consistent with previous related research [199]. Adding different proportions of SF to FA70 will affect the self-healing ability of ECC. Adding 5% or 10% of SF to FA70 will increase the recovery rate of tensile strength, especially after 30 W/D cycles, the recovery rate can reach 87.79% and 91.39%. After 60 W/D cycles, the recovery rate has not improved much, reaching 90.3% and 95.65% respectively. This shows that adding 5% or 10% of SF to FA70 can increase the recovery rate of the sample within 30 W/D cycles but this improvement is not significant after 30 W/D cycles.

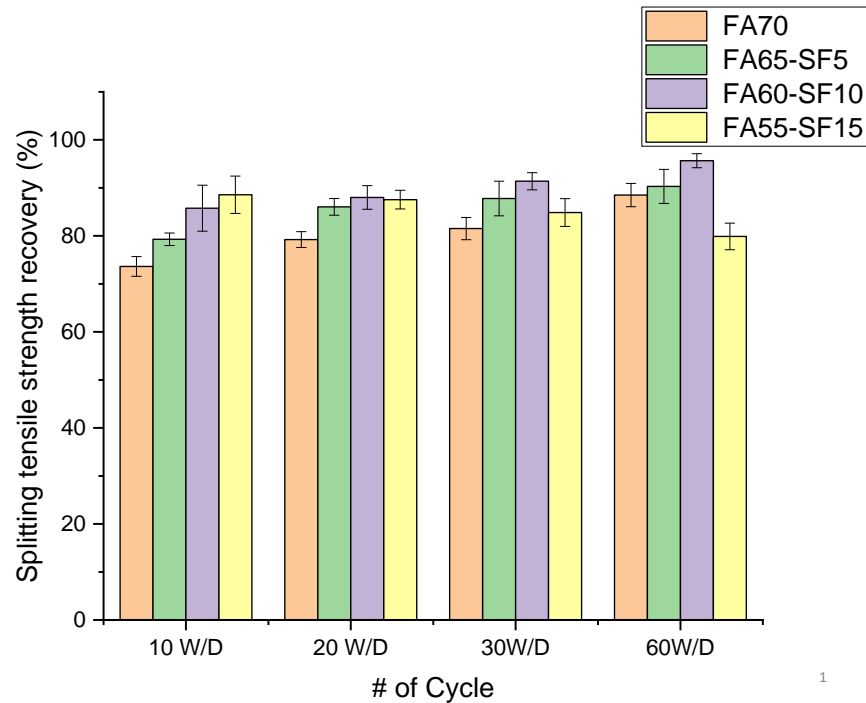


Figure 3.33: Effect of W/D environment exposure time on splitting tensile strength recovery of samples ECC incorporating SF

It is also worth noting that adding 15% of SF to FA70 significantly improves the splitting tensile strength recovery rate of ECC within 20 W/D cycles (Figure 3.33). Similar to the effect of adding 5% or 10% SF, this may be attributed to the reaction

of the SF with calcium hydroxide liberated during the hydration of cement [219]. Starting from the 30th W/D cycle, the self-healing level of FA55-SF15 began to decline, which is reflected in the decline in the recovery rate, which is lower than the ECC samples containing 5% and 10% SF. Some previous studies showed that very high percentages of SF did not significantly increase the splitting tensile strength, especially when the SF content exceeds 15% [219, 220].

After 60 W/D cycles, the splitting tensile strength recovery rate of FA55-SF15 was further reduced to 79.88%, which was lower than the recovery rate of FA70 (88.51%) in the same cycle. This may be attributed to the formation of an inhibiting layer of reaction product preventing further reaction of SF with calcium hydroxide [221].

It can be seen from the above analysis that adding 5% or 10% of SF to FA70 will significantly increase the splitting tensile strength recovery rate of ECC samples. Increasing 15% of SF to FA70 is beneficial for the recovery of splitting tensile strength in the short term, but is not conducive to the recovery of mechanical properties in the long term.

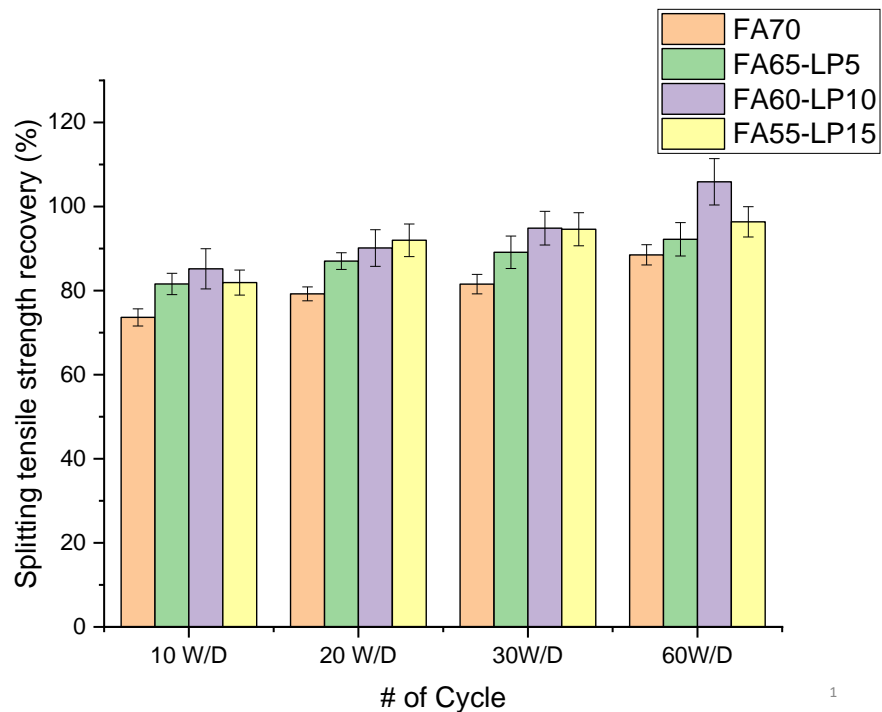


Figure 3.34: Effect of W/D environment exposure time on splitting tensile strength recovery of samples ECC incorporating LP

Compared with FA70, after replacing FA in FA70 with different proportions

of LP, the recovery rate of splitting tensile strength showed different degrees of improvement, as shown in Figure 3.34. Adding 5% or 10% of LP to FA70 will increase the recovery rate of the splitting tensile strength of ECC samples, especially for samples undergoing 60 W/D cycles, where the strength recovery rates of FA65-LP5 and FA60-LP10 reach 92.2% and 105.87%. This may be due to the addition of LP which increased the $\text{Ca}(\text{OH})_2$ content, and there is a possibility of improving the pozzolanic reaction of fly ash [222], thereby promoting the long-term strength development.

Adding 15% of LP to FA70 can also increase the recovery rate of splitting tensile strength, but the effect is not as good as adding 10% of LP. After adding 15%, in the 10th W/D and 30th W/D cycle, the recovery rate is lower than the sample with 10% LP, but slightly higher than the sample with 5% LP. After 60 W/D cycles, the recovery rate of the ECC splitting tensile strength with 10% LP was significantly higher than that of the samples with 5% and 15%, which shows that adding 10% LP is most conducive to improving the recovery of mechanical properties.

Some previous studies also pointed out that adding an appropriate amount of LP to increase the content of calcium hydroxide is beneficial for the pozzolanic reaction [111]. The addition of 15% LP may cause non-reactive hydrated lime in the binder paste matrix, which may increase the porosity, thus causing a reduction [213].

As shown in Figure 3.35, the addition of a single mineral, SF or LP, to SF70 and the addition of two minerals in different proportions leads a certain degree of improvement in the splitting tensile strength during the first 30 W/D cycles of ECC. In the case of adding the same proportion of SF or LP, although the addition of SF to FA70 has improved the recovery rate, LP has a more significant effect on the recovery rate, reaching 94.59% in the 30th W/D cycle. The splitting tensile strength recovery rate of FA70 was lower than other mixtures in the 10th cycle, the 20th cycle, and the 30th cycle, which may be due to higher fly ash content makes ECC more porous and therefore provide more aisles for charge to pass through [20].

The splitting tensile strength recovery rate of FA55-SF15 in the 60th cycle is lower than FA70 (control) and other mixtures, which may be due to the fact that an increase of 15% of SF will result in a relatively insufficient cement content, which will result in the formation of an inhibiting layer of reaction product preventing further

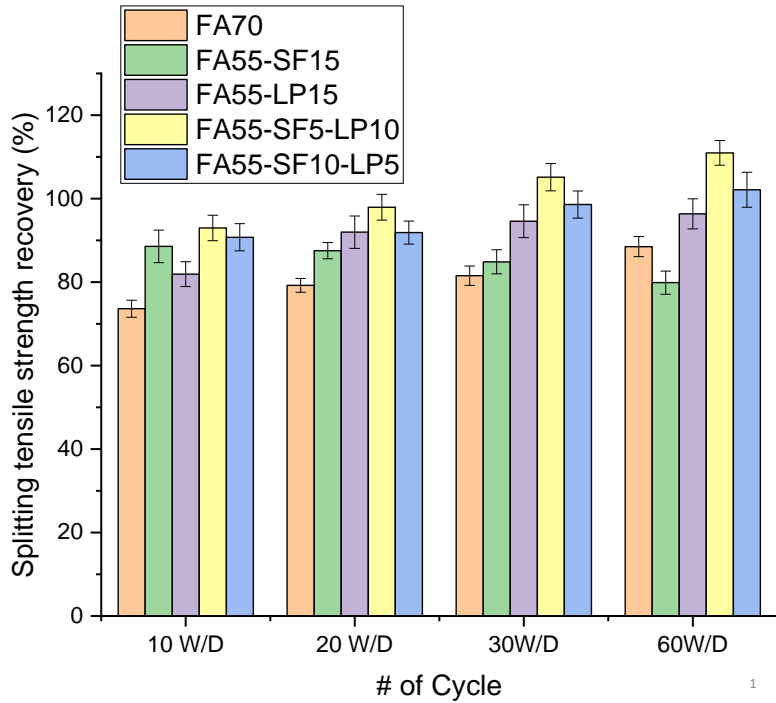


Figure 3.35: Effect of W/D environment exposure time on splitting tensile strength recovery of samples ECC incorporating multiple minerals (SF in FA65-SF15 is gradually replaced by LP)

reaction of silica fume [221]. Similar studies have shown that the reduction in the porosity was greater when silica fume was incorporated at up to 10% replacement level, beyond which the reduction was marginal or reversed [223]. The healing rate of FA55-LP15 is higher than FA70 which is mainly due to the lack of sufficient calcium hydroxide in FA70. Although the higher content of FA in FA70 is beneficial for long-term self-healing [224], the unavailability of sufficient quantities of $\text{Ca}(\text{OH})_2$ to react with the fly ash particles weakens the pozzolanic reaction, thereby affecting the healing.

When SF and LP are added at the same time, FA55-SF5-LP10 shows a high recovery rate in the first 30 W/D cycles and the 60th W/D cycle, reaching 105.14% in 30 W/D cycles , 60 W/D cycles reach 110.96% (see Figure 3.35). FA55-SF10-LP also has a higher effect on the splitting tensile strength recovery rate than adding a single mineral. This may be due to the addition of LP increased calcium hydroxide content, the addition of SF increased silica content, hence, there is a possibility of improving the pozzolanic reaction[222].

3.4.3.2 Repeatability of splitting tensile strength recovery after multiple loading cycles

As shown in Figure 3.36, the healing rate of the splitting tensile strength of FA70 continues to decrease after multiple rounds of loading. Compared with FA70, the addition of SF increased the healing rate of ECC samples in each round of self-healing cycles. In 10 W/D cycles, FA55-SF15 showed the highest healing efficiency. This may be due to high surface area and high content of amorphous silica in SF, as this highly active pozzolan reacts more quickly than ordinary pozzolans [225]. In this round of healing, the splitting tensile strength is proportional to the content of SF. However, FA60-SF10 has a higher healing efficiency during the 20th W/D cycle and the 30th W/D cycle. The healing rate of FA55-SF15 decreased from the 20th W/D cycle, probably because adding 15% SF is not conducive to self-healing after 20 W/D cycles (see related analysis in Section 3.4.3.1).

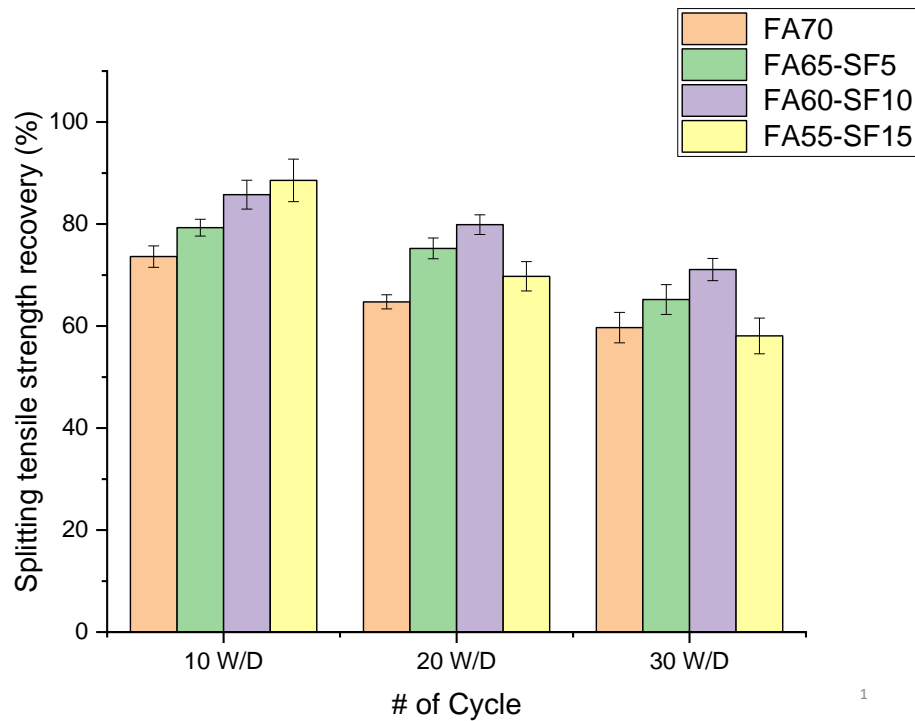


Figure 3.36: The effect of SF on splitting tensile strength recovery in the process of multiple loading

As shown in Figure 3.37, the addition of 5% or 10% of LP to FA70 can improve the recovery rate of splitting tensile strength after each load. This increase is more significant for the recovery rate of the 10 W/D cycle and the 20W/D cycle. After adding 10% of LP, ECC has the highest splitting tensile strength recovery rate after

the first load, reaching 85.17%. After three loads, the recovery rate can still reach 66.43%. This shows that adding 10% of LP can enhance the repeated self-healing ability of ECC by increasing the recovery rate of splitting tensile strength. This may be mainly due to the incorporation of the LP which can improve the self-healing performance by increasing the amount of calcium hydroxide that can trigger the pozzolanic reaction [24].

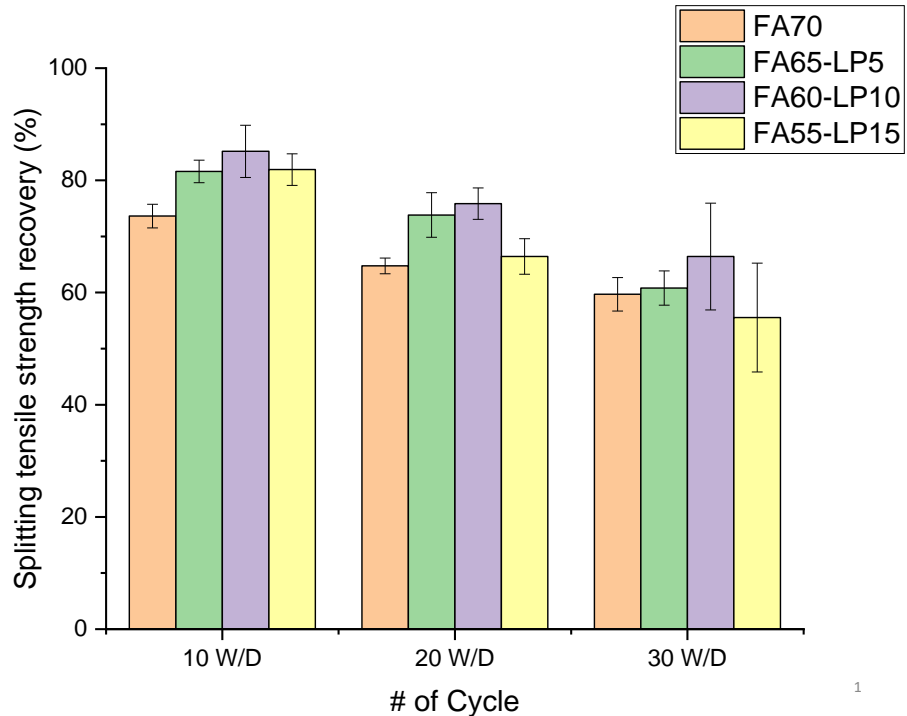


Figure 3.37: The effect of LP on splitting tensile strength recovery in the process of multiple loading

It is worth noting that after replacing the FA in FA70 with 15% LP, FA55-LP15 still has a certain effect on the splitting tensile strength recovery rate in the first two rounds of self-healing, although this effect is not as good as adding 5% or 10% LP. The recovery rate of the ECC sample with 15% LP added in the third round of self-healing is only 55.55%, which is lower than the recovery rate of FA70 (59.69%) in the third round of self-healing. This shows that adding 15% LP can improve mechanical properties to a certain extent in the short term, but it is not conducive to the long-term self-healing of splitting tensile strength. This may be due to excess non-reactive LP in the matrix that may increase the porosity [213], thereby affecting the recovery of mechanical properties.

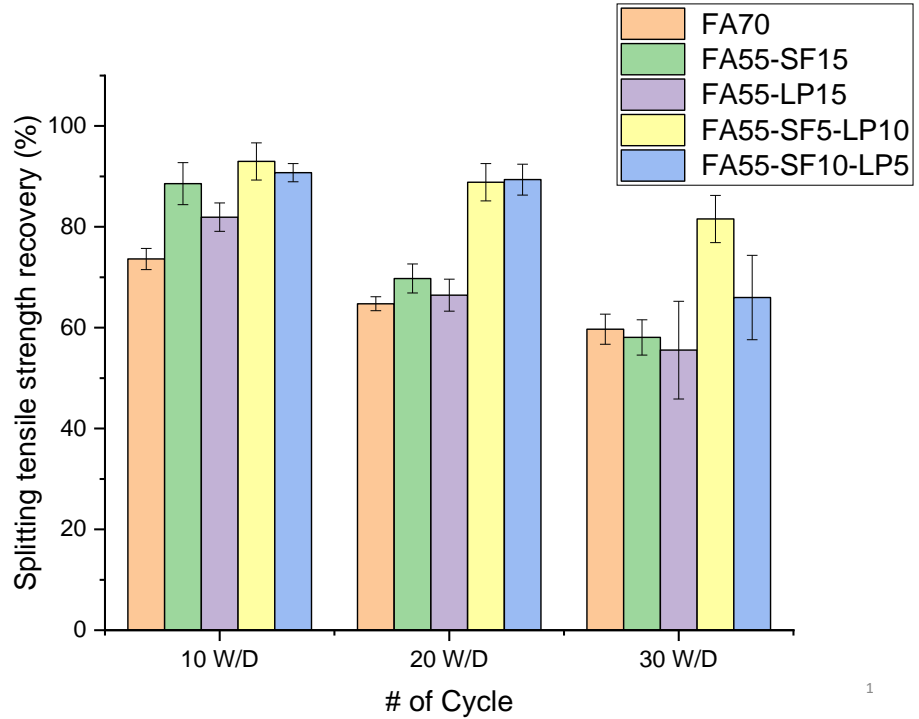


Figure 3.38: The effect of samples incorporated multiple minerals on recovery during multiple loadings. (The SF in FA65-SF15 is gradually replaced by LP)

As shown in Figure 3.38, when both SF and LP minerals are added to FA70, FA55-SF5-LP10 and FA55-SF10-LP5 have a higher splitting tensile strength healing rate than FA70 in the three rounds of self-healing. During the third round of self-repair, the splitting strength recovery rate of FA55-SF5-LP10 was significantly higher than other mixes, reaching 81.56%. In addition, the healing rate of FA55-SF10-LP5 in the first two self-healing cycles is also higher than that of FA55-SF15 and FA55-LP15, which shows that adding SF and LP at the same time has a better self-healing effect than adding a single mineral. This is mainly due to the addition of hydrated lime which increased the $\text{Ca}(\text{OH})_2$ content, and SF which is a highly active pozzolan [225], and when SF and calcium hydroxide react quickly, the rate of hydration is increased [205]. Some previous studies also show that the addition of LP and SF lowered the total porosity of FA cement pastes [222].

3.4.4 Self-healing product analysis(SEM/EDS/XRD)

After three rounds of self-healing, the morphology of the reaction products of ECC formed on crack surfaces was observed by using SEM. The morphology of the self-healing products formed in the gaps was observed by using SEM (Zeiss Sigma VP

High resolution), see Section 3.4.4.1. Images were taken by a BSE detector under water vapour mode. The acceleration voltage of 20 kV was used to capture high contrast images. XRD analysis technique was also used to chemically analyse the healing products. Combined with the results of XRD analysis, a semi-quantitative method is used to determine the composition of the main self-healing substances through element ratios, see Section 3.4.4.2.

3.4.4.1 SEM Morphological analysis

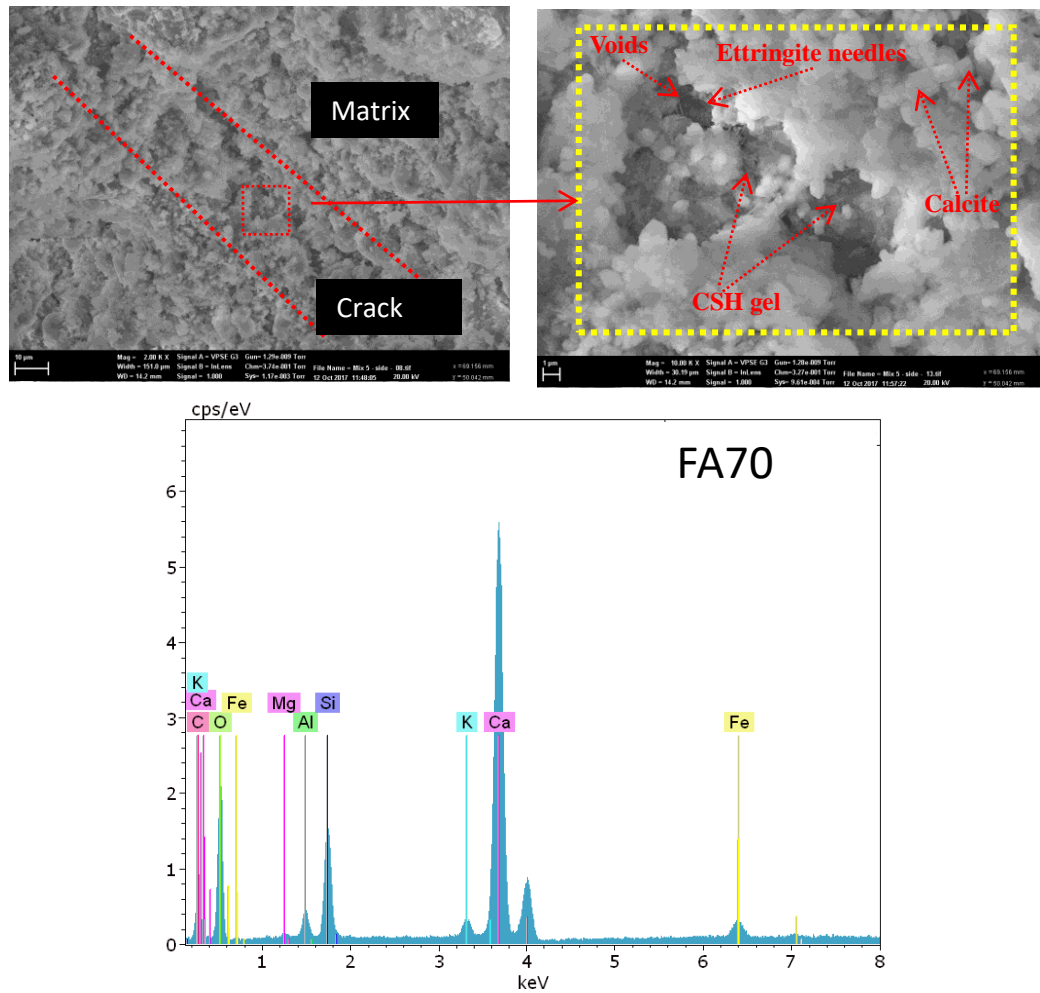


Figure 3.39: SEM micrograph with EDS pattern of products in self-healed cracks, FA70

Figure 3.39 shows the representative morphology of the healing materials of FA70 after three rounds of self-healing. The reaction products displayed in Figure 3.39 are gel-like and similar to the Calcium Silicate Hydrates (C-S-H) [29] and needle-like,

which look like ettringite [226–229] has formed in the cracks in the ECC sample. Cube-like reaction products were observed and scattered in the cracks, separated by gel-like C-S-H. These cube-like products are in the typical shape of calcite [230]. As shown in Figure 3.39, maps of elements characterized by EDS spectroscopy occur at several representative healing zones. In similar studies, Ca, Al, and Si were generally used as the main fundamental elements to detect and confirm the appearance of healing products [70, 100, 194], but it is difficult to directly determine the chemical composition from element maps [194].

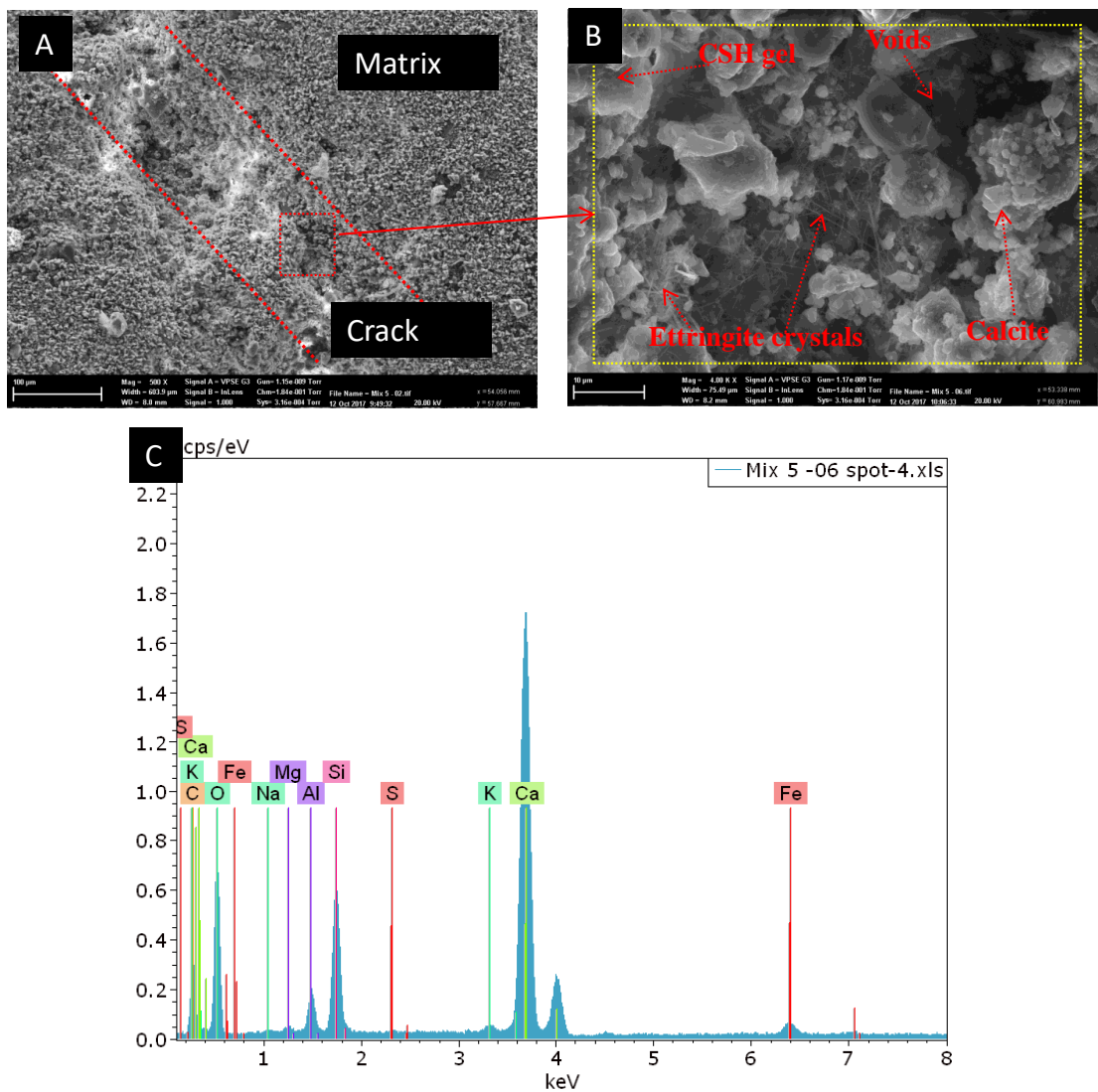


Figure 3.40: SEM micrograph with EDS pattern of products in self-healed cracks, FA55-SF15

The representative morphology of the healing products of FA55-SF15 after three rounds of self-healing is shown in Figure 3.40. The reaction products displayed

in Figure 3.40 are gel-like product and similar to the C-S-H [29] and a needle-like product, which looks like ettringite [226–229] formed in cracks. Cube-like reaction products were observed and widely distributed in the cracks, separated by needle-like ettringite. It is worth noting that more ettringite is observed than the morphology of FA70 cracks. This may be due to the relatively high content of SF. Some previous research results indicate that SF addition has promoted the formation of ettringite [231]. SF postpones the conversion of ettringite into monosulfate [232].

It was observed in Section 3.4.3.2 that after adding 15% of SF, splitting tensile strength recovery decreased from the 20th W/D cycle, and this may be due to the high content of SF in FA55-SF15, which promotes the formation of more ettringite (see Figure 3.40). Previous studies have also shown that high pozzolan SF addition improves the expansive phase formation of ettringite and causes a decrease in the strength [233].

Figure 3.41 shows the representative morphology of the healing materials of FA55-LP15 after three rounds of self-healing. The reaction products displayed in Figure 3.41 are cube-like and similar to calcite [230].

The cube-like healing material of FA55-LP15 is mainly concentrated on the periphery of the crack, and the repair material at the edge of the crack opening has a tendency to aggregate in the middle direction, as shown in Figure 3.40 B. A large amount of calcium carbonate has also gathered around the cracks (as shown in Figure 3.40 C), and part of it has fallen into the cracks (Figure 3.40 D). Other scholars also found that a large amount of crystal-like products covered the cracks, even near the healing surface [194]. This proves that self-healing substances are formed both at the opening of the crack and in the vicinity of cracks.

The analysis of the EDS pattern shows that the intensity of calcium is very strong (as shown in Figure 3.40 E), which may be related to the higher LP content in FA55-LP15. More LP will increase the content of calcium hydroxide [222], thereby increasing the proportion of calcium ions. Calcium ions are very important in the process of self-healing of cracks. Calcium ions react with carbon dioxide in a watery environment to produce calcium carbonate, which is the main mechanism for self-healing of cracks [28, 201, 234, 235]. The high content of calcium ions in FA55-LP15 promotes this reaction around the cracks and even on the surface of the sample

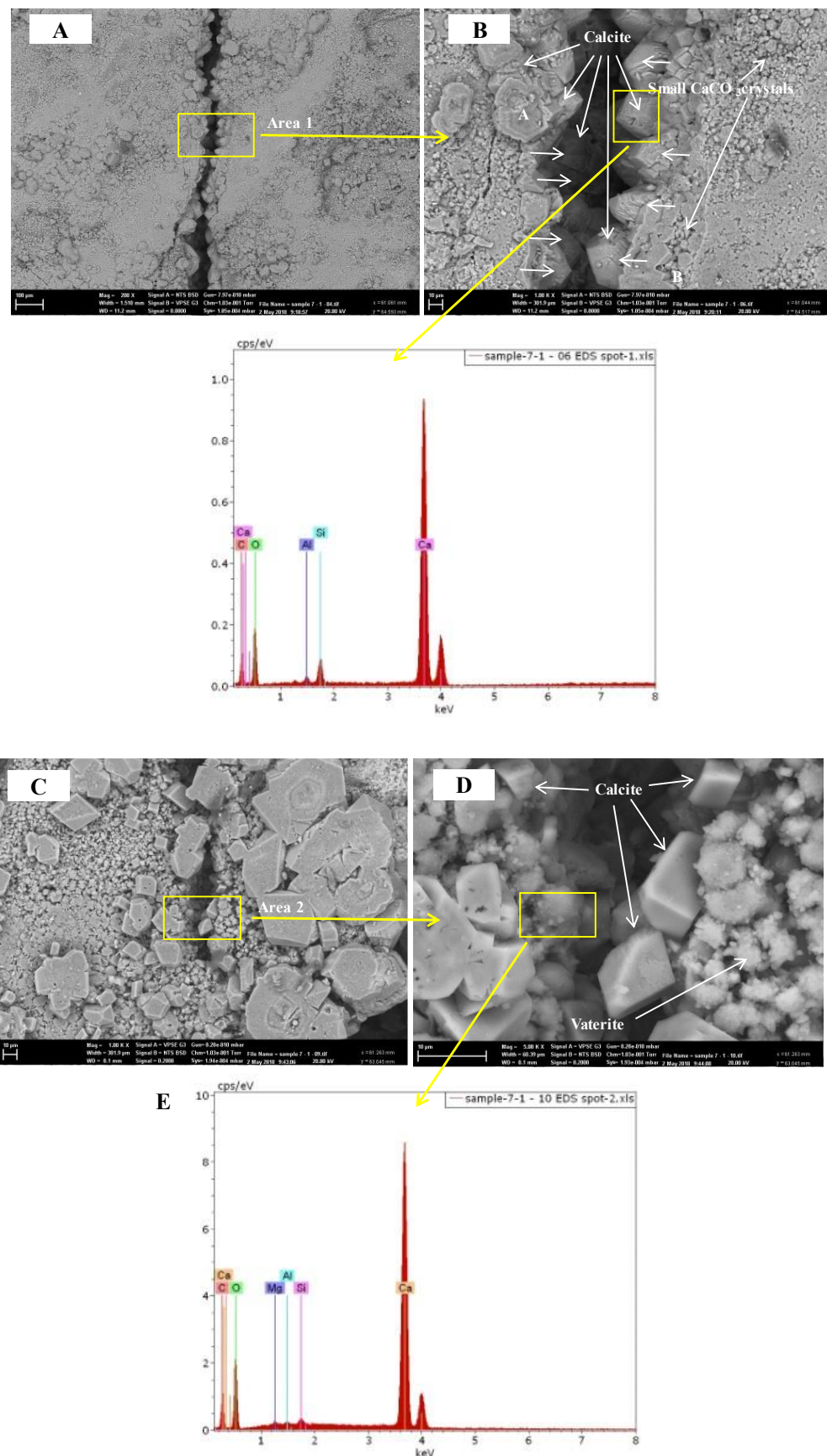


Figure 3.41: SEM micrograph with EDS pattern of products in self-healed cracks,FA55-LP15

(as shown in Figure 3.40 C). This explains the accumulation of a large amount of calcium carbonate (cube-like) similar products in the cracks and the crack gaps and around the cracks.

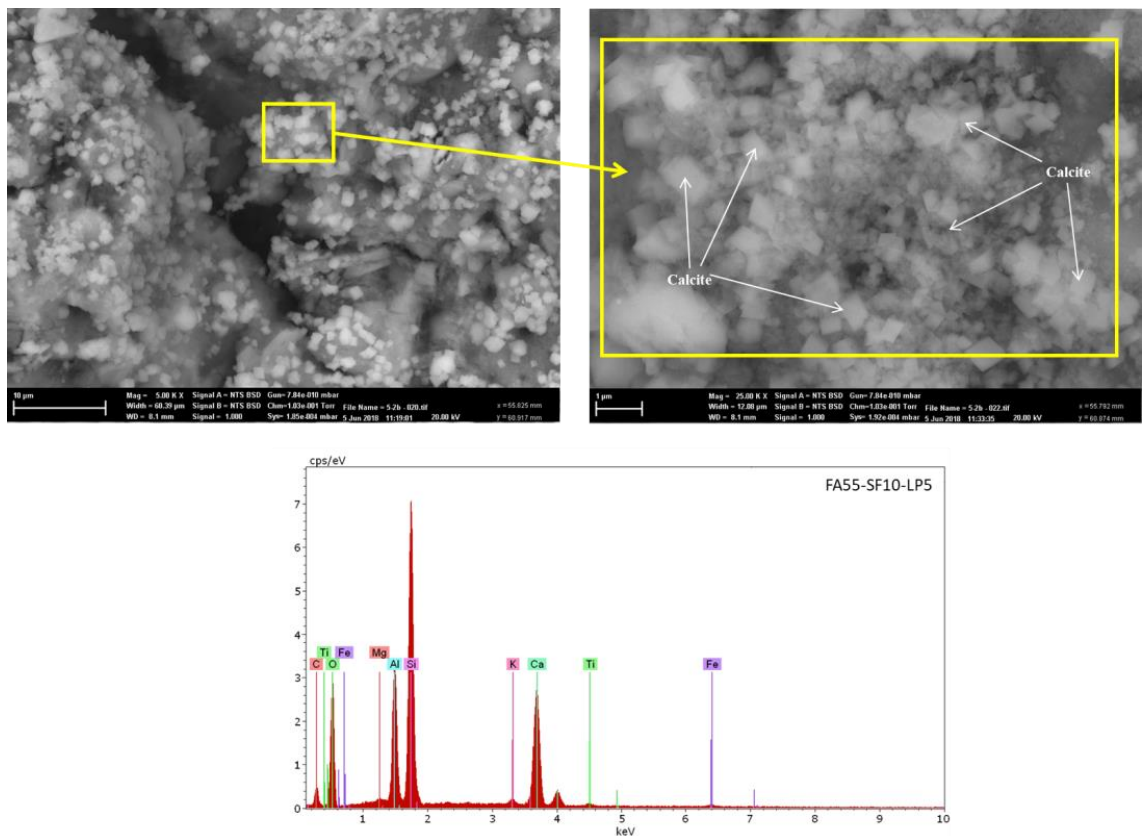


Figure 3.42: SEM micrograph with EDS pattern of products in self-healed cracks, FA55-SF10-LP5

Figure 3.42 shows the representative morphology of the healing materials of FA55-SF10-LP5 after three rounds of self-healing. The reaction products displayed in Figure 3.42 are cube-like and similar to calcite [230], evenly distributed, the surface of calcite is wrapped or covered by a layer of gel-like substance, and it is difficult to distinguish the generated substances by morphological characteristics.

The analysis from the EDS pattern shows that the intensity of silicon and calcium is very strong (as shown in Figure 3.42 E). The colour intensity expresses the element concentration [194]. According to the distribution of chemical elements and SEM morphological analysis, it can be inferred that the self-repair product may be C-S-H and calcium carbonate. Further analysis of the chemical composition ratio in the product is still needed to further confirm this.

The representative morphology of the healing product of FA55-SF5-LP10 after three rounds of self-healing is shown in Figure 3.43. Similar to FA55-SF5-LP10, the surface of new products is wrapped or covered by a layer of gel-like substance, and it is difficult to distinguish the new generated substances by morphological characteristics. The analysis from the EDS pattern shows that the intensity of calcium is strong (as shown in Figure 3.43), and this shows that calcium carbonate is likely to exist.

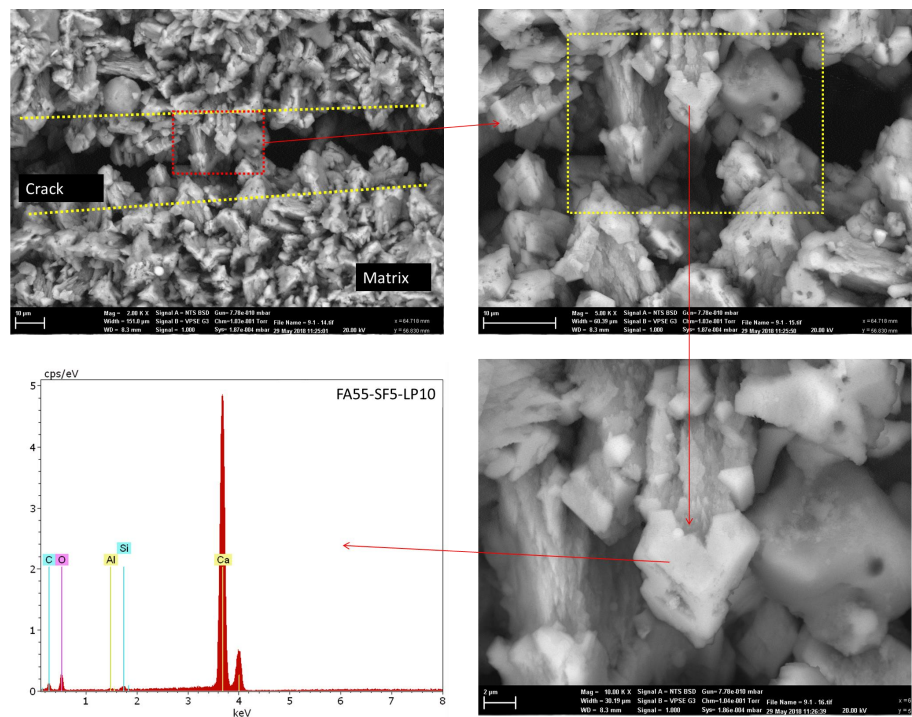


Figure 3.43: SEM micrograph with EDS pattern of products in self-healed cracks, FA55-SF5-LP10

3.4.4.2 Chemical elements

The morphological characteristics observed by SEM can be used to qualitatively describe the characteristics of self-healing materials, and EDS elemental analysis can be used to infer the composition of self-healing substances. According to the self-healing material form analysis in the previous section and the elements contained in the EDS pattern, it can be confirmed that the healing materials were composed of C-S-H and CaCO_3 . However, it is hard to identify which materials are the dominant healing products in each mixture, especially for ECC incorporating multiple minerals like FA55-SF5-LP10 and FA55-SF10-LP5 (as shown in 3.4.4.1).

Table 3.5: Chemical compositions of healing materials

Mixture	Zone No.	C	O	Al	Si	S	Ca	Fe	Ca/Si
FA70	1	20.53	55.53	1.42	7.73	1.17	13.62	0	1.76
FA70	2	13.51	60.81	2.91	9.11	1.62	12.03	0	1.32
FA70	3	21.07	58.85	1.15	3.71	0.12	14.83	0.27	4
FA55-SF15	1	15.4	44.08	1.43	11.2	0.02	27.87	0	2.49
FA55-SF15	2	15.8	43.67	3.57	14.38	1.13	21.45	0	1.49
FA55-SF15	3	12.45	54.29	1.11	5.37	0.75	26.03	0	4.85
FA55-LP15	1	19.43	58.17	0.08	0.87	0.45	20.66	0.34	23.62
FA55-LP15	2	17.5	55.73	0.06	0.78	0.03	25.9	0	33.21
FA55-LP15	3	12.26	57.03	0.05	0.94	0.41	29.31	0	31.18
FA55-SF5-LP10	1	21.09	57.97	0.43	1.47	0.06	18.84	0.13	12.83
FA55-SF5-LP10	2	22.98	59.44	0.15	0.56	1.41	15.45	0	27.38
FA55-SF5-LP10	3	15.68	56.29	0.13	0.84	0.62	26.14	0.31	31.23
FA55-SF10-LP5	1	12.11	47.5	0.52	2.62	0.46	36.79	0	14.04
FA55-SF10-LP5	2	18.34	58.54	0.34	5.03	1.31	16.01	0.43	3.18
FA55-SF10-LP5	3	21.45	55.33	1.01	3.86	0.31	17.52	0.52	4.54

To analyse chemical elements of the reaction products, random zones on the surfaces of the self-healing products are detected by EDS. The ratios of the main chemical elements, i.e. Ca/Si and Al/Si in self-healing products formed at the crack surface are then calculated. Table 3.5 summarizes the chemical elements of self-healing products for each composite mixture in terms of the Ca/Si ratio.

Previous studies have shown that a reliable method to determine the chemical composition of self-healing products is by the value of the Ca/Si ratio [29, 118]. The formation of C-S-H and calcium carbonate generally has a specific reference value to a Ca/Si ratio. In general, if the Ca/Si ratio is around 2.0, C-S-H tends to form. If the Ca/Si ratio is higher than 2.0, calcium carbonate is the primary self-healing product [194]. Based on the above analysis criteria, the semi-quantitative results are demonstrated in Figure 3.44. As shown in Figure 3.44, the results revealed that the self-healing products in FA70 and FA55-SF15 showed a strong characteristic of C-S-H and CaCO_3 , while the dominant self-healing products for FA55-LP15 and FA55-SF10-LP5 is CaCO_3 . This is consistent with the SEM morphological analysis results in Section 3.4.4.1. For FA55-SF10-LP5, the healing products had the characteristic of a mixture between C-S-H and CaCO_3 .

It is worth noting that the semi-quantitative results shown in Figure 3.44 do not reflect the existence of ettringite, but the needle-like ettringite [226–229] has actu-

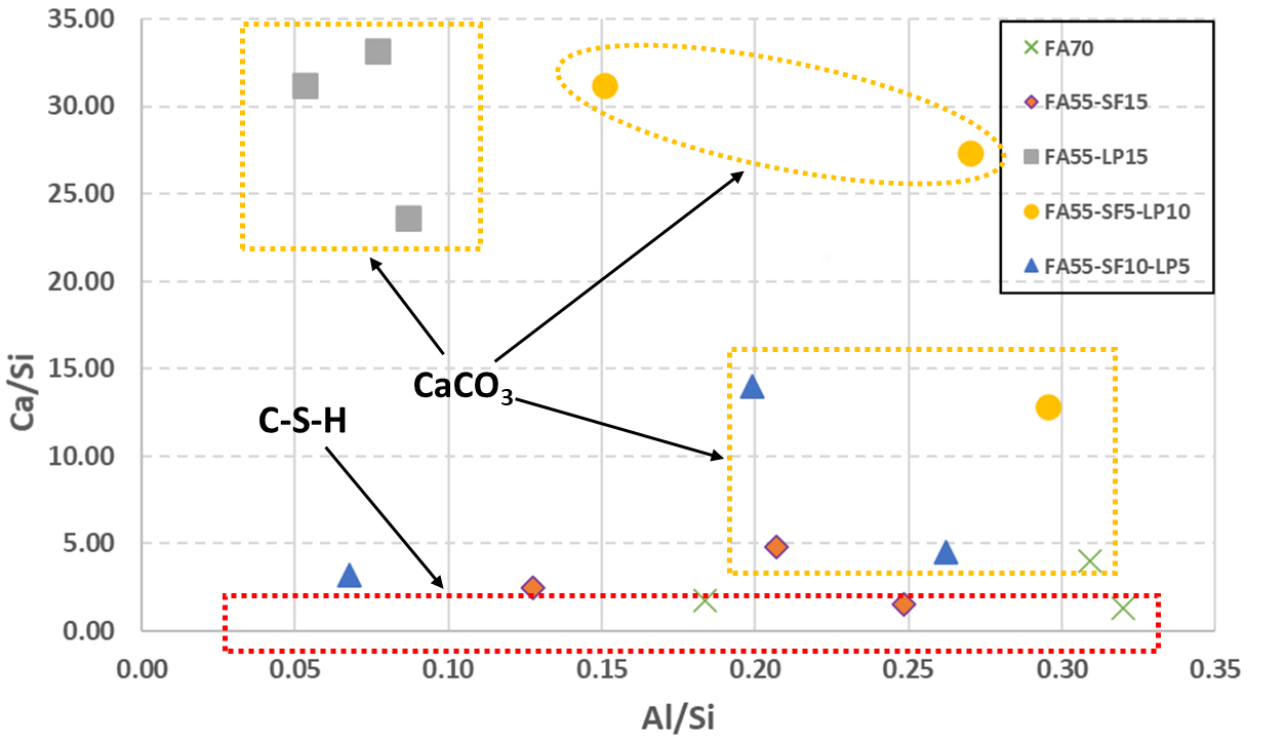


Figure 3.44: Chemical analysis of healing products by EDS

ally been observed as one of the self-healing substances in the SEM morphological analysis of FA55-SF15, as shown in Section 3.4.4.1. The presence of ettringite be may be due to the high content of silicon in FA55-SF15, some previous research indicated that SF addition promoted the formation of ettringite [231].

The analysis in Section 3.4.4.1 has pointed out that cube-like reaction products were widely distributed in the cracks in FA55-LP15. According to the SEM morphology comparison, it is speculated that this product is CaCO_3 . The results in Figure 3.44 show that the Ca/Si ratio in the healing product of FA55-LP15 is higher than 2.0. This shows that CaCO_3 is indeed the main repair product. This result is consistent with the results of SEM analysis. Moreover, previous studies reported that the Al/Si ratio required to create healing materials is commonly in a range of 0.1 to 0.3 [29, 194, 236], which is similar to the test results in the present study.

As shown in Figure 3.44, the Ca/Si ratio of FA55-LP15 and FA55-SF5-LP10 is significantly higher than other mixtures, and this is most likely due to the addition of LP which increase the content of calcium ions. Calcium ion content is a key factor for surface crack recovery. Ozbay et al. [16] showed that, in the presence of

water, Ca^{2+} from hydration products leaches out of the hardened matrix into cracks and reacts with CO_2 , which converts into CaCO_3 crystals. It is precisely because of this self-healing mechanism that FA55-LP15 and FA55-SF5-LP10 may produce more CaCO_3 crystals, and more caulking materials may appear around the cracks. This is consistent with the phenomenon observed in the previous SEM analysis, that healing materials tend to precipitate in the vicinity of healing cracks.

3.4.4.3 XRD material identification

To better clarify final self-healing products, XRD measurements were performed on self-healing products from the surface of specimens to verify the previous EDS analysis results. Figure 3.45 presents XRD patterns obtained carrying out with $\text{Cu}-\text{K}\alpha$ radiation, in the range of 5° – 70° on a diffractometer.

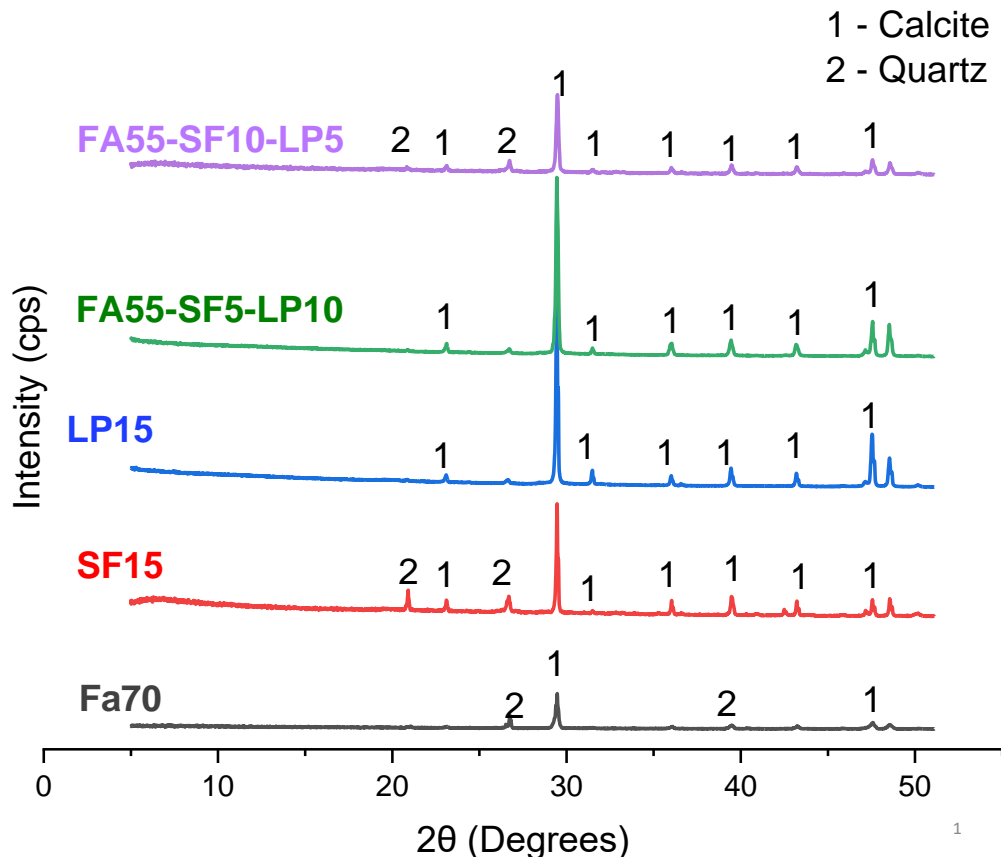


Figure 3.45: XRD patterns of self-healing products in ECC mixtures, after first self-healing

It is obvious that the spectrum of all mixtures is (at least) a superposition of the spectra of calcite, especially at around 29.5° and 47.5° 2θ for FA70, around

23.06, 29.50, 36.04, 39.41, 47.50 and 48.47 2θ for all other mixtures. SF15, LP15, FA55-SF5-LP10 and FA55-SF10-LP5 showed basically the same positions for calcite peaks; however, the most significant calcite peaks appeared at 29.50 and 48.47 2θ . Quartz peaks were detected in FA70, SF15, and FA55-SF10-LP5. The quartz peaks of SF15 and FA55-SF10-LP5 are more similar, which could be related to the addition of SF. The quartz peaks in FA70 could be more related to siliceous sand or the content of FA.

Since calcite is the most stable polymorph of CaCO_3 [237], it indicates that CaCO_3 is the the main self-healing product, which is consistent with the previous SEM topography analysis and EDS semi-quantitative analysis results. Some scholars have found that calcite is the primary product in the surfaces of healed cracks [28, 201, 234, 235]. Since the samples used for XRD in this study have undergone three rounds of self-healing, this indicates that the dominant self-healing substance in the repeated self-healing process is still CaCO_3 .

It is worth noting that in the EDS semi-quantitative analysis (Figure 3.44), the results revealed that the self-healing products in FA70 and FA55-SF15 showed a strong characteristic of C-S-H and CaCO_3 ; however, C-S-H was not detected in the XRD study. This is due to the fact that it is difficult to identify C-S-H gels (the main products of hydration) from XRD due to their amorphous nature (lack of lattice planes) [237, 238]. Nevertheless, combined with the EDS semi-quantitative analysis in 3.4.4.2, it can still be inferred that quartz peaks of FA70 and FA55-SF15 could also be a trace picked up from the crystalline structure of the SiO_2 component of C-S-H [237, 238].

3.5 Summary

The self-healing behaviour of ECC incorporating different minerals is investigated in this research, focusing on the crack width recovery, chloride ion permeation recovery, splitting tensile strength recovery and the composition of self-healing products. Based on the test results and analysis of self-healed ECC specimens incorporating with different minerals, the following conclusions are summarized.

3.5.1 Crack width recovery

In the case of designing ECC incorporating multiple minerals, it was found that the mineral additives significantly affected the formation of self-healing products, resulting in different crack width recovery rates. From this perspective, some particular mix-proportions for ECC with self-healing capability were suggested.

Under digital microscope observation, ECC containing different mineral combinations has a certain self-healing ability that is detectable on crack width recovery, but different mineral combinations and mineral content will affect the self-healing efficiency of ECC after multiple rounds of loading. In addition, the width of the crack affects the efficiency of the crack self-healing, and small cracks are easier to heal, as much less healing product is required to fill in the cracks and the healing product accumulated on both sides of the crack opening is easier to connect, and thus to realize the healing of the crack. After applying multiple rounds of load, the mineral content used to heal the cracks at the crack openings gradually decreases, which also makes large cracks more difficult to heal. The crack widths within ECC must be controlled to below $100 \mu\text{m}$, preferably below $50 \mu\text{m}$, in order to engage noticeable repeated self-healing behaviour.

Influence of SF content Adding 5% SF to the ECC of FA70 can only slightly increase the healing rate of cracks smaller than $20 \mu\text{m}$, and it is only effective for the first round of self-healing. For cracks larger than $20 \mu\text{m}$, a high content of SF is not conducive to crack width recovery.

Influence of LP content Adding 5% or 10% of LP to FA70 can significantly improve repeated self-healing, especially when the crack is less than $100 \mu\text{m}$. After the third load is applied, the healing rate of FA60-LP10 and FA55-LP15 for cracks less than $20 \mu\text{m}$ can reach more than 76%; for cracks of about $20\text{-}50 \mu\text{m}$, the healing rate can reach more than 40%. The healing rate of cracks of about $50\text{-}100 \mu\text{m}$ can reach more than 27%. FA60-LP10 and FA55-LP15 did not show a significant improvement in the healing rate of cracks greater than $100 \mu\text{m}$.

The effect of adding two minerals Compared with FA70, the addition of 5% SF and 10% LP significantly improves the healing rate of cracks less than 100 μm , and the healing ability of cracks within 50-100 μm is relatively significantly enhanced during the second self-healing process.

Adding 10% SF and 5% LP to FA70 can only improve the self-healing ability of cracks smaller than 20 μm , and this effect can only be maintained in the first round of the self-healing cycle. After the second load, the self-healing ability of FA55-SF10-LP decreased significantly.

When adding both SF and LP minerals to FA70 to design ECC, adding a relatively high proportion of LP helps to improve the repeatable self-healing ability of ECC samples. In order to maintain the capacity of repeated crack width recovery, the relative content of SF should not exceed 5%.

3.5.2 Recovery of chloride ion permeability

The addition of a small amount (5%) of SF can significantly reduce the chloride ion permeability of ECC at 28 days, and higher SF content is effective in keeping the chloride ion permeability of ECC at a relatively low level under repetitive loading, in accordance with ASTM C1202. When 5%, 10% and 15% SF were added to ECC specimens, 10% replacement showed the most significant reduction in total charge passed on the 28th day, indicating that the replacement ratio of 10% is beneficial for improving the chloride ion resistance of ECC specimens.

During the three observation periods, the change rate of ECC mixtures that incorporated FA and SF at the end of every 10 W/D cycles showed an upward trend as the SF content increased, while the sample that only contained FA and LP showed an opposite trend. The presence of SF in the ECC mixtures can improve the self-healing effect after the first loading is applied, and the 10% SF shows two times significant self-healing ability under three times repetitive loading; however, 15% SF is not conducive to repeated self-healing under multiple loading. The high SF content may result in the consumption of more calcium ions in the matrix during the early hydration reaction, thus affecting the later self-healing effect. For the ECC mixture with 5%, 10%, and 15% LP, all the three mixtures showed notable

self-healing capacity at the end of the 10th cycle. FA60-LP10 showed significant RCPT recovery during the second and third rounds of self-healing.

When SF and LP were simultaneously added to ECC mixtures, the RCPT results of FA55-SF10-LP5 and FA55-SF5-LP10 were all below the low level before and after three times of preloading and self-healing, in accordance with ASTM C1202. The addition of SF and LP in ECC (FA55-SF10-LP5 and FA55-SF5-LP10) showed better RCPT values recovery than ECC mixtures (FA60-SF10 and FA60-LP10) only containing SF or LP in all three round of the self-healing process, especially for the mix FA55-SF5-LP10, which after the third round of self-healing, is still very close to the RCPT results compared to the sound samples. These findings show that even under repetitive loading conditions, the addition of SF and LP to ECC according to a certain ratio can significantly improve the ability of repeated self-healing of chloride ion permeability.

3.5.3 Mechanical recovery

Changing the mineral ratio in ECC mixtures will have different effects on the mechanical properties of the ECC specimens. To study the self-healing ability of ECC with different proportions of minerals, the ECC samples underwent the W/D cycle (as shown in Figure 3.9). After different lengths of healing time, the corresponding splitting tensile strength healing rate was compared.

The addition of 5% or 10% of SF to FA70 can increase the splitting tensile strength recovery rate of ECC samples within 30 W/D cycles. Increasing 15% of SF to FA70 is beneficial for the recovery of splitting tensile strength in the short term but is not conducive to the recovery of mechanical properties in the long term.

The addition of 5% or 10% LP can increase the recovery rate of the splitting tensile strength of ECC samples, especially for samples undergoing 60 W/D cycles, where the strength recovery rates of FA65-LP5 and FA60-LP10 reach 92.2% and 105.87%. The addition of 10% LP is most conducive to improving the recovery of mechanical properties. In the case of adding the same proportion (15%) of SF or LP, although all show a certain improvement in splitting tensile strength recovery, LP has a more significant effect, reaching 94.59% in the 30th W/D cycle. When SF and LP are added at the same time, FA55-SF5-LP10 shown a high recovery rate

in the 30th W/D cycles and the 60th W/D cycle. FA55-SF10-LP5 has also shown a higher effect on the splitting tensile strength recovery rate than adding a single mineral.

For repeated application of load and repeated self-healing, the addition of SF increased the healing rate of ECC samples in each round of the self-healing cycle. In 10 W/D cycles, FA55-SF15 showed the highest healing efficiency. The addition of 10% LP to ECC showed the highest splitting tensile strength recovery rate after the first load, reaching 85.17%. After three loads, the recovery rate can still reach 66.43%.

When both SF and LP minerals were added to FA70, FA55-SF5-LP10, and FA55-SF10-LP5 showed a higher splitting tensile strength healing rate than FA70 in the three rounds of self-healing. The addition of SF and LP at the same time results in a better self-healing effect than adding a single mineral. After three rounds of self-healing, the splitting strength recovery rate of FA55-SF5-LP10 is significantly higher than other mixes, reaching 81.56%.

3.5.4 Self-healing products

After three rounds of loading, through SEM morphological analysis, EDS chemical composition analysis, and XRD analysis, it was found that a mixture of CaCO_3 and C-S-H were the main self-healing products, which agrees well with previous studies [20].

The proportion of healing product depends on the type and the proportion of minerals in ECC. Semi-quantitative analysis of EDS shows that C-S-H and CaCO_3 were found to be the main healing materials of the FA70 and FA55-SF15 mixtures, whereas CaCO_3 is the dominant healing product detected in the FA55-LP15 and FA55-SF5-LP10 mixtures. For FA55-SF10-LP5, the healing products had a characteristic of a mixture between C-S-H and CaCO_3 , combined with SEM morphological analysis, it is found that CaCO_3 is the dominant healing product, and ettringite is also present in a small amount. The results of XRD analysis also verified that CaCO_3 is the main self-repairing substance. Quartz peaks were also found, which may be a trace picked up from the crystalline structure of the SiO_2 component of C-S-H.

Self-healing capability was significantly affected by the supply of calcium ions. The Ca/Si ratio of the FA55-LP15 and FA55-SF5-LP10 healing products is significantly higher than other mixtures, and this is most likely due to the addition of LP increasing the content of calcium ions, with more CaCO_3 precipitate formed both at the opening of the crack and in the vicinity of cracks.

Chapter 4

Machine Learning Comparative Analysis of Self-Healing Abilities of ECC

4.1 Introduction

In the previous chapter, the self-healing capability of Engineered Cementitious Composite (ECC) containing various mineral additives, Fly Ash (FA), Silica Fume (SF) and Hydrated Lime Powder (LP) with different fractions (by weight of total cementitious material) was examined by applying a newly developed splitting tensile test apparatus to produce micro-cracks and control the width of cracks on the surface of ECC mixtures. Based on these experimental results, a profound insight was achieved into the efficiency of the self-healing ability of ECC that is significantly influenced by the composition and crack width of ECC.

However, the relationship and interactivity between different composites in the cementitious matrix, and multiple factors, such as crack width, on developing the self-healing ability of ECC, is highly interdependent, complex and non-linear [28]. Moreover, it is expensive, time consuming and not practical to accurately quantify the self-healing capability of ECC by conducting experiments only. Therefore, developing accurate and reliable prediction models for the determination of the self-healing ability of ECC can benefit both academic and industry interests through time and cost savings.

In this chapter, a comparative analysis is established for predicting the self-healing ability of ECC using machine learning techniques. The state-of-the-art technique for prediction of the self-healing ability of ECC is reported in the sec-

ond part of this chapter, which is followed by empirical data collection and pre-processing with a 10-fold cross-validation algorithm in Section 4.3. Following this, the methodology in Section 4.4 describes the concepts and formulations of individual and ensemble models used for predicting the self-healing capability of ECC. Validation and evaluation methods are introduced in Section 4.5. Computational results for all individual and ensemble models are presented and compared in Section 4.6, which demonstrates the superiority of machine learning algorithms for prediction of the self-healing capability of ECC. Finally, Section 4.7 draws some conclusions from this work and suggests directions for future research.

4.2 State-of-the-art prediction of the self-healing ability of ECC

By now, many experiments on the self-healing capability of ECC have been reported. However, research on the modelling of self-healing capability in cement-based materials with machine learning techniques is considerably rare. To the best of our knowledge, there are only two publications that have applied machine learning models to the prediction of self-healing ability. Suleiman and Nehdi [181] predicted self-healing ability in cement-based materials using a Genetic Algorithm (GA) based Artificial Neural Network (ANN) with three layers, which consists of 11 input neurons standing for influencing parameters and 14 neurons in the hidden layer, with one neuron in the output layer. Later, a comparative study was proposed [182] to predict self-healing capability in bacteria-based concrete, which adopted six machine learning approaches including Support Vector Regression (SVR), Decision Tree (DT) Regression, Gradient Boosting Regression, ANN, Bayesian Ridge Regression and Kernel Ridge Regression. However, no study has predicted the self-healing ability of ECC using a machine learning approach, let alone a comparative analysis with multiple machine learning algorithms.

In this chapter, a comprehensive comparative analysis is proposed to identify the best model among multiple machine learning algorithms for predicting the self-healing behaviour of ECC, which is also considered as a baseline prediction model for other advanced models in the next chapter. There are four individual models, including Linear Regression (LR), SVR, Back-propagation Neural Network (BPNN),

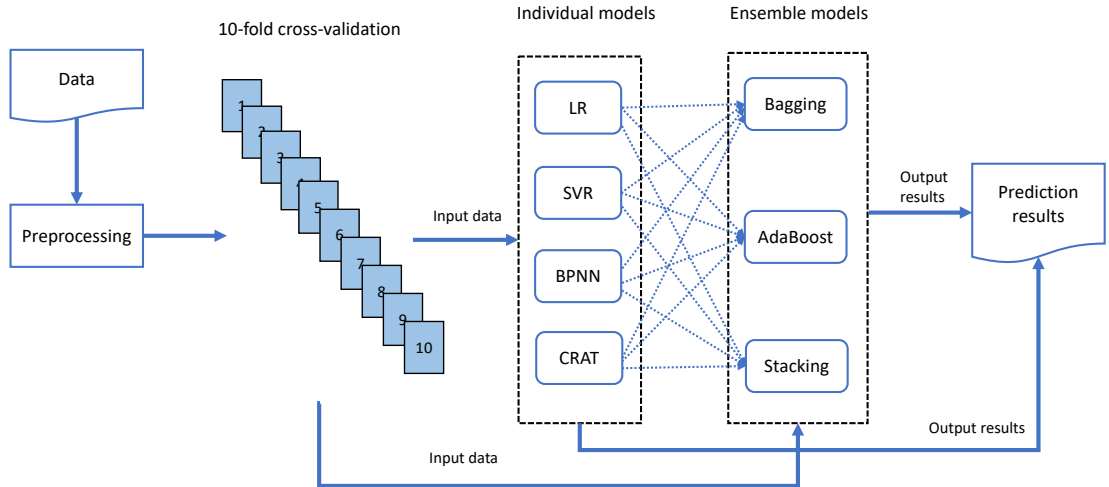


Figure 4.1: Flow chart for implementing prediction machine learning models for self-healing capability of ECC

and Classification and Regression Tree (CRAT), and three ensemble models, namely bagging, AdaBoost and stacking, adopted for the comparative analysis. The steps for prediction of the self-healing ability of ECC are summarized in Figure 4.1. First, all empirical data is collected and preprocessed for modelling. After that, a 10-fold cross-validation algorithm is employed to split whole data into training and testing datasets. In the prediction stage, four individual models are first applied to predict the self-healing ability of ECC, then they are used in turn as a base learner in each ensemble model for prediction results. Finally, all of the 13 computational prediction results are analysed and compared in Section 4.6.

4.3 Data description and preparation

4.3.1 Data collection

Empirical data used for prediction were gathered with five features, with crack width before and after self-healing representing the influencing factor for self-healing, and the weight of FA, SF and LP illustrating the variable composites of ECC. It is noteworthy that some impact factors in the test, such as General Purpose Cement (GPC), sand, Water to Cementitious Materials Ratio (W/CM), and healing time, are controlled as constants which are excluded for the prediction modelling due to no effect. There are six specimens with dimension of $\varnothing 50mm \times 100mm$ for each of

Table 4.1: Number of instances and range of input and output features collected from nine ECC mixes

Mix	Size	FA	SF	LP	Crack width before self-healing (μm)		Crack width after self-healing (μm)	
					Min	Max	Min	Max
FA70	87	816.03	0.00	-	3.28	134.69	0	121.37
FA65-SF5	77	757.74	58.29	-	4.37	135.47	0	124.01
FA60-SF10	88	699.45	116.58	-	5.18	121.78	0	113.11
FA55-SF15	88	641.16	174.86	-	3.45	115.8	0	109.53
FA65-LP5	112	757.74	-	58.29	7.65	119.45	0	105.65
FA60-LP10	37	699.45	-	116.58	5.62	126.82	0	110.97
FA55-LP15	61	641.16	-	174.86	6.42	132.65	0	115.95
FA55-SF5-LP10	34	641.16	58.29	116.58	8.74	123.09	0	110.78
FA55-SF10-LP5	33	641.16	116.58	58.29	4.64	131.57	0	119.79

nine mixtures which were observed using digital microscope to collect crack width samples before self-healing and after self-healing. For more details of the experiment, such as sample preparation, materials and mixture proportion, refer to Chapter 3. In total, 617 instances were collected from nine mixtures to construct a machine learning training-testing dataset. Table 4.1 shows the number of collected instances (size) and range of crack widths before and after self-healing for each mixture.

4.3.2 Preprocessing of data

The input and output data of different features (referring to Table 4.1) varies in range and units, which weigh all features unequally for prediction models and might end up creating bias. To eliminate this effect, we preprocessed empirical data to the range [0,1] by the min-max scaling presented in the following function.

$$x' = \frac{x - x_{min}}{x_{max} - x_{min}} \quad (4.1)$$

Where x' is the scaled value of the variable x , and x_{min} and x_{max} are the maximum and minimum values of variable x , respectively.

4.4 Methodology

Machine learning techniques used to predict the self-healing capability of ECC include four individual methods, namely LR, SVR, BPNN and CRAT, as well as three

ensemble methods, including bagging, AdaBoost and stacking. Ensemble methods are constructed using individual methods as base estimators to predict the self-healing capability of ECC. To establish a baseline for comparison, modelling parameters of individual methods are set to the same in both individual models and ensemble models. The reason for choosing these techniques is because they are the most popular, and some are even recognized as the top data mining algorithms in the related field of concrete [125]. The proposed individual and ensemble techniques are described in the following subsections.

4.4.1 Linear regression

LR attempts to determine the relationship between a dependent variable (response variable) and one or more independent variables (explanatory variables) by fitting a linear regression equation [239]. Given our dataset $T = \{(x_i, y_i), i = 1, 2, \dots, n\}$, where $n = 617$ is the size of the sample dataset. $x_i \in R^n$ is independent variables representing a sample of selected features from FA, SF, LP and crack width before self-healing, R^n is n -dimensional space, $y_i \in R^1$ is the target output (crack width after self-healing) that corresponds to x_i . Let $d = 4$ denote the number of an independent variable of a random vector $x = \{x_1; x_2; \dots; x_d\}$, and y is the corresponding output (dependent variable). The general formula of LR for predicting self-healing capability of ECC can be expressed as follows:

$$y = w_1x_1 + w_2x_2 + \dots + w_dx_d + b \quad (4.2)$$

where w , ($i = 1, 2, \dots, d$) denotes a regression coefficient, b is an error term.

4.4.2 Support vector regression

The basic idea of SVR is to provide a nonlinear function that approximates mapping input data into the high-dimensional feature space where a special type of hyperplane is constructed. The data points on the sides of the hyperplane that are closest to the hyperplane are called support vectors and are used to plot the boundary line to fit the data [240]. Therefore, SVR is used to decide the decision boundary at ϵ

distance from the hyperplane so that the support vectors are within the boundary line. After that, a regression model is built in the hyperplane [241].

Given our dataset $T = \{(x_i, y_i), i = 1, 2, \dots, n\}$, where $n = 617$ is the size of a sample dataset, $x_i \in R^n$ is the input vector representing a sample of selected features from FA, SF, LP and crack width before self-healing, R^n is n -dimensional vector space, $y_i \in R^1$ is the target output indicating crack width after self-healing that corresponds to x_i . The SVR aims to seek an optimum regression function $f(x)$ with minimized empirical risk, which can be expressed as follow:

$$f(x) = \langle w, x \rangle + b \quad \text{with } w \in T, b \in R \quad (4.3)$$

where $\langle \cdot, \cdot \rangle$ denotes the dot product in T , and w and b are the weight vector and bias value which are estimated by minimizing the empirical risk, that is, the distance between the predicted crack width and the target crack width after self-healing.

SVR adopts an ϵ -insensitive loss function penalizing predictions that have a distance between the predicted crack width and the target crack width after self-healing greater than ϵ . Therefore, the problem of finding w and b to reduce the empirical risk with respect to an ϵ -insensitive loss function is equivalent to the convex optimization problem that minimizes the margin (w) with the full prediction error within the range of ϵ . This problem can be expressed as:

$$\begin{aligned} & \text{minimize} && \frac{1}{2} \|w\|^2 \\ & \text{subject to} && \begin{cases} y_i - \langle w, x_i \rangle - b \leq \epsilon \\ \langle w, x_i \rangle + b - y_i \leq \epsilon \end{cases} \end{aligned} \quad (4.4)$$

By introducing slack variables ξ, ξ_i^* to allow some errors to cope with infeasible solution to the optimization problem, the formulation can be generated as [153]:

$$\begin{aligned} & \text{minimize} && \frac{1}{2} \|w\|^2 + C \sum_{i=1}^n (\xi_i + \xi_i^*) \\ & \text{subject to} && \begin{cases} y_i - \langle w, x_i \rangle - b \leq \epsilon + \xi_i \\ \langle w, x_i \rangle + b - y_i \leq \epsilon + \xi_i^* \\ \xi_i, \xi_i^* \geq 0 \end{cases} \end{aligned} \quad (4.5)$$

The constant C is the penalty value imposed on predictions that lie outside the ϵ margin. After calculating a Lagrange constructed from the objective function and

all constraints, a dual set of variables is introduced, as follows [242]:

$$\begin{aligned}
L_P = & \frac{1}{2} \|w\|^2 + C \sum_{i=1}^n (\xi_i + \xi_i^*) - \sum_{i=1}^n (\eta_i \xi_i + \eta_i^* \xi_i^*) \\
& - \sum_{i=1}^n \alpha_i (\epsilon + \xi_i - y_i + \langle w, x_i \rangle + b) \\
& - \sum_{i=1}^n \alpha_i^* (\epsilon + \xi_i^* + y_i - \langle w, x_i \rangle - b) \\
s.t. \quad & \alpha_i, \alpha_i^*, \eta_i, \eta_i^* \geq 0
\end{aligned} \tag{4.6}$$

Where L_P is the Lagrangian and $\alpha_i, \alpha_i^*, \eta_i, \eta_i^*$ are Lagrange multipliers.

The optimality can be achieved by the partial derivatives of L_P with respect to the primal variables following the saddle point condition. Then the function of SVR is obtained as:

$$f(x) = \sum_{i=1}^n (\alpha_i - \alpha_i^*) \langle x_i, x \rangle + b \tag{4.7}$$

As for the nonlinear regression, the input data have to be mapped into a high-dimensional feature space, in which dot product can be replaced by a kernel function $k(x_i, x_j) = \phi(x_i)^T \phi(x_j)$, and the function (4.7) can be written as:

$$f(x) = \sum_{i=1}^n (\alpha_i - \alpha_i^*) k(x_i, x) + b \tag{4.8}$$

There are various kernel functions, such as linear, polynomial, radial basis function and sigmoid kernel. In this work, the Gaussian radial basis function (RBF) is chosen, which is defined as [243]:

$$k(x_i, x_j) = \exp\left(-\frac{\|x_i - x_j\|^2}{2\sigma^2}\right) \tag{4.9}$$

4.4.3 Artificial neural network

ANN, also called neural network, originated from simulations of biological neural networks. Generally, it consists of many neurons in layers, including one input layer, one or several hidden layers and an output layer [244]. The neurons are fully interconnected between the neighbouring layers by weight, and typically there are no inter-connections between neurons within the same layer [245].

There are many possible network structures, and in this study the type utilized is the BPNN. A preliminary architecture of the BPNN is determined to be 4 - n -

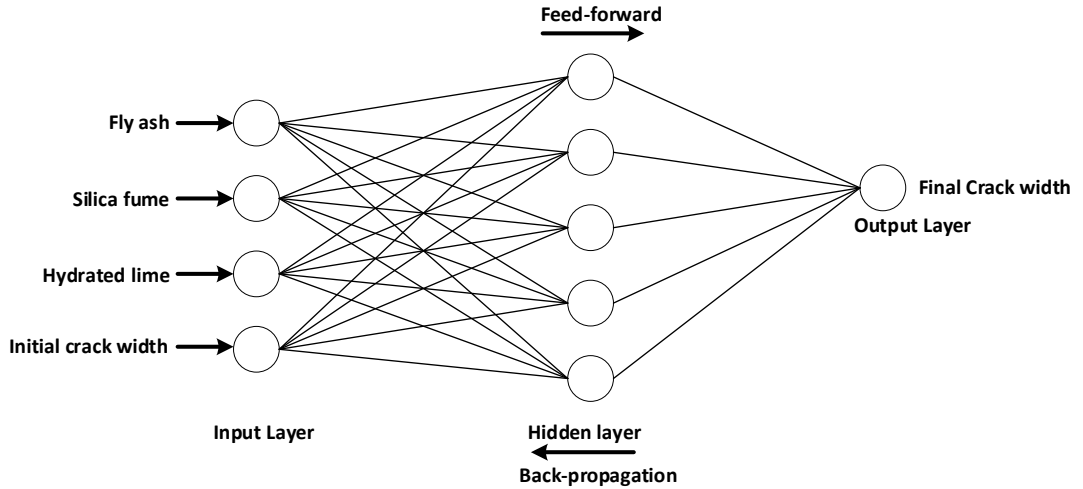


Figure 4.2: Schematic diagram of BPNN model for predicting self-healing capability of ECC

1, where 4 input neurons represent the input features standing for FA, LP, SF and crack width before self-healing, $n = 5$ indicates the number of neurons in the hidden layer, and 1 target neuron in the output layer for the predicted crack width after self-healing. This is a three-layer network with one hidden layer which is already able to approximate most continuous functions, of which the complex nonlinear relationship could be approximated with accuracy [246]. The architecture of the BPNN model for predicting self-healing is demonstrated in Figure 4.2.

Given a set of inputs $\{x_1, x_2, x_3, \dots, x_n\}$, while information is passed through the input layer to the hidden layer, each neuron in the input layer is multiplied by respective weights added by a bias and are summed together. After that, an activation function f is applied to form the output o . From the hidden layer to the output layer, information is also summed and activated. This can be expressed in the following equation [247]:

$$o = f\left(\sum_{i=1}^n w_{ij}x_i + b_j\right) \quad (4.10)$$

where w_{ij} is the connection weights between the i th neuron of input and the j th neuron in the hidden layer, and b_j is the bias of the j th neuron. The sigmoid function is applied as an activation function between the input, hidden, and output neurons to form the output.

$$f(x) = \frac{1}{1 + e^{-x}} \quad (4.11)$$

The goal of training a neural network is to determine the values of the connection weights and the biases of the neurons. The back propagation indicates an iterated method which adjusts the weights from output layer to input layer. At first, an output is a calculated feed-forward from the input layer via the hidden layer to the output layer. Then an error is generated by comparing the output with the target output. After that, the error is back propagated to the hidden layer and input layer while adjusting the connection weights and biases to reduce the error. Such a process will be repeated until the error is minimized or the termination is reached to avoid over-fitting.

4.4.4 Classification and regression tree

The CRAT [248] is a tree decision algorithm that splits data into mutually exclusive subgroups based on a recursive binary partitioning procedure. It develops the relationship between the target variables (the crack width after self-healing of ECC) and the independent variables (the input features of FA, SF, LP and crack width before self-healing of ECC) to create decision rules to form subgroups as branches and leaves.

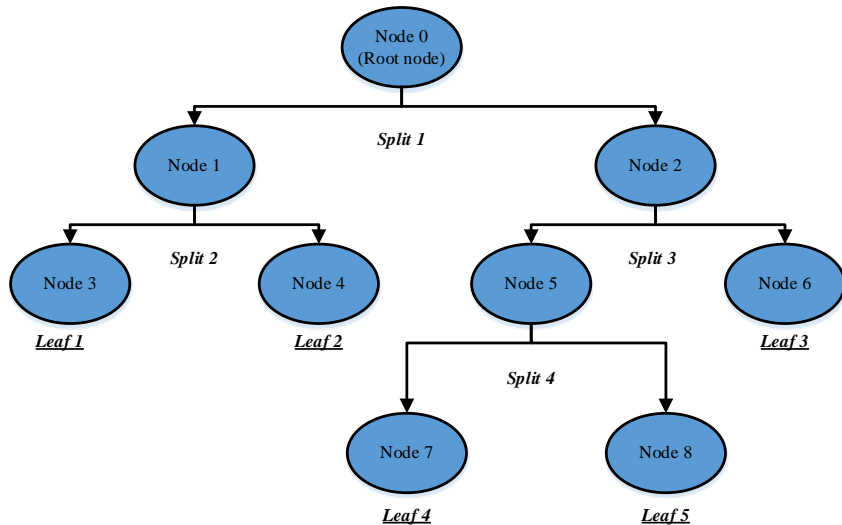


Figure 4.3: Structure of a classification and regression tree [249]

Figure 4.3 illustrates the schematic diagram of a decision tree. The process of CRAT starts from the root node, which contains the entire dataset, to construct two sub-nodes representing two categories. Then this recursion process is applied to each sub-node until all divided sub-nodes are leaf nodes. The CRAT can be either a classification tree [250] or regression tree [249] depending on the type of target and independent variables, which may be categorical or numerical.

The key idea of constructing a CRAT is achieved by selecting a variable at each node that best splits the empirical data. To locate splits, *Gini* index is used to measure the impurity of the two child nodes that contain subsets of data that are as homogeneous as possible with respect to the target variable.

Given a dataset has K classes and the probability of a sample which belongs to class i is p_i , $i \in \{1, 2, 3, \dots, K\}$, the *Gini* impurity can be expressed as:

$$G(p) = \sum_{i=1}^K p_i(1 - p_i) = 1 - \sum_{i=1}^K p_i^2 \quad (4.12)$$

4.4.5 Ensemble methods

In contrast to various learning approaches such as Support Vector Machine (SVM), and CRAT, which develop a single learner from training data, ensemble methods train multiple base learners and combine them [125] to improve generalizability over a single estimator. Therefore, weak learners (base learners) can be boosted to strong learners [251] in an ensemble method. The set of base learners in an ensemble is developed from an individual learning algorithm, which can be decision tree, SVM, or other kinds of learning algorithms. Research [252] has shown that ensemble methods are usually significantly more accurate than individual learning methods

Suppose there is a d -dimensional predictor variable X (input features of FA, SF, LP, and crack width before self-healing of ECC) and one dimensional output Y (the crack width after self-healing of ECC). Each estimator uses an individual algorithm to provide one estimated function $g(\cdot)$. The output presented by ensemble-based function $g_{en}(\cdot)$ is obtained by a linear combination of individual functions. This ensemble approach can be expressed mathematically as:

$$g_{en}(\cdot) = \sum_{j=1}^N c_j * g(\cdot) \quad (4.13)$$

Where c_j expresses the combination coefficients which are dependent on the used ensemble models.

4.4.5.1 Bagging

Bagging (bootstrap aggregating) generates multiple versions of a predictor to obtain an aggregated predictor [253]. It generates multiple models independently on different versions of a dataset which are random bootstrap replications of an original training set. That is, several training examples may repeatedly appear in different bootstrap replicated dataset. Then those individual predictions are aggregated through a combination method (either voting or averaging) to form the final prediction. By introducing randomization into the bagging method's construction procedure and making an ensemble out of it, the bagging method is used as an approach to reduce the variance of a base estimator, such as a regression tree.

4.4.5.2 AdaBoost

Liking bagging, AdaBoost [254] manipulates modified versions of training examples repeatedly to generate multiple predictions which are then combined to form the final prediction. The difference is that AdaBoost applies a weight to each of the training examples. In each iteration, the weights are individually updated based on minimizing the weighted error on the training set. It increases weights on those training examples that are incorrectly predicted in a previous iteration by the boosted model, whereas the weights are decreased for correctly predicted training examples. In subsequent iterations, therefore, AdaBoost constructs progressively more difficult learning problems. Once the training process has finished, the predictions are combined through a weighted majority vote (or sum) to produce the final prediction. This, therefore, usually achieves a high degree of accuracy in the test set.

4.4.5.3 Stacking

Stacking regression combines multiple regression models via a meta-regression, which uses an out-of-fold predicts concept [255] (shown in Figure 4.4). It splits the data

set into K folds, where $k-1$ folds are used to train the first level regressors in K successive rounds. In each round, the first level regressors are used for prediction based on the remaining 1 subset. After that, the prediction results are used and stacked as input data to the second level regressor to form a final set of predictions [256]. In this study, SVR, BPNN and CRAT are used as regression models in the first level to get prediction results, and LR is used as a met-regressor in the second level to combine and generate the final prediction.

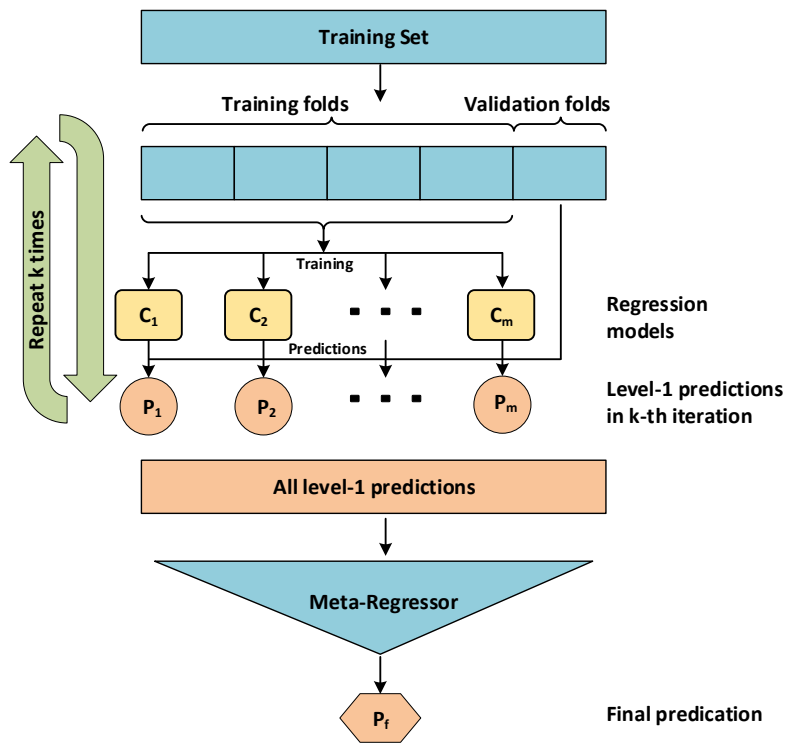


Figure 4.4: Schematic diagram of Stacking model [256]

4.4.6 Model construction

All models were implemented using Python 3.6.5 programming language and prediction models are constructed through the scikit-learn library in Python. The computational tests were done on an AMD Opteron(tm) Processor 6386 SE (2.8 gigahertz) workstation with 1 core used and 6 gigabytes of RAM. The parameters for the prediction models used in this work are summarized in Table 4.2 (The details of programming code refer to Appendix A).

Table 4.2: Prediction model parameter settings

Models	Parameters	options
SVR	Kernel	rbf
	Regularization ‘C’	1e4
	Kernel coefficient ‘gamma’	0.001
	Epsilon	0.1
	Activation function	logistic
BPNN	Hidden neurons	20
	Solver for weight optimization	lbfgs
	Learning rate	0.001
CRAT	Maximum number of iterations	800
	Maximum depth of the tree	5
	Split criterion	mse, best
Bagging	Number of base estimators	100
	Maximum number of estimators	100
AdaBoost	Learning rate	0.1
	Loss function	linear
Stacking	Base estimators	SVR, BPNN, CRAT
	Final estimators	LR

4.5 Validation and evaluation

4.5.1 Cross-validation method

Generally, the dataset is split to generate a training subset and a validation subset, keeping the properties of the original dataset as much as possible to avoid misleading estimates. To minimize bias from the random data splitting, the K-fold cross-validation is used widely [125]. In this study, a ten-fold cross-validation approach is applied to assess model performance (shown in Figure 4.5), which yields the optimal computational time and reliable variance confirmed by Kohavi [257]. The empirical dataset is split into 10 equal-size subsets with a similar distribution. After that, training tests are performed repeatedly 10 times using a different subset as the test set and the remaining subsets as the training set each time [258]. The average accuracy in 10 times validation is expressed as the model accuracy.

4.5.2 Performance evaluation

To indicate and validate the accuracy of the proposed machine learning models, three statistical methods, Mean Absolute Error (MAE), Root Mean Square Error (RMSE), and Coefficient of Determination (R^2) are used in this chapter. For details of these three statistical metrics refer to Section 2.8.1. The average deviation of the

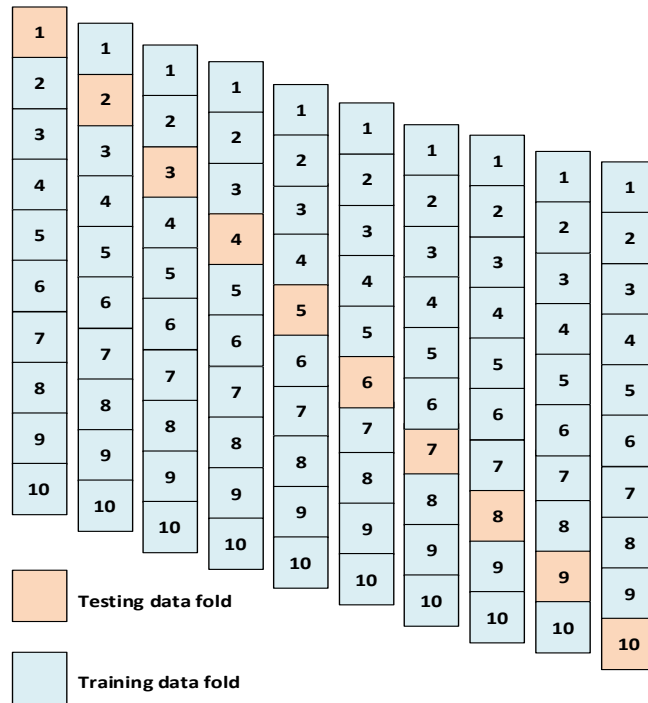


Figure 4.5: Ten-fold cross-validation approach

performance of an individual model or Ensemble Methods (EM) from a benchmark model in terms of three statistical measures (MAE, RMSE and R^2) is measured by the following equation (4.14).

- Deviation (Dev)

$$Dev(\%) = \frac{P_i - P_j}{P_j} * 100 \quad (4.14)$$

Dev indicates the statistical performance improvement compared with a benchmark model, P_i is the statistical performance (MAE, RMSE or R^2) of an individual or ensemble method, P_j is the corresponding performance of a benchmark model, LR or an individual method used in the ensemble method as the base learner, respectively.

MAE statistics is a measure of errors between the predicted value of the crack width of ECC after self-healing with the observed value of the crack width of ECC after self-healing in empirical data.

RMSE statistics computes the square root of the average residual error between the predicted values and the target values. A lower value of MAE or RMSE indicates

a better prediction performance of the model. R^2 measures the strength of association between the predicted values and the target values, based on the proportion of total variation of outcomes. A greater value close to 1 represents a better prediction performance that commendably replicates the observed crack width of ECC after self-healing. Deviation statistics indicate the improvement of the prediction performance of an individual or an ensemble model from a benchmark model that could be the LR model or the individual model used as base learners in the corresponding ensemble model.

4.6 Results and discussion

In this section, the prediction performance of individual and ensemble methods are examined by MAE, RMSE and R^2 according to ten-fold cross-validation. We use abbreviations for ease of presentation, in which Bag_LR, Bag_SVR, Bag_BPNN and Bag_CRAT express generating the bagging ensemble method by using LR, SVR, BPNN and CRAT as base estimators, respectively. Ada_LR, Ada_SVR, Ada_BPNN and Ada_CRAT represent generating an AdaBoost ensemble method by manipulating LR, SVR, BPNN and CRAT as base estimators, respectively. Stack_LR indicates developing a stacking ensemble method based on individual methods (including SVR, BPNN, and CRAT) as learning base with LR as a meta-regressor.

Table 4.3: Ten-fold cross-validation results of machine learning models on self-healing prediction for ECC

Models	MAE	Dev(%)	RMSE	Dev(%)	R^2	Dev(%)
Individual models	LR	5.012	-	7.680	-	0.860
	BPNN	4.329	-13.6	6.515	-15.2	0.899
	CRAT	4.305	-14.1	6.811	-11.3	0.887
	SVR	4.296	-14.3	6.826	-11.1	0.883
Ensemble models	Ada_LR	4.784	-4.6	7.400	-3.6	0.867
	Ada_BPNN	4.226	-15.7	6.435	-16.2	0.900
	Ada_CRAT	4.207	-16.1	6.455	-15.9	0.898
	Ada_SVR	4.145	-17.3	6.577	-14.4	0.893
	Bag_LR	5.014	0.0	7.689	0.1	0.860
	Bag_BPNN	4.143	-17.3	6.341	-17.4	0.901
	Bag_CRAT	4.093	-18.3	6.358	-17.2	0.901
	Bag_SVR	4.302	-14.2	6.820	-11.2	0.883
Stack_LR		3.934	-21.5	6.118	-20.3	0.904
						5.1

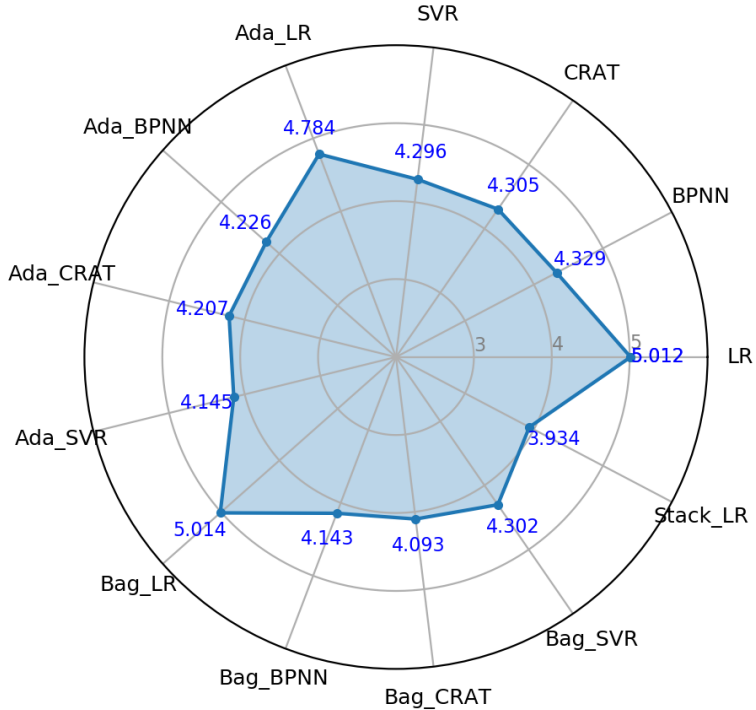


Figure 4.6: Average MAE for performance of self-healing of ECC on all machine learning models

Table 4.3 shows the average performance of ten-fold cross-validation for each model (in each row), and performance deviation from the LR model with respect of MAE, RMSE and R^2 , respectively. As it can be seen, Stack.LR is superior to all other individual or ensemble models on the basis of all three performance measures (3.934, 6.118, 0.904 for MAE, RMSE, and R^2 , respectively). Furthermore, among the individual models, SVR performs the best in terms of MAE (4.296), and BPNN has the lowest error on RMSE (6.515) and highest accuracy with R^2 0.899. For the single learning based ensemble methods, Bag_CRAT has the best performance in terms of MAE (4.093), and Bag_BPNN performs the best on RMSE (6.341). In terms of R^2 , Bag_CRAT and Bag_BPNN have the same performance and outperform other ensemble methods using an individual method as base estimator. Moreover, it can be concluded that most machine learning models are able to learn and predict empirical data with an acceptable degree of precision. The performance of all machine learning models described in Table 4.3 are depicted in Figure 4.6, 4.7 and 4.8 in terms of MAE, RMSE and R^2 , respectively.

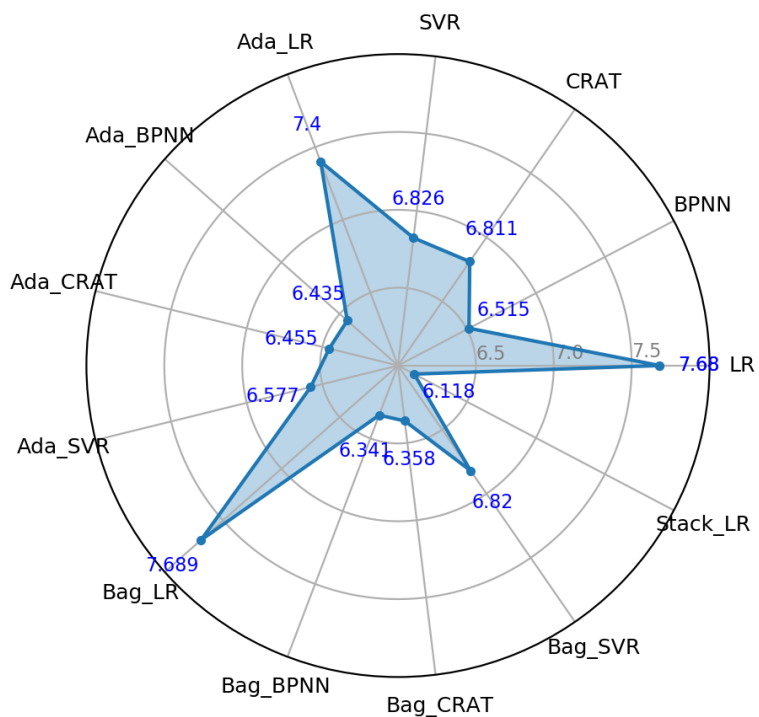


Figure 4.7: Average RMSE for performance of self-healing of ECC on all machine learning models

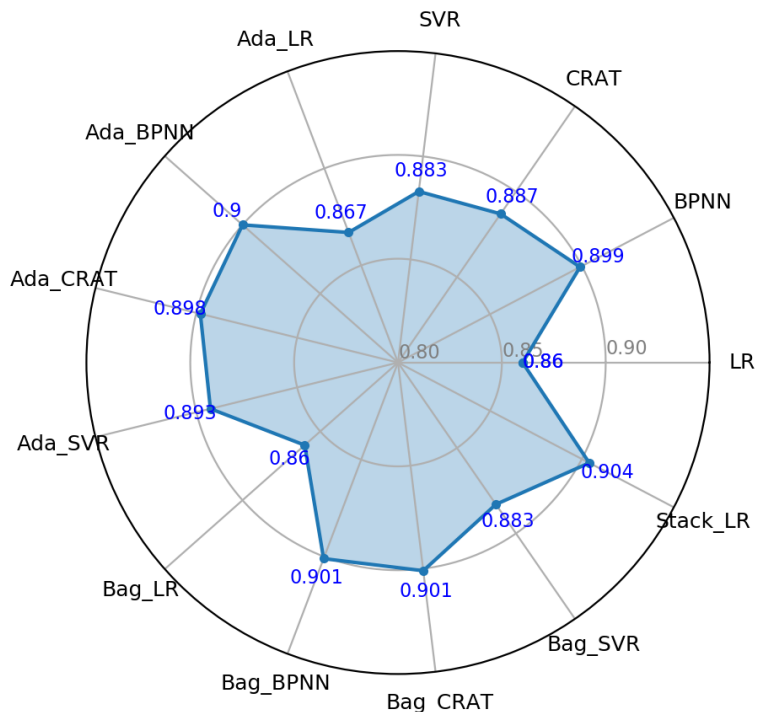


Figure 4.8: Average R^2 for performance of self-healing of ECC on all machine learning models

Overall, all models can noticeably reduce the error values and increase the prediction accuracy compared with LR, except Bag_LR. For example, of the models based on ensemble learning by AdaBoost, Ada_SVR performs the best on MAE, reducing by 17.3%, Ada_BPNN performs the best on RMSE, reducing by 16.2% and on R^2 , increasing by 4.7%. For the bagging ensemble methods, Bag_CRAT performs the best on MAE, reducing by 18.3%, Bag_BPNN performs the best on RMSE, reducing by 17.4%, and Bag_CRAT and Bag_BPNN have the same performance on R^2 , increasing by 4.8%. However, note that Bag_LR has a worse performance than LR in terms of MAE and RMSE. This may result from several training examples repeatedly appearing in different replicated datasets to train multiple base regressors.

Table 4.4 further shows the deviation of ensemble models from individual models which are used as base learners over the three statistical measures based on ten-fold cross-validation results. The results indicate that the ensemble methods using individual methods as a learning base improved the performance of the individual method on the basis of all three performance measures. For example, using BPNN as the learning base, ensemble method Bag_BPNN has the lower error (MAE and RMSE decreasing by 4.3% and 2.7%, respectively) and higher accuracy (R^2 increasing by 0.2%) than the individual method BPNN. Moreover, the comparative results showed that ensemble learning based models (Stack_LR) distinctly outperformed the single learning based models (Ada_LR and Bag_LR) in terms of overall performance measures.

Specifically, bagging ensembles substantially enhance the performance of BPNN and CRAT while the AdaBoost ensemble achieve a considerable improvement for LR and SVR. It means that BPNN and CRAT used as the base learner, bagging method achieves better results (lower error value and higher R^2) than the AdaBoost and individual method, and the LR and SVR used as the base learner, the AdaBoost method gets better results than the bagging and individual method.

The comparative analysis of observed and predicted crack width after self-healing of ECC as the self-healing capability of ECC by all machine learning techniques is presented in Figures 4.9 to 4.21. The coefficient of determination R^2 and equation of the linear least square fit line are shown in these Figures (of the form $y = ax + b$

Table 4.4: Performance deviation of ensemble models from benchmark models on self-healing of ECC

Benchmark	Model	MAE	RMSE	R^2
		<i>Dev(%)</i>		
LR	Ada_LR	-4.6	-3.6	0.8
LR	Bag_LR	0.0	0.1	0.0
BPNN	Ada_BPNN	-2.4	-1.2	0.1
BPNN	Bag_BPNN	-4.3	-2.7	0.2
CRAT	Ada_CRAT	-2.3	-5.2	1.2
CRAT	Bag_CRAT	-4.9	-6.6	1.6
SVR	Ada_SVR	-3.5	-3.6	1.1
SVR	Bag_SVR	0.1	-0.1	0.0
Ada_LR	Stack_LR	-17.8	-17.3	4.3
Bag_LR	Stack_LR	-21.5	-20.4	5.1

relating predicted crack width “ y ” after self-healing which is the dependent variable to experimental observed crack width “ x ” after self-healing which is an independent variable) indicates that the prediction output is very close to the experimental observed results. Basically, the more closely the R^2 approaches to one, and with the slope “ a ” of the fit line is closer to 1 and the “ y ” intercept “ b ” is more small, close to 0 (the fit line is more close to the target line $Y = X$), the better the prediction performance is achieved. It can be seen from Figure 4.9, for the LR model, the predicted crack width after self-healing has a reasonable performance with the coefficient R^2 for 0.860, and the slope “ a ” of the fit line for 0.799 and the “ y ” intercept “ b ” is 3.804. Similarly, as it can be seen in Figure 4.10, the BPNN model has a better performance than the LR model, which has the coefficient R^2 for 0.899, and the slope “ a ” of the fit line for 0.866 and the “ y ” intercept “ b ” is 1.817. And as shown in Figure 4.9 and 4.10, the predicted value of crack width after self-healing of ECC in the BPNN model adheres to the target line $Y = X$ better than the LR model, especially for the crack width over 100 μm , which further indicates the BPNN model is more accuracy and outperform the LR model. Specifically, the Stack_LR model has the best performance with the coefficient R^2 for 0.904, and has the slope “ a ” of the fit line for 0.899 (close to 1) and the “ y ” intercept “ b ” is 1.579 (close to 0) as shown in Figure 4.21. In addition, Figures 4.9 to 4.21 reveal the experimental data of crack width after self-healing of ECC generated from laboratory experiments is mainly distributed between 0 to 60 μm . Whereas a few samples have a crack width

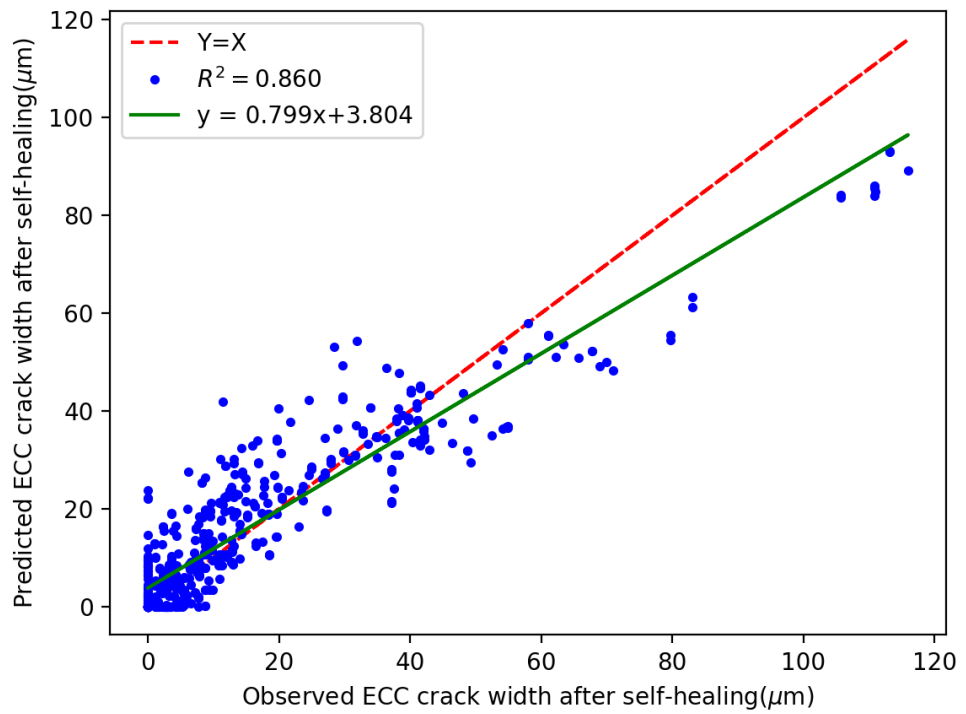


Figure 4.9: Comparison of observed and predict crack width after self-healing process of ECC by LR

over $100\mu\text{m}$. This insufficient data may result in machine learning models being trained inadequately and reducing the prediction accuracy.

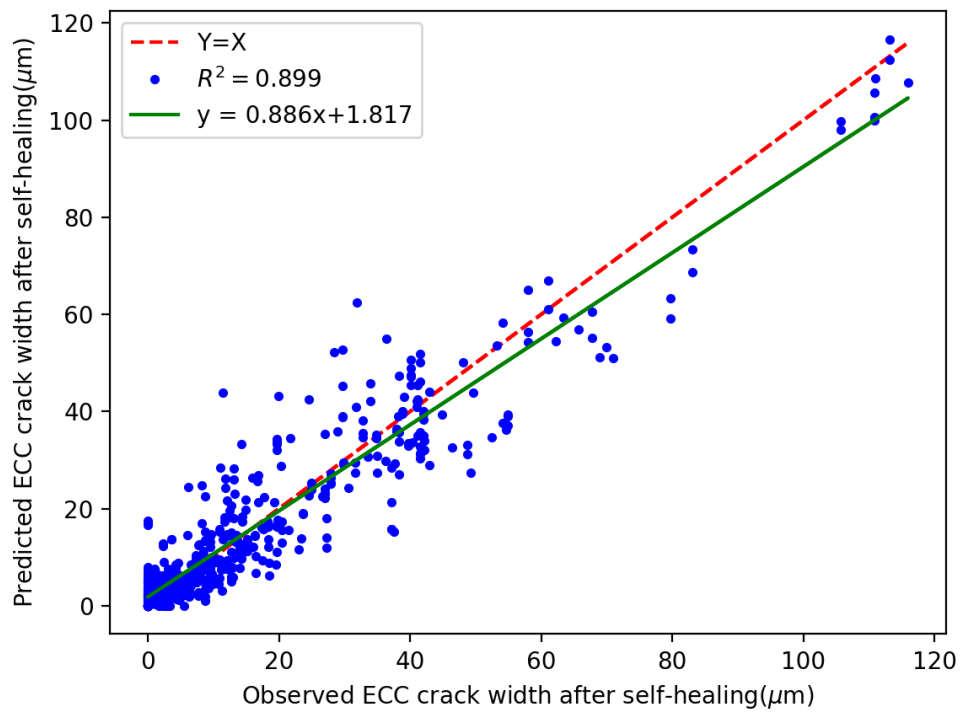


Figure 4.10: Comparison of observed and predict crack width after self-healing process of ECC by BPNN

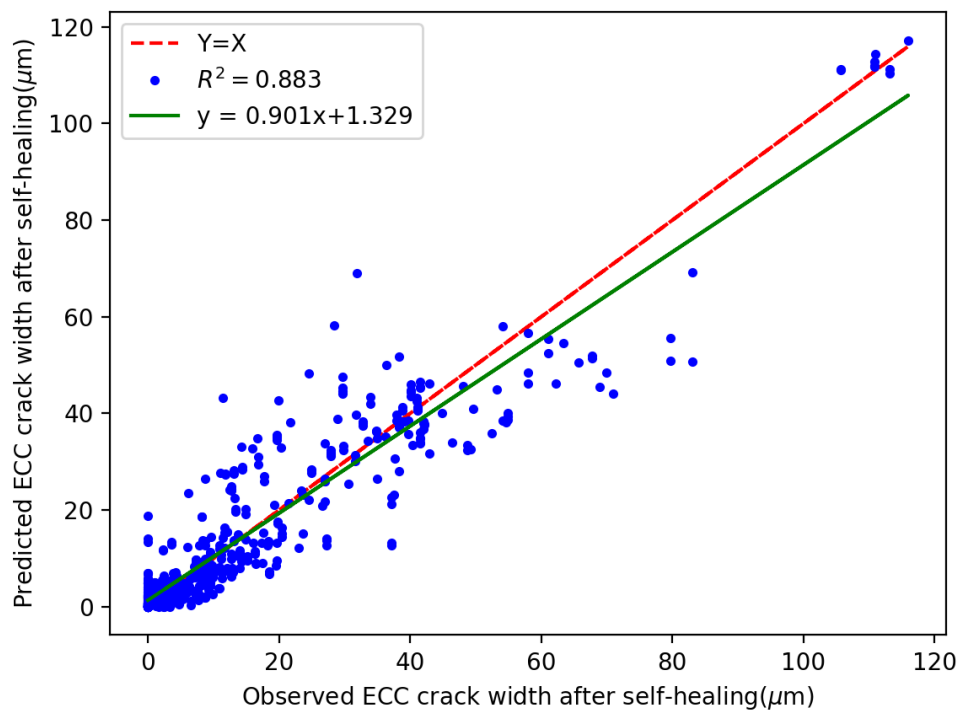


Figure 4.11: Comparison of observed and predict crack width after self-healing process of ECC by SVR

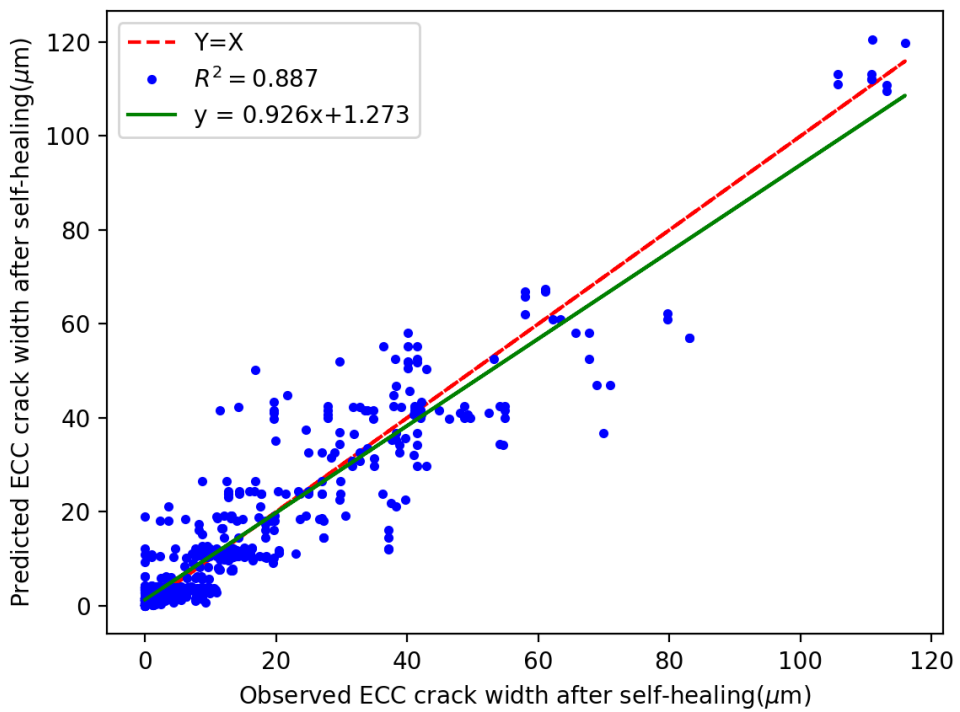


Figure 4.12: Comparison of observed and predict crack width after self-healing process of ECC by CRAT

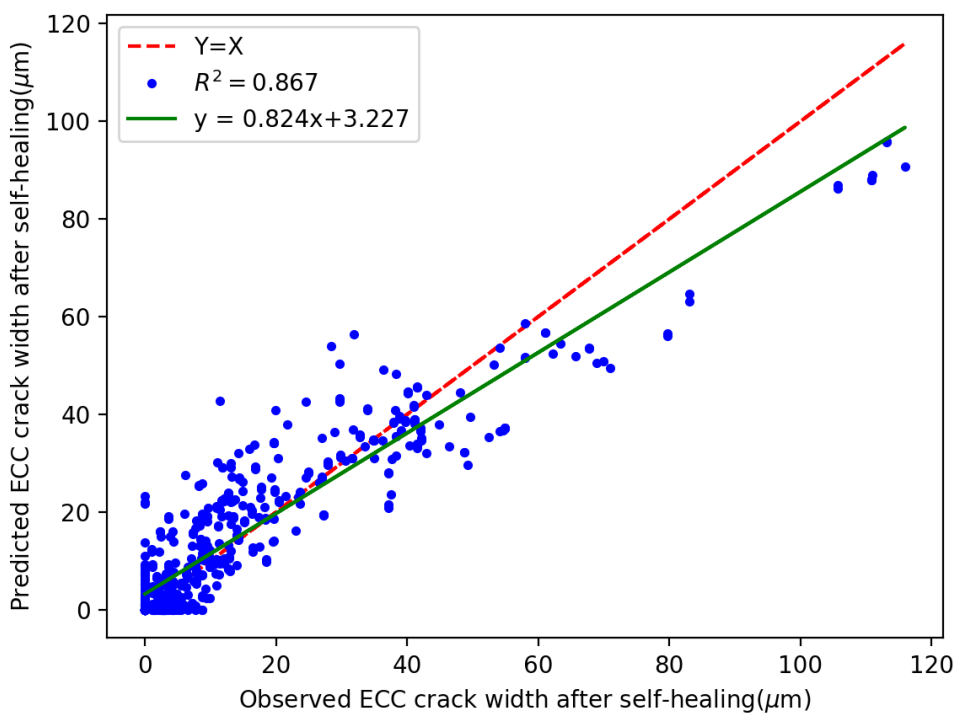


Figure 4.13: Comparison of observed and predict crack width after self-healing process of ECC by Ada_LR

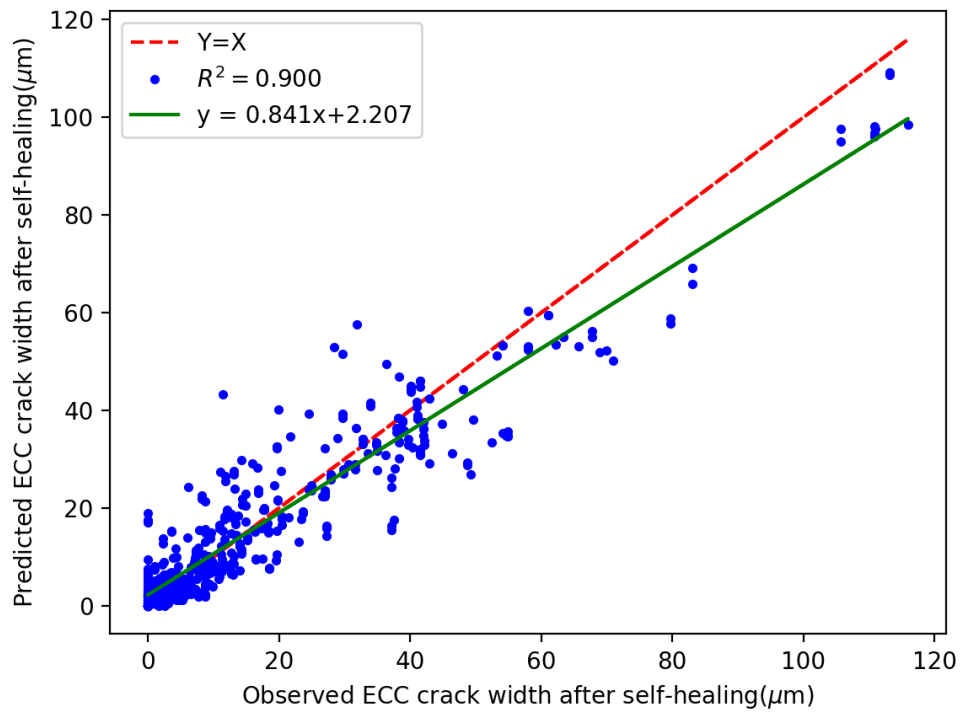


Figure 4.14: Comparison of observed and predict crack width after self-healing process of ECC by Ada_BPNN

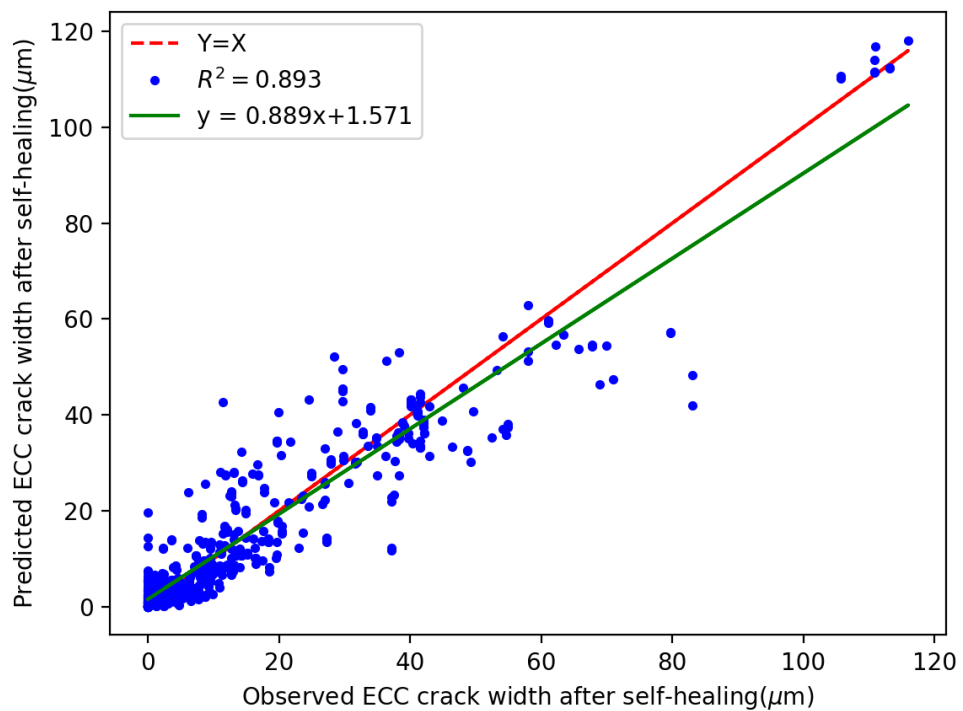


Figure 4.15: Comparison of observed and predict crack width after self-healing process of ECC by Ada_SVR

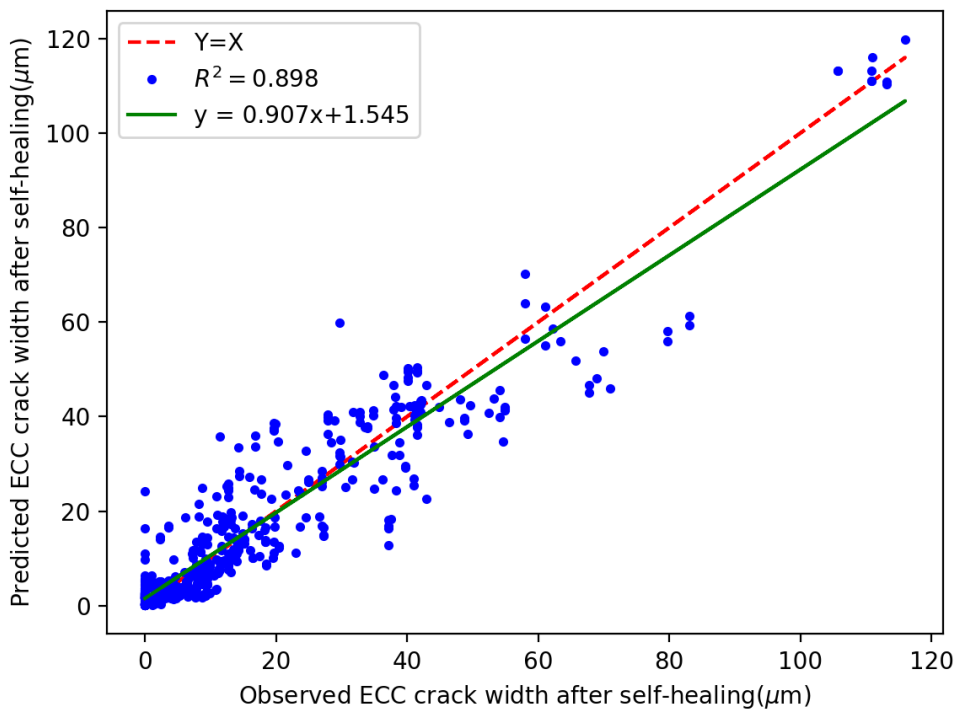


Figure 4.16: Comparison of observed and predict crack width after self-healing process of ECC by Ada_CRAT

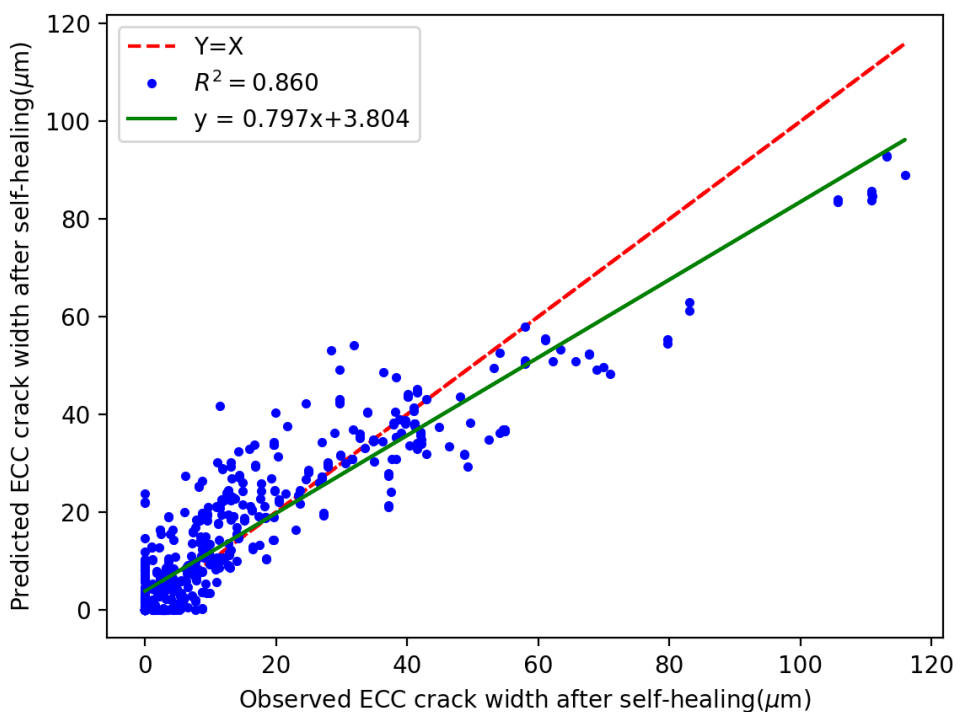


Figure 4.17: Comparison of observed and predict crack width after self-healing process of ECC by Bag_LR

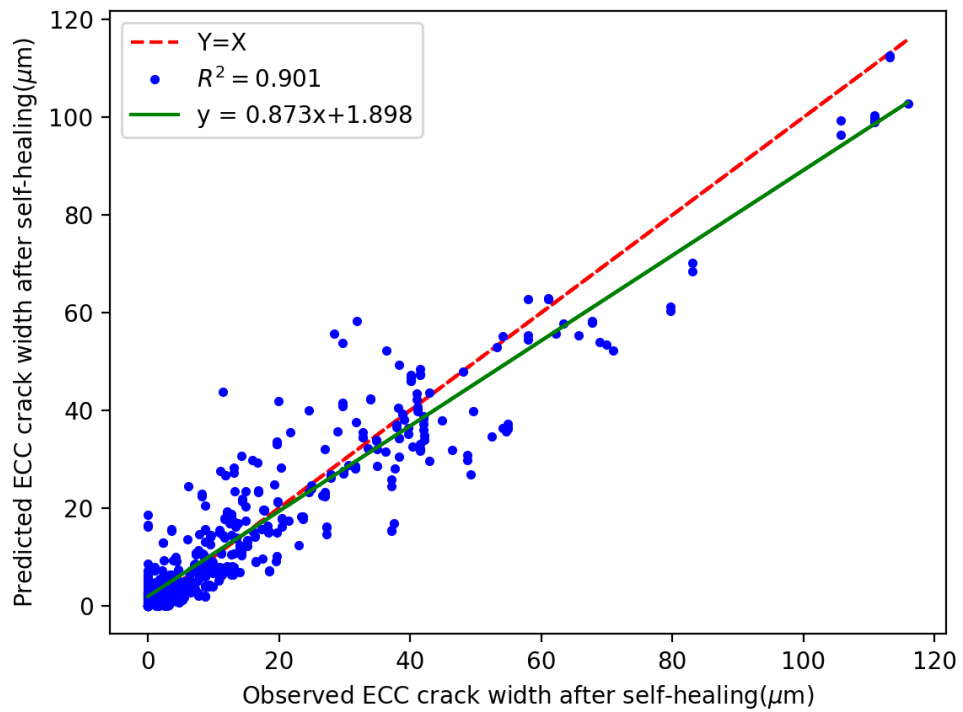


Figure 4.18: Comparison of observed and predict crack width after self-healing process of ECC by Bag_BPNN

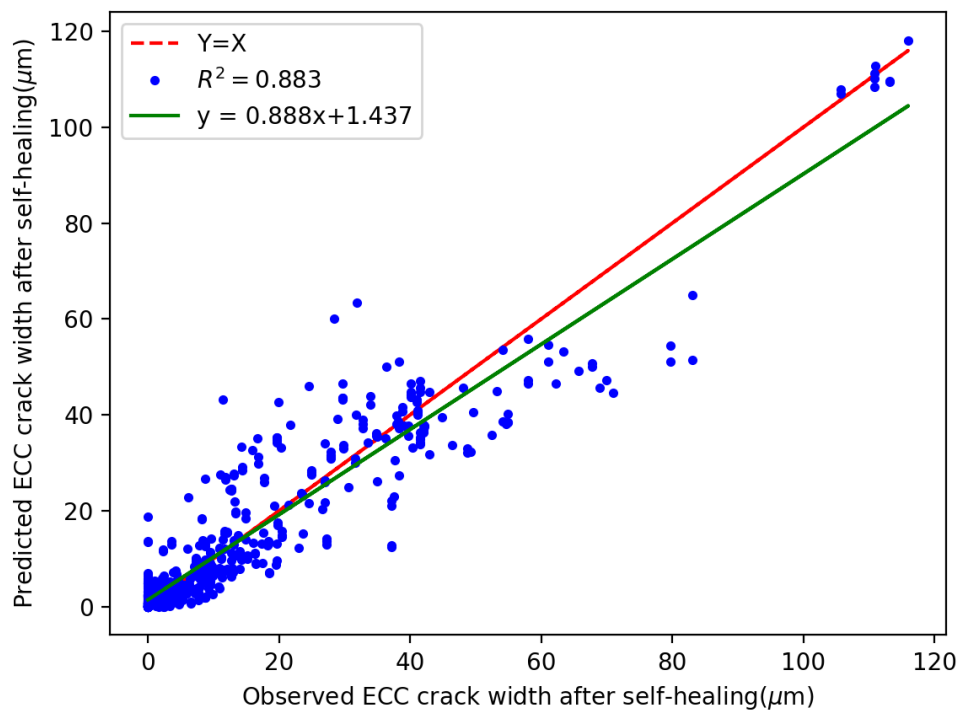


Figure 4.19: Comparison of observed and predict crack width after self-healing process of ECC by Bag_SVR

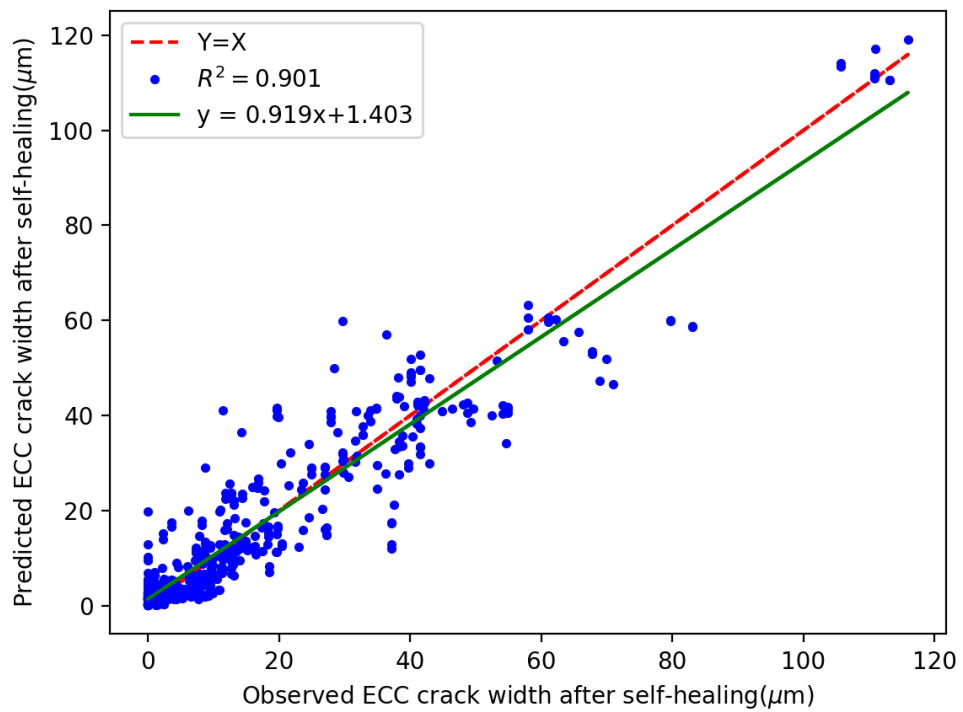


Figure 4.20: Comparison of observed and predict crack width after self-healing process of ECC by Bag-CRAT

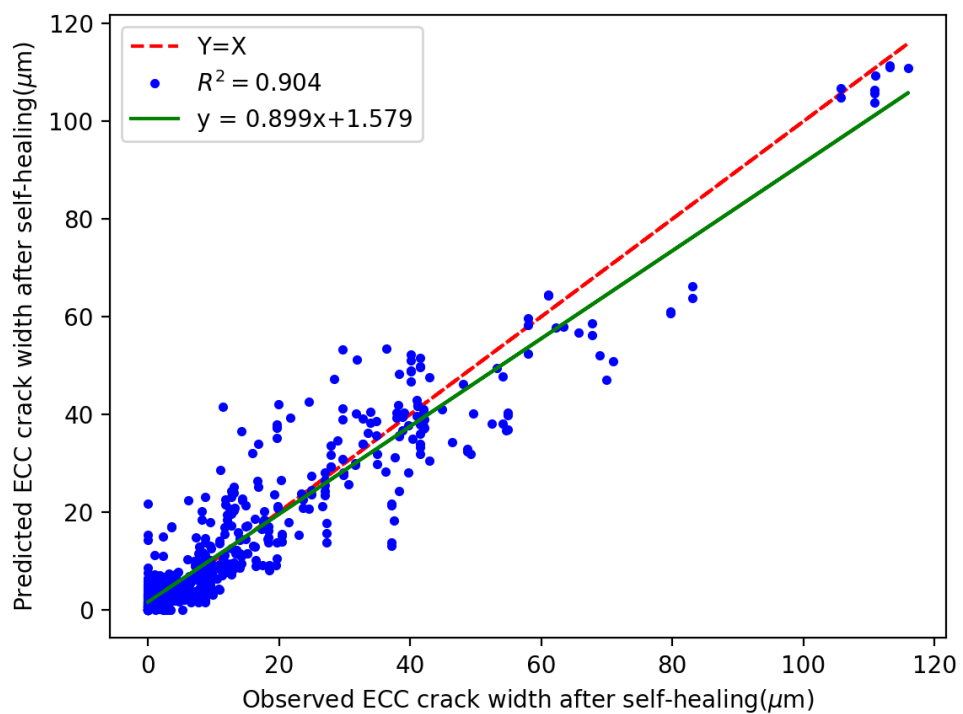


Figure 4.21: Comparison of observed and predict crack width after self-healing process of ECC by Stack_LR

4.7 Summary

In this chapter, a comprehensive comparison is proposed to analyse the performance of prediction of the self-healing ability of ECC using individual and ensemble methods. All machine learning models are trained and tested based on the experimental results from nine ECC mixtures. The comparison results provide valuable insights into proposing and validating the machine learning models for predicting self-healing on ECC.

A total of four individual methods (LR, BPNN, CRAT, and SVR) and three ensemble methods (bagging, AdaBoost, and stacking) are used to perform the prediction of the self-healing ability of ECC. In these, the performance of LR is used as a benchmark baseline to compare the performance of other individual and ensemble models. The proposed ensemble methods, bagging and AdaBoost, use one of the four individual methods as a base estimator to aggregate multiple single learning based prediction. The stacking method is used to combine multiple predictions generated by multiple regression models (SVR, BPNN, and CRAT).

The Stack_LR model demonstrated great predictive ability and the best performance among all individual and ensemble methods, showing the lowest error values on MAE 3.934 and RMSE 6.118 and the highest on R^2 0.903. Moreover, all ensemble methods present the improvement of the predictive ability of individual methods. In particular, the bagging method obviously improves the prediction performance of CRAT on MAE 4.9%, RMSE 6.6%, and R^2 1.9%. On the other hand, the BPNN model performs the best in terms of RMSE and R^2 among all individual models.

The computational results indicate the individual and ensemble methods can be used to predict the self-healing ability of ECC. However, how to choose a fit base learner for different ensemble methods is critical. Engineers engaged in the design of durable and sustainable ECC mixtures will benefit from the use of machine learning models. Also all individual and ensemble models can be used as a tool for the prediction of the properties of ECC and can be optimized to develop hybrid models for further improving predictive ability.

Future investigation and experimentation will be considered to extend the training dataset to include various crack width distributions and diverse influencing fac-

tors, such as components, W/MC rate etc., on self-healing of ECC. And more research should be undertaken to explore how to optimize parameters in machine learning models and develop hybrid modelling strategies to improve the prediction accuracy.

Chapter 5

Modeling Self-healing Repeatability of ECC With Evolutionary Algorithm Based Artificial Neural Network

5.1 Introduction

The self-healing capability of Engineered Cementitious Composite (ECC) has been revealed and modelled in chapters 2, 3, and 4, however, there is a concern about the repeatability of self-healing related to the robustness of the self-healing mechanism [9]. In the real world, cracks are likely to occur more than once, even reoccur from the same location after self-healing, over the lifetime of a concrete structure.

The major mechanism of self-healing in ECC is attributed to four aspects [14, 28]: (1) calcium hydroxide carbonation; (2) hydration of unhydrated cementitious particles; (3) further swelling of calcium silicate hydrate; (4) settlement of the debris and loose cementitious particles in the presence of water. Therefore, the self-healing repeatability of ECC is strongly influenced by the composition of matrix and the amount of available reaction products. However, it is difficult to identify and quantify reaction products due to the physico-chemical process of self-healing not being completely understood [29]. Instead, the consumed reaction products can be reflected by the crack width healed in the earlier self-healing processes. From this point of view, it would mean a step forward for modeling the self-healing repeatability of ECC based on the mixture proportion, especially mineral admixtures and earlier healed crack width, and thus predicting the self-healing repeatability of ECC.

Back-propagation Neural Network (BPNN) has been demonstrated strong potential for prediction of the self-healing capability of ECC among individual models in Chapter 4. It is proper to note that conventional applications of BPNN could be trapped in local optima and may not find the global optimum due to randomly initialized weights and biases [143]. Therefore, many researchers combine BPNN with optimization algorithms, such as Evolutionary Algorithm (EA) [259], and Genetic Algorithm (GA) [260] to improve its prediction performance. Despite numerous applications that integrated an EA with BPNN in various fields of study, the methodology has not been explored so far for modelling the self-healing repeatability of ECC. This chapter constructs two prediction models that integrate BPNN with population based optimization algorithm EA in structured ternary tree and list to develop a robust computational tool for modelling the self-healing repeatability of ECC.

5.2 Data collection and preprocessing

A total of five features are selected as input variables and one feature is selected as the output variable based on previous experimental works. The five input features are comprised of three parameters that illustrate the composites in ECC, including Fly Ash (FA), Silica Fume (SF), and Hydrated Lime Powder (LP), and two parameters related to crack changes, referred to as First Healed Crack Width (FWH) and Second Initial Crack Width (SIW). The output is the Second Final Crack Width (SFW). It is noteworthy that some impact factors in the test, such as general purpose cement, sand, Water to Cementitious Materials Ratio (W/CM), and healing time, are controlled as constants which are excluded for the prediction modelling due to no effect. As a result, there are 712 records in total which are gathered by a digital microscope, explained in the experiment sections of Chapters 3 and 4.

With the aim of training, validation and testing of the proposed EA-based BPNN model, the empirical data are divided into three subsets. The training dataset that includes 70% of the original data is used for training the EA-based BPNN model to establish the relationship between input and output data-pairs. The testing dataset, including 15% of the original data, is used to evaluate the prediction performance of the trained EA-based BPNN model. And the validation dataset, including 15%

of the original data, is used to compare the prediction performance with training and testing. The ranges of input and output parameters for the three datasets are summarized in Table 5.1.

From Table 5.1, we can see the input data are comprised of different features, varying in range and units, which weigh all features unequally to the analysis and might end up creating a bias. To eliminate this effect, we preprocess the inputs to the range [0,1] by the min-max scaling presented in the following function,

$$x' = \frac{x - x_{min}}{x_{max} - x_{min}} \quad (5.1)$$

Where x' is the scaled value of the variable x , and x_{max}, x_{min} are the maximum and minimum values of variable x , respectively.

Table 5.1: Statistical parameters of training, validation, and test datasets

	Training				Validation				Test			
	Max	Min	Mean	SD	Max	Min	Mean	SD	Max	Min	Mean	SD
<i>Input</i>												
FA (kg/m^3)	816.03	641.16	712.68	62.50	816.03	641.16	715.25	68.21	816.03	641.16	714.70	67.15
SF (kg/m^3)	174.86	0	63.79	66.79	174.86	0	61.01	68.59	174.86	0	75.18	70.26
LP (kg/m^3)	174.86	0	39.56	57.20	174.86	0	39.77	58.62	174.86	0	26.15	50.15
FHW (μm)	60.645	0	15.33	11.75	48.967	0	14.30	11.67	45.88	0	13.85	11.00
SIW (μm)	310.29	0	47.07	42.00	278.59	1.09	46.24	41.98	270.94	0	45.57	40.81
<i>output</i>												
SFW (μm)	308.08	0	34.89	41.64	273.12	0	34.01	42.39	260.26	0	32.60	40.32

5.3 Modelling self-healing repeatability of ECC

5.3.1 BPNN architecture

The architecture of a conventional 5-5-1 BPNN (shown in Figure 5.1) is a multiple layers Artificial Neural Network (ANN) which consists of five artificial neurons in an input layer representing the five features influencing self-healing repeatability of ECC, along with one hidden layer including five neurons and the output layer

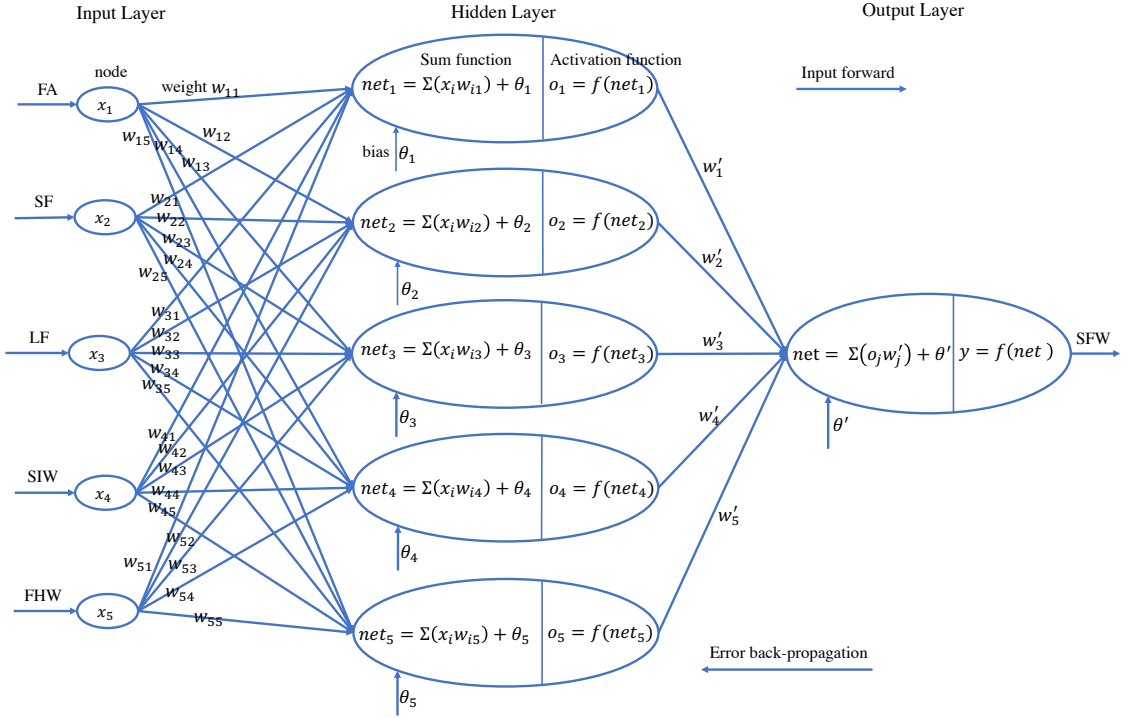


Figure 5.1: The architecture of the BPNN model for predicting self-healing repeatability of ECC

containing a single neuron representing the final crack width after repeated self-healing. The neurons are fully interconnected between the neighbouring layers by weight, and typically there are no inter-connections between neurons within the same layer [245]. Each of these neurons in different layers is made up of three elements, including several weighted inputs, a transfer function and an output [143]. The utility of the transfer function in BPNN is to introduce nonlinearity for dealing with complex, undefined and unstructured relations between the inputs and output.

In Figure 5.1, information provided as vectors by the training dataset is forward-propagated from the input layer to the output layer through the hidden layer. The output of a node in the input layer (hidden layer) is sent as an input to the connected node at the hidden layer (output layer) calculated by the weighted sum of input components x_i using the following equation:

$$f(\text{net}_j) = f\left(\sum_{i=1}^n x_i w_{ij} + \theta_i\right) \quad (5.2)$$

where $f(\text{net}_j)$ is the the neuron output, w_{ij} is weights of connections, θ_i repre-

sents biases, n is the number of neurons in each layer and f is the activation function as follows:

$$f(\text{net}_j) = \frac{1}{1 + e^{-\text{net}_j}} \quad (5.3)$$

Once the predicted output is generated, the computed square error between target and predicted is propagated backward. Based on the square error, BPNN uses a back-propagation algorithm that is a local research algorithm using steepest gradient descent to iteratively update the weights and biases of the neurons, minimizing the square error as the performance function [261]. The learning rate is a parameter that determines the size of weights adjustment during network training. A higher learning rate results in faster training with large oscillations in the weight update which may reach over the optimal value of weights. On the contrary, a lower learning rate makes convergence slower and increases the probability of getting trapped in local minima. And the momentum term is a factor used for gradient descent update to accelerate network training by adding the effect of the past weight iterations to the current one [262]. An appropriate learning rate for the weight update and momentum term for the gradient descent update are crucial for the efficient learning of BPNN which avoids being stopped in a local mimima. With these two parameters, the updates in weights are determined as follows:

$$\Delta w_n = \alpha \Delta w_{n-1} - \eta \frac{\partial E}{\partial w} \quad (5.4)$$

$$E = \frac{1}{N} \sum_{i=1}^n (y_i - y'_i)^2 \quad (5.5)$$

where w represents the weight allocated to connection between two neurons, Δw_n and Δw_{n-1} are the changes of weights at the n and $n - 1$ iterations. α, η, E and y_i, y'_i represent the momentum term, learning rate, computed square error, and the target and predicted output, respectively.

However, there is an inherent drawback of BPNN which is attributed to random initialization of weights and biases for training the BPNN, possibly leading to slow convergence and getting trapped in local minima [143]. In order to overcome this

inherent drawback, it is necessary to develop an effective methodology for evolving the optimal initial weights and biases of BPNN.

5.3.2 Principle of EA-based BPNN

The term EA refers to a probabilistic search algorithm that uses evolutionary principles, genetic inheritance and Darwinian strife for evolving the search through a space of potential solutions considered as the optimization process [263]. It is a population-based search method that explicitly employs a set of solutions and combines them together in some way to generate new solutions. The populations evolve naturally according to the principle of natural selection and survival of the fittest. This means individuals who are more adapted to their environment will have a better chance of surviving and reproducing in successive generations. With fitness-oriented and variation-driven properties, EA evolves the search toward good solutions in the form of selection, crossover and mutation operators, and thereby it is able to find global minimum for complex nonlinear problems that have many local optima.

In contrast to BPNN that uses local search, gradient descent for finding the optimal set of connection weights and biases of ANN, EA parallels search in the solution space with stochastic operators evolving the initial weights and biases of BPNN which thereby minimize the probability of being trapped in the local minima. The evolution processes of EA start with taking an initial population of individuals which is encoded into a chromosome that represents a possible solution in the solution space. The fitness of each individual is evaluated to guide the selection. Highly fit individuals are given opportunities to exchange some pieces of chromosome information in a crossover operator to generate new individuals (child). Mutation is often applied to alter some elements of the child. The offspring is then used to update the population for a new generation. This evaluation-selection-reproduction cycle is repeated until the termination criterion is satisfied.

In this chapter, we develop two structured EA to optimize BPNN. The synthesis working principle of EA-based BPNN is illustrated in Figure 5.2, which includes two stages: BPNN trained with EA, and self-healing repeatability of ECC predicted by the trained model. In the first stage, an EA is used for finding the optimal set of initial weights and biases for training the BPNN model. After that, the EA-based

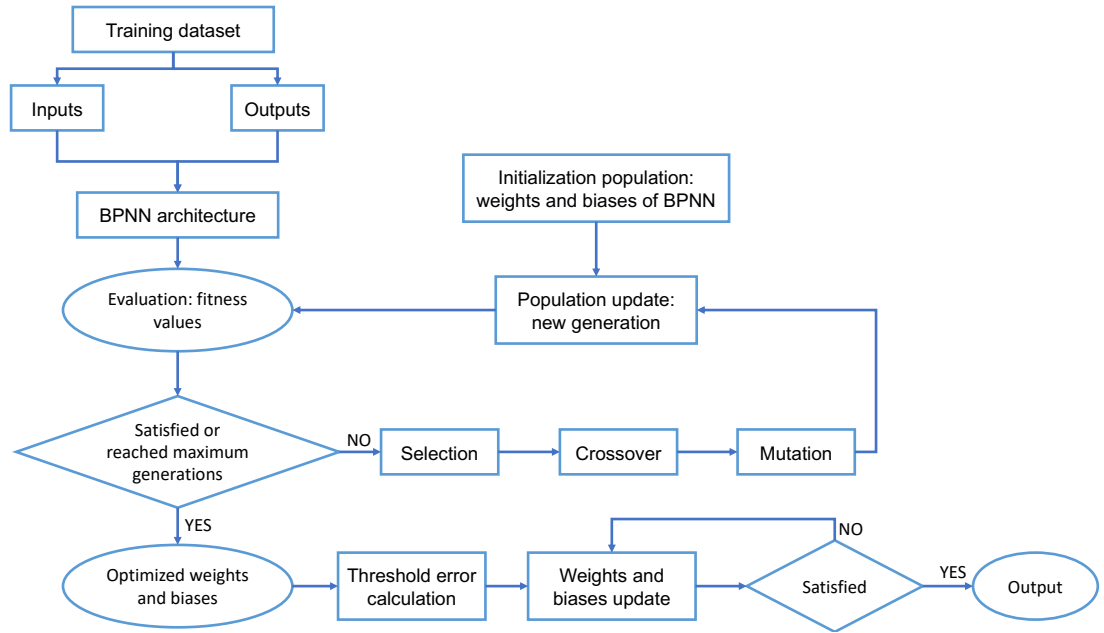


Figure 5.2: Schematic diagram of BPNN model for predicting self-healing repeatability of ECC

BPNN model uses the optimal weights and biases as the initial weights and biases of BPNN to predict self-healing repeatability of ECC in the second stage.

The pseudocode for the proposed EA-based BPNN is illustrated in Algorithm 1. At first, a set of random generated weights and biases are encoded as chromosomes to initialize a population in EA. To evaluate the fitness of chromosomes in terms of error between predicted and target value, the weights and biases are decoding to train BPNN as the starting point of learning iterations using the training dataset. Once the network training process is completed, the validation dataset is used to evaluate the performance of the network and return the forecast error (*RMSE*) between predicted and target value. After that, two individuals are selected in the subsequent evolutions in terms of operations of crossover and mutation, and are supposed to generate a better offspring (child). The worst individual in the former population is substituted by the better offspring, updating a new superior population for the next evolution iteration. Finally, an advanced individual is evolved by those filtered children after generations of evolution loops. The details of programming of EA-based BPNN models refer to Appendix B.

Algorithm 1: Pseudocode of EA-based BPNN

Input: N_i, N_h, N_o , number of input, hidden, output layer neurons
Result: $[W_n, B_n]$, weights and biases

1 **Function** Evolutionary Algorithm(EA):

2 Setup individuals (*population*)
3 **for** ∇ *individuals* \in *population* **do**
4 BPNN(*F*)
5 *fitness* \leftarrow RMSE
6 **end**
7 Organize individuals (structured)
8 $j \leftarrow 1$
9 **repeat**
10 **for** ∇ *individuals* \in *population size* **do**
11 *parents* \leftarrow Choose two parents (*population*)
12 *child* \leftarrow Crossover(*parents*)
13 *child* \leftarrow mutation(*child*)
14 BPNN(*F*)
15 *fitness* \leftarrow RMSE
16 **if** *fitness*(*child*) $<$ *fitness*(worstIndividual) **then**
17 | Replace worst individual by child
18 **end**
19 **end**
20 $j \leftarrow j + 1$
21 Update *population*
22 **until** $j > generations$ or *fitness gap* is reached
23 **End Function**
Input: $[W_n, B_n], TR, V, TS$
Result: RMSE, R^2 , MAE

24 **Function** BPNN(*F*):

25 Decoding chromosomes $w_{ij}, \theta_i \leftarrow [W_i, B_i]$
26 Setup *network*
27 **for** $i \in TR$ **do**
28 **for** n_{epoch} **do**
29 Train forward propagate network \leftarrow *output*
30 *error* \leftarrow *targetedValue* – *output*
31 Calculate errors backpropagate
32 Update w_{ij}, θ_i
33 **end**
34 *network* \leftarrow trained network
35 **for** $k \in V$ or TS **do**
36 | Predict *SFW*
37 **end**
38 Calculate RMSE, MAE, R^2
39 **end**
40 **return** RMSE, MAE, R^2

41 **End Function**

5.3.3 Structured evolutionary algorithm

EA aims to search for an optima solution based on iterative population evolutions, and the evolutionary results and efficiency of searching processes are directly influenced by the setting of key features, such as the structure of chromosome, population size, selection, crossover and mutation.

5.3.3.1 Individuals, population and initialization

In EA, each individual in the population is represented as a chromosome that resembles a possible solution to the problem. These possible solutions are distributed randomly in the search space. For the purpose of optimizing BPNN with EA, an individual is expressed as a real number containing the information of all weights and biases of BPNN in the form of a chromosome.

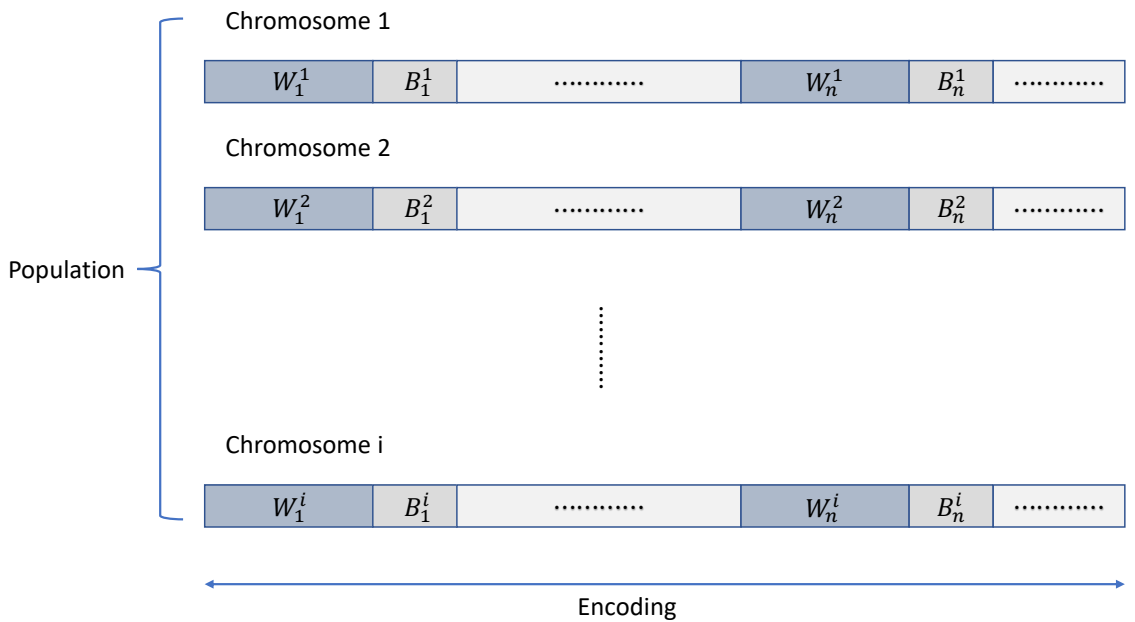


Figure 5.3: Demonstration of encoding the weights and biases of BPNN in chromosomes of EA

As shown in Figure 5.3, weights and biases are encoded as groups of weights and biases pairs $[W_n^i, B_n^i]$ to form the population in EA, and the length of chromosomes is dependent on the architecture of BPNN, specifically the number of neurons in

the input, hidden and output layers. For example, a 5-5-1 architecture of BPNN including five neurons in the input layer, five neurons in the hidden layer and one neuron in the output layer has a total of 36 weights and biases that are then encoded into groups of weights and biases $[W_n^i, B_n^i]$ to generate individuals in the form of a number of chromosomes, where i indicates the i th chromosome, and n presents the n th group of weights and biases in the i th chromosome. That means each individual contains all 36 weights and biases of a BPNN in EA. The information exchanged between the EA and BPNN is implemented through encoding and decoding operations of chromosomes.

After all individuals in the population are generated, they are arranged into two different structures, a tree and a list, which lead to different selection criterion affecting the convergence rate of evolution. Good parents drive a child to be a better and fitter solution.

In the tree structure, all individuals are hierarchically arranged as nodes in a four level ternary tree with 13 clusters, each one of them made up of four individuals, as shown in Figure 5.4. The cluster is composed of a leader and three supports, where the leader is the fitter individual (the node has the smallest fitness) in the cluster. In the first level (shown in Figure 5.4), a cluster is constituted by one node (individual) followed by three nodes (supporters) that have changed into new leaders of three clusters in the second level. Similarly, the supporters in the third level become leaders of new clusters in the fourth level. In such way, the best individual of a cluster is always allocated in the upper level of the cluster, and thus the root node of the tree stands for the best individual in the whole population. The list structure of EA is similar to the GA, which inserts individuals into a population list in the sequence in which individuals are generated.

The size of population affects the diversity of individuals that explore the solution space, leading to global optimization of the problem. A larger population size involves higher opportunities to find the superior solution consuming the higher computational time while a smaller population size limits the chance of variation resulting in quicker convergence. Thus, it is necessary to consider a compromise between accuracy and efficiency. Moreover, in order to compare the performance

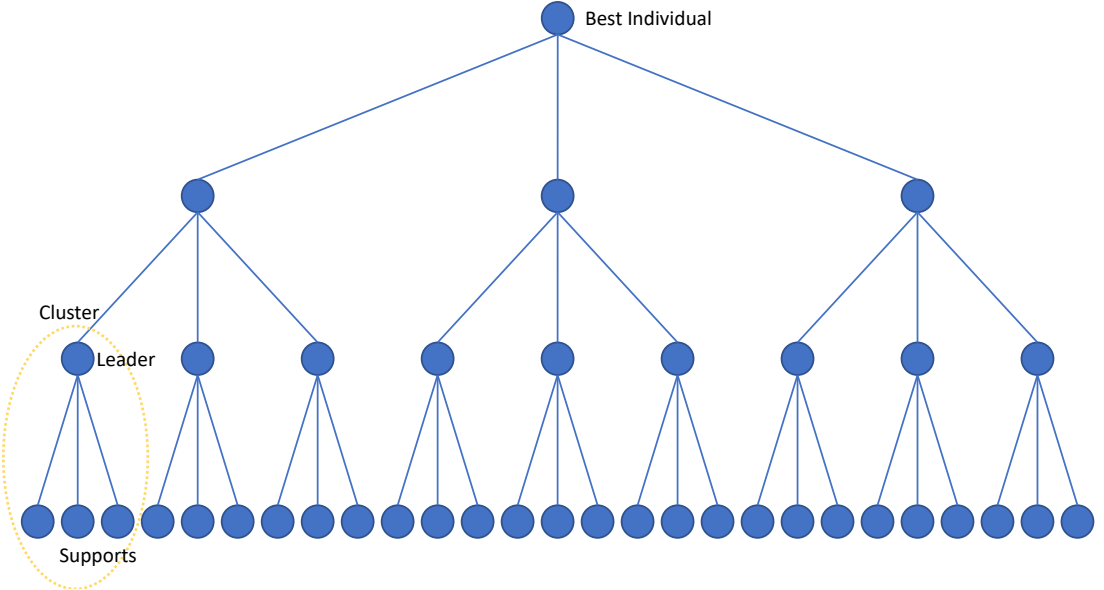


Figure 5.4: Individuals hierarchically structured in a four level ternary tree with 13 clusters in EA

between the structured tree and list in EA, the initial population is settled to the same size (40 chromosomes) in the two structures.

5.3.3.2 Fitness function

The fitness function aims to evaluate the reproductive efficiency of possible solutions to survive, which distinguishes the optimal solution from numerous suboptimal solutions. All individuals are encoded in procedure function BPNNF to calculate their respective fitness, which is the computed Root Mean Square Error (RMSE) between the target and predicted SFW value. According to the aforementioned ranking principle (in section 2.8.1), an individual with the smaller fitness demonstrates better performance. The fitness function (RMSE) can be written as:

$$RMSE = \sqrt{\frac{1}{N} \sum_{i=1}^N (T_i - P_i)^2} \quad (5.6)$$

where T_i and P_i are the target and predicted value respectively, N denotes the total number of samples in the training dataset.

5.3.3.3 Selection criterion

In the real world, individuals are independent beings who for their own reasons decide to become parents. But in EA, the selection of parents aims at selecting potentially useful solutions for recombination, which thereby guides the search into the promising regions of the solution space.

For the tree structure, two individuals as parents are chosen from a cluster consisting of a randomly selected supporter and the supporter's leader.

In contrast to the tree structure, parents in the list structure are selected by Roulette Wheel Selection (RWS) in which all individuals have a chance to be chosen as parents. However, the fitter individual has a higher probability while the weaker individual has a lower probability to be selected and go forward to form individuals in the next generation. Recall that our problem is an optimization of minimizing the RMSE between the target and predicted values, which means the fitter individuals have the lower fitness value. Therefore, the fitness of an individual f_i is modified and used to associate a probability of selection for the RWS using the following functions:

$$f_i = \frac{1}{RMSE_i} \quad (5.7)$$

$$p_i = \frac{f_i}{\sum_{i=1}^N f_i} \quad (5.8)$$

where p_i is the selection probability of the i th individual.

5.3.3.4 Crossover and mutation

The power of EA arises primarily from crossover and mutation [264]. Crossover is a recombination operator that generates offspring by swapping elements between a pair of two individuals (parents) chosen from the population based on the selection criterion. The child (offspring) is generated in the hope it will be better than its parents. Mutation operator adds diversity to the population to obtain a larger exploratory space, which exploits new better individuals to update the current population, helping the search process avoid local optima traps.

In this chapter, Single-point crossover is selected to swap elements between two parents based on a single point site that is picked randomly. Mutation operator randomly chooses and alters one or more elements of an individual with a fixed mutation rate that determines how often the elements of individuals will be mutated. The probability of mutation is usually set to a small value that coincides with the reality phenomenon. Figure 5.5 demonstrates an example of single-point crossover and mutation operator based on chromosomes consisting of weights and biases $[W_n^i, B_n^i]$ of BPNN. For the single-point crossover, a child inherits genes from parent 1 and 2 before and after the single-point, respectively, while for the single-point mutation, a gene of the child is altered by adding or subtracting a random value ε .

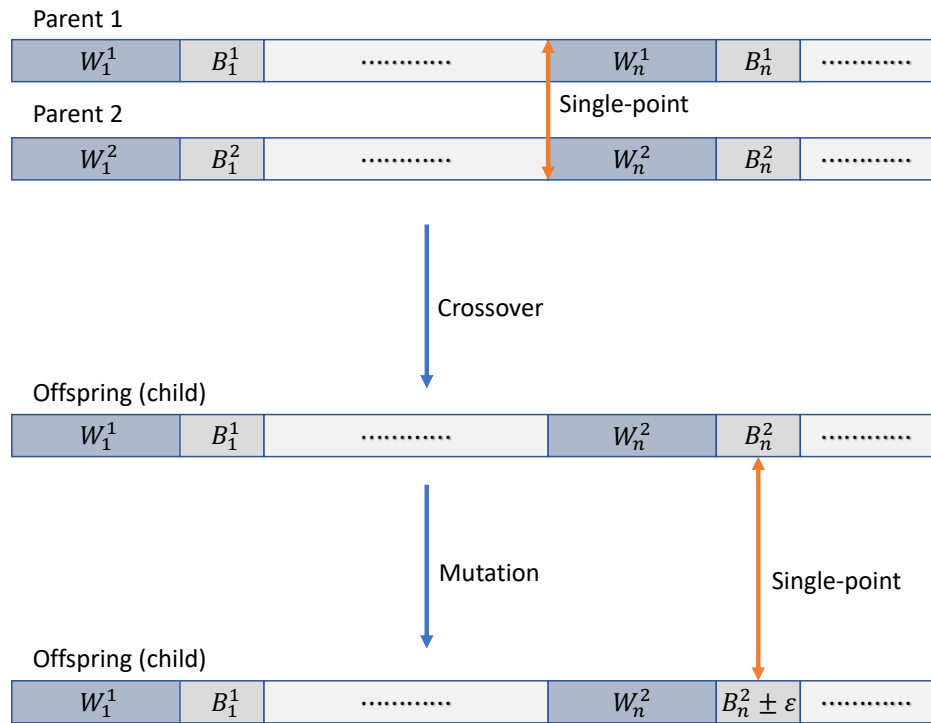


Figure 5.5: Operators of single-point crossover and mutation

After operations of crossover and mutation, the new individual (child) replaces the worst individual in the population in the list structure if it is fitter (a smaller fitness). However, it replace the worst parent in the tree structure, which needs to be reorganized to keep a hierarchical ternary tree. If a support has better fitness than its leader, the support and its leader are swapped, keeping the leader that has

better fitness than the supports.

The stopping criteria for the EA-based BPNN model can be that either it has reached the defined maximum of generations or that the fitness value remains constant or decreases marginally in the evolutionary iterations (reaches the satisfied minimum criteria). The maximum number of generations indicates the total iterations of evolutionary loop, which is set to be 50 in this work.

5.4 Computational results and discussion

Three statistical parameters have been employed for evaluating the performance of the proposed BPNN and EA-based BPNN model in structured Tree and List, which include Mean Absolute Error (MAE), RMSE and R^2 . These are explained in detail in Section 2.8.1. Computational results for the three models, BPNN model labeled as ‘BP’, EA-based BPNN in structured list labeled as ‘List’ and EA-based BPNN in structured tree labeled as ‘Tree’ on training, validation and testing dataset are presented in Table 5.2.

Table 5.2: Statistical performance of proposed BPNN and EA-based BPNN models on training, validation and testing datasets

Dataset	MAE			RMSE			R^2		
	BP	List	Tree	BP	List	Tree	BP	List	Tree
Training	6.323	5.553	5.510	9.304	7.565	7.512	0.950	0.967	0.967
Validation	7.043	6.388	6.210	11.794	10.058	9.110	0.926	0.960	0.953
Testing	9.375	9.041	6.580	14.099	13.501	9.132	0.900	0.939	0.948

As can be seen, the EA can help to improve the performance of BPNN in all three statistical measurements on all proposed datasets. The limitation of gradient search with a randomly selected point (set of weights and biases) has often resulted in inconsistent and inaccurate performance on predicting the self-healing repeatability of ECC as a complex nonlinear problem. EA is particularly prominent at efficiently searching large and complex solution spaces for global optima. With optimizing initial weights and biases of BPNN by EA to minimise the RMSE between the observed or target and predicted SFW of ECC after repeated self-healing, the performance of BPNN in terms of R^2 are improved from 0.950, 0.926 and 0.900 to 0.967, 0.960 and 0.939 in the structured list, and to 0.967, 0.853 and 0.948 in the

structured tree on training, validation and testing datasets, respectively. The errors in terms of MAE between the observed and predicted SFW of repeated self-healing of ECC is reduced from 6.323, 7.043 and 9.375 in BPNN to 5.553, 6.388 and 9.041 in the structured list, and to 5.510, 6.210 and 6.580 in the structured tree of EA optimized BPNN model; and from 9.304, 11.794 and 14.099 in BPNN to 7.565, 10.058 and 13.501 in the structured list, and to 7.512, 9.110 and 9.132 in the structured tree of EA-based BPNN model in terms of RMSE, on training, validation and testing dataset, respectively.

Compared the performance of prediction between the EA-based BPNN in structured list and tree, the computational results in Table 5.2 shows that EA-based BPNN mode in the structured tree outperforms in the structured list on training, validation and testing dataset regarding all three statistical measurements. In the training and validation dataset, the structured tree is slightly superior in MAE (5.510 and 6.210) and RMSE (7.512 and 9.110) than the structured list with MAE (5.553 and 6.388) and RMSE (7.565 and 10.058). And in the testing dataset, the structured tree is significantly superior in MAE (6.580) and RMSE (9.132) than the structured list (MAE 9.041 and RMSE 13.501).

The comparison of the target and predicted SFW as the self-healing repeatability of ECC by BPNN and EA-based BPNN models can be seen in Figures 5.6 to 5.23. These figures reveal that the empirical data for SFW of ECC generated from the laboratory experiment largely distribute between 0 to $150\mu m$, whereas a few samples have a value of SFW over $150\mu m$. This insufficient data may result in inadequate training of machine learning models and reduction of the prediction accuracy.

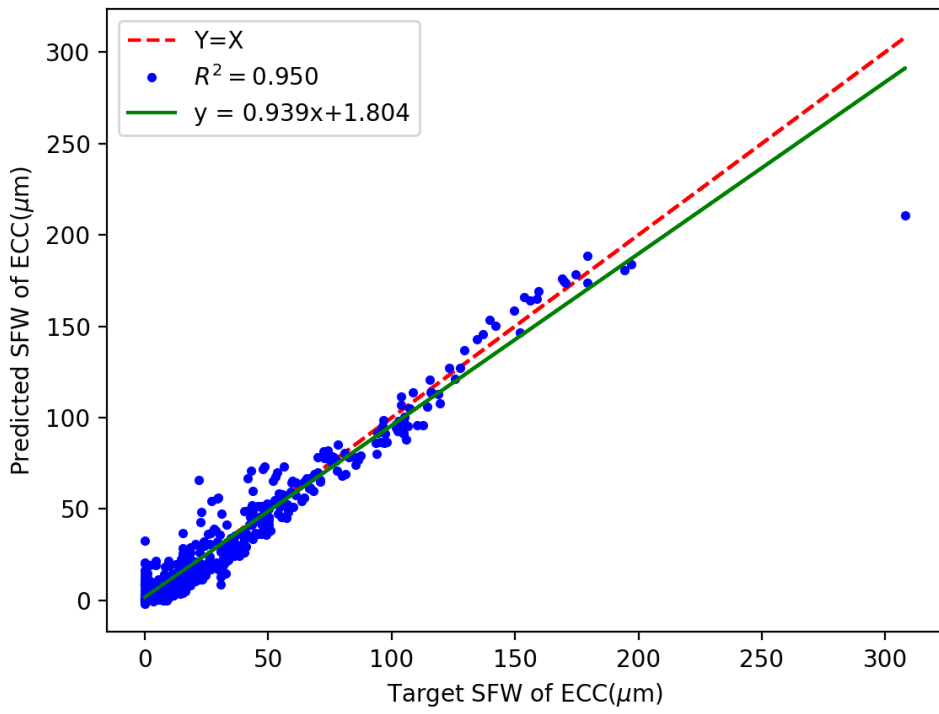


Figure 5.6: Comparison of target and predicted SFW of ECC on training dataset by BPNN

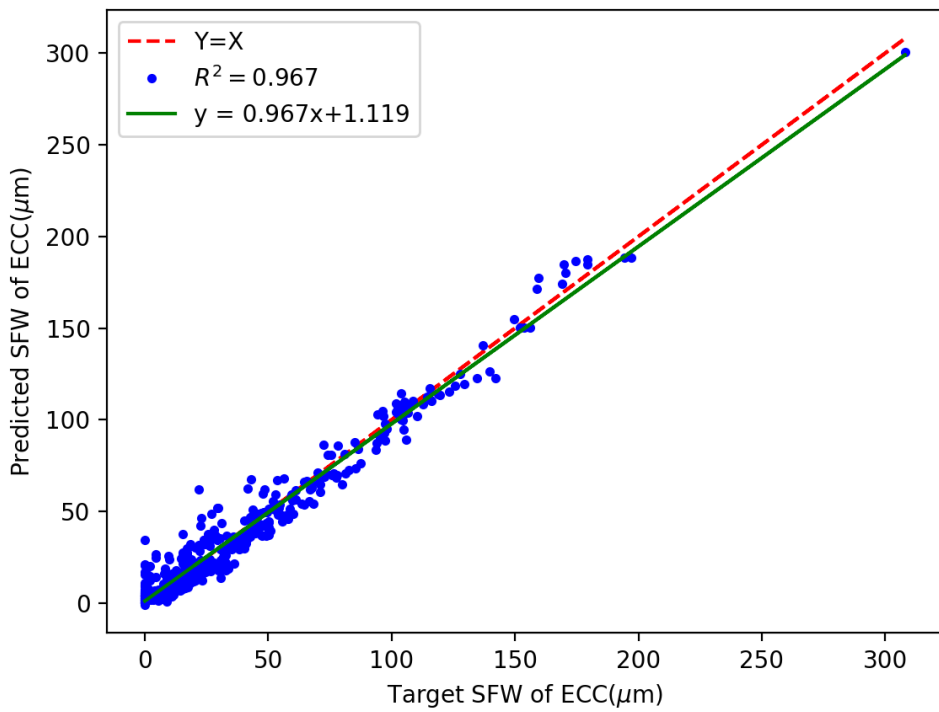


Figure 5.7: Comparison of target and predicted SFW of ECC on training dataset by EA-based BPNN in structured list

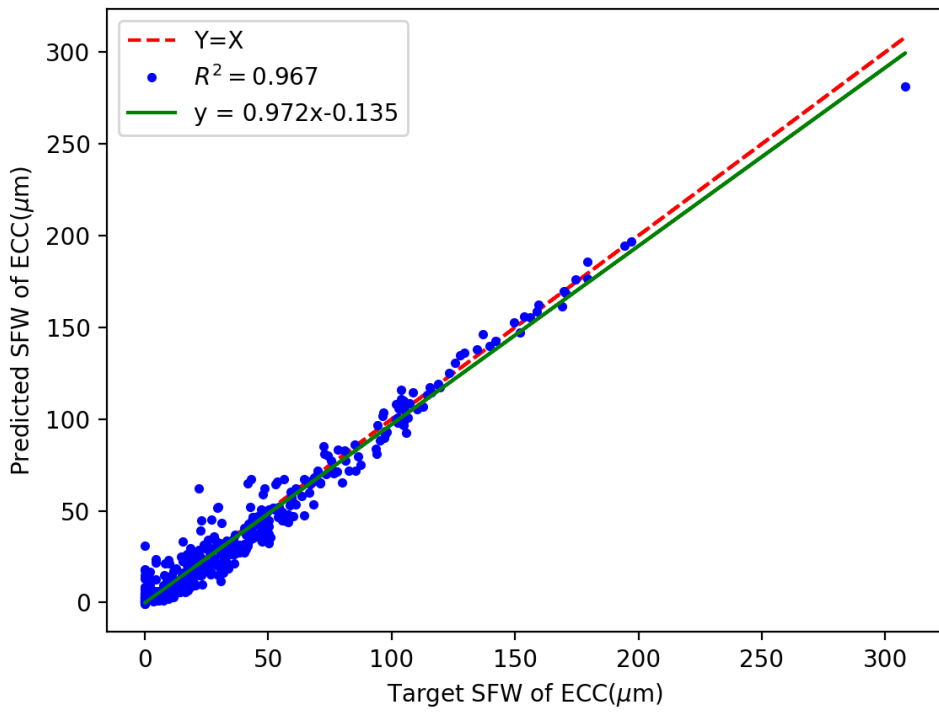


Figure 5.8: Comparison of target and predicted SFW of ECC on training dataset by EA-based BPNN in structured tree

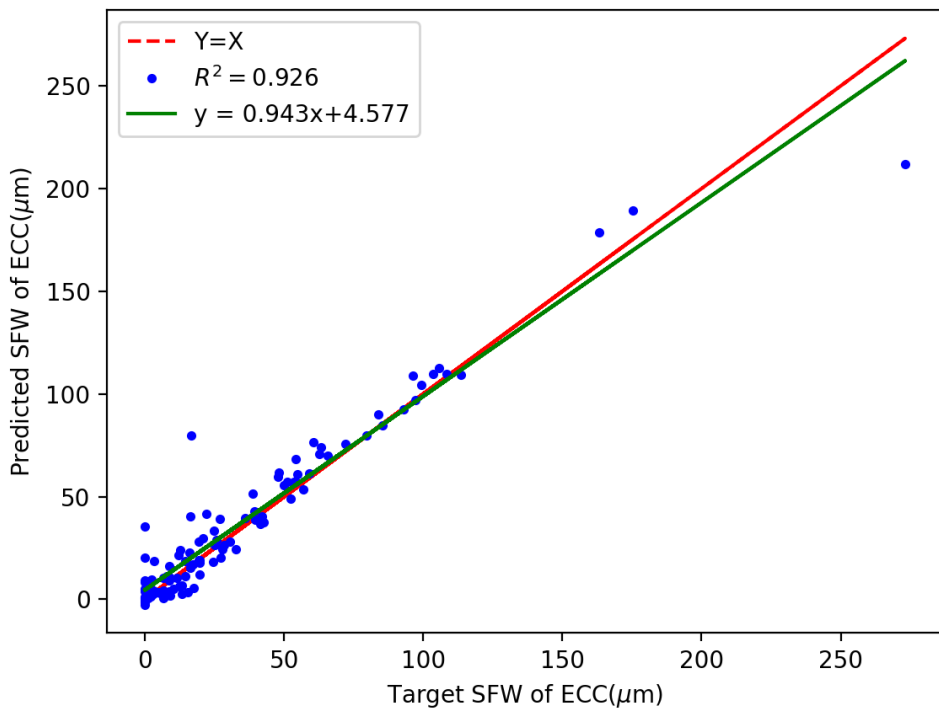


Figure 5.9: Comparison of target and predicted SFW of ECC on validation dataset by BPNN

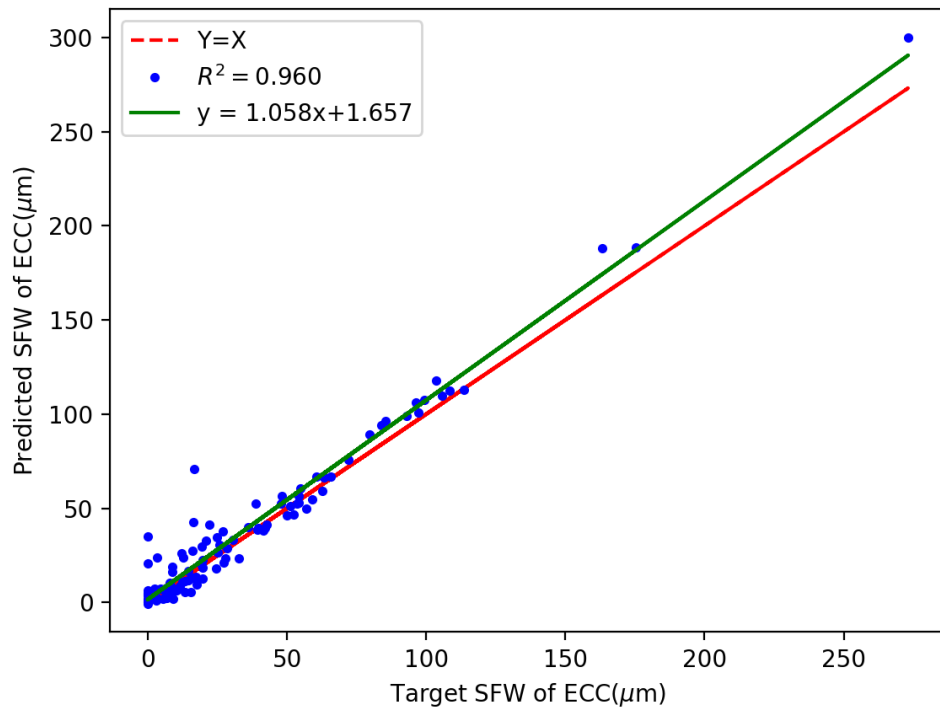


Figure 5.10: Comparison of target and predicted SFW of ECC on validation dataset by EA-based BPNN in structured list

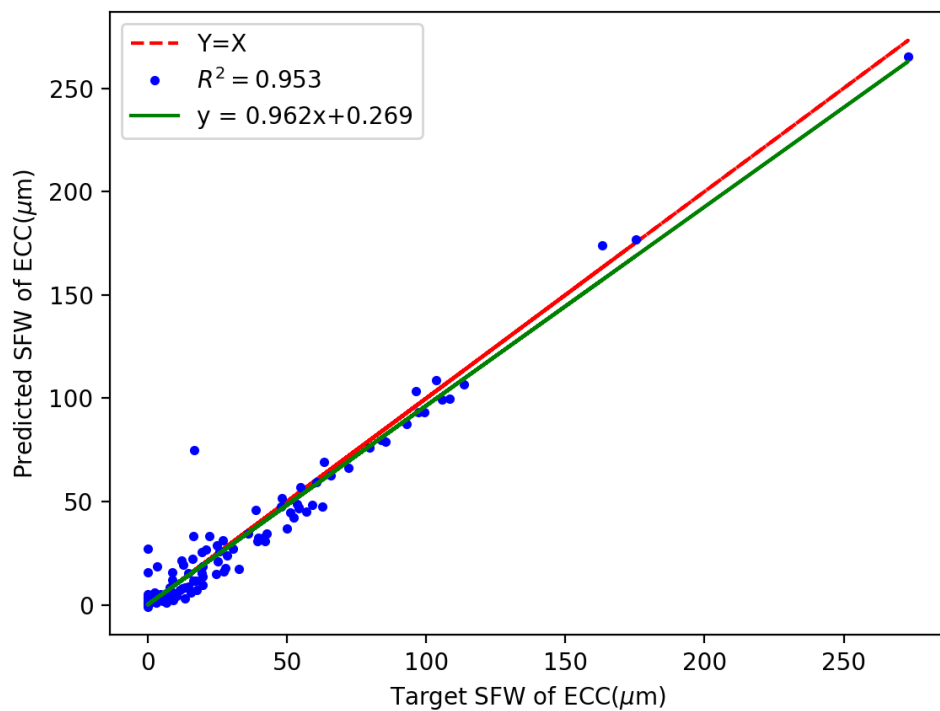


Figure 5.11: Comparison of target and predicted SFW of ECC on validation dataset by EA-based BPNN in structured tree

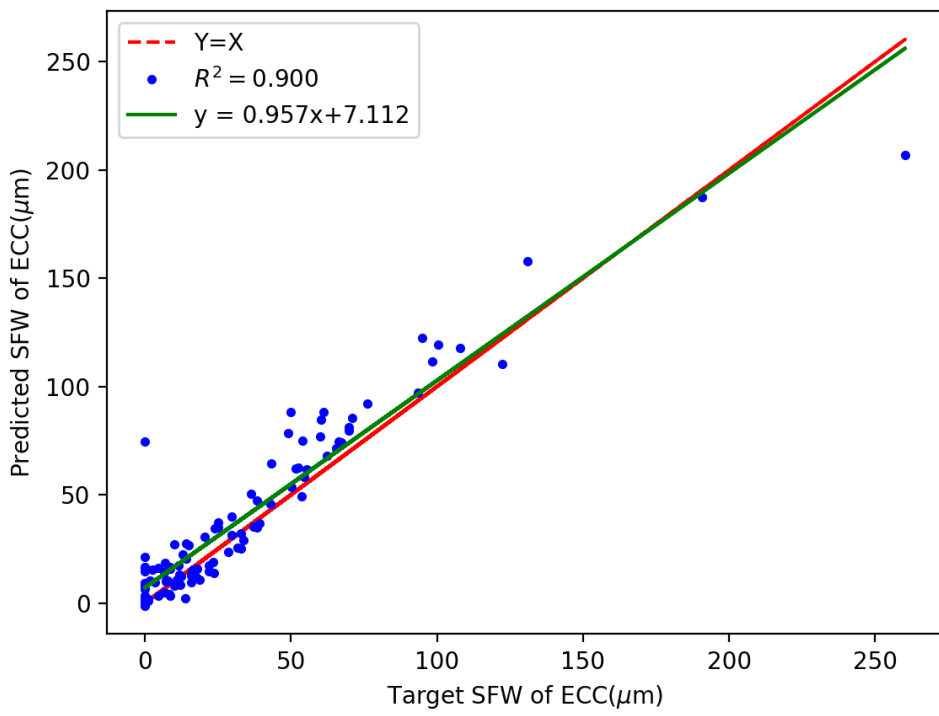


Figure 5.12: Comparison of target and predicted SFW of ECC on testing dataset by BPNN

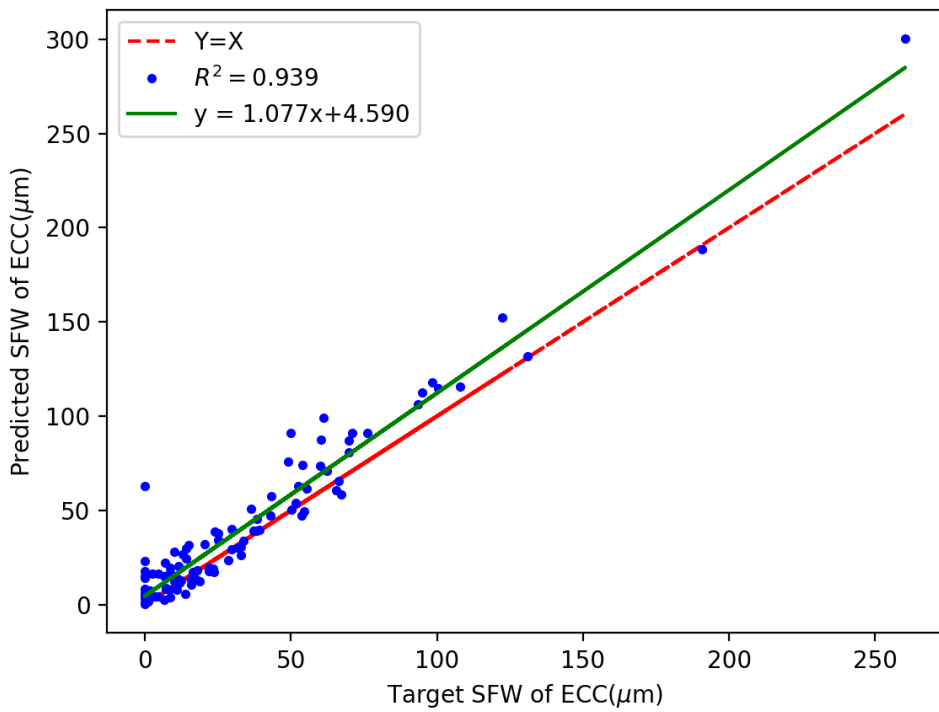


Figure 5.13: Comparison of target and predicted SFW of ECC on testing dataset by EA-based BPNN in structured list

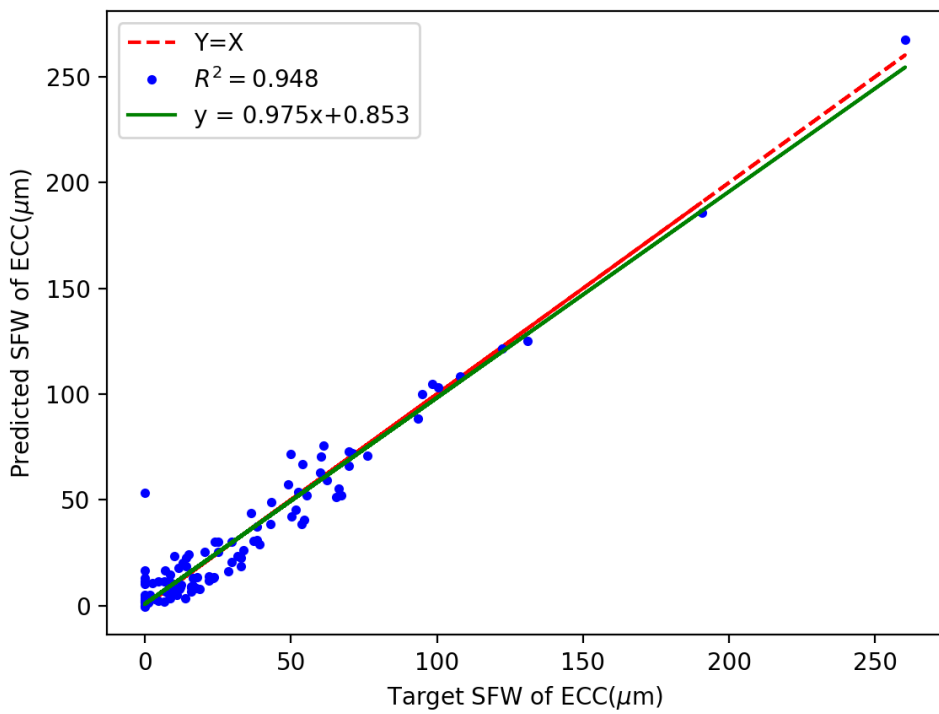


Figure 5.14: Comparison of target and predicted SFW of ECC on testing dataset by EA-based BPNN in structured tree

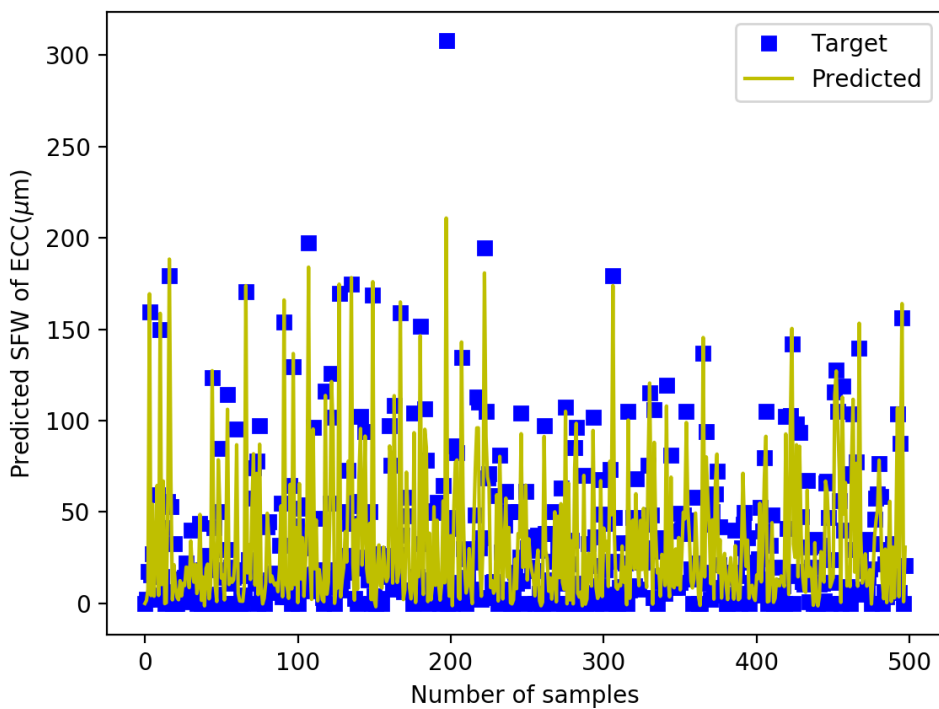


Figure 5.15: Target and predicted SFW of ECC on training dataset by BPNN

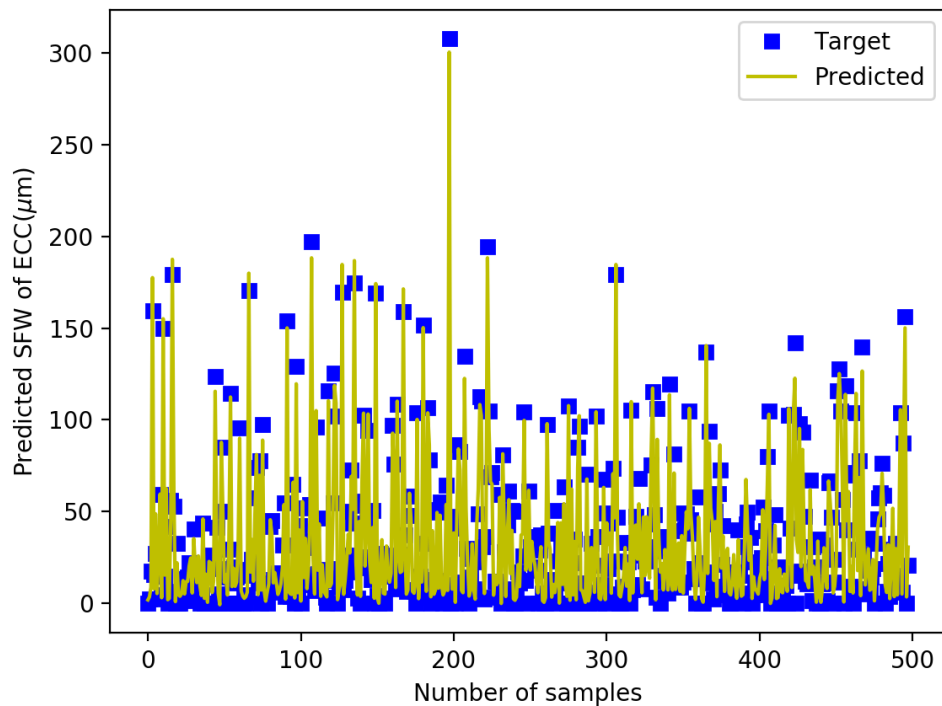


Figure 5.16: Target and predicted SFW of ECC on training dataset by EA-based BPNN in structured list

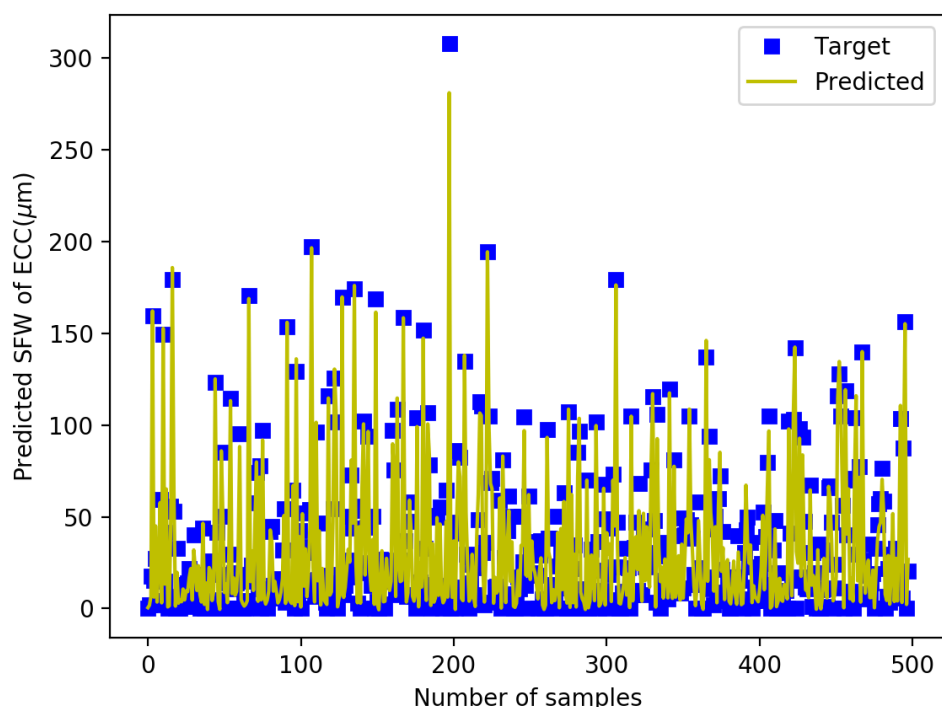


Figure 5.17: Target and predicted SFW of ECC on training dataset by EA-based BPNN in structured tree

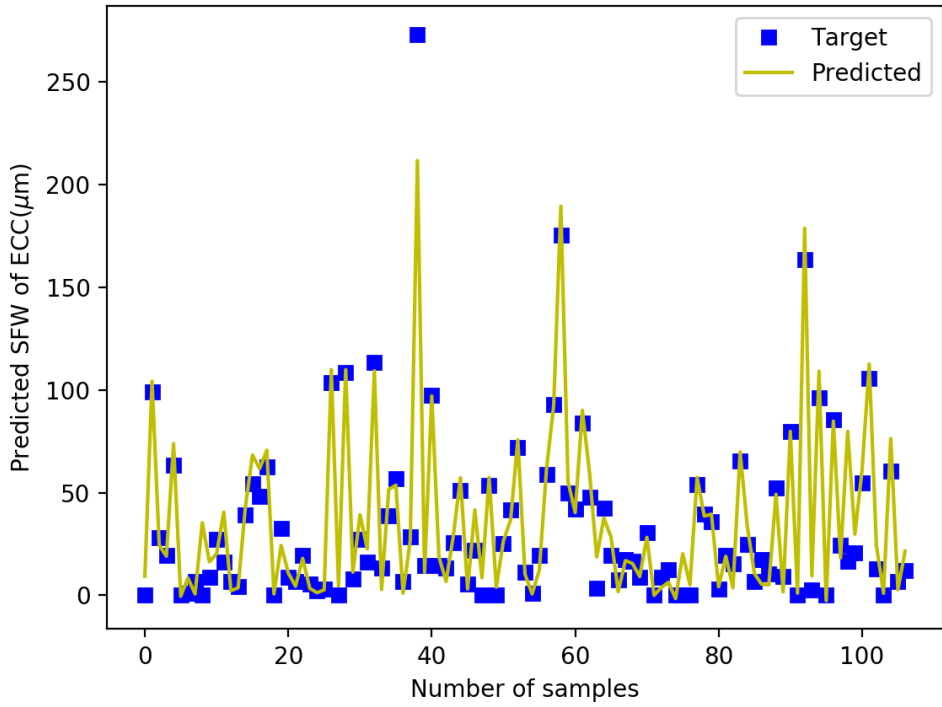


Figure 5.18: Target and predicted SFW of ECC on validation dataset by BPNN

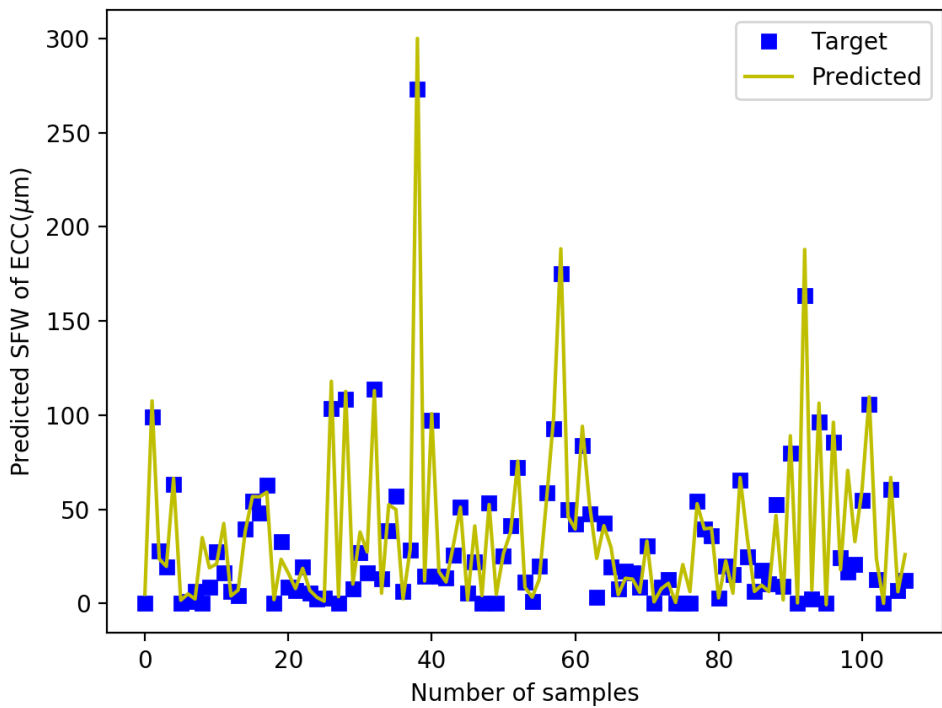


Figure 5.19: Target and predicted SFW of ECC on validation dataset by EA-based BPNN in structure list

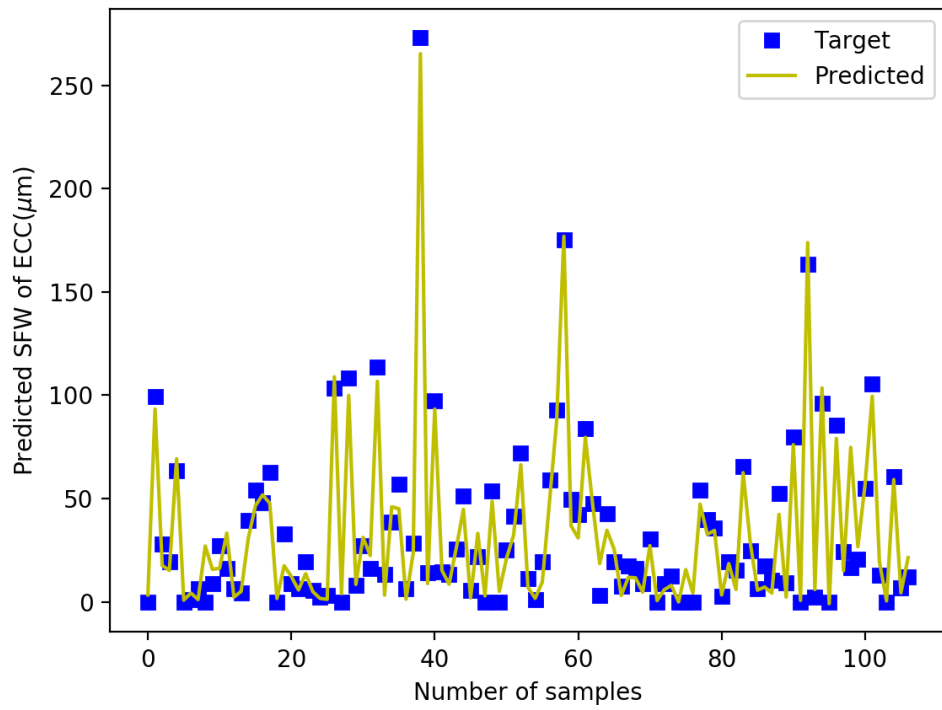


Figure 5.20: Target and predicted SFW of ECC on validation dataset by EA-based BPNN in structure tree

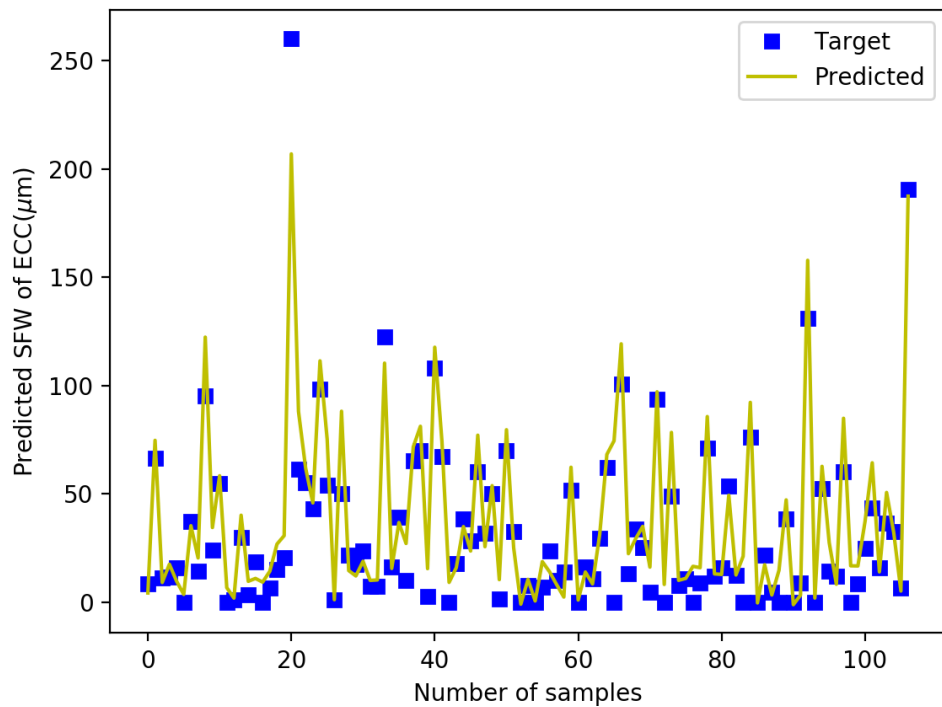


Figure 5.21: Target and predicted SFW of ECC on testing dataset by BPNN

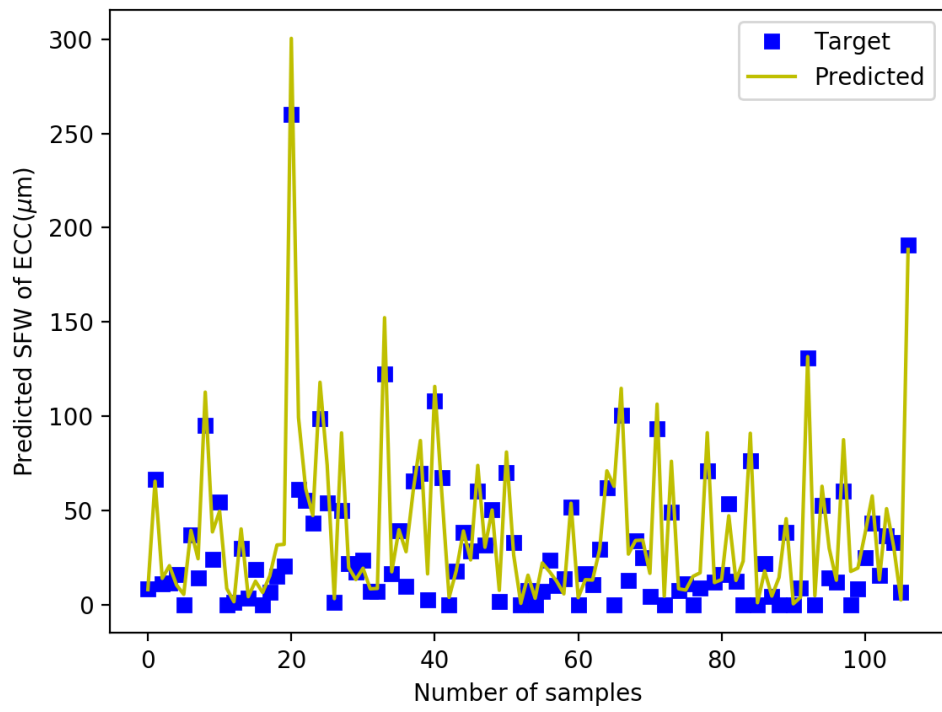


Figure 5.22: Target and predicted SFW of ECC on testing dataset by EA-based BPNN in structured list

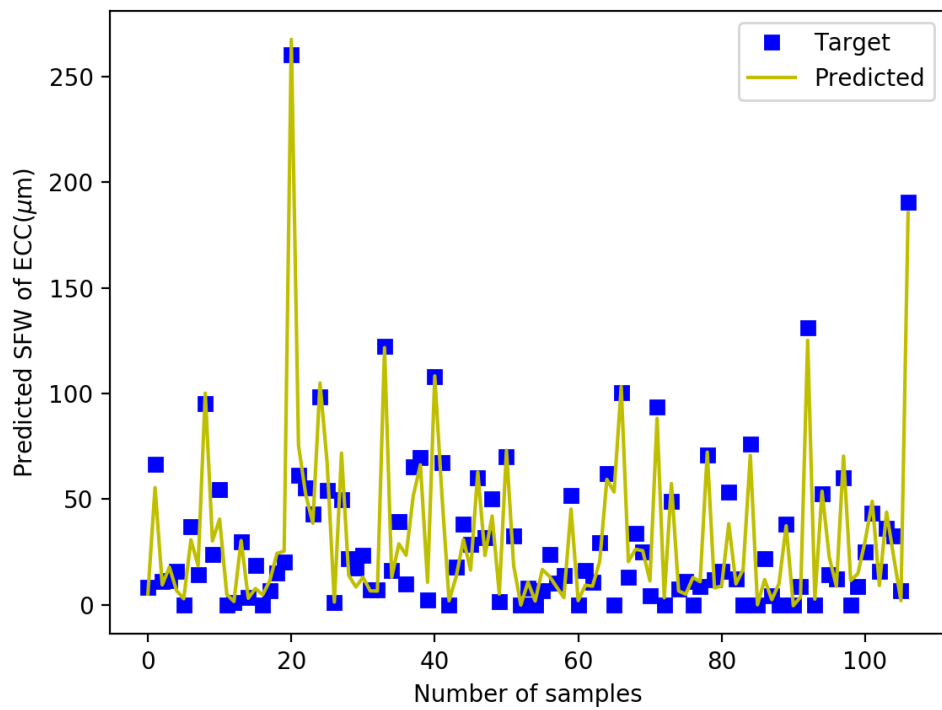


Figure 5.23: Target and predicted SFW of ECC on testing dataset by EA-based BPNN in structured tree

5.5 Summary

In this chapter, we investigated the structured and unstructured factors that affect the self-healing repeatability of ECC. The BPNN and EA-based BPNN in structured list and tree models were studied to predict the SFW value of ECC after repeated self-healing processes. Computational performance of the proposed models on training, validation and testing datasets were measured by MAE which is 6.323, 7.043 and 9.375 on BPNN, 5.553, 6.388 and 9.041 on EA-based BPNN in structured list, and 5.510, 6.210 and 6.580 on EA-based BPNN in structured tree; and measured by RMSE which is 9.304, 11.794 and 14.099 on BPNN, 7.565, 10.058 and 13.501 on EA-based BPNN in structured list, and 7.512, 9.110 and 9.132 on EA-based BPNN in structured tree; and measured by R^2 which is 0.950, 0.926 and 0.900 on BPNN, 0.967, 0.960 and 0.939 on EA-based BPNN in structured list, and 0.967, 0.953 and 0.948 on EA-based BPNN in structured tree, respectively. The following conclusion can be drawn from the works in this chapter:

- The results of analyses indicate that the BPNN model and EA-based BPNN in structured list and tree models are all capable of predicting self-healing repeatability of ECC with an adequate accuracy that is above 0.90 on training, validation and testing datasets in terms of R^2 .
- As a population based searching algorithm, EA evolves the search toward good solutions following the principle of natural selection and survival of the fittest. The application of EA optimizing BPNN with the initial weights and biases overcomes the inherent drawback of BPNN with slow convergence and getting trapped in local minima to achieve the global optimal solution. It, therefore, leads to a reliable and accurate model on the prediction of self-healing repeatability of ECC.
- The statistical analysis on three measurements has revealed that the EA-based BPNN model has expressed satisfactory results by improving the performance of BPNN on all three datasets. However, the process of optimization is complex and stochastic. There is no steady way to guarantee that the EA-based BPNN models will constantly perform valuable results.

- Compared with the traditional list structure of EA, the tree structure of EA is more space efficient, leading to quick convergence, and ensure genetic diversity and keep fit solutions, which guarantee quality children of the next generation. The computational results reveal the structured tree is superior in almost all three statistical measurements on all three datasets than the structured list.

Future investigation and experimentation will be considered to extend the training dataset to include the repeated self-healing process of ECC (more than two times tensile loading) and diverse influencing factors, such as components and W/CM rate. Moreover, the self-healing repeatability of ECC is significantly affected by water penetration and healing time. In this chapter, the Wet-Dry (W/D) cycles and healing time are constant in the experiment for all self-healing processes. Prediction of self-healing repeatability of ECC with various environmental factors (such as different submersion times in water) on time series analysis will be interesting and of great practical significance for the engineering industry.

Chapter 6

Conclusions and Prospects

6.1 Conclusions

The self-healing behaviour of Engineered Cementitious Composite (ECC) incorporating different minerals is investigated in this research, focusing on self-healing capability and repeatability. Three minerals, including Fly Ash (FA), Silica Fume (SF), and Hydrated Lime Powder (LP), are used to improve the self-healing capability of ECC in this study. The general conclusion of this research is outlined below:

6.1.1 Self-healing capability and repeatability of ECC

6.1.1.1 The effect of crack size on repeated self-healing

The crack width affects the efficiency of the crack recovery, and small cracks are easier to heal, as they required much less healing product and the healing product accumulated on both sides of the crack opening is easier to connect, so as to realize the healing of the crack. After applying multiple rounds of load, the mineral content used to heal the cracks at the crack openings gradually decreases, which also makes large cracks more difficult to heal. The crack widths within ECC must be controlled to below 100 μm , preferably below 50 μm , in order to engage noticeable repeated self-healing behaviour.

6.1.1.2 Crack width recovery

The types and proportions of minerals added to ECC have an effect on the healing ability of cracks.

- The addition of 5% SF to the ECC of FA70 can only slightly increase the healing rate of cracks smaller than $20\text{ }\mu\text{m}$, and it is only effective for the first round of self-healing. For cracks larger than $20\text{ }\mu\text{m}$, the crack healing rate in each healing cycle decreases with the increase of SF content.
- The addition of 5%, 10% or 15% of LP can significantly improve the self-healing ability compared to the reference sample, especially for cracks less than $100\text{ }\mu\text{m}$. The healing rates of FA65-LP5, FA60-LP10 and FA55-LP15 in the first healing cycle were all above 90%. The samples with the addition of 10% and 15% LP showed stronger repetitive self-healing capabilities. After three repeated loadings, the crack width recovery rate of FA60-LP10 and FA55-LP15 for cracks less than $20\text{ }\mu\text{m}$ can reach more than 76%; for cracks of about $20\text{-}50\text{ }\mu\text{m}$, it can reach more than 40%, and for cracks around $50\text{-}100\text{ }\mu\text{m}$ can reach more than 27%. FA60-LP10 and FA55-LP15 do not show a significant improvement in the healing rate of cracks greater than $100\text{ }\mu\text{m}$.
- When SF and LP are simultaneously added at the same time, compared with FA70, the addition of 5% SF and 10% LP significantly improves the healing rate of cracks less than $100\text{ }\mu\text{m}$, and the healing ability within $50\text{-}100\text{ }\mu\text{m}$ is significantly enhanced during the second self-healing process. However, the addition of 10% SF and 5% LP to FA70 does not show the effect of improving repeated crack recovery. The addition of 10% to 15% LP is beneficial for improving the repeatable self-healing ability of ECC samples. In order to maintain the ability of repeated crack width recovery, the relative content of SF should not exceed 5%.

6.1.1.3 Chloride ion permeability recovery

- The addition of a small amount (5%) of SF can significantly reduce the chloride ion permeability of ECC at 28 days, and higher SF content is effective at keeping the chloride ion permeability of ECC at a relatively low level under repetitive loading in accordance with ASTM C1202.
- During three observation periods, the change rate of ECC mixtures incorporating FA and SF show an upward trend at the end of every 10 cycles, as the

SF content increased, with the sample that only contains FA and LP showing an opposite trend. The presence of SF in the ECC mixtures can improve the self-healing effect after the first loading is applied, and the 10% SF shows two times significant self-healing ability under three times repetitive loading; however, 15% SF is not conducive to repeated self-healing under multiple loading. The high silica fume content may result in the consumption of more calcium ions in the matrix during the early hydration reaction, thus affecting the later self-healing effect.

- For the ECC mixture with 5%, 10%, and 15% LP, all the three mixtures show notable self-healing capacity at the end of the 10th cycle. FA60-LP10 shows significant recovery in Rapid Chloride Permeability Test (RCPT) during the second and third rounds of self-healing.
- When SF and LP were simultaneously added to ECC mixtures, the RCPT results of FA55-SF10-LP5 and FA55-SF5-LP10 were all below the previous low level, and after preloading and self-healing three times, in accordance with ASTM C1202. The addition of SF and LP in ECC (FA55-SF10-LP5 and FA55-SF5-LP10) show better values recovery in RCPT than ECC mixtures (FA60-SF10 and FA60-LP10) only containing SF or LP in all three rounds of the self-healing process. These findings show that even under repetitive loading conditions, the addition of SF and LP to ECC according to a certain ratio can significantly improve the ability of repeated self-healing of chloride ion permeability.

6.1.1.4 Splitting tensile strength recovery

Different mineral ratios in ECC have an effect on the recovery rate of splitting tensile strength.

(1) Effect of W/D environment exposure time on recovery of splitting tensile strength

- When the load is applied only once, the addition of 5% or 10% of SF to FA70 can increase the splitting tensile strength recovery rate of ECC samples within 30 Wet-Dry (W/D) cycles. Increasing 15% of SF to FA70 is beneficial for short

term mechanical recovery but is not conducive to the recovery of mechanical properties in the long term.

- The addition of 10% LP is most conducive to improve the recovery of mechanical properties, especially for samples undergoing 60 W/D cycles, and the strength recovery rate of FA60-LP10 reached 105.87%. This indicates that a longer healing time is more beneficial for the recovery of tensile strength in the splitting tensile test.
- When SF and LP are added at the same time, FA55-SF5-LP10 shows a higher recovery rate, 105.14% after 30 W/D cycles, and 110.96% after 60 W/D cycles. FA55-SF10-LP also shows a higher effect on the splitting tensile strength recovery rate than adding a single mineral. It demonstrates that the addition of various minerals in a certain proportion can improve the self-healing ability of ECC.

(2) Repeatability of splitting tensile strength recovery after multiple loading cycles

- In the case of repeated load application and self-healing, for the combination of FA and SF, FA55-SF15 show the highest healing efficiency after 10 W/D cycles. For the combination of FA and LP, the addition of 10% LP to ECC shows the highest splitting tensile strength recovery rate after the first load, reaching 85.17%, and after three loads, the recovery rate can still reach 66.43%.
- ECC with all three minerals (FA, SF, LP) added shows a higher splitting tensile strength recovery rate than ECC with only two minerals added in all three healing rounds. After three rounds of self-healing, the splitting strength recovery rate of FA55-SF5-LP10 is significantly higher than other mixes, reaching 81.56%. It can be inferred that adding minerals (FA, SF, LP) to ECC in a certain proportion can significantly improve its repeatable self-healing ability.

6.1.2 Self-healing products after re-healing

After three rounds of loading, samples are examined through Scanning Electron Microscope (SEM) morphological analysis, Energy Dispersive Spectroscopy (EDS)

chemical composition analysis, and X-ray Diffraction Analysis (XRD) analysis. On the basis of results obtained from those tests, the following conclusions can be drawn:

- A mixture of CaCO_3 and Calcium Silicate Hydrates (C-S-H) are found to be the main self-healing products, however, the dominant healing product depends on the type and the proportion of minerals in ECC.
- C-S-H and CaCO_3 are found to be the main healing products of the FA70 and FA55-SF15 mixtures, whereas CaCO_3 is the dominant healing product detected in FA55-LP15.
- For self-healing products under the synergistic effect of multiple minerals, CaCO_3 was found to be the main healing products of FA55-SF5-LP10. For FA55-SF10-LP5, the healing products have a characteristic mixture between C-S-H and CaCO_3 , and ettringite is also present in a small amount.
- The results of XRD analysis also verifies that, for all mixtures, CaCO_3 is one of the main self-healing products.
- The production of self-healing products is affected by the supply of calcium ions. The Ca/Si ratio of FA55-LP15 and FA55-SF5-LP10 healing products is significantly higher than other mixtures. More CaCO_3 precipitate is formed both at the opening of the crack and in the vicinity of cracks.

6.1.3 Prediction of the self-healing capability of ECC

By comparing individual and ensemble methods of Machine Learning (ML) models in terms of their performance in predicting the self-healing capability of ECC, it is found that all models including three individual methods (Back-propagation Neural Network (BPNN), Support Vector Regression (SVR), and Classification and Regression Tree (CRAT)) and three Ensemble Methods (EM) (bagging, AdaBoost, and stacking) are qualified for the prediction of self-healing capability of ECC with acceptable accuracy. These models improve the performance of Linear Regression (LR) with reducing error values and decreasing prediction accuracy. Moreover, All EM models used individual methods as base learners, which achieve good outcomes

by enhancing the performance of the individual models in terms of overall performance measures. The stack_LR model is superior to all other individual or ensemble models on the basis of all the performance measures.

6.1.4 Predict the repeatability of self-healing

The comprehensive comparative analysis has demonstrated that BPNN has the highest accuracy among all individual models in terms of predicting the self-healing capability of ECC. By applying Evolutionary Algorithm (EA) in tree and list structure on optimization of the initial weights and biases of BPNN, satisfactory results are achieved by improving the prediction performance of BPNN over all statistical measurements. The proposed structured tree EA-based BPNN model is more space efficient, leading to quick convergence, and ensure genetic diversity and keep fit solutions, which guarantee quality children of the next generation. The computational results demonstrate that the structured tree EA-based BPNN model is superior in all statistical measurements on all datasets than other models on prediction of self-healing repeatability of ECC.

6.2 Prospects

This thesis mainly focuses on the fundamental aspects of ECC self-healing ability and repeatability. Further research on improving the self-healing ability of this type of ECC, and the application of self-healing, is still necessary:

- In this thesis, only the repeatability of self-healing in ECC with a Water to Cementitious Materials Ratio (W/CM) of 0.29 was investigated. Since W/CM has an impact on the strength and durability of ECC, it is interesting to get quantitative information about the effect of W/CM ratio, and type of cement and FA on self-healing.
- In this thesis, the ECC samples have undergone different times of W/D cycles, and the water used in the experiment does not fully represent the situation encountered in engineering practice. In reality, rainwater and groundwater are affected by different environments and usually contain a variety of ions.

Therefore, it is particularly necessary to analyse the influence of different types of water on self-healing in engineering practice.

- The engineering application cost of ECC containing various minerals is one of the most important considerations in engineering practice. The economic feasibility of ECC combined with self-healing efficiency, mineral content and price should be given attention in further research.
- The datasets used for training, validation and testing of ML models and the input features that have impacts on the output of prediction are limited. In particular, the healing time has a significant influence on the self-healing capability and repeatability of ECC. Therefore, developing prediction models for self-healing capability and repeatability of ECC with various features based on time series will be attractive and have great practical significance for the engineering industry.
- After a wide range of influencing factors (features) are considered, including internal factors such as different materials and mix composition and external environmental factors such as W/D cycles and healing time, future investigations are necessary to validate the relativity and sensitivity of features. Feature selection and sensitivity of features method in this field could produce interesting findings that account more for achieving better accuracy for machine learning models. The feature selection method analyzes the relationship between each input variable and the self-healing ability of ECC to select those factors that have a strong influence on self-healing ability. The sensitivity analysis will further evaluate the influence level of these selected input variables on the self-healing ability of ECC.

Appendix A

Programming of comparative analysis

```
1 ##########
2 ##### import python packages
3 #########
4 from sklearn.linear_model import LinearRegression ## linear
    regression
5 from sklearn.svm import SVR ## SVR
6 from sklearn.neural_network import MLPRegressor ## BPNN
7 from sklearn.tree import DecisionTreeRegressor ## CRAT
8 from sklearn.ensemble import AdaBoostRegressor ## boosting
9 from sklearn.ensemble import BaggingRegressor ### bagging
10 from mlxtend.regressor import StackingCVRegressor ## stacking
11 from mlxtend.regressor import StackingRegressor
12 from sklearn.metrics import mean_squared_error
13 from sklearn.metrics import mean_absolute_error
14 from sklearn.metrics import r2_score
15 from sklearn.model_selection import ShuffleSplit
16 from sklearn.model_selection import cross_val_score
17 from sklearn import preprocessing
18 from math import sqrt
19 import matplotlib.pyplot as plt
20 import numpy as np
21 import pandas as pd
22 import statistics as stat
23 import random
24
25 #####
26 ##### import dataset
27 #####
28 scaler = preprocessing.MinMaxScaler()
29 data = np.loadtxt('crack_No.txt')
30 X_data = data[:, :-1]
31 y_target = data[:, -1]
32
33 #####
34 ##### Build predict models #####
35 #####
36 linear = LinearRegression()
37
38 svr = SVR(kernel='rbf', C=1e4, gamma=0.001, epsilon=0.1)
39
```

```

40 bpnn = MLPRegressor(solver='lbfgs', activation='logistic',
41                      hidden_layer_sizes=20, max_iter=800) #BPNN
42
43 crat = DecisionTreeRegressor(max_depth=5)
44 ##### Ensemble adaboost #####
45 ada_linear = AdaBoostRegressor(base_estimator = LinearRegression(),
46                                n_estimators=100, learning_rate=0.1)
47
48 ada_svr = AdaBoostRegressor(base_estimator = SVR(kernel='rbf', C=1
49                             e4, gamma=0.001, epsilon=0.1), n_estimators=100, learning_rate
50                             =0.1)
51
52 ada_bpnn = AdaBoostRegressor(base_estimator = MLPRegressor(solver='
53                                lbfgs', hidden_layer_sizes=20, max_iter=800), n_estimators = 100,
54                                learning_rate=0.1)
55
56 ada_crat = AdaBoostRegressor(base_estimator = DecisionTreeRegressor(
57                             max_depth=5), n_estimators=100, learning_rate=0.1)
58 ##### bagging #####
59 bag_linear = BaggingRegressor(base_estimator = LinearRegression(),
60                                n_estimators= 100, random_state = 50 )
61
62 bag_svr = BaggingRegressor(base_estimator = SVR(kernel='rbf', C= 1e4
63                             , gamma=0.001, epsilon=0.1), n_estimators=100, random_state = 50
64                             )
65
66 bag_bpnn = BaggingRegressor(base_estimator = MLPRegressor(solver='
67                                lbfgs', hidden_layer_sizes=20, max_iter=800), n_estimators = 100,
68                                random_state = 50 )
69
70 bag_crat = BaggingRegressor(base_estimator = DecisionTreeRegressor(
71                             max_depth=5), n_estimators=100, random_state = 50 )
72 ##### stacking #####
73 stack_linear = StackingCVRegressor(regressors=(svr, bpnn, crat),
74 meta_regressor=linear)
75
76
77
78 ##########
79 cv = ShuffleSplit(n_splits=10, test_size=0.1, random_state = 27)
80
81 methodDict = {
82     'LinearRegression': linear,
83     'SVR': svr,
84     'BPNN': bpnn,
85     'CRAT': crat,
86     'Ada_Linear': ada_linear,
87     'Ada_SVR': ada_svr,
88     'Ada_BPNN': ada_bpnn,
89     'Ada_CRAT': ada_crat,
90     'Bag_Linear': bag_linear,
91     'Bag_SVR': bag_svr,
92     'Bag_BPNN': bag_bpnn,
93     'Bag_CRAT': bag_crat,
94     'Stack_Linear': stack_linear
95 }
96
97 mae_AC = []
98 rmse_AC = []

```

```

85 r2_AC = []
86
87 ##### prediction results for all methods
88 #####
89
90 statcs = []
91 for train_index, test_index in cv.split(X_data):
92     X_train, y_train = X_data[train_index], y_target[train_index]
93     X_test, y_test = X_data[test_index], y_target[test_index]
94     for names, methods in methodDict.items():
95         print(names)
96         retr = methods
97         retr.fit(X_train, y_train)
98         prediction = retr.predict(X_test)
99         prediction = prediction.clip(0)
100        MAE = mean_absolute_error(y_test, prediction)
101        RMSE = sqrt(mean_squared_error(y_test, prediction))
102        score_R2 = r2_score(y_test, prediction)
103        print(MAE, RMSE, score_R2)
104        statcs.append([names, MAE, RMSE, score_R2])
105 df = pd.DataFrame(statcs, columns = ['methods', 'MAE', 'RMSE', 'R2'])
106
107 #####
108 PivotTable = pd.pivot_table(df, index ='methods', values = ['MAE', ,
109                             'RMSE', 'R2'], aggfunc= np.mean)
110 print(PivotTable)
111 PivotTable.to_csv('pivotTable.csv')

```

Appendix B

Programming of BPNN optimized with EA in structured tree and list

```
1 #####  
2 ##### import python packages  
3 #####  
4 from math import sqrt  
5 from math import exp  
6 from sklearn.model_selection import train_test_split  
7 import numpy as np  
8 import pandas as pd  
9 import random  
10 import copy  
11 from anytree import Node, RenderTree, LevelOrderIter  
12  
13  
14 # Dataset split  
15 def preprocess(dataset):  
16     minmax = [[min(dataset[column]), max(dataset[column])] for column  
17             in dataset]  
18     train, TEST = train_test_split(dataset, test_size=0.3,  
19                                     random_state=42)  
20     valid, test = train_test_split(TEST, test_size=0.5, random_state  
21                                     =42)  
22     train = dataset_scalar(train,minmax)  
23     test = dataset_scalar(test,minmax)  
24     validation = dataset_scalar(valid,minmax)  
25     return train, validation, test  
26  
27 # Data normalization  
28 def dataset_scalar(dataset,minmax):  
29     for index, row in dataset.iterrows():  
30         for i in range(len(row) - 1):  
31             row[i] = (row[i] - minmax[i][0]) / (minmax[i][1] - minmax[i  
32             ][0])  
33     return dataset  
34  
35 # Evolutionary Algorithm with List structure  
36 def EAList(train,validation,n_inputs, n_hidden,n_outputs,l_rate,  
37             n_epoch):  
38     pop_size = 40 # Population size 40  
39     generation = 50
```

```

36 population = []
37 fitness = []
38 r = 1
39 iter_count = 0
40 pc = 0.8 # Probability of crossover
41 pm = 0.1 # Probability of mutation
42
43 # Generate initial individuals
44 for i in range(pop_size):
45     chromosome = initialize_population(n_inputs,n_hidden,n_outputs)
46     network = reset_network(chromosome)
47     fitness_value = get_fitness(network,train,validation,l_rate,
48     n_epoch)
49     if fitness_value <= 3:
50         return chromosome
51     else:
52         population.append(chromosome)
53         fitness.append(fitness_value)
54 # save the best individual
55 best_fitness = min(fitness)
56 best_individual = population[fitness.index(best_fitness)]
57 tmp_best = best_fitness
58 while r <= generation or iter_count < 10:
59     print(f'r = {r}')
60     print(f'best, {best_fitness}')
61     for recombination in range(int(pc*pop_size)):
62         parents_index = RWS(fitness)
63         parents = [population[idx] for idx in parents_index]
64         offspring = SP_crossover(parents)
65         offspring = SP_mutation(offspring,pm)
66         network = reset_network(offspring)
67         fitness_value = get_fitness(network,train,validation,l_rate,
68         n_epoch)
69         if fitness_value <= 3:
70             return offspring
71         else:
72             worse_case = max(fitness)
73             if fitness_value < worse_case:
74                 idx = fitness.index(worse_case)
75                 fitness[idx] = fitness_value
76                 population[idx] = offspring
77 # update the best individual
78 best_case = min(fitness)
79 if best_case < best_fitness:
80     idx = fitness.index(best_case)
81     best_individual = population[idx]
82 if tmp_best == best_fitness:
83     iter_count += 1
84 else:
85     tmp_best = best_fitness
86     iter_count = 0
87     r += 1
88 return best_individual
89
90 # Evolutionary Algorithm with Tree structure
91 def EATree(train,validation,n_inputs, n_hidden,n_outputs,l_rate,
92 n_epoch):
93     pop_size = 40 # Population size 40

```

```

91     generation = 50
92     population = []
93     fitness = []
94     r = 1
95     iter_count = 0
96     pc = 0.8 # Probability of crossover
97     pm = 0.1 # Probability of mutation
98     # Generate initial individuals
99     for i in range(pop_size):
100         chromosome = initialize_population(n_inputs,n_hidden,n_outputs)
101         network = reset_network(chromosome)
102         fitness_value = get_fitness(network,train,validation,l_rate,
103         n_epoch)
104         if fitness_value <= 3:
105             return chromosome
106         else:
107             population.append(chromosome)
108             fitness.append(fitness_value)
109             zipped = zip(fitness,population)
110             fitness, population = zip(*sorted(zipped, key = lambda t: t[0]))
111             # create Tree structure
112             # root -> branch -> node -> leaf
113             root = Node("Root", fitness = fitness[0] , indv = population
114             [0])
115             brancha = Node("BranchA", fitness = fitness[1] , indv = population
116             [1], parent = root)
117             branchb = Node("BranchB", fitness = fitness[2] , indv = population
118             [2], parent = root)
119             branchc = Node("BranchC", fitness = fitness[3] , indv = population
120             [3], parent = root)
121             Nodea = Node("Nodea", fitness = fitness[4] , indv = population
122             [4], parent = brancha,
123             children = [ Node("Leafa", fitness = fitness[13] , indv =
124             population[13]),
125             Node("Leafb", fitness = fitness[14] , indv = population[14]),
126             Node("Leafc", fitness = fitness[15] , indv = population[15]) ])
127             Nodeb = Node("Nodeb", fitness = fitness[5] , indv = population
128             [5], parent = brancha,
129             children = [ Node("Leafa", fitness = fitness[16] , indv =
130             population[16]),
131             Node("Leafb", fitness = fitness[17] , indv = population[17]),
132             Node("Leafc", fitness = fitness[18] , indv = population[18]) ])
133             Nodec = Node("Nodec", fitness = fitness[6] , indv = population
134             [6], parent = brancha,
135             children = [ Node("Leafa", fitness = fitness[19] , indv =
136             population[19]),
137             Node("Leafb", fitness = fitness[20] , indv = population[20]),
138             Node("Leafc", fitness = fitness[21] , indv = population[21]) ])
139             Nodeee = Node("Nodeee", fitness = fitness[7] , indv = population
140             [7], parent = branchb,
141             children = [ Node("Leafa", fitness = fitness[22] , indv =
142             population[22]),
143             Node("Leafb", fitness = fitness[23] , indv = population[23]),
144             Node("Leafc", fitness = fitness[24] , indv = population[24]) ])
145             Nodeef = Node("Nodef", fitness = fitness[8] , indv = population
146             [8], parent = branchb,
147             children = [ Node("Leafa", fitness = fitness[25] , indv =

```

```

    population[25]),
135 Node("Leafb", fitness = fitness[26], indivs = population[26]),
136 Node("Leafc", fitness = fitness[27], indivs = population[27]) ])
137 Nodeg = Node("Nodeg", fitness = fitness[9], indivs = population
138     [9], parent = branchb,
139     children = [ Node("Leafa", fitness = fitness[28], indivs =
140         population[28]),
141         Node("Leafb", fitness = fitness[29], indivs = population[29]),
142         Node("Leafc", fitness = fitness[30], indivs = population[30]) ])
143
144 Nodeh = Node("Nodea", fitness = fitness[10], indivs = population
145     [4], parent = branchc,
146     children = [ Node("Leafa", fitness = fitness[31], indivs =
147         population[31]),
148         Node("Leafb", fitness = fitness[32], indivs = population[32]),
149         Node("Leafc", fitness = fitness[33], indivs = population[33]) ])
150 Nodei = Node("Nodeb", fitness = fitness[11], indivs = population
151     [5], parent = branchc,
152     children = [ Node("Leafa", fitness = fitness[34], indivs =
153         population[34]),
154         Node("Leafb", fitness = fitness[35], indivs = population[35]),
155         Node("Leafc", fitness = fitness[36], indivs = population[36]) ])
156 Nodej = Node("Nodec", fitness = fitness[12], indivs = population
157     [6], parent = branchc,
158     children = [ Node("Leafa", fitness = fitness[37], indivs =
159         population[37]),
160         Node("Leafb", fitness = fitness[38], indivs = population[38]),
161         Node("Leafc", fitness = fitness[39], indivs = population[39]) ])
162
163 best_fitness = root.fitness
164
165 while r <= generation:
166     print(r)
167     for node in reversed(root.descendants):
168         offspring = SP_crossover([node.indivs, node.parent.indivs])
169         offspring = SP_mutation(offspring, pm)
170         network = reset_network(offspring)
171         fitness_value = get_fitness(network, train, validation, l_rate,
172             n_epoch)
173         if fitness_value <= 3:
174             return offspring
175         else:
176             if fitness_value < node.fitness:
177                 node.fitness = fitness_value
178                 node.population = offspring
179             for node in reversed(root.descendants):
180                 if node.fitness < node.parent.fitness:
181                     node.fitness, node.parent.fitness = node.parent.fitness,
182                     node.fitness
183                     node.indivs, node.parent.indivs = node.parent.indivs, node.
184                     indivs
185                 if best_fitness == root.fitness:
186                     iter_count += 1
187                 else:
188                     best_fitness = root.fitness
189                     iter_count = 0
190                     r += 1
191     return root.indivs

```

```

181
182 # Roulette wheel selection
183 def RWS(fitness):
184     fitness_dprivate = [1/x for x in fitness]
185     fitness_probability = np.cumsum(fitness_dprivate)/np.sum(
186         fitness_dprivate) # cumulative probability
187     parents_index= []
188     for i in range(2):
189         flag = np.random.random()
190         k = 0
191         while k < len(fitness):
192             if flag < fitness_probability[k]:
193                 parents_index.append(k)
194                 break
195             else:
196                 k += 1
197     return parents_index
198
199 # Single point crossover in items
200 def SP_crossover(parents):
201     length = len(parents[0])
202     offspring = []
203     i = np.random.randint(1,length)
204     if np.random.random() < 1:
205         offspring[:i] = parents[0][:i]
206         offspring[i:] = parents[1][i:]
207     else:
208         offspring[:i] = parents[1][:i]
209         offspring[i:] = parents[0][i:]
210     return offspring
211
212 # single point mutation
213 def SP_mutation(offspring,pm):
214     mutation_number = int(pm * len(offspring))
215     for i in range(mutation_number):
216         index = random.randint(0,len(offspring)-1)
217         element = random.randint(0,len(offspring[index])-1)
218         weight = random.random()
219         offspring[index][element] += weight
220     return offspring
221
222 # Fitness of chromosome
223 def get_fitness(network,train,validation,l_rate,n_epoch):
224     network_initial = copy.deepcopy(network)
225     accuracy = train_network(network_initial,train,validation,l_rate,
226                               n_epoch)
227     return accuracy
228
229 # Get a chromosome in population
230 def initialize_population(n_inputs, n_hidden, n_outputs):
231     chromosome = list()
232     for i in range(n_hidden):
233         chromosome.append([random.random() for i in range(n_inputs + 1)])
234     for j in range(n_outputs):
235         chromosome.append([random.random() for i in range(n_hidden + 1)])
236     return chromosome

```

```

235
236 def reset_network(chromosome):
237     network = list()
238     hidden_layer = [dict.fromkeys(['weights'], value) for value in
239                     chromosome[:-1]]
240     network.append(hidden_layer)
241     output_layer = [dict.fromkeys(['weights'], chromosome[-1])]
242     network.append(output_layer)
243     return network
244
245 # Initialize a network
246 def initialize_network(n_inputs, n_hidden, n_outputs):
247     network = list()
248     hidden_layer = [{ 'weights' : [random.random() for i in range(
249                     n_inputs + 1)]} for i in range(n_hidden)]
250     network.append(hidden_layer)
251     output_layer = [{ 'weights' : [random.random() for i in range(
252                     n_hidden + 1)]} for i in range(n_outputs)]
253     network.append(output_layer)
254     return network
255
256 # Calculate neuron activation for an input
257 def activate(weights, inputs):
258     activation = weights[-1]
259     for i in range(len(weights) - 1):
260         activation += weights[i] * inputs[i]
261     return activation
262
263 def sigmoid(activation):
264     output = 1.0 / (1.0 + exp(-activation))
265     return output
266
267 def sigmoid_derivative(output):
268     return output * (1 - output)
269
270 # Forward propagate input to a network output
271 def forward_propagate(network, row):
272     inputs = row
273     for i in range(len(network)):
274         inputs_new = []
275         if i != len(network) - 1:
276             for neuron in network[i]:
277                 activation = activate(neuron['weights'], inputs)
278                 neuron['output'] = sigmoid(activation)
279                 inputs_new.append(neuron['output'])
280             inputs = inputs_new
281         else:
282             for neuron in network[i]:
283                 neuron['output'] = activate(neuron['weights'], inputs)
284             output = neuron['output']
285     return output
286
287 # Backpropagate error and store in neurons
288 def backward_propagate_error(network, expected):
289     for i in reversed(range(len(network))):
290         layer = network[i]
291         if i == len(network) - 1:
292             neuron = layer[0]

```

```

290     neuron['delta'] = expected - neuron['output']
291 else:
292     for j in range(len(layer)):
293         error = 0.0
294         for neuron in network[i+1]:
295             error += (neuron['weights'][j] * neuron['delta'])
296         neuron = layer[j]
297         neuron['delta'] = error * (neuron['output'] * (1 - neuron['output']))
298
299
300 # Update network weights with error
301 def update_weights(network, row, l_rate):
302     for i in range(len(network)):
303         inputs = row[:-1]
304         if i != 0:
305             inputs = [neuron['output'] for neuron in network[i - 1]]
306         for neuron in network[i]:
307             for j in range(len(inputs)):
308                 neuron['weights'][j] += l_rate * neuron['delta'] * inputs[j]
309
310         neuron['weights'][-1] += l_rate * neuron['delta']
311
312 # Train a network for a fixed number of epochs
313 def train_network(network, train, validation, l_rate, n_epoch):
314     for epoch in range(n_epoch):
315         error = 0
316         for index, row in train.iterrows():
317             inputs = list(row)[:-1]
318             expected = list(row)[-1]
319             outputs = forward_propagate(network, inputs)
320             error += sqrt((outputs - expected)**2)
321             backward_propagate_error(network, expected)
322             update_weights(network, row, l_rate)
323             accuracy = prediction_accuracy(network, validation)
324     return accuracy
325
326 def prediction_accuracy(network, validation):
327     outputs = []
328     for index, row in validation.iterrows():
329         inputs = list(row)[:-1]
330         output = forward_propagate(network, inputs)
331         outputs.append(output)
332     accuracy = sqrt(sum([(expected - output)**2 for output, expected
333                         in zip(outputs, validation.iloc[:, -1])])/len(validation))
334     return accuracy
335
336 def prediction_evaluation(network, dataset):
337     outputs = []
338     expects = dataset.iloc[:, -1]
339     mean_expects = np.mean(expects)
340     for index, row in dataset.iterrows():
341         inputs = list(row)[:-1]
342         output = forward_propagate(network, inputs)
343         outputs.append(output)
344     MAE = sum([abs(expected - output) for output, expected in zip(
345               outputs, expects)]) / len(dataset)

```

```

344     RMSE = sqrt(sum([(expected - output)**2 for output, expected in
345         zip(outputs, expects)]) / len(dataset))
346     R2 = 1 - sum([(expected - output)**2 for output, expected in zip(
347         outputs, expects)]) / sum([(expected - mean_expects )**2 for
348             expected in expects])
349     return [MAE, RMSE, R2], outputs
350
351
352
353
354
355
356
357
358
359
360
361
362
363
364
365
366
367
368
369
370
371
372
373
374
375
376
377
378
379
380
381
382
383
384
385
386
387

```

```

RMSE = sqrt(sum([(expected - output)**2 for output, expected in
    zip(outputs, expects)]) / len(dataset))
R2 = 1 - sum([(expected - output)**2 for output, expected in zip(
    outputs, expects)]) / sum([(expected - mean_expects )**2 for
        expected in expects])
return [MAE, RMSE, R2], outputs

def back_propagation(train, validation, test, n_inputs, n_hidden,
    n_outputs, l_rate, n_epoch):
    score = {}
    predictions = {}
    network = initialize_network(n_inputs, n_hidden, n_outputs)
    accuracy = train_network(network, train, validation, l_rate, n_epoch)
    score['Train'], predictions['Train'] = prediction_evaluation(
        network, train)
    score['Validation'], predictions['Validation'] =
        prediction_evaluation(network, validation)
    score['Test'], predictions['Test'] = prediction_evaluation(
        network, test)
    with open('results.txt', 'a+') as f:
        f.write(f'BPNN\n')
        f.write(f'score:{score}\n')
        f.write(f'predictions:{predictions}\n')
    return score, predictions

def EA_BPNN(train, validation, test, n_inputs, n_hidden, n_outputs,
    l_rate, n_epoch, applyEA):
    if applyEA == 0:
        network = EAList(train, validation, n_inputs, n_hidden, n_outputs,
            l_rate, n_epoch)
    if applyEA == 1:
        network = EATree(train, validation, n_inputs, n_hidden, n_outputs,
            l_rate, n_epoch)
    accuracy = train_network(network, train, validation, l_rate, n_epoch)
    score = {}
    predictions = {}
    score['Train'], predictions['Train'] = prediction_evaluation(
        network, train)
    score['Validation'], predictions['Validation'] =
        prediction_evaluation(network, validation)
    score['Test'], predictions['Test'] = prediction_evaluation(
        network, test)
    with open('results.txt', 'a+') as f:
        f.write(f'EA 0List/1Tree:{applyEA}\n')
        f.write(f'score:{score}\n')
        f.write(f'predictions:{predictions}\n')
    return score, predictions

if __name__ == "__main__":
    random.seed(50)
#####
##### Data preprocess
#####
dataset = pd.read_csv('crack_SP2_New2.txt', delimiter = "\t",
    header = None)
train, validation, test = preprocess(dataset)

```

```
388 n_inputs = len(train.iloc[0]) - 1
389 n_hidden = 7
390 n_outputs = 1
391 l_rate = 0.001
392 n_epoch = 251
393
394 score, predictions = back_propagation(train, validation, test,
395     n_inputs, n_hidden, n_outputs, l_rate, n_epoch)
396 print(f'BP score:{score}')
397 ##  

398 for applyEA in [0,1]: # 0 for List, 1 for Tree
399     score = EA_BPNN(train, validation, test, n_inputs, n_hidden,
        n_outputs, l_rate, n_epoch, applyEA)
    print(f'EA score:{score}')
```

Appendix C

Summary of machine learning application

Table C.1: Summary of the application of ML models in the prediction of the mechanical properties of concrete.

Size	TR	V	TS	Concrete type	Method category	Input variables	Output	Evaluation	Ref
1462	70%	15%	15%	concrete	ANN	cement, W/CM, type and dosage of supplementary cementitious materials, bio-healing materials, expansive and crystalline additives	self-healing	RMSE, MAPE, R^2	[181]
1223	70%	NA	30%	bacteria-based concrete	ANN, DT, SVR	number of bacteria, healing time, initial crack width	self-healing	MSE, R	[182]
99	42	23	34	cellular concrete	ANN	cement, W/CM, foam-cementitious materials ratio, sand-cementitious materials ratio	compressive strength	average algebraic error, Average Absolute Deviation (AAE)	[135]
187	169	NA	18	high strength concrete	ANN	W/CM, water, Fine Aggregates (S) ratio, FA, air entraining agent, Superplasticizer (SP), SF	compressive strength, slump	RMSE, MAPE, R^2 , Sum of the Squares Error (SSE)	[136]
96	79	NA	17	no-slump concrete	ANN	cement, SF, water, S, Coarse Aggregates (CA), filler, W/CM	compressive strength	correlation factor, RMSE	[137]
300	ten-fold cross validation	High Performance Concrete (HPC)	HPC	ANN, DT,	cements, FA, BFS, S, water, SP, coarse aggregate, age of testing	cement, Blast Furnace Slag (BFS), FA, water, SP, CA, S, age	compressive strength	RMSE, MAE, R	[169]
1030				ANN, SVR			compressive strength	R, MAE, RMSE, R^2	[138]

	168	NA	NA	NA	recycled aggregate concrete	ANN	water, cement, sand, natural CA, recycled CA, W/CM, fineness modulus of sand, water absorption of the aggregates, saturated surface-dried, density, maximum size of aggregates, impurity content and replacement ratio of recycled CA, conversion coefficient of different concrete specimen	compressive strength	RMSE, MAPE, [140] R^2
	1655				ten-fold cross validation	HPC	ANN, SVR, DT, EM	Cement, BFS, FA, water, SP, SF, curing time, bottom ash	compressive strength R, RMSE, MAE, [142] MAPE
	1030				ten-fold cross validation	HPC	DT, EM	cement, FA, water, BFS, SP, age, CA, S	compressive strength R^2 [175]
1675					ten-fold cross validation	HPC	ANN, SVR, DT, EM	Cement, BFS, FA, water, SP, SF, CA, S, age of testing	compressive strength R, RMSE, MAE, [125] MAPE
	180	150	NA	30	concrete	ANN	cement, BFS, FA, water, SP, CA, S	compressive strength R^2 , RMSE [124]	
	239				ten-fold cross validation	HPC	SVR	cement, sand, small CA, medium CA, water, SP	compressive strength RMSE, MAPE, [163] R^2
36	NA	NA	NA		environmentally friendly concrete	SVR, DT, EM	water, age, cement, FA, sand, pea gravel, haydite, micro air	compressive strength R , R^2 , RMSE, [170] MAE	
	1912	85%	NA	15%	normal concrete, HPC	DT	cement, water, FA, BFS, CA, S, SP, sand, age	compressive strength correlation coefficient, MAE, RMSE, MAPE, R^2 [171]	

					ten-fold cross validation						
1133		HPC	ANN	cement, water, BFS, CA, S, SP, FA, age of testing		compressive strength	R, RMSE, MAE,	[144]	MAPE		
91	95%	lightweight foamed concrete	ANN, Decision Tree (DT), SVR	cementitious material, oven dry density, water/binder ratio, foam volume		compressive strength	R, RMSE, MAE,	[145]			
49	70% 15% 15%	concrete	ANN, DT, EM	W/CM, water, cement, workability, age		compressive strength	RMSE, R^2	[172]			
17	NA NA NA	recycled concrete aggregates	ANN	cement, recycled CA, slump		compressive strength	RMSE, R^2 , readjusted correlation coefficient, relative percent deviation	[146]			
[87]	2817	NA NA NA	concrete	ANN	CA, S, water, cement, BFS, FA, SP	compressive strength	RMSE, MAE,	[149]	R^2		
	1030	70% NA 30%	HPC	ANN	cement, BFS, FA, water, SP, CA, S, concrete age	compressive strength	R^2 , RMSE,	[150]	MAE		
	117	70% 15% 15%	geopolymer concrete	ANN	specimen age, sodium hydroxide concentration, natural zeolite, SF, ground granulated blast-furnace slag	compressive strength	MSE, R	[151]			
1030		HPC with waste materials	ANN, SVR, DT, EM	binder, S, CA, water, concrete age, SP, ground granulated BFS		compressive strength	MAE, RMSE, root mean squared log error	[180]	MSE, [176]		
1030	927	NA 103	HPC	EM	CA, S, water, cement, BFS, FA, SP, age	compressive strength	R , MAE, RMSE	[176]			

	131	70%	NA	30%	lightweight self- compacting concrete	EM	crumb rubber, PP fibre, steel fibre, natural S, CA, water to binder ratio	uniaxial compressive strength	RMSE, R	[177]
	162	75%	NA	25%	concrete	ANN	curing type, curing time, BFS ratio, corrosion inhibitor ratio	compressive strength, splitting tensile strength, chloride ion permeability	accuracy	[139]
	512	90	422	NA	pervious concrete	SVR	compressive strength, tensile strength, curing age, the maximum size of the crushed stone, stone powder content in sand, fine modulus of sand, water-to-binder ratio, W/CM, water, and sand ratio	permeability coefficient, uniaxial compressive strength	R , RMSE	[167]
∞	270	ten-fold cross validation	pervious concrete	SVR			W/CM, aggregate-to-cement ratio, aggregate size	permeability coefficient, 28-day unconfined compressive strength	RMSE, R	[166]
	24	test-set- cross validation	permeable concrete	SVR			nominal coarse aggregate size, cement, W/CM, CA	compressive strength, tensile strength	R , RMSE, MAE, MAPE	[159]
	1847	ten-fold cross validation	HPC	EM, SVR			age, cement, CA, water, S, BFS, FA, SP	compressive strength, tensile strengths	RMSE	[179]

	640	70%	NA	30%	manufactured sand concrete	DT, EM	compressive strength, tensile strength, curing age, the maximum size of the crushed stone, water-to-binder ratio , and sand ratio, stone powder content in sand, fine modulus of sand	splitting tensile strength, uniaxial compressive strength	RMSE, R	[178]
	324	70%	15%	15%	rubberised concrete	ANN	W/CM, rubber fibre content, elevated temperature, exposure duration	compressive strength, static elasticity, dynamic elasticity, mass loss	MSE, RMSE, R , Coefficient of Variation (COV),AAE	[148]
	446	70%	NA	30%	bentonite plastic concrete	ANN, DT	silty clay addition, bentonite dosage, water content, curing time	slump, compressive strength, elastic modulus	R^2 , RMSE, MAPE, AAE	[147]
68	324	224	50	50	recycled aggregate concrete	ANN	cement, W/CM, total aggregate to cement ratio, S percentage, mass substitution rate of natural aggregate by recycled aggregate, CA, recycled CA, type and preparation methods of CA, cement type, specimen size	elastic modulus	RMSE, MAPE, R^2	[141]
	1569	80%	NA	20%	recycled aggregate concrete	DT, SVR	W/CM, coarse recycled concrete aggregate, aggregate-to-cement ratio, bulk density of recycled concrete aggregate, water	compressive strength, elastic modulus, flexural strength, splitting tensile strength	RMSE, MAE, MAPE	[164]
	139	104	NA	35	steel fibre- reinforced concrete beam	SVR, ANN	concrete strength, longitudinal steel strength, shear span-to-depth ratio, effective depth of beam, beam width, maximum aggregate size, longitudinal steel ratio, steel fibre volume fraction, fibre length, equivalent fibre diameter	sheer strength	RMSE, MAE, best agreement	[162]

	NA	NA	NA	NA	fibre-reinforced concrete beam	SVR, ANN	reinforcement ratio, compressive strength, fibre factor, volume percentage of fibre, fibre length to diameter ratio, effective depth, shear span-to-strength ratio	sheer strength	MAPE, RMSE, MAE, R^2 , relative error	[161]
267	80%	NA	20%		reinforced concrete	SVR, ANN	diameter of the bar, development length, compressive strength, cover to the concrete maximum and minimum	splice strength	absolute average relative error, RMSE, mean relative error	[160]
218	90%	NA	10%		corroded steel reinforcement and surrounding concrete	SVR, ANN, DT	compressive strength, concrete cover, steel type, diameter of steel bar, bond length, corrosion level	ultimate bond strength	RMSE, MAPE, R^2	[165]
560	70%	15%	15%		ready mix concrete	ANN	cement, FA, sand, CA, admixture and water-binder ratio	slump	R, RMSE, MAPE, coefficient of efficiency, normalized mean bias error, root mean square error to observation's standard deviation ratio	[143]

References

- [1] Michael F Ashby. *Materials and the environment: eco-informed material choice*. Elsevier, 2012.
- [2] Waiching Tang, Omid Kardani, and Hongzhi Cui. Robust evaluation of self-healing efficiency in cementitious materials – A review. *Construction and Building Materials*, 81:233–247, 2015. ISSN 0950-0618. doi: 10.1016/j.conbuildmat.2015.02.054.
- [3] Diane Gardner, Robert Lark, Tony Jefferson, and Robert Davies. A survey on problems encountered in current concrete construction and the potential benefits of self-healing cementitious materials. *Case studies in construction materials*, 8:238–247, 2018.
- [4] K Van Breugel. Is there a market for self-healing cement-based materials. In *Proceedings of the first international conference on self-healing materials*, pages 1–9, 2007.
- [5] E. Cailleux and V. Pollet. Investigations on the development of self-healing properties in protective coatings for concrete and repair mortars. In *2nd International Conference on Self Healing Materials, Chicago, USA*, volume 29, 2009.
- [6] Victor C. Li and Emily Herbert. Robust Self-Healing Concrete for Sustainable Infrastructure. *Journal of Advanced Concrete Technology*, 10:207–218, 2012. doi: 10.3151/jact.10.207.

- [7] Zhigang Zhang, Qian Zhang, and Victor C. Li. Multiple-scale investigations on self-healing induced mechanical property recovery of ECC. *Cement and Concrete Composites*, 103:293–302, 2019.
- [8] Clifford L Freyermuth. Life-cycle cost analysis for large bridges. *Concrete international*, 23(2):89–95, 2001.
- [9] Mustafa Şahmaran, Gürkan Yıldırım, Rezhin Noori, Erdogan Ozbay, and Mohamed Lachemi. Repeatability and Pervasiveness of Self-Healing in Engineered Cementitious Composites. *ACI Materials Journal*, 112, 2015. ISSN 0889-325X. doi: 10.14359/51687308.
- [10] Kim Van Tittelboom. *Self-Healing Concrete through Incorporation of Encapsulated Bacteria-or Polymer-Based Healing Agents ('Zelfhelend beton door incorporatie van ingekapselde bacteri)*. PhD thesis, Ghent University, 2012.
- [11] Swapan Kumar Ghosh. *Self-Healing Materials: Fundamentals, Design Strategies, and Applications*. John Wiley & Sons, 2009. ISBN 978-3-527-62538-3.
- [12] G. W. Hyde and W. J. Smith. Results of experiments made to determine the permeability of cements and cement mortars. *Journal of the Franklin Institute*, 128:199–207, 1889.
- [13] Natalya Hearn and CT Morley. Self-sealing property of concrete—experimental evidence. *Materials and structures*, 30(7):404–411, 1997.
- [14] Carola Edvardsen. Water permeability and autogenous healing of cracks in concrete. *ACI Materials Journal*, 96(4), 1999.
- [15] S. Granger, Ahmed Loukili, Gilles Pijaudier-Cabot, and G. Chanvillard. Experimental characterization of the self-healing of cracks in an ultra high performance cementitious material: Mechanical tests and acoustic emission analysis. *Cement and Concrete Research*, 37:519–527, 2007.
- [16] Erdogan Özbay, Mustafa Şahmaran, Mohamed Lachemi, and Hasan Erhan Yücel. Self-Healing of Microcracks in High-Volume Fly-Ash-Incorporated

Engineered Cementitious Composites. *ACI Materials Journal*, 110:33–43, 2013/01//Jan/Feb2013. ISSN 0889325X.

- [17] Toshiro Kamada and Victor C Li. The effects of surface preparation on the fracture behavior of ecc/concrete repair system. *Cement and Concrete Composites*, 22(6):423–431, 2000.
- [18] Victor C Li and Tetsushi Kanda. Innovations forum: engineered cementitious composites for structural applications. *Journal of Materials in Civil Engineering*, 10(2):66–69, 1998.
- [19] En-Hua Yang, Yingzi Yang, and Victor C. Li. Use of high volumes of fly ash to improve ECC mechanical properties and material greenness. *ACI Materials Journal*, 104:620–628, 2007.
- [20] Zhigang Zhang, Shunzhi Qian, and Hui Ma. Investigating mechanical properties and self-healing behavior of micro-cracked ECC with different volume of fly ash. *Construction and Building Materials*, 52:17–23, 2014. ISSN 0950-0618. doi: 10.1016/j.conbuildmat.2013.11.001.
- [21] Ahmed R Suleiman, Andrew J Nelson, and Moncef L Nehdi. Visualization and quantification of crack self-healing in cement-based materials incorporating different minerals. *Cement and Concrete Composites*, 103:49–58, 2019.
- [22] J. Zhou, S. Qian, M. G. Sierra Beltran, G. Ye, E. Schlangen, and K. van Breugel. Developing engineered cementitious composite with local materials. In *International Conference on Microstructure Related Durability of Cementitious Composites, Nanjing, China*, 2008.
- [23] Victor C. Li and En-Hua Yang. Self healing in concrete materials. In *Self Healing Materials*, pages 161–193. Springer, 2007.
- [24] Gürkan Yıldırım, Mustafa Sahmaran, and Hemn Unis Ahmed. Influence of hydrated lime addition on the self-healing capability of high-volume fly ash incorporated cementitious composites. *Journal of Materials in Civil Engineering*, 27:04014187, 2014.

- [25] Ahmed Alyousif, Mohamed Lachemi, Gurkan Yildirim, and Mustafa Sahmaran. Effect of Self-Healing on the Different Transport Properties of Cementitious Composites. *Journal of Advanced Concrete Technology*, 13:112–123, 2015.
- [26] Gurkan Yildirim, Ahmed Alyousif, Mustafa Sahmaran, and Mohamed Lachemi. Assessing the self-healing capability of cementitious composites under increasing sustained loading. *Advances in Cement Research*, 27:581–592, 2015. ISSN 0951-7197. doi: 10.1680/adcr.14.00111.
- [27] Mustafa Sahmaran, Gurkan Yildirim, and Tahir K. Erdem. Self-healing capability of cementitious composites incorporating different supplementary cementitious materials. *Cement and Concrete Composites*, 35:89–101, 2013. ISSN 0958-9465. doi: 10.1016/j.cemconcomp.2012.08.013.
- [28] Min Wu, Björn Johannesson, and Mette Geiker. A review: Self-healing in cementitious materials and engineered cementitious composite as a self-healing material. *Construction and Building Materials*, 28:571–583, 2012. ISSN 0950-0618.
- [29] Haoliang Huang, Guang Ye, and Denis Damidot. Characterization and quantification of self-healing behaviors of microcracks due to further hydration in cement paste. *Cement and Concrete Research*, 52:71–81, 2013. ISSN 0008-8846.
- [30] Haoliang Huang, Guang Ye, Chunxiang Qian, and Erik Schlangen. Self-healing in cementitious materials: Materials, methods and service conditions. *Materials & Design*, 92:499–511, 2016. ISSN 0264-1275. doi: 10.1016/j.matdes.2015.12.091.
- [31] Nataliya Hearn. Self-sealing, autogenous healing and continued hydration: What is the difference? *Materials and Structures*, 31:563–567, 1998.
- [32] William H. Glanville. *The Permeability of Portland Cement Concrete*. [HM Stationery Office [printed by Harrison and sons, Limited], 1931.

- [33] V. J. Soroker and A. J. Denson. Autogenous healing of concrete. *Zement*, 25: 76, 1926.
- [34] F. Brandeis. Autogenous healing of concrete. *Beton und Eisen*, 36:12, 1937.
- [35] Kim Van Tittelboom and Nele De Belie. Self-Healing in Cementitious Materials—A Review. *Materials*, 6:2182–2217, 2013. ISSN 1996-1944. doi: 10.3390/ma6062182.
- [36] E. Schlangen, N. ter Heide, and K. van Breugel. CRACK HEALING OF EARLY AGE CRACKS IN CONCRETE. In MARIA S. KONSTANTIDOUTOS, editor, *Measuring, Monitoring and Modeling Concrete Properties*, pages 273–284. Springer Netherlands, 2006.
- [37] Hirozo Mihashi and Y. Kaneko. Fundamental study on development of intelligent concrete with self-healing capability for prevention of water leakage. *Journal of architecture and building science*, 115:1–4, 2000.
- [38] F Xing, Z Ni, NX Han, BQ Dong, XX Du, Z Huang, and M Zhang. Self-healing mechanism of a novel cementitious composite using microcapsules. In *Proceedings of the International Conference on Durability of Concrete Structures, Hangzhou, China*, volume 2627, 2008.
- [39] I. Kaltzakorta and E. Erkizia. Silica microcapsules encapsulating epoxy compounds for self-healing cementitious materials. In *Proceedings of 3rd International Conference on Self Healing Materials, Bath, UK*, pages 27–29, 2011.
- [40] Tran Diep Phuoc Thao, Tay Jang Shen Johnson, Quek Ser Tong, and Pang Sze Dai. Implementation of self-healing in concrete—proof of concept. *The IES Journal Part A: Civil & Structural Engineering*, 2:116–125, 2009.
- [41] Zhengxian Yang, John Hollar, Xiaodong He, and Xianming Shi. A self-healing cementitious composite using oil core/silica gel shell microcapsules. *Cement and Concrete Composites*, 33:506–512, 2011. ISSN 0958-9465. doi: 10.1016/j.cemconcomp.2011.01.010.

- [42] Carolyn Dry and William McMillan. Three-part methylmethacrylate adhesive system as an internal delivery system for smart responsive concrete. *Smart materials and structures*, 5:297, 1996.
- [43] C. M. Dry. Three designs for the internal release of sealants, adhesives, and waterproofing chemicals into concrete to reduce permeability. *Cement and Concrete Research*, 30:1969–1977, 2000.
- [44] C. Joseph, A. D. Jefferson, and M. B. Cantoni. Issues relating to the autonomic healing of cementitious materials. In *Proceedings of the 1st International Conference on Self-Healing Materials, Noordwijk, the Netherlands. CD-ROM*, 2007.
- [45] Christopher Joseph. *Experimental and Numerical Study of the Fracture and Self-Healing of Cementitious Materials*. Phd, Cardiff University, 2008.
- [46] Victor C Li, Yun Mook Lim, and Yin-Wen Chan. Feasibility study of a passive smart self-healing cementitious composite. *Composites Part B: Engineering*, 29:819–827, 1998. ISSN 1359-8368.
- [47] Kim Van Tittelboom, Nele De Belie, Denis Van Loo, and Patric Jacobs. Self-healing efficiency of cementitious materials containing tubular capsules filled with healing agent. *Cement and Concrete Composites*, 33:497–505, 2011.
- [48] U. K. Gollapudi, C. L. Knutson, S. S. Bang, and M. R. Islam. A new method for controlling leaching through permeable channels. *Chemosphere*, 30(4):695–705, 1995.
- [49] Kim Van Tittelboom. *Self-Healing Concrete through Incorporation of Encapsulated Bacteria-or Polymer-Based Healing Agents ('Zelfhelend Beton Door Incorporatie van Ingekapselde Bacteri)*. PhD thesis, Ghent University, 2012.
- [50] Henk M. Jonkers, Arjan Thijssen, Gerard Muyzer, Oguzhan Copuroglu, and Erik Schlangen. Application of bacteria as self-healing agent for the development of sustainable concrete. *Ecological Engineering*, 36:230–235, 2010. ISSN 0925-8574. doi: 10.1016/j.ecoleng.2008.12.036.

- [51] Willem De Muynck, Nele De Belie, and Willy Verstraete. Microbial carbonate precipitation in construction materials: a review. *Ecological engineering*, 36(2):118–136, 2010.
- [52] Adam M Neville et al. *Properties of concrete*, volume 4. Longman London, 1995.
- [53] Kenneth R. Lauer. Autogenous healing of cement paste. In *ACI Journal Proceedings*, volume 52. ACI, 1956.
- [54] Adam Neville. Autogenous Healing—A Concrete Miracle? *Concrete International*, 24:76–82, 2002. ISSN 0162-4075.
- [55] Timo G. Nijland, Joe A. Larbi, Rob PJ van Hees, Barbara Lubelli, and Mario de Rooij. Self healing phenomena in concretes and masonry mortars: A microscopic study. In *Proc. 1st Int. Conf. on Self Healing Materials*, volume 1, pages 1–9, 2007.
- [56] Benoit Hilloulin, Damien Hilloulin, Frédéric Grondin, Ahmed Loukili, and Nele De Belie. Mechanical regains due to self-healing in cementitious materials: Experimental measurements and micro-mechanical model. *Cement and Concrete Research*, 80:21–32, 2016. ISSN 0008-8846. doi: 10.1016/j.cemconres.2015.11.005.
- [57] Hans-Wolf Reinhardt and Martin Jooss. Permeability and self-healing of cracked concrete as a function of temperature and crack width. *Cement and Concrete Research*, 33:981–985, 2003. ISSN 0008-8846. doi: 10.1016/S0008-8846(02)01099-2.
- [58] C. A. Clear. The effects of autogenous healing upon the leakage of water through cracks in concrete. Technical report, Slough. Technical Report 42.559, 1985.
- [59] Stefan Jacobsen, Jacques Marchand, and Hugues Hornain. Sem observations of the microstructure of frost deteriorated and self-healed concretes. *Cement and Concrete Research*, 25(8):1781–1790, 1995. ISSN 0008-8846.

- [60] M Ismail, A Toumi, R François, and R Gagné. Effect of crack opening on the local diffusion of chloride in inert materials. *Cement and Concrete Research*, 34:711–716, 2004. ISSN 0008-8846. doi: 10.1016/j.cemconres.2003.10.025.
- [61] S. Jacobsen, J. Marchand, and B. Gerard. Concrete cracks I: Durability and self healing—a review. *Proc Consec*, 98:217–231, 1998.
- [62] Victor C Li. On engineered cementitious composites (ecc). *Journal of advanced concrete technology*, 1(3):215–230, 2003.
- [63] Pankaj Munjal and SB Singh. Out-of-plane response of ecc-strengthened masonry walls. *Journal of Structural Integrity and Maintenance*, 5(1):18–30, 2020.
- [64] Victor C Li, Shuxin Wang, Cynthia Wu, et al. Tensile strain-hardening behavior of polyvinyl alcohol engineered cementitious composite (pva-ecc). *ACI Materials Journal-American Concrete Institute*, 98(6):483–492, 2001.
- [65] Li-li Kan, Ruo-xin Shi, and Jin Zhu. Effect of fineness and calcium content of fly ash on the mechanical properties of Engineered Cementitious Composites (ECC). *Construction and Building Materials*, 209:476–484, 2019. ISSN 0950-0618. doi: 10.1016/j.conbuildmat.2019.03.129.
- [66] Hui Ma, Emily Herbert, Motohiro Ohno, and Victor C. Li. Scale-linking model of self-healing and stiffness recovery in Engineered Cementitious Composites (ECC). *Cement and Concrete Composites*, 95:1–9, 2019. ISSN 0958-9465. doi: 10.1016/j.cemconcomp.2018.10.006.
- [67] Zhigang Zhang, Yuanzhao Ding, and Shunzhi Qian. Influence of bacterial incorporation on mechanical properties of engineered cementitious composites (ECC). *Construction and Building Materials*, 196:195–203, 2019.
- [68] Zhigang Zhang, Jing Hu, and Hui Ma. Feasibility study of ECC with self-healing capacity applied on the long-span steel bridge deck overlay. *International Journal of Pavement Engineering*, 20:884–893, 2019. ISSN 1029-8436. doi: 10.1080/10298436.2017.1356173.

- [69] Zhigang Zhang, Ananya Yuvaraj, Jin Di, and Shunzhi Qian. Matrix design of light weight, high strength, high ductility ECC. *Construction and Building Materials*, 210:188–197, 2019. ISSN 0950-0618.
- [70] Xinchun Guan, Chenchen Zhang, Yazhao Li, and Shengying Zhao. Effect of exposure conditions on self-healing behavior of engineered cementitious composite incorporating limestone powder. *Cement and Concrete Composites*, 114:103808, 2020. ISSN 0958-9465. doi: 10.1016/j.cemconcomp.2020.103808.
- [71] Duo Zhang, Beata Jaworska, He Zhu, Kensey Dahlquist, and Victor C. Li. Engineered Cementitious Composites (ECC) with limestone calcined clay cement (LC3). *Cement and Concrete Composites*, 114:103766, 2020. ISSN 0958-9465.
- [72] Zhigang Zhang, Jin-Cheng Liu, Xiaoqing Xu, and Liqun Yuan. Effect of sub-elevated temperature on mechanical properties of ECC with different fly ash contents. *Construction and Building Materials*, 262:120096, 2020. ISSN 0950-0618. doi: 10.1016/j.conbuildmat.2020.120096.
- [73] Haoliang Wu, Jing Yu, Yanjun Du, and Victor C. Li. Mechanical performance of MgO-doped Engineered Cementitious Composites (ECC). *Cement and Concrete Composites*, 115:103857, 2021. ISSN 0958-9465.
- [74] Victor C Li. Engineered cementitious composites (ecc)-tailored composites through micromechanical modeling. 1998.
- [75] Victor C. Li. Engineered Cementitious Composites (ECC) Material, Structural, and Durability Performance. 2008.
- [76] Yingzi Yang, Michael D. Lepech, En-Hua Yang, and Victor C. Li. Autogenous healing of engineered cementitious composites under wet-dry cycles. *Cement and Concrete Research*, 39:382–390, 2009. ISSN 0008-8846. doi: 10.1016/j.cemconres.2009.01.013.
- [77] Xia Hua, K. van Breugel, Guang Ye, P. C. J. Hoogenboom, and Ir LJM Houben. *Self-Healing of Engineered Cementitious Composites (ECC) in Concrete Repair System*. PhD thesis, Master thesis, Delft University of Technology, 2010.

- [78] Hanwen Deng and Shunzhi Qian. Influence of superabsorbent polymer particles on the self-healing behavior of engineered cementitious composites. 2012.
- [79] Carolyn Dry. Matrix cracking repair and filling using active and passive modes for smart timed release of chemicals from fibers into cement matrices. *Smart Materials and Structures*, 3(2):118, 1994. ISSN 0964-1726. doi: 10.1088/0964-1726/3/2/006.
- [80] Mustafa Şahmaran and Victor C. Li. Durability properties of micro-cracked ECC containing high volumes fly ash. *Cement and Concrete Research*, 39: 1033–1043, 2009. ISSN 0008-8846. doi: 10.1016/j.cemconres.2009.07.009.
- [81] Tae-Ho Ahn and Toshiharu Kishi. Crack Self-healing Behavior of Cementitious Composites Incorporating Various Mineral Admixtures. *Journal of Advanced Concrete Technology*, 8:171–186, 2010.
- [82] Yong-Soo Lee and Jae-Suk Ryou. Self healing behavior for crack closing of expansive agent via granulation/film coating method. *Construction and Building Materials*, 71:188–193, 2014. ISSN 0950-0618. doi: 10.1016/j.conbuildmat.2014.08.045.
- [83] Zhengwu Jiang and Zhenghong Yang. Self-healing of cracks in concrete with various crystalline mineral additives in underground environment. *Journal of Wuhan University of Technology-Mater. Sci. Ed.*, 29:938–944, 2014. ISSN 1000-2413, 1993-0437. doi: 10.1007/s11595-014-1024-2.
- [84] K. Sisomphon, O. Copuroglu, and E. A. B. Koenders. Self-healing of surface cracks in mortars with expansive additive and crystalline additive. *Cement and Concrete Composites*, 34:566–574, 2012. ISSN 0958-9465.
- [85] M. Roig-Flores, S. Moscato, P. Serna, and L. Ferrara. Self-healing capability of concrete with crystalline admixtures in different environments. *Construction and Building Materials*, 86:1–11, 2015. ISSN 0950-0618. doi: 10.1016/j.conbuildmat.2015.03.091.

- [86] Kazim Turk and Serhat Demirhan. The mechanical properties of engineered cementitious composites containing limestone powder replaced by microsilica sand. *Canadian Journal of Civil Engineering*, 40:151–157, 2013. ISSN 0315-1468. doi: 10.1139/cjce-2012-0281.
- [87] S. Z. Qian, J. Zhou, and E. Schlangen. Influence of curing condition and pre-cracking time on the self-healing behavior of Engineered Cementitious Composites. *Cement and Concrete Composites*, 32:686–693, 2010. ISSN 0958-9465. doi: 10.1016/j.cemconcomp.2010.07.015.
- [88] S. Qian, J. Zhou, M. R. de Rooij, E. Schlangen, G. Ye, and K. van Breugel. Self-healing behavior of strain hardening cementitious composites incorporating local waste materials. *Cement and Concrete Composites*, 31:613–621, 2009. ISSN 0958-9465. doi: 10.1016/j.cemconcomp.2009.03.003.
- [89] Hocine Siad, Ahmed Alyousif, Ozlem Kasap Keskin, Suleyman Bahadir Keskin, Mohamed Lachemi, Mustafa Sahmaran, and Khandaker M. Anwar Hosain. Influence of limestone powder on mechanical, physical and self-healing behavior of Engineered Cementitious Composites. *Construction and Building Materials*, 99:1–10, 2015. ISSN 0950-0618. doi: 10.1016/j.conbuildmat.2015.09.007.
- [90] Zhengwu Jiang, Wenting Li, and Zhengcheng Yuan. Influence of mineral additives and environmental conditions on the self-healing capabilities of cementitious materials. *Cement and Concrete Composites*, 57:116–127, 2015. ISSN 0958-9465. doi: 10.1016/j.cemconcomp.2014.11.014.
- [91] Tanvir Qureshi and Abir Al-Tabbaa. The effect of magnesia on the self-healing performance of Portland cement with increased curing time. In *1st International Conference on Ageing of Materials & Structures*, page 635, 2014.
- [92] T. H. Ahn and T. Kishi. The effect of geo-materials on the autogenous healing behavior of cracked concrete. In *Proceeding of 2nd ICCRRR2008, Cape Town, South Africa*, pages 235–240, 2008.

- [93] T. Kishi, T. H. Ahn, A. Hosoda, S. Suzuki, and H. Takaoka. Self-healing behaviour by cementitious recrystallization of cracked concrete incorporating expansive agent. In *First International Conference on Self-Healing Materials*. Springer, Dordrecht, 2007.
- [94] S. A. L. de Koster, R. M. Mors, H. W. Nugteren, H. M. Jonkers, G. M. H. Meesters, and J. R. van Ommen. Geopolymer Coating of Bacteria-containing Granules for Use in Self-healing Concrete. *Procedia Engineering*, 102:475–484, 2015. ISSN 1877-7058. doi: 10.1016/j.proeng.2015.01.193.
- [95] E. Mostavi, S. Asadi, M. Hassan, and M. Alansari. Evaluation of Self-Healing Mechanisms in Concrete with Double-Walled Sodium Silicate Microcapsules. *Journal of Materials in Civil Engineering*, 27:04015035, 2015. ISSN 0899-1561. doi: 10.1061/(ASCE)MT.1943-5533.0001314.
- [96] A. Kanellopoulos, T. S. Qureshi, and A. Al-Tabbaa. Glass encapsulated minerals for self-healing in cement based composites. *Construction and Building Materials*, 98:780–791, 2015. ISSN 0950-0618. doi: 10.1016/j.conbuildmat.2015.08.127.
- [97] Haoliang Huang, Guang Ye, Christopher Leung, and KT WAN. Application of sodium silicate solution as self-healing agent in cementitious materials. In *International RILEM Conference on Advances in Construction Materials through Science and Engineering*, pages 530–536. RILEM Publications SARL: Hong Kong, China, 2011.
- [98] Wenhui Zhong and Wu Yao. Influence of damage degree on self-healing of concrete. *Construction and Building Materials*, 22:1137–1142, 2008. ISSN 0950-0618. doi: 10.1016/j.conbuildmat.2007.02.006.
- [99] Mustafa Sahmaran, Suleyman B. Keskin, Gozde Ozerkan, and Ismail O. Yaman. Self-healing of mechanically-loaded self consolidating concretes with high volumes of fly ash. *Cement and Concrete Composites*, 30:872–879, 2008. ISSN 0958-9465. doi: 10.1016/j.cemconcomp.2008.07.001.

- [100] Haoliang Huang, Guang Ye, and Denis Damidot. Effect of blast furnace slag on self-healing of microcracks in cementitious materials. *Cement and Concrete Research*, 60:68–82, 2014. ISSN 0008-8846. doi: 10.1016/j.cemconres.2014.03.010.
- [101] Dechkhachorn Jaroenratanapirom and Raktipong Sahamitmongkol. Effects of different mineral additives and cracking ages on self-healing performance of mortar. In *Proceedings of the 6th Annual Concrete Conference, Petchaburi, Thailand*, pages 551–6, 2010.
- [102] Navid Ranjbar, Mehdi Mehrali, Arash Behnia, U. Johnson Alengaram, and Mohd Zamin Jumaat. Compressive strength and microstructural analysis of fly ash/palm oil fuel ash based geopolymers mortar. *Materials & Design*, 59: 532–539, 2014. ISSN 0261-3069. doi: 10.1016/j.matdes.2014.03.037.
- [103] Chung-Chan Hung and Yen-Fang Su. Medium-term self-healing evaluation of Engineered Cementitious Composites with varying amounts of fly ash and exposure durations. *Construction and Building Materials*, 118:194–203, 2016. ISSN 0950-0618. doi: 10.1016/j.conbuildmat.2016.05.021.
- [104] Yu Zhu, Zhaocai Zhang, Yingzi Yang, and Yan Yao. Measurement and correlation of ductility and compressive strength for engineered cementitious composites (ECC) produced by binary and ternary systems of binder materials: Fly ash, slag, silica fume and cement. *Construction and Building Materials*, 68:192–198, 2014. ISSN 0950-0618. doi: 10.1016/j.conbuildmat.2014.06.080.
- [105] Hui Ma and Zhigang Zhang. Paving an engineered cementitious composite (ECC) overlay on concrete airfield pavement for reflective cracking resistance. *Construction and Building Materials*, 252:119048, 2020.
- [106] Pipat Termkhajornkit, Toyoharu Nawa, Yoichi Yamashiro, and Toshiki Saito. Self-healing ability of fly ash–cement systems. *Cement and Concrete Composites*, 31:195–203, 2009. ISSN 0958-9465. doi: 10.1016/j.cemconcomp.2008.12.009.

- [107] Ali Abd Elhakam, Abd Elmoaty Mohamed, and Eslam Awad. Influence of self-healing, mixing method and adding silica fume on mechanical properties of recycled aggregates concrete. *Construction and Building Materials*, 35:421–427, 2012.
- [108] G. Perez, J. J. Gaitero, E. Erkizia, I. Jimenez, and A. Guerrero. Characterisation of cement pastes with innovative self-healing system based in epoxy-amine adhesive. *Cement and Concrete Composites*, 60:55–64, 2015. ISSN 0958-9465. doi: 10.1016/j.cemconcomp.2015.03.010.
- [109] Minoru Kunieda, Kang Choonghyun, Naoshi Ueda, and Hikaru Nakamura. Recovery of protective performance of cracked Ultra High Performance-Strain Hardening Cementitious Composites (UHP-SHCC) due to autogenous healing. *Journal of Advanced Concrete Technology*, 10:313–322, 2012.
- [110] Zafri Muhd Azzuhry. *Self Healing Concrete by Incorporating Palm Oil Fuel Ash (POFA) as Cement Replacement Material*. PhD thesis, Universiti Malaysia Pahang, 2010.
- [111] Nurdeen M. Altwair, M. A. Megat Johari, and Syed F. Saiyid Hashim. Influence of treated palm oil fuel ash on compressive properties and chloride resistance of engineered cementitious composites. *Materials and Structures*, 47:667–682, 2013.
- [112] S. Nagataki and H. Gomi. Expansive admixtures (mainly ettringite). *Cement and Concrete Composites*, 20:163–170, 1998. ISSN 0958-9465. doi: 10.1016/S0958-9465(97)00064-4.
- [113] Mustafa Şahmaran and Victor C. Li. De-icing salt scaling resistance of mechanically loaded engineered cementitious composites. *Cement and Concrete Research*, 37:1035–1046, 2007. ISSN 0008-8846. doi: 10.1016/j.cemconres.2007.04.001.
- [114] Shuxin Wang and Victor C. Li. Engineered cementitious composites with high-volume fly ash. *ACI Materials Journal-American Concrete Institute*, 104:233–241, 2007.

- [115] Jin-Keun Kim, Jeong-Su Kim, Gee Joo Ha, and Yun Yong Kim. Tensile and fiber dispersion performance of ECC (engineered cementitious composites) produced with ground granulated blast furnace slag. *Cement and Concrete Research*, 37:1096–1105, 2007. ISSN 0008-8846. doi: 10.1016/j.cemconres.2007.04.006.
- [116] Thierry Vidal, Arnaud Castel, and Raoul François. Analyzing crack width to predict corrosion in reinforced concrete. *Cement and concrete research*, 34(1):165–174, 2004.
- [117] Kejin Wang, Daniel C Jansen, Surendra P Shah, and Alan F Karr. Permeability study of cracked concrete. *Cement and concrete research*, 27(3):381–393, 1997.
- [118] Jishen Qiu, Han Siang Tan, and En-Hua Yang. Coupled effects of crack width, slag content, and conditioning alkalinity on autogenous healing of engineered cementitious composites. *Cement and Concrete Composites*, 73:203–212, 2016.
- [119] J Qiu. Effects of slag content on self-healing behavior of engineered cementitious composites.
- [120] Mian Luo, Chun-xiang Qian, and Rui-yang Li. Factors affecting crack repairing capacity of bacteria-based self-healing concrete. *Construction and Building Materials*, 87:1–7, 2015. ISSN 0950-0618. doi: 10.1016/j.conbuildmat.2015.03.117.
- [121] Mario de Rooij, Kim Van Tittelboom, Nele De Belie, and Erik Schlangen, editors. *Self-Healing Phenomena in Cement-Based Materials*, volume 11 of *RILEM State-of-the-Art Reports*. Springer Netherlands, Dordrecht, 2013.
- [122] Nele De Belie, Elke Gruyaert, Abir Al-Tabbaa, Paola Antonaci, Cornelia Baera, Diana Bajare, Aveline Darquennes, Robert Davies, Liberato Ferrara, Tony Jefferson, et al. A review of self-healing concrete for damage management of structures. *Advanced Materials Interfaces*, 5(17):1800074, 2018.

- [123] Wassim Ben Chaabene, Majdi Flah, and Moncef L Nehdi. Machine learning prediction of mechanical properties of concrete: Critical review. *Construction and Building Materials*, 260:119889, 2020.
- [124] Zhe Yuan, Lin-Na Wang, and Xu Ji. Prediction of concrete compressive strength: Research on hybrid models genetic based algorithms and anfis. *Advances in Engineering Software*, 67:156–163, 2014.
- [125] Jui-Sheng Chou, Chih-Fong Tsai, Anh-Duc Pham, and Yu-Hsin Lu. Machine learning in concrete strength simulations: Multi-nation data analytics. *Construction and Building Materials*, 73:771–780, 2014.
- [126] Michael I Jordan and Tom M Mitchell. Machine learning: Trends, perspectives, and prospects. *Science*, 349(6245):255–260, 2015.
- [127] R Saravanan and Pothula Sujatha. A state of art techniques on machine learning algorithms: a perspective of supervised learning approaches in data classification. In *2018 Second International Conference on Intelligent Computing and Control Systems (ICICCS)*, pages 945–949. IEEE, 2018.
- [128] Ethem Alpaydin. *Introduction to machine learning*. MIT press, 2020.
- [129] Woubishet Zewdu Taffese and Esko Sistonen. Machine learning for durability and service-life assessment of reinforced concrete structures: Recent advances and future directions. *Automation in Construction*, 77:1–14, 2017.
- [130] Hyunjun Kim, Eunjong Ahn, Myoungsu Shin, and Sung-Han Sim. Crack and noncrack classification from concrete surface images using machine learning. *Structural Health Monitoring*, 18:725–738, 2019.
- [131] C Antony Jeyasehar and K Sumangala. Damage assessment of prestressed concrete beams using artificial neural network (ann) approach. *Computers & structures*, 84(26-27):1709–1718, 2006.
- [132] Rodrigo Moraes, João Francisco Valiati, and Wilson P Gavião Neto. Document-level sentiment classification: An empirical comparison between svm and ann. *Expert Systems with Applications*, 40(2):621–633, 2013.

- [133] MA DeRousseau, JR Kasprzyk, and WV Stribar III. Computational design optimization of concrete mixtures: A review. *Cement and Concrete Research*, 109:42–53, 2018.
- [134] Stuart Russell and Peter Norvig. Artificial intelligence: a modern approach. 2002.
- [135] M Nehdi, Y Djebbar, and A Khan. Neural network model for preformed-foam cellular concrete. *Materials Journal*, 98(5):402–409, 2001.
- [136] Ahmet Oztacs, Murat Pala, Erdogan Ozbay, Erdogan Kanca, Naci Caglar, and M Asghar Bhatti. Predicting the compressive strength and slump of high strength concrete using neural network. *Construction and building materials*, 20(9):769–775, 2006.
- [137] Jafar Sobhani, Meysam Najimi, Ali Reza Pourkhorshidi, and Tayebeh Parhizkar. Prediction of the compressive strength of no-slump concrete: A comparative study of regression, neural network and anfis models. *Construction and Building Materials*, 24(5):709–718, 2010.
- [138] Min-Yuan Cheng, Jui-Sheng Chou, Andreas FV Roy, and Yu-Wei Wu. High-performance concrete compressive strength prediction using time-weighted evolutionary fuzzy support vector machines inference model. *Automation in Construction*, 28:106–115, 2012.
- [139] Ahmet Raif Bouga, Murat Ozturk, and Ilker Bekir Topcu. Using ann and anfis to predict the mechanical and chloride permeability properties of concrete containing ggbfs and cni. *Composites Part B: Engineering*, 45(1):688–696, 2013.
- [140] Zhen-Hua Duan, Shi-Cong Kou, and Chi Sun Poon. Prediction of compressive strength of recycled aggregate concrete using artificial neural networks. *Construction and Building Materials*, 40:1200–1206, 2013.
- [141] Zhen-Hua Duan, Shi-Cong Kou, and Chi-Sun Poon. Using artificial neural networks for predicting the elastic modulus of recycled aggregate concrete. *Construction and Building Materials*, 44:524–532, 2013.

- [142] Jui-Sheng Chou and Anh-Duc Pham. Enhanced artificial intelligence for ensemble approach to predicting high performance concrete compressive strength. *Construction and Building Materials*, 49:554–563, 2013.
- [143] Vinay Chandwani, Vinay Agrawal, and Ravindra Nagar. Modeling slump of ready mix concrete using genetic algorithms assisted training of artificial neural networks. *Expert Systems with Applications*, 42(2):885–893, 2015.
- [144] Dac-Khuong Bui, Tuan Nguyen, Jui-Sheng Chou, H Nguyen-Xuan, and Tuan Duc Ngo. A modified firefly algorithm-artificial neural network expert system for predicting compressive and tensile strength of high-performance concrete. *Construction and Building Materials*, 180:320–333, 2018.
- [145] Zaher Mundher Yaseen, Ravinesh C Deo, Ameer Hilal, Abbas M Abd, Laura Cornejo Bueno, Sancho Salcedo-Sanz, and Moncef L Nehdi. Predicting compressive strength of lightweight foamed concrete using extreme learning machine model. *Advances in Engineering Software*, 115:112–125, 2018.
- [146] Abdelkader Hammoudi, Karim Moussaceb, Cherif Belebchouche, and Farid Dahmoune. Comparison of artificial neural network (ann) and response surface methodology (rsm) prediction in compressive strength of recycled concrete aggregates. *Construction and Building Materials*, 209:425–436, 2019.
- [147] Amir Tavana Amlashi, Seyed Mohammad Abdollahi, Saeed Goodarzi, and Ali Reza Ghanizadeh. Soft computing based formulations for slump, compressive strength, and elastic modulus of bentonite plastic concrete. *Journal of Cleaner Production*, 230:1197–1216, 2019.
- [148] Trilok Gupta, KA Patel, Salman Siddique, Ravi K Sharma, and Sandeep Chaudhary. Prediction of mechanical properties of rubberised concrete exposed to elevated temperature using ann. *Measurement*, 147:106870, 2019.
- [149] Emadaldin Mohammadi Golafshani, Ali Behnood, and Mehrdad Arashpour. Predicting the compressive strength of normal and high-performance concretes using ann and anfis hybridized with grey wolf optimizer. *Construction and Building Materials*, 232:117266, 2020.

- [150] Dong Van Dao, Hojjat Adeli, Hai-Bang Ly, Lu Minh Le, Vuong Minh Le, Tien-Thinh Le, and Binh Thai Pham. A sensitivity and robustness analysis of gpr and ann for high-performance concrete compressive strength prediction using a monte carlo simulation. *Sustainability*, 12(3):830, 2020.
- [151] Amir Ali Shahmansouri, Maziar Yazdani, Saeed Ghanbari, Habib Akbarzadeh Bengar, Abouzar Jafari, and Hamid Farrokh Ghatte. Artificial neural network model to predict the compressive strength of eco-friendly geopolymers concrete incorporating silica fume and natural zeolite. *Journal of Cleaner Production*, 279:123697, 2021.
- [152] Corinna Cortes and Vladimir Vapnik. Support-vector networks. *Machine learning*, 20(3):273–297, 1995.
- [153] Vladimir Naumovich Vapnik. An overview of statistical learning theory. *IEEE transactions on neural networks*, 10(5):988–999, 1999.
- [154] Xu Juncai, Ren Qingwen, and Shen Zhenzhong. Prediction of the strength of concrete radiation shielding based on ls-svm. *Annals of nuclear energy*, 85:296–300, 2015.
- [155] Johan AK Suykens and Joos Vandewalle. Least squares support vector machine classifiers. *Neural processing letters*, 9(3):293–300, 1999.
- [156] Baojuan Zheng, Soe W Myint, Prasad S Thenkabail, and Rimjhim M Aggarwal. A support vector machine to identify irrigated crop types using time-series landsat ndvi data. *International Journal of Applied Earth Observation and Geoinformation*, 34:103–112, 2015.
- [157] Paresh Chandra Deka et al. Support vector machine applications in the field of hydrology: a review. *Applied soft computing*, 19:372–386, 2014.
- [158] Jigar Patel, Sahil Shah, Priyank Thakkar, and Ketan Kotecha. Predicting stock market index using fusion of machine learning techniques. *Expert Systems with Applications*, 42(4):2162–2172, 2015.

- [159] Adeshina A Adewumi, Taoreed O Owolabi, Ibrahim O Alade, and Sunday O Olatunji. Estimation of physical, mechanical and hydrological properties of permeable concrete using computational intelligence approach. *Applied Soft Computing*, 42:342–350, 2016.
- [160] Mohammad Suhaib Ahmad, Sayed Mohammad Adnan, Sadaf Zaidi, and Pradeep Bhargava. A novel support vector regression (svr) model for the prediction of splice strength of the unconfined beam specimens. *Construction and Building Materials*, 248:118475, 2020.
- [161] Zaher Mundher Yaseen, Minh Tung Tran, Sungwon Kim, Taha Bakhshpoori, and Ravinesh C Deo. Shear strength prediction of steel fiber reinforced concrete beam using hybrid intelligence models: a new approach. *Engineering Structures*, 177:244–255, 2018.
- [162] Behrooz Keshtegar, Mansour Bagheri, and Zaher Mundher Yaseen. Shear strength of steel fiber-unconfined reinforced concrete beam simulation: Application of novel intelligent model. *Composite Structures*, 212:230–242, 2019.
- [163] Anh-Duc Pham, Nhat-Duc Hoang, and Quang-Trung Nguyen. Predicting compressive strength of high-performance concrete using metaheuristic-optimized least squares support vector regression. *Journal of Computing in Civil Engineering*, 30(3):06015002, 2016.
- [164] Aliakbar Gholampour, Iman Mansouri, Ozgur Kisi, and Togay Ozbakkaloglu. Evaluation of mechanical properties of concretes containing coarse recycled concrete aggregates using multivariate adaptive regression splines (mars), m5 model tree (m5tree), and least squares support vector regression (lssvr) models. *Neural Computing and Applications*, 32(1):295–308, 2020.
- [165] Nhat-Duc Hoang, Xuan-Linh Tran, and Hieu Nguyen. Predicting ultimate bond strength of corroded reinforcement and surrounding concrete using a metaheuristic optimized least squares support vector regression model. *Neural Computing and Applications*, 32(11):7289–7309, 2020.

- [166] Junbo Sun, Junfei Zhang, Yunfan Gu, Yimiao Huang, Yuantian Sun, and Guowei Ma. Prediction of permeability and unconfined compressive strength of pervious concrete using evolved support vector regression. *Construction and Building Materials*, 207:440–449, 2019.
- [167] Junfei Zhang, Yimiao Huang, Guowei Ma, Junbo Sun, and Brett Nener. A metaheuristic-optimized multi-output model for predicting multiple properties of pervious concrete. *Construction and Building Materials*, 249:118803, 2020.
- [168] Amin Karbassi, Benyamin Mohebi, Shaliz Rezaee, and Pierino Lestuzzi. Damage prediction for regular reinforced concrete buildings using the decision tree algorithm. *Computers & Structures*, 130:46–56, 2014.
- [169] C Deepa, K SathiyaKumari, and V Pream Sudha. Prediction of the compressive strength of high performance concrete mix using tree based modeling. *International Journal of Computer Applications*, 6(5):18–24, 2010.
- [170] Behzad Abounia Omran, Qian Chen, and Ruoyu Jin. Comparison of data mining techniques for predicting compressive strength of environmentally friendly concrete. *Journal of Computing in Civil Engineering*, 30(6):04016029, 2016.
- [171] Ali Behnood, Venous Behnood, Mahsa Modiri Gharehveran, and Kursat Esat Alyamac. Prediction of the compressive strength of normal and high-performance concretes using m5p model tree algorithm. *Construction and Building Materials*, 142:199–207, 2017.
- [172] Palika Chopra, Rajendra Kumar Sharma, Maneek Kumar, and Tanuj Chopra. Comparison of machine learning techniques for the prediction of compressive strength of concrete. *Advances in Civil Engineering*, 2018, 2018.
- [173] Bradley Efron and Robert J Tibshirani. *An introduction to the bootstrap*. CRC press, 1994.
- [174] Jane Elith, John R Leathwick, and Trevor Hastie. A working guide to boosted regression trees. *Journal of Animal Ecology*, 77(4):802–813, 2008.

- [175] Halil Ibrahim Erdal. Two-level and hybrid ensembles of decision trees for high performance concrete compressive strength prediction. *Engineering Applications of Artificial Intelligence*, 26(7):1689–1697, 2013.
- [176] Qinghua Han, Changqing Gui, Jie Xu, and Giuseppe Lacidogna. A generalized method to predict the compressive strength of high-performance concrete by improved random forest algorithm. *Construction and Building Materials*, 226:734–742, 2019.
- [177] Junfei Zhang, Guowei Ma, Yimiao Huang, Farhad Aslani, Brett Nener, et al. Modelling uniaxial compressive strength of lightweight self-compacting concrete using random forest regression. *Construction and Building Materials*, 210:713–719, 2019.
- [178] Junfei Zhang, Dong Li, and Yuhang Wang. Toward intelligent construction: prediction of mechanical properties of manufactured-sand concrete using tree-based models. *Journal of Cleaner Production*, 258:120665, 2020.
- [179] Hoang Nguyen, Thanh Vu, Thuc P Vo, and Huu-Tai Thai. Efficient machine learning models for prediction of concrete strengths. *Construction and Building Materials*, 266:120950, 2021.
- [180] Furqan Farooq, Wisal Ahmed, Arslan Akbar, et al. Predictive modelling for sustainable high-performance concrete from industrial wastes: A comparison and optimization of models using ensemble learners. *Journal of Cleaner Production*, page 126032, 2021.
- [181] Ahmed Ramadan Suleiman and Moncef L Nehdi. Modeling self-healing of concrete using hybrid genetic algorithm–artificial neural network. *Materials*, 10(2):135, 2017.
- [182] Xiaoying Zhuang and Shuai Zhou. The prediction of self-healing capacity of bacteria-based concrete using machine learning approaches. *Computers, Materials & Continua* 59 (2019), Nr. 1, 2019.
- [183] Standards Australia 2010. General purpose and blended cements. AS 3972-2010, Standards Association of Australia, Sydney, Australia, 2010.

- [184] Estefanía Cuenca, Antonio Tejedor, and Liberato Ferrara. A methodology to assess crack-sealing effectiveness of crystalline admixtures under repeated cracking-healing cycles. *Construction and Building Materials*, 179:619–632, 2018. ISSN 0950-0618.
- [185] ASTM. *ASTM C1202 Standard Test Method for Electrical Indication of Concrete's Ability to Resist Chloride Ion Penetration*. 2012.
- [186] Stefan Jacobsen and Erik J. Sellevold. Self healing of high strength concrete after deterioration by freeze/thaw. *Cement and Concrete Research*, 26:55–62, 1996. ISSN 0008-8846. doi: 10.1016/0008-8846(95)00179-4.
- [187] Gurkan Yildirim, Gulsum Hasiloglu Aras, Qais Sahib Banyhussan, Mustafa Şahmaran, and Mohamed Lachemi. Estimating the self-healing capability of cementitious composites through non-destructive electrical-based monitoring. *NDT & E International*, 76:26–37, 2015. ISSN 0963-8695.
- [188] C09 Committee. Standard Test Method for Splitting Tensile Strength of Cylindrical Concrete Specimens. Technical report, ASTM International. URL <http://www.astm.org/cgi-bin/resolver.cgi?C496C496M-17>. West Conshohocken, PA, 2017, www.astm.org.
- [189] Michael T Postek. The scanning electron microscope. 1997.
- [190] Haoliang Huang. *Thermodynamics of Autogenous Self-Healing in Cementitious Materials*. PhD thesis, [s.n.], S.l., 2014.
- [191] Jian Zhou, Shunzhi Qian, M. Guadalupe Sierra Beltran, Guang Ye, Klaas van Breugel, and Victor C. Li. Development of engineered cementitious composites with limestone powder and blast furnace slag. *Materials and Structures*, 43: 803–814, 2010.
- [192] Jun-Feng Su, Ying-Yuan Wang, Ning-Xu Han, Peng Yang, and Shan Han. Experimental investigation and mechanism analysis of novel multi-self-healing behaviors of bitumen using microcapsules containing rejuvenator. *Construction and Building Materials*, 106:317–329, 2016. ISSN 0950-0618. doi: 10.1016/j.conbuildmat.2015.12.120.

- [193] Babatunde Abiodun Salami, Megat Azmi Megat Johari, Zainal Ariffin Ahmad, and Mohammad Maslehuddin. Impact of added water and superplasticizer on early compressive strength of selected mixtures of palm oil fuel ash-based engineered geopolymers composites. *Construction and Building Materials*, 109: 198–206, 2016. ISSN 0950-0618. doi: 10.1016/j.conbuildmat.2016.01.033.
- [194] Huy Hoang Nguyen, Jeong-Il Choi, Se-Eon Park, Sang Lyul Cha, Jungwon Huh, and Bang Yeon Lee. Autogenous healing of high strength engineered cementitious composites (ecc) using calcium-containing binders. *Construction and Building Materials*, 265:120857, 2020.
- [195] Kevin Rhodes, Roberta Meisner, Yoongu Kim, Nancy Dudney, and Claus Daniel. Evolution of phase transformation behavior in li (mn1. 5ni0. 5) o4 cathodes studied by in situ xrd. *Journal of the electrochemical society*, 158: A890, 2011.
- [196] P Saravanakumar, K Abhiram, and B Manoj. Properties of treated recycled aggregates and its influence on concrete strength characteristics. *Construction and Building Materials*, 111:611–617, 2016.
- [197] Emily N Herbert and Victor C Li. Self-healing of microcracks in engineered cementitious composites (ecc) under a natural environment. *Materials*, 6(7): 2831–2845, 2013.
- [198] Hezhi Liu, Qian Zhang, Chongshi Gu, Huaizhi Su, and Victor Li. Influence of microcrack self-healing behavior on the permeability of engineered cementitious composites. *Cement and Concrete Composites*, 82:14–22, 2017.
- [199] Yu Zhu, Yingzi Yang, and Yan Yao. Use of slag to improve mechanical properties of engineered cementitious composites (ECCs) with high volumes of fly ash. *Construction and Building Materials*, 36:1076–1081, 2012. ISSN 0950-0618. doi: 10.1016/j.conbuildmat.2012.04.031.
- [200] Tanvir Qureshi, Antonios Kanellopoulos, and Abir Al-Tabbaa. Autogenous self-healing of cement with expansive minerals-i: Impact in early age crack healing. *Construction and Building Materials*, 192:768–784, 2018.

- [201] Li-Li Kan, Hui-Sheng Shi, Aaron R. Sakulich, and Victor C. Li. Self-Healing Characterization of Engineered Cementitious Composite Materials. *Aci Materials Journal*, 107:617–624, 2010. ISSN 0889-325X.
- [202] En-Hua Yang. *Designing Added Functions in Engineered Cementitious Composites*. ProQuest, 2008.
- [203] Didier Snoeck and Nele De Belie. Mechanical and self-healing properties of cementitious composites reinforced with flax and cottonised flax, and compared with polyvinyl alcohol fibres. *Biosystems Engineering*, 111(4):325–335, 2012. ISSN 1537-5110. doi: 10.1016/j.biosystemseng.2011.12.005.
- [204] Jayant D Bapat. *Mineral admixtures in cement and concrete*. CRC Press, 2012.
- [205] RD Hooton, P Pun, T Kojundic, and P Fidjestol. Influence of silica fume on chloride resistance of concrete. In *Proceeding International Symposium of High Performance Concrete, Chicago, (P. Johal, Precast Prestressed Concrete Institute) pp*, pages 245–249, 1997.
- [206] Sung-Hoon Kang, Yeonung Jeong, Min Ook Kim, and Juhyuk Moon. Pozzolanic reaction on alkali-activated class f fly ash for ambient condition curable structural materials. *Construction and Building Materials*, 218:235–244, 2019.
- [207] Gürkan Yıldırım, Arash Hamidzadeh Khiavi, Seda Yeşilmen, and Mustafa Şahmaran. Self-healing performance of aged cementitious composites. *Cement and Concrete Composites*, 87:172–186, 2018.
- [208] Terence C Holland. *Silica fume user's manual*. Federal Highway Administration, 2005.
- [209] G Appa Rao. Investigations on the performance of silica fume-incorporated cement pastes and mortars. *Cement and Concrete Research*, 33(11):1765–1770, 2003.
- [210] Zemei Wu, Kamal H Khayat, and Caijun Shi. Changes in rheology and mechanical properties of ultra-high performance concrete with silica fume content. *Cement and Concrete Research*, 123:105786, 2019.

- [211] Mustafa Şahmaran and Victor C Li. Durability properties of micro-cracked ecc containing high volumes fly ash. *Cement and Concrete Research*, 39(11):1033–1043, 2009.
- [212] Kim Van Tittelboom, Nele De Belie, Erik Schlangen, and Mario De Rooij. *Self-Healing Phenomena in Cement-Based Materials State-of-the-Art Report of RILEM Technical Committee 221-SHC Self-Healing Phenomena in Cement-Based Materials*. Springer, 2013.
- [213] R Sriravindrarajah and Gavin Baracz. High strength ultrafine fly ash concrete with silica fume or hydrated lime addition. *International Journal of Constructive Research in Civil Engineering*, 1(1):14–18, 2015.
- [214] FIP Commission on concrete, Working Group on Condensed Silica Fume in Concrete, editor. *Condensed Silica Fume in Concrete*. FIP State of Art Report. Telford, London, 1988. ISBN 978-0-7277-1373-5.
- [215] P. K. Mehta and O. E. Gjørv. Properties of portland cement concrete containing fly ash and condensed silica-fume. *Cement and Concrete Research*, 12(5):587–595, 1982.
- [216] Khashayar Ebrahimi, Mohammad Javad Daiezadeh, Mohammad Zakertabrizi, Farhad Zahmatkesh, and Asghar Habibnejad Korayem. A review of the impact of micro- and nanoparticles on freeze-thaw durability of hardened concrete: Mechanism perspective. *Construction and Building Materials*, 186:1105–1113, 2018. ISSN 0950-0618. doi: 10.1016/j.conbuildmat.2018.08.029.
- [217] Davoud Tavakoli, Masoumeh Hashempour, and Ali Heidari. Use of Waste Materials in Concrete: A review. *Pertanika Journal of Science & Technology*, 26(2), 2018.
- [218] Mohammad Iqbal Khan and Rafat Siddique. Utilization of silica fume in concrete: Review of durability properties. *Resources, Conservation and Recycling*, 57:30–35, 2011. ISSN 0921-3449. doi: 10.1016/j.resconrec.2011.09.016.
- [219] Rafat Siddique. Utilization of silica fume in concrete: Review of hardened properties. *Resources, Conservation and Recycling*, 55(11):923–932, 2011.

- [220] S. Bhanja and B. Sengupta. Influence of silica fume on the tensile strength of concrete. *Cement and Concrete Research*, 35:743–747, 2005. ISSN 0008-8846.
- [221] S Wild, BB Sabir, and JM Khatib. Factors influencing strength development of concrete containing silica fume. *Cement and Concrete Research*, 25(7):1567–1580, 1995.
- [222] S. A. Barbhuiya, J. K. Gbagbo, M. I. Russell, and P. A. M. Basheer. Properties of fly ash concrete modified with hydrated lime and silica fume. *Construction and Building Materials*, 23:3233–3239, 2009. ISSN 0950-0618.
- [223] MI Khan. Isoresponses for strength, permeability and porosity of high performance mortar. *Building and Environment*, 38(8):1051–1056, 2003.
- [224] Alaa M. Rashad. A brief on high-volume Class F fly ash as cement replacement – A guide for Civil Engineer. *International Journal of Sustainable Built Environment*, 4:278–306, 2015. ISSN 2212-6090. doi: 10.1016/j.ijsbe.2015.10.002.
- [225] Vikas Srivastava, Rakesh Kumar, V. C. Agarwal, and P. K. Mehta. Effect of Silica Fume on Workability and Compressive Strength of OPC Concrete. *J. Environ. Nanotechnol*, 3(3):32–35.
- [226] Camelia M Vladu, Christopher Hall, and Geoffrey C Maitland. Flow properties of freshly prepared ettringite suspensions in water at 25 degree. *Journal of colloid and interface science*, 294(2):466–472, 2006.
- [227] Wentao Li, Yaolin Yi, and Anand J Puppala. Suppressing ettringite-induced swelling of gypseous soil by using magnesia-activated ground granulated blast-furnace slag. *Journal of Geotechnical and Geoenvironmental Engineering*, 146(7):06020008, 2020.
- [228] Pavan Akula and Dallas N Little. Mineralogical characterization and thermodynamic modeling of synthesized ettringite from ca-al-so₄ suspensions. *Construction and Building Materials*, 269:121304, 2021.

- [229] Marcelo Tramontin Souza, Lucas Onghero, Bruna Nunes Correa, Maria Angelica Selhorst, Ariely Miranda Dias, Wellington Longuini Repette, Fabiano Raupp Pereira, and Antonio Pedro Novaes de Oliveira. Novel low-cost shrinkage-compensating admixture for ordinary portland cement. *Construction and Building Materials*, 230:117024, 2020.
- [230] Lian-Hua Fu, Yan-Yan Dong, Ming-Guo Ma, Shu-Ming Li, and Run-Cang Sun. Compare study caco₃ crystals on the cellulose substrate by microwave-assisted method and ultrasound agitation method. *Ultrasonics sonochemistry*, 20(3):839–845, 2013.
- [231] Ahmad Shayan, GW Quick, and CJ Lancucki. Morphological, mineralogical and chemical features of steam-cured concretes containing densified silica fume and various alkali levels. *Advances in Cement Research*, 5(20):151–162, 1993.
- [232] Yongqi Wei, Wu Yao, Xiaoming Xing, and Manjian Wu. Quantitative evaluation of hydrated cement modified by silica fume using qxrd, 27al mas nmr, tg-dsc and selective dissolution techniques. *Construction and Building Materials*, 36:925–932, 2012.
- [233] Ismail Demir and M Serhat Baspinar. Effect of silica fume and expanded perlite addition on the technical properties of the fly ash–lime–gypsum mixture. *construction and Building Materials*, 22(6):1299–1304, 2008.
- [234] Shuai Fan and Mo Li. X-ray computed microtomography of threedimensional microcracks and self-healing in engineered cementitious composites. *Smart Materials and Structures*, 24(1), 2015. ISSN 0964-1726. doi: 10.1088/0964-1726/24/1/015021.
- [235] Andrej Ipavec, Roman Gabrovšek, Tomaž Vuk, Venčeslav Kaučič, Jadran Maček, and Anton Meden. Carboaluminate phases formation during the hydration of calcite-containing portland cement. *Journal of the American Ceramic Society*, 94(4):1238–1242, 2011.

- [236] Magdalena Rajczakowska, Karin Habermehl-Cwirzen, Hans Hedlund, and Andrzej Cwirzen. The effect of exposure on the autogenous self-healing of ordinary portland cement mortars. *Materials*, 12(23):3926, 2019.
- [237] Robert Elfed Davies. *Micromechanical Modelling of Self-Healing Cementitious Materials*. Phd, Cardiff University, 2014.
- [238] D Eliche-Quesada, J Sánchez-Martínez, MA Felipe-Sesé, and A Infantes-Molina. Silica–calcareous non fired bricks made of biomass ash and dust filter from gases purification. *Waste and Biomass Valorization*, 10:417–431, 2019.
- [239] John Neter, Michael H Kutner, Christopher J Nachtsheim, and William Wasserman. *Applied linear statistical models*, volume 4. Irwin Chicago, 1996.
- [240] SF Fang, MP Wang, WH Qi, and F Zheng. Hybrid genetic algorithms and support vector regression in forecasting atmospheric corrosion of metallic materials. *Computational Materials Science*, 44(2):647–655, 2008.
- [241] Yankun Li, Xueguang Shao, and Wensheng Cai. A consensus least squares support vector regression (ls-svr) for analysis of near-infrared spectra of plant samples. *Talanta*, 72(1):217–222, 2007.
- [242] P Yuvaraj, A Ramachandra Murthy, Nagesh R Iyer, SK Sekar, and Pijush Samui. Support vector regression based models to predict fracture characteristics of high strength and ultra high strength concrete beams. *Engineering fracture mechanics*, 98:29–43, 2013.
- [243] Alex J Smola and Bernhard Schölkopf. A tutorial on support vector regression. *Statistics and computing*, 14(3):199–222, 2004.
- [244] Abhijit Mukherjee and Sudip Nag Biswas. Artificial neural networks in prediction of mechanical behavior of concrete at high temperature. *Nuclear engineering and design*, 178(1):1–11, 1997.
- [245] Hosein Naderpour, Amir Hossein Rafiean, and Pouyan Fakharian. Compressive strength prediction of environmentally friendly concrete using artificial neural networks. *Journal of Building Engineering*, 16:213–219, 2018.

- [246] Fei Yan, Zhibin Lin, Xingyu Wang, Fardad Azarmi, and Konstantin Sobolev. Evaluation and prediction of bond strength of gfrp-bar reinforced concrete using artificial neural network optimized with genetic algorithm. *Composite Structures*, 161:441–452, 2017.
- [247] Marai M Alshihri, Ahmed M Azmy, and Mousa S El-Bisy. Neural networks for predicting compressive strength of structural light weight concrete. *Construction and Building Materials*, 23(6):2214–2219, 2009.
- [248] Leo Breiman. *Classification and regression trees*. 2017.
- [249] R Put, C Perrin, F Questier, D Coomans, DL Massart, and Y Vander Heyden. Classification and regression tree analysis for molecular descriptor selection and retention prediction in chromatographic quantitative structure–retention relationship studies. *Journal of Chromatography A*, 988(2):261–276, 2003.
- [250] S Dan and P Colla. Cart: Tree-structured non-parametric data analysis. *Salford Systems, San Diego, CA*, 1995.
- [251] Dimitrios Frosyniotis, Andreas Stafylopatis, and Aristidis Likas. A divide-and-conquer method for multi-net classifiers. *Pattern Analysis & Applications*, 6(1):32–40, 2003.
- [252] Thomas G Dietterich. Ensemble methods in machine learning. In *International workshop on multiple classifier systems*, pages 1–15. Springer, 2000.
- [253] Leo Breiman. Bagging predictors. *Machine learning*, 24(2):123–140, 1996.
- [254] Yoav Freund, Robert E Schapire, et al. Experiments with a new boosting algorithm. In *Icml*, volume 96, pages 148–156. Citeseer, 1996.
- [255] An ensemble-learning meta-regressor for stacking regression. http://rasbt.github.io/mlxtend/user_guide/regressor/StackingCVRegressor/#stackingcvregressor. Accessed: 2020-01-30.
- [256] Joseph Sill, Gábor Takács, Lester Mackey, and David Lin. Feature-weighted linear stacking. *arXiv preprint arXiv:0911.0460*, 2009.

- [257] Ron Kohavi et al. A study of cross-validation and bootstrap for accuracy estimation and model selection. In *Ijcai*, volume 14, pages 1137–1145. Montreal, Canada, 1995.
- [258] Ofer Dor and Yaoqi Zhou. Achieving 80% ten-fold cross-validated accuracy for secondary structure prediction by large-scale training. *Proteins: Structure, Function, and Bioinformatics*, 66:838–845, 2007.
- [259] Xin Yao. Evolutionary artificial neural networks. *International journal of neural systems*, 4(03):203–222, 1993.
- [260] Morteza Vadood, Majid Safar Johari, and Alireza Rahai. Developing a hybrid artificial neural network-genetic algorithm model to predict resilient modulus of polypropylene/polyester fiber-reinforced asphalt concrete. *The Journal of the Textile Institute*, 106(11):1239–1250, 2015.
- [261] Han-Xiong Huang, Jiong-Cheng Li, and Cheng-Long Xiao. A proposed iteration optimization approach integrating backpropagation neural network with genetic algorithm. *Expert Systems with Applications*, 42(1):146–155, 2015.
- [262] Nii O Attoh-Okine. Analysis of learning rate and momentum term in back-propagation neural network algorithm trained to predict pavement performance. *Advances in Engineering Software*, 30(4):291–302, 1999.
- [263] Darrell Whitley, Soraya Rana, John Dzubera, and Keith E Mathias. Evaluating evolutionary algorithms. *Artificial intelligence*, 85(1-2):245–276, 1996.
- [264] Wen-Yang Lin, Wen-Yung Lee, and Tzung-Pei Hong. Adapting crossover and mutation rates in genetic algorithms. *J. Inf. Sci. Eng.*, 19(5):889–903, 2003.